Department of Applied Physics

University of Granada

Study Of Structured Surfaces From Micro- to Nano-Scale Topography For Bioadhesive Applications

A thesis presented by:

Pedro Jesús Ramón Torregrosa.

Thesis supervisors:

Dr. **Miguel Ángel Cabrerizo Vílchez.**

Dr. **Miguel Ángel Rodríguez Valverde.**

- November 2015 -

Editor: Universidad de Granada. Tesis Doctorales
Autor: Pedro Jesús Ramón Torregrosa
ISBN: 978-84-9125-721-9
URI: http://hdl.handle.net/10481/43485

El doctorando Pedro Jesús Ramón Torregrosa, junto con sus directores de tesis doctoral; D. Miguel Ángel Cabrerizo Vílchez, Catedrático de Universidad, y D. Miguel Ángel Rodríguez Valverde, Profesor Titular de Universidad

GARANTIZAMOS, al firmar esta tesis doctoral, titulada Study Of Structured Surfaces From Micro- to Nano-Scale Topography For Bioadhesive Applications, que el trabajo realizado por el doctorando bajo la dirección de los directores de la tesis y hasta donde nuestro conocimiento alcanza, en la realización del trabajo, se han respetado los derechos de otros autores a ser citados, cuando se ha utilizado sus resultados o publicaciones.

Granada, 10 de Noviembre de 2015

Fdo: Miguel Ángel Cabrerizo Vílchez Miguel Ángel Rodríguez Valverde

Fdo: Pedro Jesús Ramón Torregrosa

Trabajo presentado para aspirar al grado de
DOCTOR EN CIENCIAS FÍSICAS

Este trabajo ha sido financiado por el “Ministerio Español de Economía
y Competitividad”a través del proyecto MAT2014-60615-R, por la
Junta de Andalucía y FEDER mediante el proyecto P12-FQM-1443,
y la beca de Formación de Profesorado Universitario (FPU)
con referencia AP-2004-2915

Contents

Agradecimientos

Dí a quien pretenda una ciencia enciclopédica:
Sabes algo, pero se te escapan cosas.

Abú Nuwás

Puede que ésta sea la única página de la tesis que escribo con absoluta satisfacción, y con plena seguridad, ahora que por fin se adivina el final del camino en el que hace ya tantos años me embarqué y que tantas veces, sobre todo en los últimos años, dudé ser capaz de recorrer. En estos años han sido muchas las etapas que he ido superando y no de todas me puedo sentir orgulloso. De cualquier modo, en todo mi periplo hay gente a la que tengo demasiado que agradecer y a muchos de ellos no debería bastarles con estas simples palabras.

En primer lugar, mi más sincero agradecimiento va para Miguel Ángel Rodríguez Valverde, quien ha aportado la experiencia, fuerza, determinación e ilusión que tantas veces me faltó durante la realización de este trabajo. Tras los muchos años que he tenido el placer de conocerlo como profesor, amigo y jefe, descubro que sólo tengo buenas palabras hacia su encomiable labor como científico y tutor. Inquebrantable ante el desaliento, a él también le debo muchos de los mejores momentos en el trabajo, tardes de animada discusión en las que la investigación en física recobraba el matiz romántico y emocionante que alguna vez para mí tuvo.

Toda mi gratitud también para Miguel Cabrerizo Vílchez, estimado profesor. Desde mis comienzos como doctorando, siempre ha sabido enfocar los problemas con una gran simplicidad y me ha "obligado" a esforzarme para explicar las ideas que me rondaban la cabeza con la didáctica que requerían. Sin duda, él ha sido mi público más duro y por elllo le agradezco enormemente su ayuda y amabilidad, así como los certeros consejos que me supo dar.

A Roque Hidalgo, por su impulso para que, finalmente, decidiera acabar y defender esta tesis. Como tú dirías: ¡Bendita burocracia! la que ha evitado que tirara a la basura 4 años de trabajo, buenos ratos, sinsabores,...

I would like to express my deepest gratitude to Dr. Alidad Amirfazli, a talented teacher and passionate scientist, for his excellent guidance, caring and patience.

Agradecer a Felix Daniel Nieto y su grupo de investigación de la Universidad Nacional de San Luís (Argentina), la hospitalidad y amabilidad mostrada durante la estancia que disfruté por allá hace ya unos añitos.

Muchas gracias, en general, a todos los miembros del grupo de investigación de Física de Coloides e Interfases de la Universidad de Granada por haberme tratado tan afectuosamente durante esos años. Un placer.

Sin duda, como todo problema físico, la solución siempre depende de las condiciones de contorno, y esas condiciones, en el caso de esta tesis doctoral, son todas aquellas personas que de alguna manera intervinieron en ella. Así que muchas gracias a Julia, Alberto, María, Catalina,

Pedro, Miguel Wulff, Miguel Alberto Pelaez, Fernando Vereda,... Seguramente se me quede alguno en el tintero pero habéis sido muchos y se supone que los agradecimientos no deberían ser más extensos que la propia tesis.

He querido dejar al margen del párrafo anterior a cinco personas a las que quiero agradecer, especialmente, el que estuvieran a mi lado durante todo el tiempo que dediqué a la elaboración de este trabajo.

Javi, compañero de fatigas en el subsuelo de la facultad de ciencias durante tanto tiempo, siento haberte traicionado. Quizás debieras haberme juzgado por sedición. Muchas gracias por escucharme siempre y tener siempre una palabra de aliento.

Sándalo, el científico más puro y purista que he conocido y uno de mis mejores maestros, gracias por las conversaciones sobre física, matemáticas, literatura, parrafadas filosófica,...

Fernando Martínez, gracias por tus mil y una caras, por ser puro teatro y por enseñarme a reirme de mis propios fantasmas.

Alberto de la Ossa y Juan Carlos, los Zipi y Zape con los que he compartido en todos estos años alegrías, llantos, amarguras y penas ahogadas en palabras y risas. Gracias por estar siempre ahí y ser siempre vosotros. Os debo mucho más de lo que soy capaz de expresar en palabras.

Además de los que he mencionado anteriormente no puedo olvidarme de Sabina (compartiste conmigo muchos de los malos tragos y alegrias de esta tesis, gracias por ser mi apoyo en esos momentos), Evangelia (ángel de la guarda e incondicional apoyo), Victor y Chica (gracias por enseñarme a ver la vida con otros ojos y contemplar una paleta de colores más viva que el binario blanco y negro), Ahinoa, Ana Antúnez, Rafael Serrano, Rocio, Antonio Reyes, Pepe Navarro, Juan Pedro, Leticia... sois muchos más de los que aparecéis aunque os prometo que no me olvido de ninguno.

Por último, me gustaría agradecer y dedicar esta tesis a las personas que siempre me han apoyado y que me llenan de amor y confianza; mis padres, Pedro y Quiteria, y a mi hermano y su mujer, Raúl y Mari. No os suelo decir cuan importantes sois para mi, valgan esta palabras para pagar parcialmente esa deuda.

Raúl y Jorge aún no están en disposición de entender ésto pero quizás algún día...

Pedro J. Ramón Torregrosa

Chirivel, 15 de Octubre de 2015.

Chapter 1

Introduction

This chapter collects the theoretical background of the current dissertation. The chapter is divided into three sections.

- The first section is devoted to titanium surfaces. Due to their good biocompatibility, titanium surfaces are widely used as biosurfaces in the implantology field to design dental implants.To improve the biological response of titanium surfaces, their surface properties and/or chemical composition are modified. In this sense, this section summarizes the typical methods used to modify titanium surface properties and to improve their osseointegration to the host.
- The second section of this chapter presents a brief historical review of the impact of surfaces on science and technology and it introduces the mathematical tools used in this thesis to characterize surface morphology, such as scaling analysis and Minkowski functionals.
- The third section describes the wetting properties of solid surfaces providing their theoretical background. This section deals the different wetting behaviors for smooth and rough surfaces, and chemically homogeneous and heterogeneous surfaces.

1.1 Titanium as Biomaterial

From the mathematical point of view, a surface is defined as a two-dimensional topological manifold. However, from the surface science, this definition must be adapted because a surface or interface is the space region forming a common boundary among two different phases. Particularly, a biomaterial surface (natural or man-made) interacts with biological systems.

As biomaterial, unalloyed or alloyed titanium[1] has been widely used to construct dental implants because of its good biocompatibility and mechanical properties. Rapid achievement of a stable osseointegration between implant and bone tissues of the host is the main aim. Because surface properties play a critical role to achieve successful osseointegration, many efforts have been addressed to modify titanium surfaces.

Titanium is classified into two types: commercially pure titanium (Ti), which is used in chemical process industries, and titanium alloys with additives such as aluminium (Al) and vanadium (V), which are used for jet aircraft engines, airframes and other components. According to the content of oxygen, commercially pure titanium is classified into four grades, from grade 4 (0.4%) to grade 1 (0.18%) [1]. The good biocompatibility of the unalloyed and alloyed titanium surface is due to the rapid formation of a thin film of Titanium dioxide (TiO_2) in rich oxygen atmospheres. This thin oxide layer, with a thickness between 2 and 10 nm and which it is spontaneously developed, provides corrosion resistance to the surface [2–4]. The interaction between the titanium surfaces and biological fluids is through this stable oxide layer [5, 6]. Thickness and chemical composition of titanium oxide layers play an important role for adsorption of proteins from biological fluids as precursor stage of cell adhesion. From the formation or controlled deposition of the oxide layer, unalloyed and alloyed titanium have been widely used as joint replacement parts, bone fixation materials or dental implants [2–6].

Good osseointegration should be essentially reached at the interface between implant surface and living bone during healing procedure after implantation surgery [7]. Surface properties of the implant play a very important role in the immediate reactions on the implant surface after exposure to tissue. During the past decades, many surface modifications such as coating, abrasion, blasting, acid etching, oxidation, or combinations of these techniques, were proposed to improve the biocompatibility of the implant surface by altering surface topography, physical characteristics and chemical properties of titanium [8].

1.1.1 Surface Treatments in Biomaterial Engineering

In order to improve the bioactivity of commercially pure titanium surfaces, and consequently to improve the osseointegration capabilities of titanium implants, many methods have been employed. According to the nature of the process used to modify the biomaterial surface, these methods can be classified into three categories:

1. Physical techniques, which mostly make changes on surface morphology/topography without alteration of chemical composition of titanium surfaces. Physical modifications of the titanium surfaces mainly affect the roughness. Machined, sandblasted, and titanium plasma-sprayed titanium have been already tested in vitro by many authors [9–11]. These methods have been applied by manufacturers to produce commercial implant systems [12].

[1] Titanium was discovered some 200 years ago in England, and began to be used practically in 1948 when its commercial production started in the United States of America. Titanium is a lightweight and strong material with a tensile strength comparable to carbon steels, and because the Young's modulus of titanium is only a half of carbon steel, titanium is soft and improve readily worked.

2. Chemical treatments, which exclusively affect the surface chemistry rather than the surface topography. It is well known that the chemical composition of titanium surfaces is important for protein adsorption from biological fluids and for the following cell response. Any change on surface chemistry affects to cell behavior (attachment, adhesion, proliferation,...) [13–16]. Moreover, it has been reported that titanium surfaces are reachly contaminated by adventitious elements from still air, such as C and N. Contamination of titanium surfaces also affects its biocompatibility [17]. The methods more used to modify the surface chemistry are acid etching (the use of HF, HNO_3, H_2SO_4 as etchant agents is very common.) [11,18,19], and the formation of hydroxyapatite as surface coatings [20, 21].

3. Combinations of physical and chemical techniques can alter both physical characteristics and chemical composition of titanium surfaces at the same time, or produce a more intensive modification than by using only one unique technique. The combinated techniques more used are sandblasted with large grit and acid etched [22, 23] and electropolishing technique [24].

1.1.2 Cell Response on Titanium Surfaces

Since titanium surfaces are employed to manufacture dental implants, from the implantology point of view, the target cells are usually the osteoblast-like cells. An osteoblast-like cell is, according to Oxford Dictionary of Biochemistry, a mesenchymal cell that secretes the organic matrix of bone (i.e. osteoid, consisting chiefly of collagen); as the matrix becomes calcified the osteoblast becomes trapped and at is known as an osteocyte.

The story of osteoblast-like cells gone back to 1853 when Tomes and de Morgen described the existence of a type of cells intimately associated with newly formed bone [25]. In 1864, the term "osteoblast" was first used by Gegenbaur to refer to the "granular corpuscles found in all developing bone as the active agents of osseous growth" [26].

Osteoblasts, which are originated from osteoprogenitor cells and preosteoblasts, play a pivotal role in bone formation. During differentiation of the osteoblastic cell lineage, the preosteoblast expresses transforming growth factor, which induces osteoblast cell proliferation [27]. Osteoblasts settle at the surface of the existing matrix and deposit fresh layers of bone onto it. New bone matrix is secreted by osteoblasts, and osteoid is formed, which consists chiefly of type I collagen and the small portion $(10-20\%)$ of embedded osteoblasts. While osteoid is rapidly converted into hard bone matrix by the deposition of calcium phosphate crystals, osteoblasts differentiate into mature bone cells, osteocytes. Although the osteocyte continues to secret new bone matrix around itself, it cannot further divide. Besides osteocytes, osteoblasts can also differentiate into the other mature cell type, bone-lining cells. The lining cell is inactive and lacks the ability to secret new bone matrix. However, investigations from Chow and coworkers have shown that these cells can be reactivated into bone-producing osteoblasts [28].

The proliferation and differentiation of osteoblastic cells are regulated by systemic agents and a large number of growth factors and cytokines existing in extracellular matrix, for instance, the insulin-like growth factors, the transforming growth factors, fibroblast growth factors, bone morphogenetic proteins,... Correspondingly, there are many sorts of receptors for these factors on the cell membrane of osteoblasts, and binding of these factors to their receptors activates signal transduction pathways that finally lead to nuclear responses.

Recently, literature has reported that surface roughness, wettability and chemical compositions may influence on protein adsorption onto the titanium surface and hence, cell response on substrates [29–33]. However, how these surface properties affect the cell behavior is still unclear. The cell response can be divided into cytotoxicity, cell attachment/adhesion and spreading, and cell

proliferation and differentation.

Cytotoxicity: The cytotoxicity is defined as the degree to which an agent has specific destructive action on certain cells. Although it is well known that titanium has no cytotoxicity for human cells and therefore it can be used to be implanted into human bodies, some reports showed that titanium ions released into the body fluid from titanium implants during application may cause cellular damages [34, 35] due to the dissolution, under spetial conditions, of these ions into the surrounding tissues. These special conditions mentioned above could be promoted by the surface modification methods due to the changes on the physical and chemical characteristics of the resultant titanium surface. Also, these physicochemical changes could affect to the dynamic mechanisms for titanium ion release or contaminate titanium oxides with some toxic chemical elements or molecules.

Attachment/adhesion and spreading: Cell attachment can be defined as the binding of a cell to another cell or to an extracellular matrix component. On the other hand, cell spreading means the extension of cells on the surface material once the cell is attached. These responses involve multiple steps: (1) adsorption of proteins to the substrate, mainly integrin, selectin, mucin family,... [36, 37]; (2) interaction between special receptors on the cell membrane which combine with the proteins adsorbed onto the substrate; and (3) spreading of cells on the substrate [38]. Therefore they are considered as crucial indexes of the biocompatibility of materials. Particularly, for dental implants, these processes are so important because osteoblasts contact the surface of implanted biomaterials in very short time when biomaterials are implanted into the host. Consequently, since cellular attachment, adhesion and spreading belong to the first phase of cell/material interactions, the quality of this phase will influence on posterior cell responses, i.e. proliferation and differentiation, on biomaterials surfaces.

Cell adhesion may be affected by surface characteristics of materials, such as their physical properties, chemical composition, and topography. In fact, as several works demonstrated, adhesion and proliferation of osteoblasts in vitro or the extent of bone contact in vivo is positively correlated with the increasing of roughness [39,40], though these relationships are not clear. So, some authors found that the correlation between roughness and bone apposition is not a simple relationship, as it was found that a significantly increased bone apposition to an implant surface was only achieved inside a specific roughness range, and smoother or rougher surfaces produced lower bone response [41, 42]. On the other hand, the contrary conclusion was also drawn, i.e. that cell attachment to rougher titanium surfaces was lower than to smoother titanium surfaces [10]. Moreover, surface roughness needs to be considered not only in term of amplitude but also in terms of texture [43]. Surface roughness was extensively analyzed at scales above cell size (macro-roughness) or below cell size (micro/nano-roughness), and it was found that when the surface roughness was below cell scale, human osteoblasts (hOBs) appreciated their isotropic smooth aspect, although when topography was considered above cell scale, hOBs appreciated their rough isotropic surface [44]. At the molecular level, it has been proven that surface roughness modulates the local regulatory factors produced by osteoblast-like Mg-63 cells [30], i.e., secretion of prostaglandin E2 (PGE2) and transforming growth factor $\beta - 1$ ($TGF - \beta - 1$) was increased when cultured on rough surfaces. Boyan and co-workers have reviewed the mechanism that surface roughness mediates several effects on osteoblasts [45].

Traditional titanium modification methods can produces irregular surface topography with valleys or spikes, while special physical or chemical techniques could create regular surface topographies. Jayaraman et al. [46] compared the influence of two different titanium implant surfaces on attachment of osteoblast-like cells in vitro, a sandblasted and acid etched surface and an experimental-engraved surface. It was found that osteoblast-like cells performed better concerning, adhesion and proliferation, on the engraved surfaces than on rough surfaces. In addition, the

porous geometries of titanium surfaces may also affect osteoblastic cell behavior to materials [47].

Chemical composition of the titanium surfaces should also be carefully investigated. X-ray photoemission spectroscopy (XPS) and Auger electron spectroscopy (AES) have been widely used to measure the chemical composition of biomaterial surfaces [48–50]. Moreover, although the chemical compositions of *c.p. Ti* grade 1 and 4 are more than 99% similar, a differential response of human osteoblast-like cells was found towards these two grades of commercially pure titanium (*c.p. Ti*). Ahmad et al. found that between 4 and 24 h after seeding cells onto titanium specimens, the rate of cell attachment to grade 1 Ti was significantly different to grade 4 and glass, which served as control. Significant differences in expression of vinculin, collagen synthesis and calcium content were detected as well between grade 1 and grade 4 *c.p. Ti* [51].

By comparing the initial attachment and subsequent spreading of human osteoblastic cells on *c.p. Ti*, hydroxyapatite and glass, Okumura et al. found that on hydroxyapatite the cells started extension earlier and more quickly than on titanium. They also suggested that earlier osteogenesis may occur on hydroxyapatite rather than on other materials [52]. Equally, collagen, which acts as one of the important component of extracellular matrix, can be covalently linked to the surface of titanium producing a significant increase of bone growth and bone-to-implant contact [53].

Cell proliferation: Cell proliferation is defined as the increase in cell number by division. Like to the cell response presented above, osteoblast-like cell proliferation also depends on physicochemical characteristics of biomaterial surface [13]. Degasne et al. [29] found that cell proliferation was increased on rough titanium surfaces rather than smooth ones. Otherwise, other authors revealed the opposite results [9, 54, 55].

1.2 Solid Surfaces

The importance of surfaces is known many years ago. The first surface science problem studied was related to engineering and architectural aspects 5500 years ago when Egyptians built their monuments with huge stones which had to be transported for large distances. It is amazing that they already knew that adding lubricants reduced friction during the transportation of these heavy stones. Fig. 1.1 illustrates the use of sledges to transport statues in Egypt 4000 years ago. In this figure, it is possible to see how a man, standing on the sledge supporting the statue, pours a lubricant liquid into the path of motion. So, this man was the first surface engineer of history [56]. Even Leonardo Da Vinci or Coulomb suspected that surfaces were important in phenomena as friction, lubrication or wear [57–59].

Actually, surface characterization is becoming more important especially due to miniaturization progresses and with the advent of micro and nano mechanics. In this context, the need for knowledge of surface properties for a special task has been increased. As material surfaces are very complex objects, all the physical phenomena where surfaces are involved, as wetting, adhesion, tribology,... are also very complicated. Perhaps, this is the reason that led to Wolfgang Pauli to say his famous claim *God made solids, but surfaces were the work of the devil*.

The knowledge of surface properties involves its characterization at physical and chemical levels. Appendix A details the operation of several experimental techniques used in this thesis to characterize the surface chemistry and morphology. For this reason, this section of Chapter 1 is focused on describing different mathematical tools to characterize surface morphology. In this scientist field, much theoretical effort has been devoted to the study of the influence of roughness on contact mechanics adhesion, friction, wetting, and sealing [60–62] and, although many questions remain unanswered, the knowledge on how surface morphology influences these above-mentioned physical phenomena are continuously increasing.

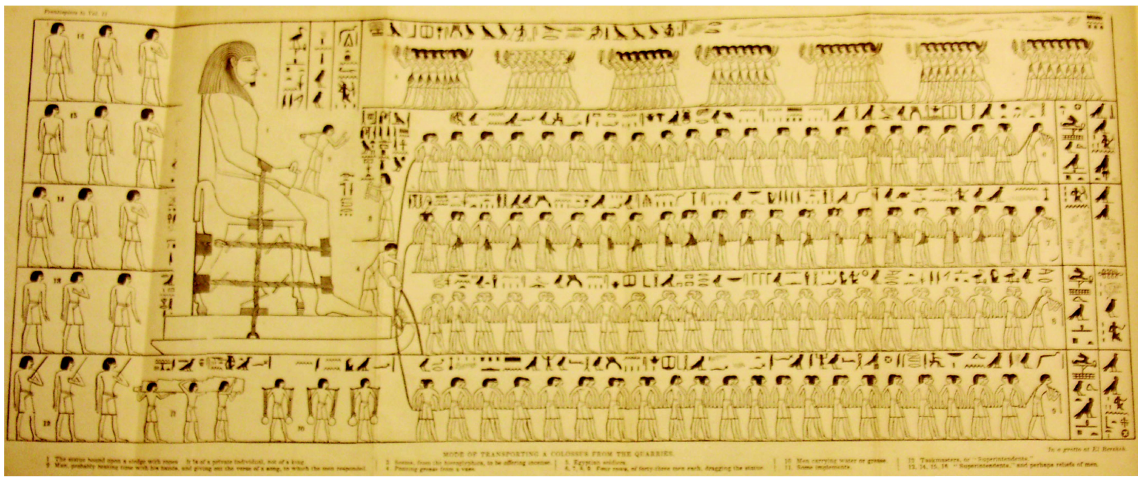

Figure 1.1: Egyptians used lubricant in order to reduce friction facilitating the displacement of colossus. Adapted from Ref. [56].

1.2.1 Rough Surfaces

Everybody knows that *the nature is wise*. Therefore, as almost all the surfaces found in nature are rough, we must surrender to the evidence, all real surfaces are rough, but, not under the same observation scale. So, although a real surface may seem smooth macroscopically, a careful examination at smaller length-scale reveals a rough, random microscopic topography [63], i.e. if surface roughness is not observed at a given observation scale, the problem of "smoothness" is related with the observation scale, because the surface is always rough. Therefore, previously to perform any experiment with surface, the morphology of such surface should be always characterized. In fact, this characterization should be done with an observation scale similar to the physical scale where the physical phenomenon occurs. In convenient remembering that method, scale and experimental technique used to characterize the surface morphology depends on the application. Therefore, we will center this study on rough surfaces. Moreover, the use of mathematics involves that surface roughness characterization might be done regardless of the scale of such roughness.

Surface Topography. Roughness

Real surfaces exhibit details and variations in several scales and sizes. A clarifier example of this can be human skin which appears as a smooth surface observed from longer distance, but at closer inspection all the lines, pores and other small details are revealed. This scale variability of surface defects, both in size/scale, height and shape, makes that the characterization of surface morphology is extremely complex. Respect to height variation, it is possible to find asperities or defects in the same surface with amplitudes varying from millimetres to nanometres or less. Equally, for length variations, the things are not significantly different. Moreover, surfaces tend to have spacing parameters which can be very different to height ones by several orders of magnitude. Fig. 1.2 illustrates an individual profile of the surface with the scale-dependent features. Moreover, in addition to scale problem, surface can reveal a wide range in shape because surface defects can be patterned or randomly distributed.

Surface morphology characterization is performed through surface topography which can be roughly defined as the set of all natural or artificial geometrical peculiarities which conform the

surface. Moreover, as new devices for acquisition of surface topography are developed, the topographical characterization of a surface has still become more deep and difficult. From a topographical point of view, rough surfaces can be classified in two main types: deterministic or structured rough surface (e.g. machined surfaces), and random or stochastic rough surfaces (e.g. fractured surfaces).

In general, any surface topography shows three different scales of surface defects (see Fig. 1.2), which they can classified in four orders through their typical wavelengths as:

- **Underlying Shape:** Underlying shape corresponds to the macroscopic shape of the surface.
- **Waviness:** Waviness is composed by the irregularities which can be periodic or non-periodic irregularities. It could just be a narrow-band random waveform.
- **Roughness:** Roughness is usually defined as deviation, quasi-periodic or not, from an ideal, smooth reference plane.

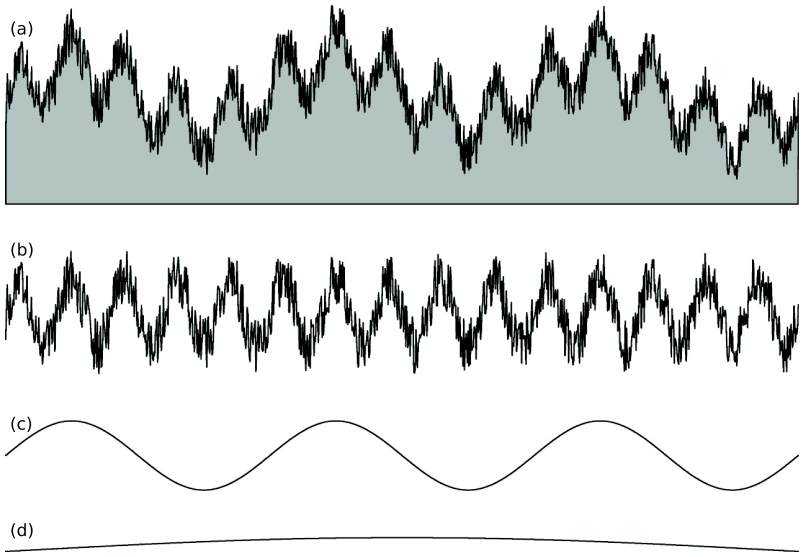

Figure 1.2: The surface topography of any wavy rough surface (a) encloses information of several wavelength scale which it must be isolated in order to evaluate surface roughness. According to its wavelength, the surface defects are classified as: roughness (b), waviness (c) and underlying shape (d).

As surface topographies enclose surface information of several wavelength scales, experimentally, surface analysis requires the isolation of the surface defects exposed above according to their wavelength. Consequently, previously to characterize the roughness of a surface from its topography, the acquired surface topography requires a numerical pre-processing in order to isolate, exclusively, the roughness (see Fig. 1.2). Further, topography data depend on the device used to acquire it and on the observation scale used to study each physical phenomenon.

Roughness Characterization

The numerical pre-processing or filtering of the surface topography commented above is a complex process composed by different steps driven to remove (except for the surface roughness)

the surface defects previously classified.

The first step of this filtering process consists to remove the underlying shape. Underlying shape of a surface can be removed by leveling of surface topography for flat surfaces or by its fitting to a geometric function for curved ones.

Once the underlying geometry has been removed it is necessary to isolate the roughness of the waviness. Traditionally, it has be performed using cut-off frequency (or wavelength) filters [64–66], but these methods involve the distortion of the some roughness peak parameters due to their intrinsic nature [65, 66]. Actually, the filtering processes used to separate waviness and roughness are derived from Gaussian filters [67]. Gaussian filters are based on passing a Gaussian, weighted average through the primary topography - resulting in the waviness topography. On the other hand, the roughness topography is made up of all of the peaks and valleys (residuals) above and below the waviness one.

Finally, once upon surface roughness is isolated it is possible to characterize it. However, the grade of characterization of a surface roughness will depend on the physical phenomenon which it is being studied. So, it is possible that a only parameter may be sufficient to characterize a surface for some purposes, whereas in other cases the description degree of the same surface roughness must be greater is required. The descriptors introduced in this section will form the basis for modelling all the surfaces used throughout this thesis. Moreover, as essential scales for roughness characterization are application dependent, we can classify into three different classes: nano-roughness at length scales smaller than $1\mu m$, micro-roughness at $1 - 100\mu m$, and macro-roughness at $0.1 - 0.5mm$.

1.2.2 Mathematical Tools for Surface Roughness Characterization

Statistical Analysis of Surface Roughness

Statistical methods describe the joint distribution of the measurements height values. Most of the profile characterization parameters defined in the standard ISO 4287 ([66, 67], the so-called R parameter set) can be regarded as statistical, and also the major part of the S parameter set [67,68] designed for a real characterization (they are the indeed two-dimensional generalization of the R parameters) belong to the statistical methods. This text areal parameters were be considered and noted as R. These parameters are usually divided into amplitude, spacing, hybrid and functional parameters [67, 69, 70].

Although, parameters which make the R set are very numerous[2], this section only collects and defines the statistical parameters actively used on it.

First of all, we supposse that $h(x, y)$ is the topography of a purely rough surface S, where underlying shape and waviness are been removed by the pre-processing of its surface topography, with physical dimensions L_X and L_Y. Moreover, the pre-process of the surface involves that $\frac{1}{A_z}\iint_S h(x,y)dxdy = 0$, where A_z is the surface area of the the topography projected over XY-plane. Therefore, if the physical dimensions of the topography are L_X and L_Y,
$\frac{1}{L_X L_Y}\int_0^{L_X}\int_0^{L_Y} h(x,y)dxdy = 0.$

Since these clarifications, statistical parameters can be well defined. So, their mathematical definitions are:

- Arithmetic surface height average R_a (also known as average roughness): The arithmetic average height parameter is the most universally used roughness parameter for general quality control. It is defined as the average absolute height deviation of the roughness irregularities

[2]The mathematical definitions of the R parameters can be consulted in Ref. [66, 67]

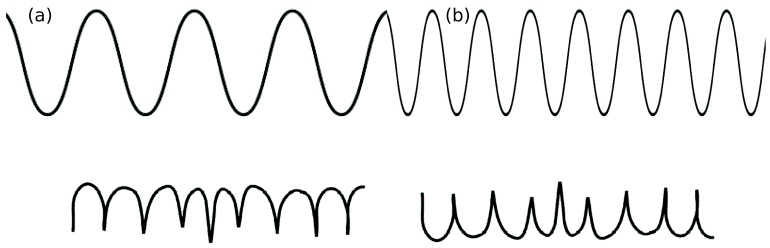

Figure 1.3: Profiles (a) and (b) show a very different aspect but their R_a values are identical. Therefore, it is clear that R_a is not sensitive to small changes in surface topography.

from the mean plane over one sampling area1. This parameter does not give any information about the wavelength and it is not sensitive to small changes in surface topography (see Fig. 1.3). The mathematical definition and the digital implementation, for a surface topography with resolution equals to $MN\ pixels^2$, of this parameter are, respectively, as follows:

$$R_a = \frac{1}{L_X L_Y}\int_0^{L_X}\int_0^{L_Y}|h(x,y)|dxdy \xrightarrow[\text{digital}]{} R_a = \frac{1}{MN}\sum_{i=1}^{M}\sum_{j=1}^{N}|h(x_i,y_j)| \tag{1.1}$$

- Root mean square roughness R_q (also noted as RMS): This parameter represents the standard deviation of the distribution of surface topography heights, so it is an important parameter to describe the surface roughness by statistical methods. This parameter is more sensitive than R_a to large deviation from the mean plane. The RMS mean plane is the plane that divides the surface topography so that the sum of the squares of the deviations of the surface heights from it is equal to zero. The mathematical definition and the digital implementation, for a surface topography with resolution equals to $MxN\ pixels^2$, of this parameter are, respectively, as follows:

$$R_q = \sqrt{\frac{1}{L_X L_Y}\int_0^{L_X}\int_0^{L_Y}\left(h(x,y)\right)^2 dxdy} \xrightarrow[\text{digital}]{} R_q = \sqrt{\frac{1}{MN}\sum_{i=1}^{M}\sum_{j=1}^{N}[h(x_i,y_j)]^2} \tag{1.2}$$

- Surface skewness R_{sk}: The skewness of a surface topography is the third central moment of the distribution of surface topography heights, measured over the assessment area. It is used to measure the symmetry of the surface topography about the mean plane. This parameter is sensitive to occasional deep valleys or high peaks. A symmetrical height distribution, i.e. with as many peaks as valleys, has zero skewness. Surface topographies with peaks removed or deep scratches have negative skewness. Surface topographies with valleys filled in or high peaks have positive skewness (see Fig. 1.4). This parameter can be used to distinguish between two surface topographies having the same R_a or R_q values but with different shapes. The mathematical definition and the digital implementation, for a surface topography with resolution equals to $MN\ pixels^2$, of this parameter are, respectively, as follows:

$$R_{sk} = \frac{1}{R_q^3}\int_0^{L_X}\int_0^{L_Y}\left(h(x,y)\right)^3 dxdy \xrightarrow[\text{digital}]{} R_{sk} = \frac{1}{MNR_q^3}\sum_{i=1}^{M}\sum_{j=1}^{N}[h(x_i,y_j)]^3 \tag{1.3}$$

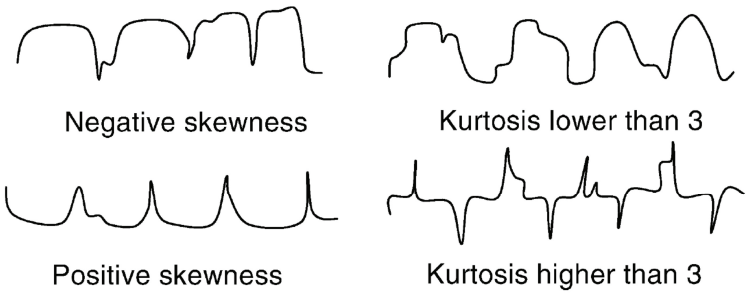

Figure 1.4: General aspect of surface profiles according to their values of R_{sk} and R_{ku}

- Surface kurtosis R_{ku}: the kurtosis is the fourth central moment the distribution of surface topography heights, measured over the assessment area. It describes the sharpness of the probability density of the surface topography. If $R_{ku} < 3$ the distribution curve is said to be platykurtoic and has relatively few high peaks and low valleys. If $R_{ku} > 3$ the distribution curve is said to be leptokurtoic and has relatively many high peaks and low valleys (see Fig. 1.4). The mathematical definition and the digital implementation, for a surface topography with resolution equals to $MNpixels^2$, of this parameter are, respectively, as follows:

$$R_{ku} = \frac{1}{R_q^4} \int_0^{L_X} \int_0^{L_Y} (h(x,y))^4 \, dxdy \xrightarrow[\text{digital}]{} R_{ku} = \frac{1}{MNR_q^4} \sum_{i=1}^{M} \sum_{j=1}^{N} [h(x_i, y_j)]^4 \tag{1.4}$$

- Surface area ratio or roughness factor r (it is also noted as Sdr): Surface area ratio r is defined as the cocient between real surface area of the topography A an its geometrical area A_g, where A_g is defined as the area of the projected surface topography over XY-plane, i.e. $A_g = L_X L_Y$ for a topography with physical dimensions L_X and L_Y. By its own definition, $r \geq 1$ ($r = 1$ for perfectly smooth surfaces). This parameter is interesting for fiction and wetting phenomena. The mathematical definition is the following[3]:

$$r = \frac{A}{A_g} = \frac{1}{L_X L_Y} \int_0^{L_X} \int_0^{L_Y} \left(1 + \left(\frac{\partial h(x,y)}{\partial x} \right)_X^2 + \left(\frac{\partial h(x,y)}{\partial y} \right)_Y^2 \right) dxdy \tag{1.5}$$

Traditionally, surface roughness has been characterized through the study of height distribution of the surface topography in a classical statistical sense. For real rough surfaces, statistical parameters are not always able to provide a complete knowledge of surface roughness. For this reason, we propose to use other methods to characterize the roughness of real surfaces.

Fractal Geometry and Surface Roughness

Fractals, which were first introduced in 1977 by Mandelbrot [71] and developed further at the end of 1980's by Barnsley and Feder [72, 73], have been used to describe irregular shapes that do not lend themselves to description by Euclidean geometry. Fractals have been used in many different scientist fields due to their capability to describe structures that exhibit the highly irregular

[3]The expression of the digital implementation of this parameter can be consulted in these webpages: http://www.imagemet.com and http://zeus.plmsc.psu.edu

behaviour commonly found in nature[4]. Mathematically, a fractal, term coined by Mandelbrot in 1975 and derived from the Latin "fractus" which means "broken", is basically defined as an object with non-integer dimension. Fractals are commonly used to model nature phenomena in many different scientist fields, but, particularly interesting for this work, are the application of fractals to the study of rough surfaces [74–79], cell adhesion [80, 81] and wetting phenomena [82, 83].

Attempts in adopting the fractal geometry for rough surface characterization have been based on the computation of the fractal dimension D_f as a basis for characterisation. D_f is the most popular parameter used to characterize any fractal, particularly a surface, although it is not the unique parameter which can be used to characterize a fractal surface (Mandelbrot defined the concepts of lacunarity and connectivity in order to characterize fractal sets with identical D_f but different aspect [71]. Fig. 1.5 illustrates this fact.). D_f analysis measures the complexity of a surface and it is defined from a power law relationship between a complexity measure and the applied measurement scale.

Characterization of surface roughness using fractal tools, particularly D_f, has been used in

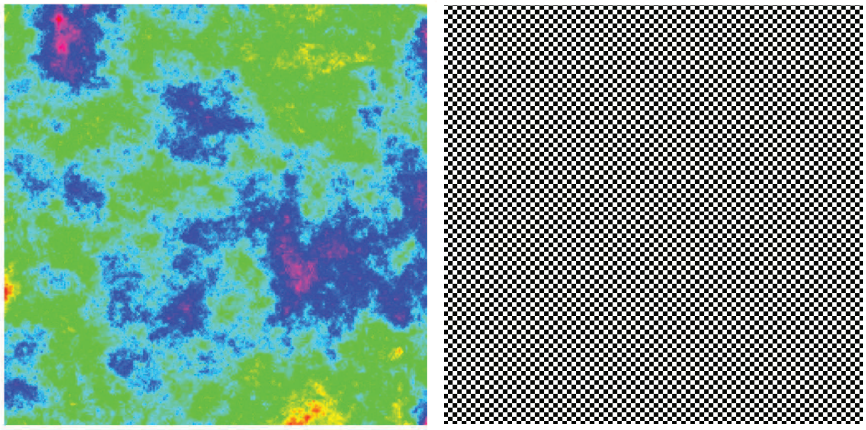

Figure 1.5: Fractal sets with different aspect but identical fractal dimension ($D_f = 2.5$).

this work in order to describe surface roughness of titanium surfaces where osteoblast-like-cells were afterwards deposited, i.e. an implant. The main reason to use D_f to characterize the to roughness of an implant surface is that, roughly speaking, D_f is a measure of the "complexity" of a surface and, in this sense, fractal dimension might be used to quantify the role of the features of implant topography on the cell growth, proliferation and adhesion. For this reason, fractal analysis might be more helpful than conventional statistical roughness descriptions in order to elucidate the complex mechanisms occurring at the implant surface in contact with the surrounding biological tissues.

A complete review of the different methods and algorithms used to compute fractal dimension for an image, particularly a surface topography, can be found in reference [84]. But, in this work, the methods used were the so-called Cube counting method [85, 86], which is an algorithm derived directly from a definition of box-counting fractal dimension, and Power spectral method [87]. The algorithm steps developed to implement these methods are similar to the implemented

[4]In *Fractals Everywhere*, Barnsley wrote the following reader warning "Fractal geometry will make you sees everything differently. You risk the loss of your childhood vision of clouds, forests, flowers, rocks, mountains, torrents of water and much else besides. Never again will your interpretation of these things be quite the same".

in [88] free-software (Gwyddion[5] free-software was used to test the D_f values computed with our own software).

Minkowski Functionals

One of the problems that arise in the investigation of the real surface is its complicated spatial structure, and it is the principal motivation behind the application of Minkowski functionals (MF) in the framework of this thesis

The use of Minkowski functionals to characterize the roughness of a surface from its surface

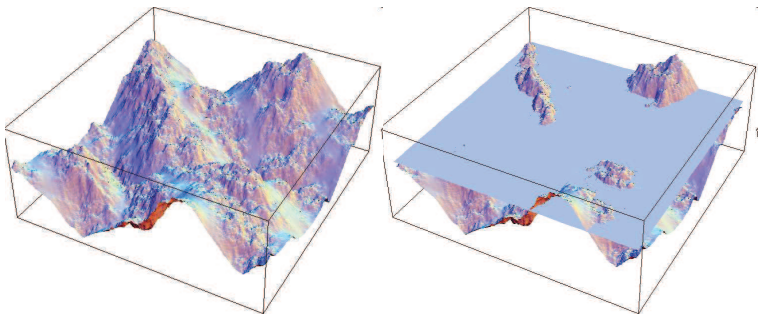

Figure 1.6: A surface and a level set. The cutting plane is indicated by a mesh in the left image.

topography is based on the capabilities which level sets have in order to study the topography of any surface as it has been proven in many applications [89–91]. A level set is the result of a thresholding operation on the surface topography at a given height keeping the points where the cutting plane hits the material as a set. Its complement is the region where the thresholding level cuts through thin air. Thus, a level set $A_S(u)$ is the set of points in $\mathbb{R}^2$ at which the height of the surface S exceeds the height u (see Fig. 1.6 for help). It is clear that if a threshold is chosen above the highest surface peak yields an empty set; otherwise, choosing a threshold below the deepest pit yields the full domain.

The simplest features of a level set are the material ratio, which is the ratio between the material hit by the threshold level and the area of the sampling window; and its complementary, the void area, which is defined as the region where the threshold level does not hit the material. Calculating the material ratio at different thresholds u yields the material ratio curve, also known as Abbott-Firestone curve, which is an important tool in surface characterization (a large part of the surface parameters such as R_q, R_{sk} or R_{ku} are directly related with it [92]). On the other hand, void area represents valleys, dales or cavities in the surface. The void area is of interest in tribology or wetting phenomena because these void zones could affect the wetting properties of the surface [93, 94]. Apart from the area, one can also investigate the contour length and the number of isolated void/material (cavities/peaks respectively) areas of the level sets. The contour length obviously contains information on how smooth is a given level set and the ratio between isolated void/material areas is important in the field of percolation [95] because, percolation is related with so-called Euler characteristic χ. So, if $\chi < 0$ then the material is predominantly characterized by isolated holes, where a liquid can be trapped if χ is very low. On the other hand, if $\chi > 0$, the material would consist mainly of isolated objects, where a liquid can flow freely if χ is high.

Area, contour length and the Euler characteristic of a 2D set are known in mathematics as

[5] http://www.gwyddion.net

Minkowski functionals[6] noted as A, C and χ respectively[7]. From Hadwiger's theorem [101] it is possible to conclude that each level set characteristic can be expressed in terms of the Minkowski functionals only. This completeness makes the Minkowski functionals a very important tool for describing sets and, as a consequence, Minkowski functionals have been used to solve problems in areas ranging from astrophysics [100] to materials science [102, 103].

In this work, Minkowski functionals of any surface were computed using a own software developed taking as reference Gwyddion software (Gwyddion was used in order to validate our software). Minkowski functionals were used to describe global geometric characteristics of structures of AFM topographies previously transformed into a series of black-and-white images (so-called level sets) changing threshold level, where white represents points which its height is greater than threshold level, and, obviously, black denotes points which its height is lower than threshold level. Each one of this level sets was characterized by three morphological measures provided by the Minkowski functionals: the covered area $F(u)$ and the boundary length $U(u)$ of the white features, as well as the Euler characteristic $\chi(u)$, defined as the difference between the number of separated white (higher) and black (lower) features. The measures ($F(u)$, $U(u)$, $\chi(u)$) were normalized by the total imaged area to provide easy comparison between the values determined for topographic maps with different scan ranges. So, the expression used to compute these measures are:

$$F(u) = \frac{N_{White}}{N} \tag{1.6}$$

$$U(u) = \frac{N_{Bound}}{N} \tag{1.7}$$

$$\chi(u) = \frac{C_{White} - C_{Black}}{N} \tag{1.8}$$

where N denotes the total number of surface topography pixels, N_{White} denotes the number of pixels that are above threshold level (white pixels), and, equally, N_{Black} denotes the number of pixels that are below pixels that are below threshold level (black pixels). N_{Bound} denotes the number of white-black pixel boundaries. Finally, C_{White} and C_{Black} denote the number of continuous sets of white and black pixels respectively.

Apparently, and regardless of $F(u)$ which physical interpretation is trivial, these new measures seem to have a difficult physical interpretation. The boundary length functional $U(u)$ can be used to describe spatial features. So, for surfaces with smooth slopes, $U(u)$ has a lower amplitude than for surfaces with short-wavelength structures. The latter will yield level sets with many small or jagged objects as the surface will cross the threshold very often. Thus, the maximal amplitude can be related to the spatial aspect of roughness. On the other hand, Euler characteristic $\chi(u)$, for high thresholds u, is a good estimate for the number of peaks above this threshold u. The explanation is that for Gaussian random functions, the Euler characteristic of a level set is the number of local maxima plus the number of local minima minus the number of saddle points above this threshold. As there are only a negligible number of minima and saddle points above a high threshold, one can use the Euler characteristic to count peaks. The same result holds for low thresholds, where one can count pits. Moreover, the Euler characteristic can also be used to define a percolation threshold as the height level where the Euler characteristic function has its zero crossing. If is supposed that the surface data has zero mean, a high percolation threshold suggests better fluid retention properties.

Finally, it is possible to relate and compare Minkowski functional values with amplitude and

[6] For a set $G \in \mathbb{R}^d$, there are $d + 1$ Minkowski functionals.

[7] The mathematical properties and detailed descriptions and exact definitions of Minkowski functionals can be found in [96–100].

hybrid parameters values, because all of them find in Abbott-Firestone curve a common point, and therefore, it is often possible to show that both techniques basically catch the same information content. It is well-known that [92, 104] R_q, R_{sk} or R_{ku} can be derived from Abbot-Firestone curve and therefore, they can be derived from the Minkowsky functionals. Equally, surface area, i.e. roughness factor r, which is the integral over the surface's normal vector, is very similar to the integral over the local gradient, which in turn is the integral over the boundary length. Therefore, any functionality of the surface which can be related to the surface area can expected to be expressed also in terms of the boundary length functional. As consequence, for example, it is possible to study porous imbibition in terms of boundary length functional and Euler characteristic.

General Theory of Dynamic Scaling Laws in Kinetic Roughening

This subsection is a short introduction to kinetic roughening processes and its scaling laws. In this sense, this section introduces the generic theory of dynamic scaling in kinetic roughening applied in this thesis [8].

Probably, the most powerful tool to study roughening processes and to characterize them is *scaling*. This is due to its power prediction and the facilities which provide in order to connect measurable statistical quantities and exponents, which are apparently independent, through scaling relationships, which they can be simple or more complicated. The study of the scaling relations of different statistical quantities with time and system size allows to define universality classes. Universality classes permit to relate different roughening processes through their scaling behaviors.

Previously to begin the study of the tools which enable the analysis of kinetic roughening, it is necessary to present the concept of roughening in the statistical sense. So, in many cases, rough surfaces are generated by a growing interface which advances as new parts are added according to some dynamical process. If the conditions of the growth are such that the surface is marginally stable and the fluctuations are relevant, the resulting structure is a rough surface (similar arguments could be applied to describe the origin of rough surface due to erosion).

So, among the great variety of complex and disordered systems, the complexity of surface roughness is attracting a great deal of scientific interest [107, 113–115]. As for many applications, surface roughness plays a critical role, scientists had looked for new and powerful methods to its characterization [111, 112, 116, 117].

Studying the growth, formation, and morphologies of interfaces, in general kinetic roughening processes, deals with the fate of surface roughening occurs in nonequilibrium conditions [107, 113, 118]. Therefore, an enormous amount of study has been approaches to the study of the dynamics of growing surfaces [107, 111, 113, 119]. Most popular methods used today for the characterization of surface roughness are based on the concepts of self-similarity and multiaffinity, where multifractality has been regarded as the most complete characterization of a surface [73, 107, 113, 114, 118].

To monitor completely the roughening process qualitatively, different statistical quantities must be measured. In the case of this thesis, different quantities which provide information, through their scaling laws, about the roughness of the surface were studied. These functions were interface width $w(l,t)$, structure functions $G_q(l,t)$, where $q \in \mathbb{N} - \{0\}$ and, power spectral density or structure factor $PSD(k,t)$.

Scaling behavior of statistical functions used

[8] This theory is detailed in references [105–107]. Experimental and numerical studies can be found in [107], where a general idea of surface growth and roughening phenomena problems is exposed and presents the tools to characterize them [108–112]

a) **Interface width**

The *interface width* is formally defined as

$$w(l,t) = \left\langle \left\langle [h(\vec{r}+l,t) - h(\vec{r},t)]^2 \right\rangle_l \right\rangle^{1/2} \tag{1.9}$$

where $\langle \bullet \rangle$ denotes an average over (x, y) in windows of size l, if the window size is equal to the size of the system this function is called global interface width and if the window size is lower than the system size it is called local interface width. This function obey a power law in time t and distance l, with two scaling exponents, α_{gl}[9] α_{loc}, the roughness exponent (global or local), and β, the growth exponent, defined as:

$$w(L,t) \propto \begin{cases} t^{\beta} & \text{if } x<<1 \\ l_{gl}^{\alpha} & \text{if } x>>1 \end{cases} \tag{1.10}$$

where $t_0 \approx L^{\alpha_{gl}/\beta}$, and l is a window size varying from the smallest length scale to the system size L. The values of α_{gl} and β determine what is the universality class which a growth process belongs. Examples of such universality clasess are $\alpha_{gl} + \alpha_{gl}/\beta = 2$ for isotropic systems [120–123], $\alpha_{gl}/\beta = 4$ in the surface diffusion universality class [119] and $\alpha_{gl} = \beta$ in some pinned systems [124].

b) **Power spectral density**

The mathematical definition of the power spectral density is

$$PSD(k,t) =< \widehat{h}(k,t)\widehat{h}(-k,t) > \tag{1.11}$$

where $\widehat{h}(k,t)$ symbolizes the Fourier transform of $h(\vec{r},t)$ in a system of size L, k is the spatial frequency in reciprocal space and t is the growth time and the angular brackets denote the average over different realizations of the system. The $PSD(k,t)$ quantity is a positive real function of a frequency variable associated with a stochastic or deterministic process. Intuitively, the $PSD(k,t)$ captures the frequency content of a stochastic process and helps to indentify periodicities. The $PSD(k,t)$ quantity of the interfacial fluctuations permits to determine the scaling behavior of the surface. For a 2+1-dimensional system, this scaling law is

$$PSD(k,t) = k^{-2(\alpha_{gl}+1)} f(kt^{1/z}) \tag{1.12}$$

but, as it was shown by [111], for an anomalous 2+1-dimensional system, this scaling law presented changes to

$$f(x) \propto \begin{cases} x^{2(\alpha_{gl}+1)} & \text{if } x>>1 \\ x^{2(\alpha_{gl}-\alpha_S)} & \text{if } x<<1 \end{cases} \tag{1.13}$$

c) **Structure functions: multiscaling analysis and intermittency exponents**

If we assume the statistical translacional invariance, it is possible to define the so-called structure functions $G_q(l,t)$ which scale as:

$$G_q(l,t) = (< |h(\vec{r}+l,t) - h(\vec{r},t)|^q >_L)^{1/q} \sim l^{\alpha_q} \tag{1.14}$$

[9] In literature α_{gl} can be found as α.

where $\langle\bullet\rangle$ denotes statistical average (for non-overlapping increments of length l), q is the order of the momentum ($q \in \mathbb{N} - \{0\}$) and α_q are called intermittency exponent or generalized local roughness exponents. The intermittency exponents are used to characterize the surface as monofractal or multifractal. Thus, if the relationship between α_q and q is non-linear, the surface is multifractal, otherwise, the surface is monofractal. So, it is possible to discriminate if one growth process produces monofractal or multifractal surfaces.

The physical quantities exposed above scale with different functions by monomials with non-integer exponents. However, this dependence should always be dimensionally homogeneous [125]. This detail is often implicitly ignore in scaling analysis through the inclusion of different proporcionality constants which homogenize the physical dimensions of the scaling law. As in some cases it can confuse the non-specialist readers, Appendix B analyzies this point in detail.

Family-Vicseck scaling laws

A self-affine surface $h(\vec{r},t)$ (where $h(\vec{r},t)$ is referred to the height of the surface point placed at $\vec{r}$ at time t) is invariant under an anisotropic scale transformation, in the sense $h(\vec{r},t)$ has the same statistical properties as $\lambda^{-\alpha_{gl}} h(\lambda\vec{r},t)$, where α_{gl} is the roughness exponent.

In a typical situation of kinetic roughening, an initially smooth and chemically homogeneous surface is continuously roughened according to some external forces. These forces, or noises, can have thermal origin (such as, for instance, fluctuations in the flux of particles in a deposition process) or a quenched disorder (such as in the motion of driven interfaces through porous media). The resulting rough surface may be characterized through the fluctuations of the height around its mean value. So, it is common the use of the global interface width $w(L,t)$ to characterize the roughness of the surface through the root mean square fluctuation in the height. Mathematically $w(L,t)$ is defined as $w(L,t) = \left\langle \overline{[h(\vec{r},t) - \overline{h}]^2} \right\rangle^{1/2}$ where the overline denotes average over all (x,y) in a system of dimensions L^2, $\overline{h} \equiv \frac{1}{L}\sum_{i=1}^{L} h(\vec{r},t)$ is the mean height of the surface, and the brackets denote average over different measurements[10]. So, rough surfaces correspond to situations in which the stationary width, $w(L, t \to \infty)$, grows with the system size. Alternative, one may calculate other functions related to the correlations over a distance l as the height-height correlation function, $G_2(l,t) = \left\langle \overline{[h(\vec{r}+l,t) - h(\vec{r},t)]^2} \right\rangle$, or the local width, $w(l,t) = \left\langle \left\langle [h(\vec{r}+l,t) - h(\vec{r},t)]^2 \right\rangle_l \right\rangle^{1/2}$, where $\langle\bullet\rangle_l$ denotes an average over (x,y) in windows of size l.

In absence of any characteristic correlation length in the problem, the growth processes are expected to follow a power-law behavior of the correlation functions in space and time, and the Family-Vicsek dynamic scaling ansatz ought to hold [107, 113, 119, 126]. The Family-Vicseck dynamic scaling ansatz is:

$$w(L,t) = t^{\alpha_{gl}/z} f(L/\xi(t)) \tag{1.15}$$

Scaling function $f(x)$ which appears in Family-Viseck dynamic scaling ansatz behaves as:

$$f(x) \approx \begin{cases} x_{gl}^{\alpha} & \text{if } x << 1 \\ const & \text{if } x >> 1 \end{cases} \tag{1.16}$$

where α_{gl} is the roughness exponent and it characterizes the stationary regime, in which the lateral correlation length $\xi(t) \approx t^{1/z}$ (z is the so called dynamic exponent) has reached a value larger than the system size L. The ratio $\beta = \alpha_{gl}/z$ is called growth exponent and characterizes the early time

[10] $\langle\bullet\rangle$ and $\overline{\bullet}$ will keep their meanings during all the text. Any change on their meanings will be explicitly written in the text.

behavior of the surface. As occurs in equilibrium critical phenomena, the corresponding critical exponent does not depend on the microscopic details of the system. Consequently, growth processes can be divided into universality classes according to the values of the characteristic exponents presented above [107, 113, 126].

Anomalous roughening

Many studies have proved that the above standard scaling based on global width differs substantially from the scaling behavior of the local interface fluctuations (measured by the local height-height correlation function). In some growth models the local width scales as in Eq. (1.16), i.e., $w(l,t) = t^{\beta} f_{\Delta}(l/\xi(t))$, but being the anomalous scaling function

$$f_{\Delta}(x) \approx \begin{cases} x^{\alpha_{loc}} & \text{if } x<<1 \\ const & \text{if } x>>1 \end{cases} \tag{1.17}$$

where the α_{loc} is the local roughness exponent. This has been called anomalous roughening, and has been found to occur in many growth models [108, 109, 127, 128] as well as experiments [110–112, 117]. Moreover, it has been shown [105, 129–131] that anomalous scaling can take two different forms, there are super-rough processes where $\alpha > 1$ and $\alpha_{loc} = 1$, and intrinsic anomalous roughening ones where $\alpha_{loc} < 1$ and $\alpha > \alpha_{loc}$. Therefore, new universality classes appear associated to the existence of two different roughness exponent, α and α_{loc}, which, in general, are different.

Lopez et al. [105] have constructed a general theory of dynamic scaling. This theory incorporates all the different forms for dynamic scaling; Family-Vicseck, super-rough, and intrinsic anomalous scalings. Their theory predicts the existence of new classes of growth models with novel scaling properties. They assumed that any growing surface satisfies a generic dynamic scaling when there exists a correlation length $\xi(t)$, i.e., the distance over which the correlations have propagated up to time t, and $\xi(t) \approx t^{1/z}$, being z the dynamic exponent.

If the roughening process of a surface shows generic dynamic scaling, without assumptions such as surface self-affinity or implicit bounds for the exponent values, and the scaling behavior of the surface is studied from its $PSD(k,t)$ (see Eq. 1.11), the scaling law followed is given by Eq. 1.12 where the scaling function $f(x)$ has the following general form:

$$f(x) \approx \begin{cases} x^{2(\alpha_{gl}+1)} & \text{if } x<<1 \\ x^{2(\alpha_{gl}-\alpha_S)} & \text{if } x>>1 \end{cases} \tag{1.18}$$

where α_S is called as the spectral roughness exponent.

Thus, from the definitions of α, α_S and α_{loc} scaling exponents and their values, the generic theory of Lopez et al. [105] can be summarized as:

$$\begin{cases} if\ \alpha_S < 1 \Rightarrow \alpha_{loc} = \alpha_S \begin{cases} \alpha_S = \alpha \Rightarrow \text{Family-Vicseck} \\ \alpha_S \neq \alpha \Rightarrow \text{Intrinsic anomalous} \end{cases} \\ if\ \alpha_S > 1 \Rightarrow \alpha_{loc} = 1 \begin{cases} \alpha_S = \alpha \Rightarrow \text{super-rough} \\ \alpha_S \neq \alpha \Rightarrow \text{new class} \end{cases} \end{cases} \tag{1.19}$$

1.3 Wetting Phenomena

The wetting of liquids on solid surfaces is a research topic of fundamental interest [132] with a wide variety of technological implications as micro-fluidics for biotechnology, thin film technology, lubrication, textiles, self-cleaning and anti-sticking surfaces. Moreover, wetting phenomena are

Figure 1.7: Dew drops on a spider web early a summer morning in Cantabria, near to Soplao's Cave.

common in nature, where it is possible to find out in many different situations as, for example, rain droplets captured on a spider web (see Fig. 1.7), movement of certain insects on water, the curvature of rain water drops,....

Before introducing the main thermodynamical equations which describe the wetting phenomena, it is necessary to describe the physical system and to define some basic concepts. When a fluid is displacing another immiscible fluid on a solid surface, the point at which the three phases[11] meet is known as three phase boundary. Consequently, if a liquid drop comes into contact with a solid surface, its morphology will be governed by the interfacial properties of liquid/vapor, solid/liquid and solid/vapor interphases. An interphase is the space transition region, with a thickness of some molecules, where two different substances meet [133], i.e. an interphase is the space region where things happen. On the other hand, an interface, also called Gibb's surface, corresponds with the ideal mathematical surface where it is possible to define the position of the interphase [134].

Wetting is the part of interphase thermodynamics which studies the interface phenomena which occur in three-phases themodynamical systems. From an energetic point of view, the existence of interfaces is not favourable and therefore the system responds decreasing its Gibb's free energy ($dG = VdP - SdT + \sum_{i=1}^{n} \mu_i dN_i + ...$), and as themodynamical response, the system decrease the interface extension/area. This energy is known as interfacial energy or free surface energy or, simply, surface energy(although really is an energy density given its physical dimensions) [132].

From a mechanical point of view, surface energy, which it is a numerical magnitude, corresponds

[11] A phase will be defined in our context as each one of the homogenous parts which define a heterogeneous themodynamical system. In this study, these phases will be always one liquid phase, other one solid and, finally, one vapor phase.

to surface tension or interfacial tension, which it is a tensorial magnitude[12]. Surface tension is the response of the system to minimize the interfacial area and, therefore, it can be understood as a force that opposes to the possible increasing of interfacial area. The term "surface energy" is used for solid interfaces because, in that cases, interfacial area does not change, whereas "surface tension" is used where deformable interfaces are involved. In this text, surface energy will be noted as γ_{ij} where subscripts i and j are referred to phases, involved into the origin of the interface, i and j, respectively.

Microscopically, surface tension is originated due to the attractive cohesive forces acting between the neighboring molecules (or atoms) of a liquid (interactions between far particles are negligible because only low-range potentials are considered [135]). In the bulk liquid, one molecule is isotropically surrounded by other molecules, so that the resultant intermolecular force exerted by all the neighboring molecules is zero. However, the resultant intermolecular force acting on a molecule located at the surface of the liquid is non-zero because of the missing neighbors in the upper half-space. This non-vanishing force points inwards into the liquid. Therefore, work is required to bring a molecule from the bulk to the surface, and thus to increase the surface area. This work can be regarded as a surface tension, also described as surface free energy. To reach thermodynamic equilibrium, a system must minimize its surface, and therefore, its area/volume ratio (as the sphere is the geometrical object with the smallest surface-to-volume ratio, a drop in absence of external fields will take on a spherical shape). So, the effect of surface tension on the geometry of a interface will depend of the physico-chemical state of each component of such interface. That effect will be greater as more flexible will be the interfaces.

1.3.1 The Young-Laplace Equation

The surface tension described above can be seen as a two-dimensional pressure acting in the plane of the interface and its mechanical effect on the interface can be explained considering a single direction curved interface $z(x)$ (see Fig. 1.8 A) with a curfvature radius R. In order to keep the interface bent, it is necessary a pressure difference ΔP between inside and outside of the bent interface, also called Laplace pressure. In equilibrium situation, the forces per unit length verify:

$$\Delta P R d\alpha = 2\gamma_{lg} \sin(d\alpha/2) \Rightarrow \Delta P = \frac{\gamma_{lg}}{R} \tag{1.20}$$

If the interface $z(x, y)$ is curved in two directions, with curvature radii R_1 and R_2, then an additional pressure difference between both sides of the interface should be applied in order to compensate this new curvature term. As consequence, in equilibrium situation (see Fig. 1.8 B) must be verified the following equation:

$$\Delta P = \gamma_{lg}\left(\frac{1}{R_1} + \frac{1}{R_2}\right) \Rightarrow \Delta P = 2\gamma_{lg} H(x, y) \tag{1.21}$$

where $H(x, y) = \frac{1}{2}\left(\frac{1}{R_1} + \frac{1}{R_2}\right)$ is the mean curvature of the interface, γ_{lg} is the liquid/fluid surface tension. If a spherical interface is considered ($R_1 = R_2$), Eq. 1.21 is reduced to Eq. 1.20. [13] The Young-Laplace equation tells us that of a curved liquid/fluid (or liquid/liquid) interface is always accompanied by a change in pressure proportional to the mean surface curvature H of the interface.

[12] Both, surface energy and surface tension, are indiscriminately used, although they are referred to different physical quantities. They are numerically identical for equilibrium situations at the liquid-fluid interphases

[13] Eq. 1.21 is known as Young-Laplace equation because it was demonstrated, by different ways and simultaneously, by Thomas Young and Pierre Simon Laplace in 1805 [136, 137].

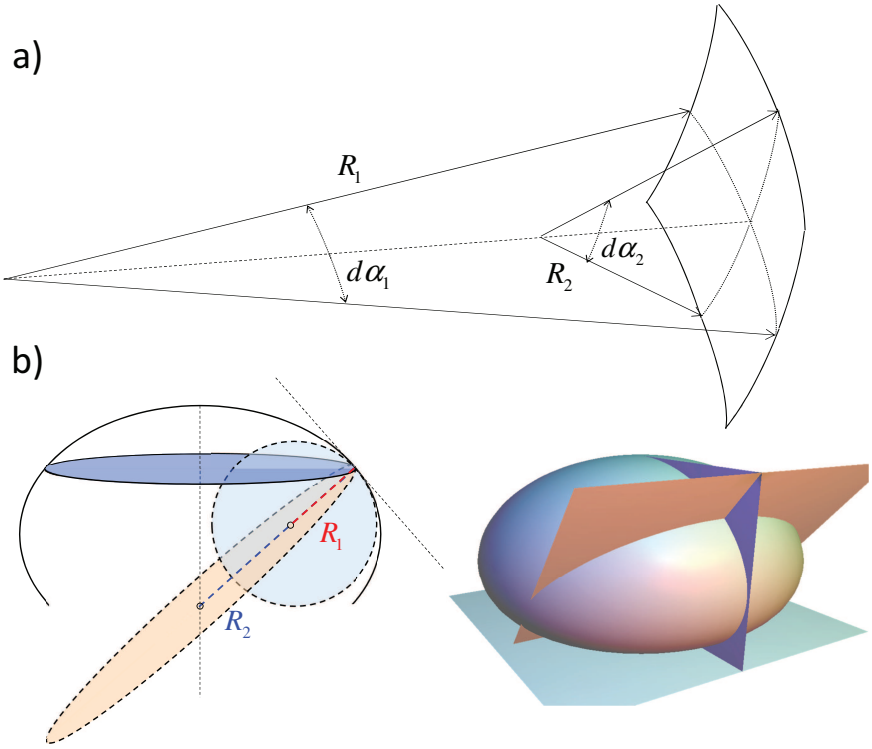

Figure 1.8: a) Two directions of the principal curvature of a curved liquid-air interface at equilibrium. b) The two radii of principal curvature R_1 and R_2 which define the mean and Gaussian surface (H, K).

A higher interfacial curvature results in a higher Laplace pressure. It is noteworthy that a two-dimensional pressure (surface tension) can generate three-dimensional pressure [14].

From Eq. 1.21, it is clear that the form of any interface is defined by the signs of ΔP and H, i.e. interface curvature radii. Since the interface is referred to liquid/fluid interface, one can write Laplace pressure as $\Delta P = P_l - P_g$, where P_l and P_g are the pressures in the liquid and fluid phases respectively. In this case, the signs of interface curvature radii will be defined by the direction of the center of each radius, i.e. positive if the center points into the liquid, and negative if the center points towards the gas phase. Therefore, a liquid droplet interface will have $H > 0$, whereas an air bubble imprisoned in a liquid will have $H < 0$.

Thermodynamically, Eq. 1.21 can also be derived, for that it is necessary to remember that minimizing the total surface energy involves minimizing the surface area of the liquid-gas interface. and that interfacial energy γ_{lg} was defined to be the energy necessary to increase by one unit area the interfacial surface. According to conservation of mass principle, any reduction in interfacial area is accompanied by a change of pressure in the media enclosed by the interface. Let be an interface, spanned over two angles $d\alpha_1$ and $d\alpha_1$ define in perpendicular planes (see Fig. 1.8 a). In this case, the area of the initial surface element is defined by the two radii of curvature R_1 (in the plane of $d\alpha_1$) and R_2 (in the plane of $d\alpha_2$) as $A(z) = R_1 d\alpha_1 R_2 d\alpha_2$. If the surface is displaced a

[14] To deepen the details of the Young-Laplace equation see the following references [134, 138, 139].

distance dz, its new area will be $A(z+dz) = (R_1+dz)d\alpha_1(R_2+dz)d\alpha_2$, so that in a first order approximation the increase of the surface will be: $dA = (R_1+R_2)d\alpha_1 d\alpha_2 dz$. If it is supposed that the thermodynamical system is in equilibrium state, then:

$$\gamma_{lg}\left(R_1+R_2\right)d\alpha_1 d\alpha_2 dz = \Delta P R_1 R_2 d\alpha_1 d\alpha_2 dz \tag{1.22}$$

where ΔP is the existing pressure difference across the surface and which this pressure difference acts over the area $A(z)$, and therefore

$$\Delta P = \gamma_{lg}\left(\frac{R_1+R_2}{R_1 R_2}\right) \Rightarrow \Delta P = \gamma_{lg}\left(\frac{1}{R_1}+\frac{1}{R_2}\right) \tag{1.23}$$

which is the Young-Laplace equation (Eq. 1.21) again.

1.3.2 Wetting of Ideal Surfaces

An ideal solid surface is defined as a smooth, homogeneous, rigid, non-porous and chemically inert one. So, when a drop of liquid is placed on a solid surface, the drop can either spread over the surface, or adopt a ball-like shape. The driving force to reach the final state is the minimization of the total interfacial energy, i.e. to minimize the solid/gas (sg), solid/liquid (sl), and liquid/gas (lg) interfacial areas. Thermodynamically, this system will reach the equilibrium state when the total surface free energy will be minimized, with the additional constraint of mass conservation for the drop (or volume conservation). For our system, the total surface energy is determined as follows:

$$W_{tot} = A_{sl}\gamma_{sl} + A_{sg}\gamma_{sg} + A_{lg}\gamma_{lg} \tag{1.24}$$

where A_{ij} is the surface area of the ij-interface. Thermodynamic equilibrium involves $dW_{tot} = 0$. Thus:

$$\gamma_{sg} = \gamma_{sl} + \gamma_{lg}\frac{dA_{lg}}{dA_{sl}}\Big|_{V=const} \tag{1.25}$$

In absence of external fields, the minimization of surface energy leads to a spherical drop shape. Therefore, as first approximation and in absence of any external field, a liquid drop placed on a homogenous solid surface should has a shape like a spherical-cap, as shown in Fig. 1.9. Thus, it

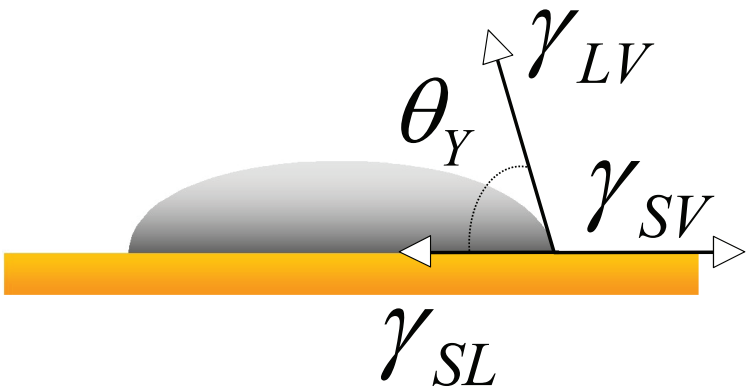

Figure 1.9: Young contact angle, θ_Y, at the three-phase contact line of a sessile drop is defined as sketched. Depending on the surface wettability, the contact angle lies between 0° and 180°.

is possible to find out that the differential of Eq. 1.25 is $\frac{dA_{lg}}{dA_{sl}}|_{V=const} = \cos(\theta_Y)$ [15] where θ_Y is known as intrinsic contact angle or Young contact angle of the liquid l on the solid s. The angle θ_Y is defined between the plane formed by the interface solid/liquid and a tangential plane to the liquid/fluid interface at the three-phase contact line (See Fig.1.9).

Introducting the previous results into Eq. 1.25, the Young equation is obtained:

$$\gamma_{sg} = \gamma_{sl} + \gamma_{lg}\cos(\theta_Y) \tag{1.26}$$

It is important to note that Young's equation (Eq. 1.26) is invariant under gravity and valid for any geometry of the liquid drop ruled by the Young-Laplace's equation (Eq. 1.21) [140–142]. Moreover, the Young's equation is also valid for curved but smooth surfaces because it is a local equation [143], and therefore, it is valid for each point of the three-phase contact line at equilibrium situation.

From a mechanical point of view, the Young's equation (Eq. 1.26) describes the force balance at the contact line of the three forces resulting from the three interfacial tensions (see Fig. 1.9).

1.3.3 Wetting of Real Surfaces

The Young equation (Eq. 1.26) is only valid for ideal surfaces. But this kind of surfaces does not exist in reality. Usually, any surface, regardless of the scale at which it is observed, presents topographical and/or chemical defects. Therefore, it is possible to find rough and chemically homogeneous surfaces (for a chemically homogeneous but rough surface, the intrinsic contact angle of each point of the surface is always the same), smooth and chemically heterogeneous surfaces (each intrinsic contact angle of the surface corresponds to each one of its chemical realities) and rough and chemically heterogeneous surfaces.

The non-ideality of surfaces has some consequences on the wetting properties:

- The observable contact angle θ_{app} (experimentally accesible contact angle) in a non-ideal surface is not the intrinsic contact angle (see Fig. 1.10). So, for a rough chemically homogeneous surface, where the intrinsic contact angle of eahc point of the surface is always the same, the difference between the observable and intrinsic contact angles is exclusively due to the "resistance" which topographical defects of the surface offer to the deplacement of the

[15] The detailed derivation of Eq. 1.25, taking into account geometrical and thermodynamical arguments exclusively, can be found in Appendix C

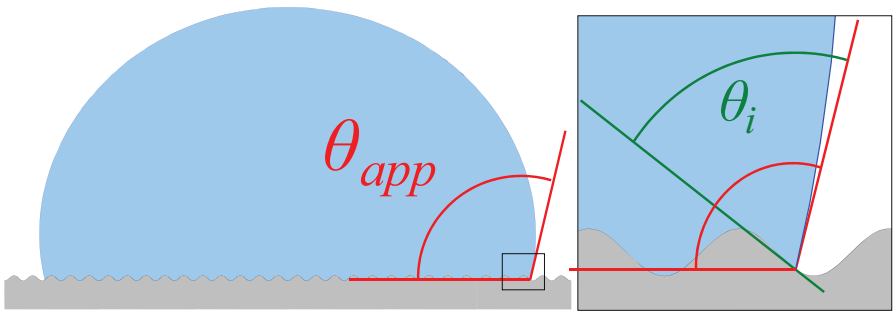

Figure 1.10: Intrinsic and apparent contact angles for a rough chemically homogeneous surface.

contact line. On the other hand if a smooth chemically heterogeneous surface is considered, the three-phase contact line is not affected by surface topography, but its chemically heterogeneity means that the intrinsic contact angle is different for each point of the surface (each instrinsic contact angle of the surface corresponds to each one of the chemical domains of the surface). As consequence, the value of the observable contact angle is a "mean value" of all intrinsic contact angle of the surface.

- Non-ideality of any real surface involves the existence of different values of observable contact angle for each point of the three-phase contact line. This phenomenon is referred to contact angle multiplicity and it is caused by the corrugation of the three-phase contact angle [144] due to the presence of chemical patches.

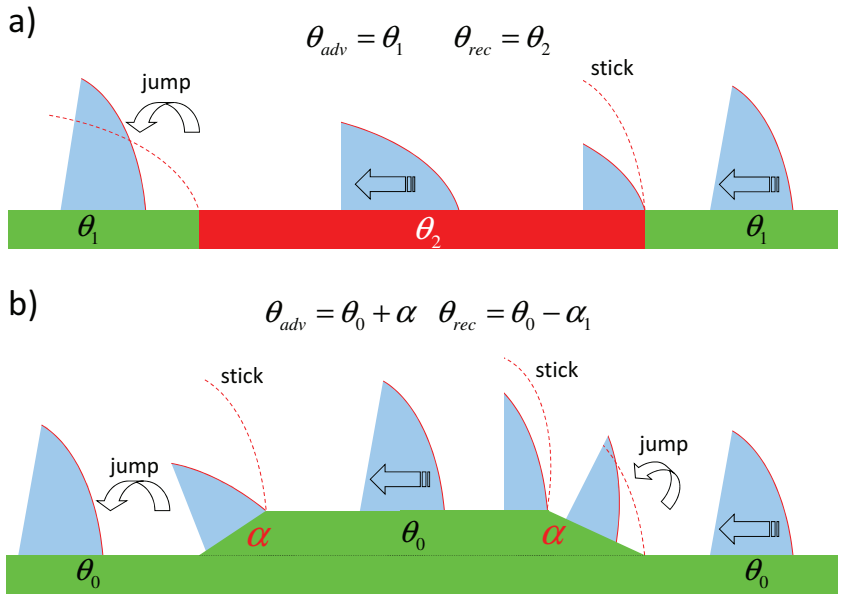

Figure 1.11: Advancing and receding contact angles for a moving drop (blue arrow indicates the direction of movement) on a chemically heterogeneous and smooth surface a) and a chemically homogeneous but rough surface b). On a chemically heterogeneous and smooth surface, the contact angle at the boundary can take any value between the contact angle of the more hydrophilic patch and the contact angle value of the more hydrophobic patch. As a consequence, the contact line becomes immobilized and its position gets fixed to the line of discontinuity as long as the contact angle falls into the free range between those two angles. Similarly, on a chemically homogeneous but rough surface, the advancing and receding contact lines will be pinned at the peaks and valleys.

- The geometry and, therefore, the contact angle, of the drop deposited on any real surface depends on how it was placed. When a drop came in contact with that surface, its observable contact angle can take any value within a set of values between a maximum (advancing) θ_{adv}, and a minimum (receding) θ_{rec} contact angle values. Three-phase contact line is advancing when the line moves towards the solid-gas interface and it is receding when the line moves towards the solid-liquid interface. This phenomenon is known as contact angle hysteresis, identically to the magnitude used to measure it, i.e. contact angle hysteresis $\Delta\theta$[16]. Con-

[16]Contact angle hysteresis of a real surface is easily observable if we look carefully how a rain drop sliding down

tact angle hysteresis is defined as the difference between θ_{adv} and θ_{rec}, $\Delta\theta = \theta_{adv} - \theta_{rec}$. Moreover, contact angle hysteresis is usually accompanied with contact angle multiplicity phenomena. From an energetic point of view, contact angle hysteresis occurs due to the wide range of "metastable" states, due to the non-ideality of the surface, which can be observed as the liquid drop scans the surface of a solid at the solid/liquid/vapor interface. The mechanical consequence of these meta-states is the pinning of the three-phase contact line due to these surface defects. The reduced mobility of the contact line caused by pinning gives rise to the contact angle hysteresis phenomena (see Fig. 1.11).

Chemically Homogeneous and Rough Surfaces. The Wenzel Equation

If a liquid drop is placed on a rough chemically homogeneous surface, the apparent contact angle θ_{app}, which is the contact angle measured with respect to the average surface, is generally different from the local contact angle, measured with respect to the tangential plane at one local point of the three-phase contact line. Wenzel treated to explain this behavior around one century ago [145–147]. Wenzel's explanation was based on that the interfacial energy per unit area is higher on a rough surface than on a smooth surface, because of the solid surface area for a rough surface is greater than for smooth one. So, a liquid drop placed on a rough surface responses to this increasing of exposed contact area increasing the solid/liquid and solid/fluid interfacial areas, i.e. changing its apparent contact angle.

In order to model mathematically their ideas, Wenzel modified the Young equation by the introduction of a factor which takes into account the rough nature of the surface. The factor proposed by Wenzel was the surface area ratio or so-called the Wenzel or roughness factor r (see Eq. 1.5), which is defined as the ratio between the real surface area and the projected surface area (see Eq. 1.5). So, the Wenzel correction to Eq.1.26 is known as the Wenzel equation:

$$\cos(\theta_{app}) = r\cos(\theta_Y) \tag{1.27}$$

From this equation, it is possible to understand that surface roughness increases the intrinsic behavior of the surface.

$$\begin{cases} \text{For hydrophilic surfaces } \theta_Y < 90^\circ \Rightarrow \theta_{app} < \theta_Y \\ \text{For hydrophobic surfaces } \theta_Y > 90^\circ \Rightarrow \theta_{app} > \theta_Y \end{cases}$$

The Wenzel regime is the wetting regime where the Eq. 1.27 applies and it is based on the assumption that the liquid of the drop is completely in contact with the surface, filling all their asperities.

The Wenzel equation is valid when the drop size becomes larger with respect to the typical size of the topographical asperities, and the observable Wenzel contact angle represents the most stable observable contact angle corresponding to the global minimum of the system free energy.

Chemically Heterogeneous and Smooth Surfaces. The Cassie Equation

If a liquid droplet is placed on a smooth chemically heterogeneous surface, the observable contact angle θ_{app} is generally different from the local contact angle. In 1948, Cassie [148] proposed a model which described the observable contact angle θ_{app} on heterogeneous solid surfaces composed of two different materials, each one characterized by an intrinsic contact angle. The Cassie's modification to Eq.1.26 was similar to the explanation given by Wenzel for chemically homogeneous

from car windscreens. Just when the movement of the three-phase contact line is imminent, the values of the front (advancing) and rear (receding) contact angles are different (the downhill angle is always smaller than the uphill one).

and rough surfaces. So, if the chemical composition of a smooth surface is heterogeneous (e.g. two different chemical components), the interfacial energy per unit area changes with respect to the own interfacial energy of a chemically homogeneous and smooth surface composed of each one of the different chemical components. Thus, when a liquid droplet is placed on a heterogeneous surfaces, it responses changing its original configuration and, consequently, its observable contact angle θ_{app}. Cassie introduced two new terms (f_1 and f_2) with respect to the Young's equation (Eq. 1.26) in order to take into account the surface heterogeneity ($f_i = A_i/A$, $i = 1, 2$ where A_i is the total surface area corresponding to the i-component). So, the Cassie's equation is expressed as:

$$\cos(\theta_{app}) = f_1 \cos(\theta_1) + (1 - f_1) \cos(\theta_2) \tag{1.28}$$

where θ_i is the intrinsic contact angle of the smooth surface made by i-component. This equation can be generalized for a surface composed of n chemical patches as:

$$\cos(\theta_{app}) = \sum_i^n f_i \cos(\theta_i); \qquad \text{where } \sum_i^n f_i = 1 \tag{1.29}$$

The Cassie equation is valid when the drop size becomes larger with respect to the typical size of the chemical heterogeneity [149], and similarly to the Wenzel case, the observable Cassie contact angle represents the most stable observable contact angle corresponding to the global minimum of the system free energy [149, 150].

Chapter 2

Taking Care to Capture Surface Morphology

This chapter is divided into two different sections which analize aspects related to the capture of surface topography and how to obtain from its information about surface roughness, about the Wenzel's factor r due to its usefulness in wetting or adhesion studies where the knowledge of surface roughness is crucial.

The first part is focused on the study of the effect of some parameters, such as the triangular tesselation algorithm used to capture continous topographies, the topography resolution, the scan-size,..., on the measure of r, and how these parameters affect to measures which requiere the determination of surface roughness through surface area ratio parameter (r), particularly, wetting studies of rough surfaces.

The second part of this chapter analizes numerically, from a mathematical point of view, the influence of the directional character (vertical or normal) of the addition between waviness and roughness on the surface area ratio (roughness factor) of rough wavy surfaces. Different double-scale surfaces were simulated as perturbations, in both directions, of an analytically-defined wavy surface using a fractional Brownian noise.

2.1 Factors Affecting the Measurement of Roughness Factor of Surfaces and its Implications for Wetting Studies

The first part of this chapter [1] intends to be an introduction to those aspects which must be taken into account when a surface topography is acquired regardless of the instrument or device used to do it. As it is mentioned above, this part emphasizes the effect of experimental and processing parameters on the measure of the roughness factor. Roughness factor is widely used for topography characterization of surfaces in wetting phenomena. The measurement of meaningful values of roughness factor depends on the instrument settings, e.g. spatial resolution and scan-size, the instrument characteristics (e.g. voxel dimensions), the post-treatment of discrete data array (tessellation algorithm), and finally the nature of the surface texture (e.g. fractal). It is evident that if roughness factor is affected by these non-physics parameters, all the indirect quantities where the roughness factor appears for their estimation, such as wetting phenomena and solid surface energy, should be also affected by them.

2.1.1 Introduction

Surface metrology is the science which studies the set of procedures to measure local or global features of surfaces at any scale. Topography data are superposition of surface features found at different scales. These features can be grouped according to their characteristic horizontal distance (i.e. the spatial wavelength). In decreasing order of wavelength, these features are the shape, the waviness, and the roughness. The roughness is related to the surface fluctuations (periodic or non-periodic) of short wavelengths features, whereas waviness describes surface periodic and non-periodic features at intermediate wavelengths. In general, in many surface phenomena (e.g. wetting, and friction), shape is less relevant to the characteristic scale of the phenomenon. For example, for a given shape, roughness determines the behaviour of a surface in problems related to wetting and tribology, reflecting the surface-nature of these phenomena [151–154].

Any wavy rough surface $z(x, y)$, which is single-valued, can mathematically be defined as a superposition of two terms, one associated with the waviness $f(x, y)$ and another to the roughness $n(x, y)$. The superposition of waviness and roughness will be different depending on the process which governs the surface evolution. These processes can be grouped as ballistic-wise process [155], where the roughness is added to the waviness in the vertical direction, and growth/erosion process [156], where that addition occurs in the normal direction.

However, practical surfaces are not univocally well defined because a topography acquired by finite-resolution techniques is actually an array of equispatial points (i.e. discrete surface). This limitation explains the dependence of any topographic descriptor on the surface reconstruction (tessellation or meshing), the resolution (length of array) and the sample size (scan-size or scan-length). Hence, depending on the measuring parameters (lateral resolution, scan-size, meshing) [157–161] and the instrument characteristics (vertical range, pixel size, voxel shape), different values of topography descriptors for the same surface can be found. Furthermore, since many natural surfaces are self-affine fractals [160,162,163], an intrinsic scale dependence on geometrical features is observed regardless of the mentioned discretization and instrument effects.

Roughness descriptors based on the amplitude fluctuations of the roughness of a surface are widely used in surface engineering. However, statistical parameters, mainly the average height, R_a, and the root mean square height, R_q, provide no information about the horizontal distances between the surface features and therefore, the possible surface anisotropy [67].

[1] P.J. Ramón-Torregrosa, M.A. Rodríguez-Valverde, A. Amirfazli, M.A. Cabrerizo-Vílchez published in Colloids and Surfaces A: Physicochemical and Engineering Aspects, Volume 323, Issues 1-3, 20 June 2008, Pages 83-93

In order to describe surface roughness and texture properly, hybrid parameters (based on a combination of height and spatial wavelength) [67, 164], such as the surface slope, are employed together with the amplitude parameters. In fact, surface area (three-dimensional interpretation of surface slope) is especially useful in phenomena such as wetting where the liquid-solid interactions depend on their contact area [165, 166].

A special case of dimensionless hybrid parameter relevant to wetting is the surface area ratio or roughness factor, r. This parameter is defined as the ratio between the area (A) of the topography determined by any measurement technique, and the nominal or geometrically projected area (A_g) of the topography:

$$r = \frac{A}{A_g} \tag{2.1}$$

Since A_g is obtained from the projection of the microscopic area, A, onto a reference surface, it is also known as apparent area. This reference surface is generally a horizontal plane obtained after a vertical filtering process [167]. As such, A_g will be equal to the scan area (product of the transversal and longitudinal scan-lengths).

The scan-size and sampling interval dependence of statistical, spatial and hybrid parameters have been studied by several authors [154, 166–169]. Scan-size and spatial resolution was studied using different techniques such as white light confocal microscopy (WLCM) [167], profilometry [169] and atomic force microscopy (AFM) [154,166,169]. These studies have shown that roughness descriptors are affected by the resolution and the scan-size. The effect of the scan-size over the roughness factor from scanning force microscopy (SFM) topographies have also been studied [168]. However, comparative importance of roughness descriptors and their dependence on measurement parameters is very difficult to understand from above studies as each have looked at a particular system using a particular instrument. As such, a general understanding is lacking currently.

Furthermore, before applying the definition of roughness factor, r, in any measurement technique the waviness of a surface should be filtered (by instrument) in order to isolate the information corresponding to the roughness. The waviness filtering algorithms remove the waviness from topographical data by fitting functions or using different filters [170–172]. The practical filters used, are generally based on the minimization of vertical offsets [173]. Therefore, such algorithms can be only applied to surfaces governed by ballistic-wise processes. For surfaces governed by growth/erosion processes, a least-squares orthogonal distance fitting technique should be used [174,175]. The effect of the waviness filtering is not discussed in this section. It will be studied in following part.

In wetting phenomena, Wenzel [145] related the effect of topography of a rough, but chemically homogeneous surface to contact angle of that of an ideally smooth surface through Eq. 2.2

$$cos\theta_{app} = r\, cos\theta_Y \tag{2.2}$$

where θ_{app} is the apparent contact angle (experimentally accessible angle) and θ_Y is the Young's contact angle (the angle related to the solid surface energy observed on a smooth surface). Consequently, the estimation of meaningful values of surface energy for rough surfaces will depend partially on a correct evaluation of roughness factor. Recently, several authors have studied the variation of apparent contact angle with roughness factor [166, 176] and the scan-size effect on the determination of roughness factor [168]. The surface roughness also plays an important role in study of superhydrophobic surfaces and its thermodynamic description [177–179].

The principal aim of this study is to comprehensibly analyze the parameters related to the measurement of r, i.e. scan-size, lateral resolution and meshing, and that of instrument characteristics, by using two different instruments. Therefore, one of the aims of this study is to evaluate, compare and determine the importance of the effects of each of these parameters on r. This is done by experimenting with synthetic (mathematically constructed) surfaces as well as roughened

titanium surfaces. Furthermore, the results will be discussed in the context of wetting and contact angle interpretation, as an example. As such, this will be the first study that has examined the evaluation of r using a multitude of parameters and two instruments in a single study, and has analyzed the finding in the context of wetting.

2.1.2 Estimation of Roughness Factor

From differential geometry, the definition of surface area as an integral parameter does not allow it to be a useful parameter to distinguish surface topographies; because a surface is only well-defined, if its metric and curvature tensors are known [180, 181]. Consequently, two surfaces with different surface morphology can have identical surface area. As an example, These surfaces

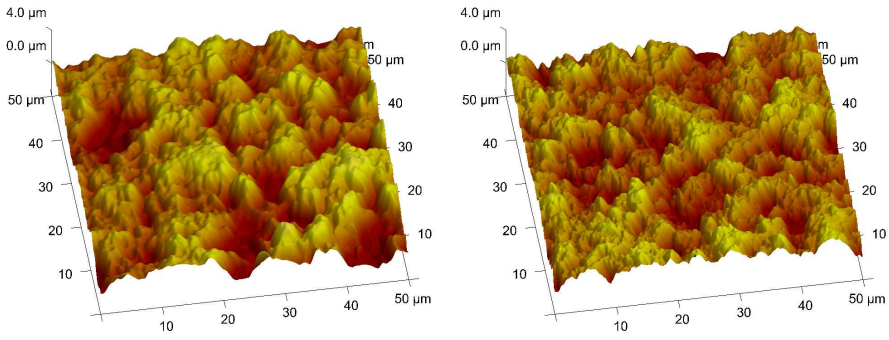

Figure 2.1: Carbon aerogel surfaces topographies acquired by AFM in ContactMode^{TM} with a resolution of 1024x1024 pixels. These topographies exhibit identical area ($3545\mu m^2$) and geometrical area ($50x50\mu m^2$), although they show different textures.

present identical values of A_g and A (consequently r values), but obviously have different topographies. Consequently, r is not able to characterize univocally a surface.

Lai and Irene [170] concluded that there is no method that yields the true surface area for microscopically rough surfaces. Therefore, complete description of a surface is not possible due to limitations of the instrument and the discrete character (due to discrete information collection by the instrument) of the topography. Therefore, the true roughness value is non-accessible experimentally because it would require the acquisition of infinite number of points (i.e. a continuous topography) and this is technically impossible at the moment. Consequently, due to the discrete acquisition and the treatment of the topography some information about the surface is always lost.

Koinkar and Bhushan [154]shown that the sampling interval should be always lower than the correlation length (average distance between points at some specific elevation). For a given sampling interval, the scan size should be sufficiently large to contain the necessary topographical information and to provide meaningful values of the topography descriptors.

The scale effect is not only observed in discrete topographies, but also for particular continuum surfaces, like fractals, where the scale dependence is intrinsic to their topology. Fractals are used to describe structures that exhibit the highly irregular behavior commonly found in the nature. The scale dependence of self-affine fractal surfaces has been widely studied [71, 182–184]. A self-affine rough surface exhibits different area depending on the observation scale. This means that the area of a self-affine surface does not have a unique value, instead it depends on the scale. Hence, roughness factor of self-affine surfaces is a scale-sensitive parameter, regardless the instrument used.

In the following two sections, the necessity and fundamentals of the need for study of measuring parameters affecting r will be discussed in detail.

Area Computation of Discrete Surfaces

Rough surfaces can be reconstructed by triangular facets (different triangular tessellations) whose vertices are given in a discrete height map. Hence, the surface area can be estimated by the cumulative area of the triangles embedded in three-dimensional space (Fig. 2.2). Since topography

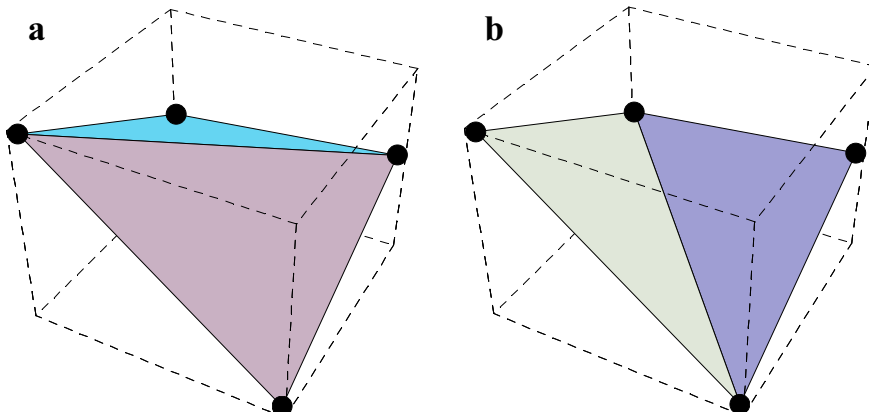

Figure 2.2: Two possible triangular tessellations of a grid cell of rectangular lattice. The dots represent the discrete data collected by the instrument. (a) Counter-clockwise: triangle facets placed in counter-clockwise sense; (b) Clockwise: triangle facets placed in clockwise. Note that according to the height map, these triangulations cause a concave (CCW) and convex (CW) shape in the topography.

data are usually acquired on rectangular lattices, the grid cell area is approximated by the sum of the areas of two triangles (4 vertices, 2 triangles), see Fig. 2.2. However, there are at least two ways to place triangular patches per grid cell, i.e. clockwise (CW) and counter-clockwise (CCW) triangulations (these two triangulations will be considered as the basic ones); see Fig. 2.2. More complex tessellations can be applied for irregular grids (e.g. Delaunay triangulations) [185]. Delaunay triangulation is based on finding the nearest neighbors, and it is on average an intermediate case of the basic triangulations above.

Since there is no unique tessellation solution for a rough surface, the area, and consequently the roughness factor could take several values depending on the tessellation algorithm used. To show the effect of the tessellation algorithms, synthetic surfaces are used in this study.

Measuring Parameters

A greater number of points measured per unit area allows for a refined description of a topography and thus, to increase the accuracy of numerical value of roughness factor. The discrete character of acquisition methods for the topographies implicitly involves the dependence of roughness factor with the sampling interval; on therefore, with the resolution and the scan-size. The resolution and scan-size are also strongly related to the characteristic of the instrument employed. Hence, an unbalance between the vertical and spatial ranges of instrument (not cubic voxels) can cause artifacts in the surface area estimation, hence r.

To study systematically and quantify the effect of the scan-size, resolution and instrument characteristics on the roughness factor value, different experiments must be designed to tackle these parameters separately. As such, to evaluate the effect of the spatial resolution, the same surface region was studied but the number of points acquired in the topography was changed (various resolutions). The effect of the scan-size was measured from the acquisition of topographies with identical spatial resolution but changing the scan-size for the different topographies. To study the effect of instrument and to enlarge the scan-size range in this study, two different instruments were used.

2.1.3 Materials and Methods

Surfaces

The effects of tessellation algorithms, resolution and scan-size have been studied in this paper using synthetic (mathematically constructed) and acid etched and passivated titanium surfaces. Moreover, in order to compare the results obtained for the behavior of r with resolution and scan-size from synthetic surfaces, titanium surface topographies were acquired by AFM and WLCM.

1. Synthetic Surfaces

   To study the effect of using different tessellation algorithms on the value of r, a synthetic discrete surface (11x11 points) was constructed with a unit geometrical area ($A_g = 1$), see Fig. 2.3a. The height map of the rough surface was created using the fractional Brownian

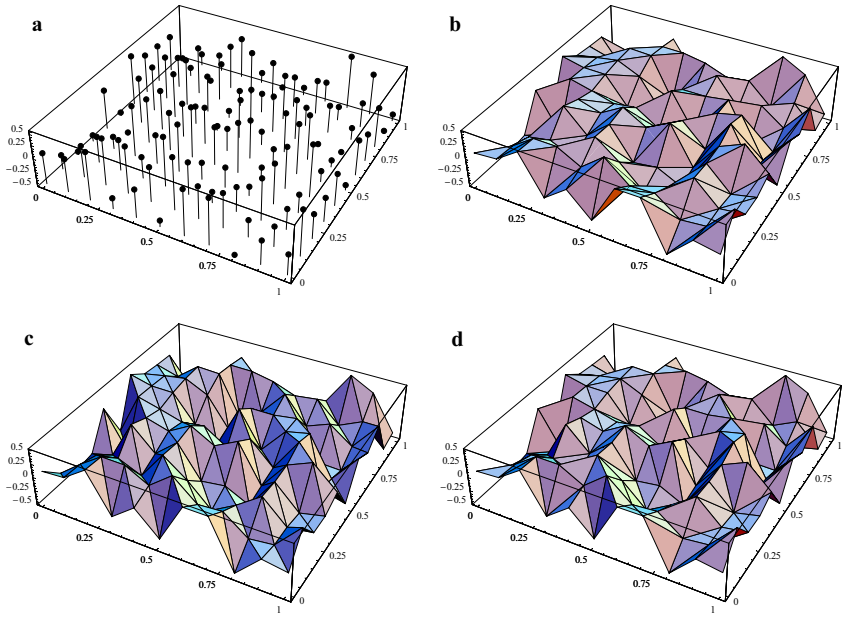

Figure 2.3: Roughness factor calculated using different triangular tessellations of the same discrete surface, i.e. a 11x11 points height map shown in (a). (b) Counter-Clockwise triangulation $r = 4.98$, (c) Clockwise triangulation r=4.90, (d) Delaunay Triangulation $r = 4.91$.

   motion (fBm) technique [186, 187]. Amongst many possibilities to mesh a surface, three different tessellation algorithms (two basic ones and the Delaunay triangulation) were used to

mesh and compute the respective topographic area (A), and therefore its roughness factor r of the synthetic surfaces (note $A_g = 1$).
The effect of resolution on the roughness factor value was computed for synthetic surfaces with different surface roughness patterns (i.e. fractal and non-fractal). All the surfaces were constructed with unit geometrical area ($A_g = 1$) and all of them were generated at maximum resolution of 1024x1024 pixels. For surfaces with fractal patterns, fBm technique with a fixed fractal dimension of $D_f = 2.8$ was used. Different sinusoidal patterns were generated from the respective analytical expression for each surface:

$$\begin{cases} z_{1\mathrm{D}}(x,y) = z_0 \cos\left(2\pi\dfrac{y}{\lambda}\right) \\ \\ z_{2\mathrm{D}}(x,y) = z_0 \cos\left(2\pi\dfrac{x}{\lambda}\right)\cos\left(2\pi\dfrac{y}{\lambda}\right) \\ \\ z_{\mathrm{packing}}(x,y) = \dfrac{z_0}{2}\left(\cos\left(2\pi\dfrac{x}{\lambda}\right)+1\right)\left(\cos\left(2\pi\dfrac{y}{\lambda}\right)+1\right) \end{cases} \tag{2.3}$$

where the spatial period λ was varied (0.1, 0.5, 1.0 and 2.0 in arbitrary units (a.u.)), z_0 was accordingly varied to fixing the r value in all surfaces and the scan-size range was 2.0 a.u.
Fractal-sinusoidal patterns were simulated as the addition of one sinusoidal family and one fractal pattern. To study the effect of resolution on the roughness factor, the spatial resolution was reduced by skipping points in the original synthetic surface (1024x1024 pixels) to achieve the desirable resolution down to 2x2 pixels, keeping the data as a square array. Moreover, the roughness factor was always computed using CW tessellation algorithm. This was an arbitrary choice to exclude the influence of tessellation method on calculation of r. The roughness factor computed for the 1024x1024 pixels synthetic surface can be considered as the base line roughness factor of each surface (i.e. sinusoidal, fractal, and fractal-sinusoidal patterns).
The effect of the scan-size on the roughness factor value was also studied from synthetic surfaces. The synthetic surfaces used were similar to the ones used for the resolution study. The scan-size range varied from 0.5 to 2.0 arbitrary units (a.u.). To reduce the scan-size, the base surface with a scan-size of 2.0 a.u. was cut successively to smaller scan-sizes, i.e. 1.0 and 0.5 a.u. As the resolution was set to 512x512 pixels, for the case where scan-size was 0.5 a.u., it was necessary to perform an interpolation on the available number of points, which was reduced to 256x256 pixels as result of cutting operation. The interpolation allowed a final resolution of 512x512 pixels for the surface with scan-sizes of 0.5 a.u. This interpolation was linear. Finally, the roughness factor was also computed using CW tessellation algorithm.

2. Titanium Surfaces

   For experiments, commercially pure (grade II) unalloyed titanium disks (Manfredi, S. Secondo di Pinerolo, Italy) were used. These disks were polished, with wetted metallographic SiC papers at 2400 grits and 0.05 μm alumina powders, and etched, by complete immersion, using a hydrofluoric acid solution at 10% . The etching time was 420s. After etching, the surfaces were passivated by immersion in a nitric acid solution at 30% during 20 minutes.

Instruments

The topographies of the titanium surface were acquired using atomic force microscopy (AFM) and white light confocal microscopy (WLCM), in order to explore several scan-sizes from nanometer to millimeter scale.

AFM experiments were performed in TappingMopde^{TM} under ambient conditions using a Nanoscope IV from Digital Instruments, (Santa Barbara, California, USA). Veeco Silicon Nitride cantilevers for topography measurements (resonance frequency 275 kHz, force constant 37 N/m) were used for height imaging. WLCM experiments were done with a Plμ white light confocal microscope by Sensofar with three objectives (10x, 20x and 50x). Optical properties and specifications are described elsewhere in http://www.sensofar.com.

To explore the resolution effect on the roughness factor, the same area was scanned using various resolutions. For the AFM, the resolution was varied from 2x2 to 1024x1024 pixels at the following constant scan-sizes: 0.5, 1, 5 and 10 μm. For WLCM, the resolution was varied from 2x2 to 512x512 pixels at the following constant scan-sizes: 200, 500 and 1000 μm.

2.1.4 Results and Discussion

Triangular Tessellation Effect

Fig. 2.2 shows application of three different triangulations (CW, CCW and Delaunay) for the same discrete surface, i.e. height map shown in Fig. 2.2a (each point in Fig. 2.2a represents a discrete data point typically obtained by an instrument).

The value of roughness factor for each meshing varies slightly, 2%, depending on the triangulation method used (CCW triangulation $r = 4.98$; CW triangulation $r = 4.90$; and Delaunay triangulation $r = 4.91$). The r values of basic triangulations (CW and CCW) provide the extreme values of roughness factor, because these triangulations display a predominantly convex or concave surface [188]; the r value for Delaunay triangulation gives an intermediate value. The difference between the r values is not very large for the case studied. It seems that this is a general trend as Russ [188] also found the difference between the area calculated by clockwise (CW) and counterclockwise (CCW) tessellations was only about 3.5%. To account for this variation, it is suggested to use the average value of the roughness factor found using the CW and CCW methods. It is also a good practice for comparison purposes to indicate the tessellation algorithms used. Note that to see a difference between the r values obtained through different algorithms and provide an accurate value of roughness factor, the surfaces have been simulated by assigning a high relative value to the ratio between the maximum vertical distance (z_{max}) in the topography and sampling interval ($f \approx 12$). Otherwise, for surfaces with large vertical to horizontal scale ratio (high height fluctuation and small scan-size), the roughness factor obtained by any triangulation algorithm is underestimated and the accuracy of its value cannot be ascertained as Lai and Irene [170] concluded. Lai and Irene establish that for $f > 10$, the triangulation algorithms provide an accurate value for the roughness factor, where f is defined as follows

$$f = \frac{z_{max} \cdot \text{resolution}}{\text{scan-size}} \tag{2.4}$$

Measuring Parameter Effect

The evaluation of the resolution and scan-size effects on roughness factor was studied experimentally using acid-etched/passivated titanium surfaces. Moreover, the effects of the resolution and the nature (fractal or non-fractal) of the surface roughness on the r value have been studied from synthetic surfaces.

1. Resolution effect

To explore how the nature of the surface affects the behavior of the roughness factor value vs. resolution of the topography, synthetic rough surfaces were used. Note that the true r value is computed from the synthetic surfaces obtained at maximum resolution (1024x1024 pixels). This maximum resolution corresponds to the mathematically defined resolution for the synthetic surfaces (see Section 2.1.3). Fig. 2.4 shows that the fractal or non-fractal

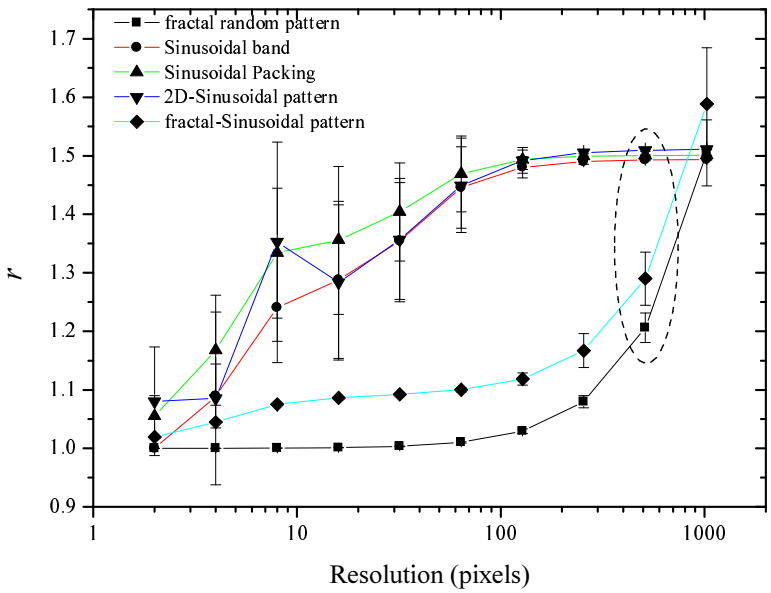

Figure 2.4: Roughness factor vs. resolution for synthetic surfaces with identical scan-size (1 arbitrary units). Different types of surfaces were synthesized in order to explore the effect of the roughness nature on the behaviour of roughness factor with the resolution. These surfaces can be grouped as fractal patterns, simulated by fractional Brownian motion (fBm), sinusoidal patterns, computed from their analytical function, and fractal-sinusoidal patterns, which were designed by means of the addition of the fractal pattern to the sinusoidal pattern. The lines are to guide the eyes.

nature of the surface influences the dependence of r on resolution. Thereby, for pure fractal surfaces, if the topography resolution is lower than 128x128 pixels, the r value is very near to 1 (perfectly smooth surface), but for resolutions greater than 256x256 pixels, the r value increases strongly as resolution increases. For sinusoidal patterns, the behavior of the r value with the resolution is different. In this case, the r value increases gradually for resolution range from 2x2 to 128x128 pixels, and remains constant afterward. This trend is kept regardless of type of sinusoidal roughness pattern (see Fig. 2.4). Therefore, for non-fractal patterns, e.g. sinusoidal, the true r value is reached at lower resolution than that of one used to define the surface; i.e. 1024x1024 pixels. This behavior can be understood if the ratio between the sampling interval and the spatial period/amplitude of the sinusoidal functions is taken into account. When the r value for these surfaces reaches a constant value, the sampling interval is lower than the spatial period of the sinusoidal surface, and therefore the surface information is completely collected from the topography. Otherwise, when the resolution decreases, the sampling interval increases, and part of the surface information is lost and therefore the r value decreases. For fractal-sinusoidal surface roughness patterns,

the behavior of the r value vs. resolution differs little from that of pure fractal ones. In this case, from 8x8 to 16x16 pixel resolution, the r values increases slightly, and remains constant (with a value near to 1.1) till spatial resolution increases to 128x128 pixels (similar to pure fractal surfaces). Then, for resolutions greater than 256x256 pixels, the r value increases rapidly as resolution increases to 1024x1024 pixels. This suggests that the fractal nature of the surface seems to be the dominating parameter in determining the behavior of r value with changing resolution.

In Fig. 2.5, the dependence of the roughness factor on the resolution is shown for both

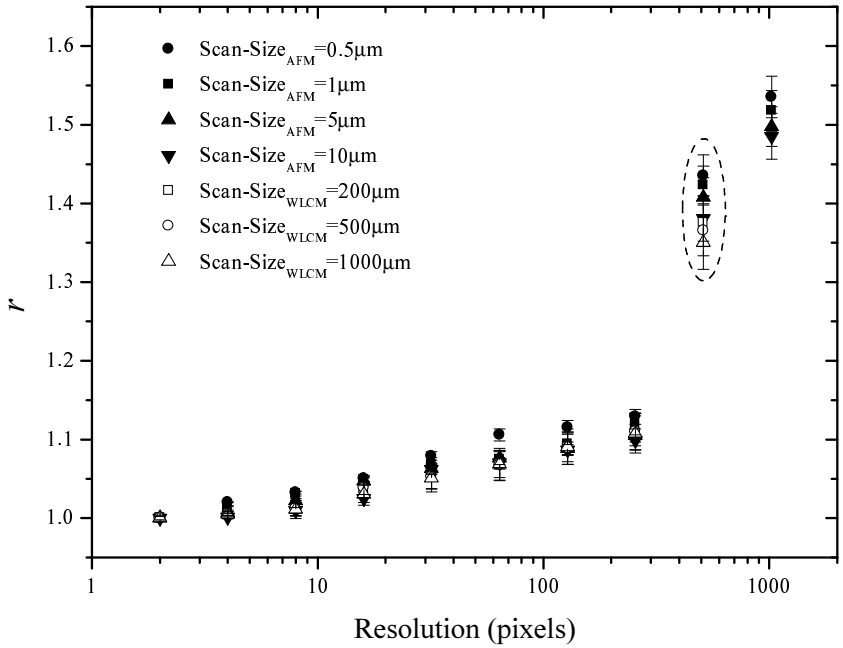

Figure 2.5: Roughness factor vs. resolution for topographies acquired by AFM (solid symbols) and WLCM (open symbols) for different scan-sizes (0.5, 1, 5 and 10μm for AFM measurements; 200, 500 and 1000μm for WLCM ones).

AFM and WLCM experiments. Since all topographies were measured over the same region at the same resolution and scan-size, the error bars are only due to instrumental errors. These instrumental errors have two different origins: one associated with thermal/electronic noises and another is due to the characteristic pixel/voxel dimensions (size and shape) associated with each device. Assuming that the thermal/electronic noises are random and that the order of magnitude of the noise is similar for both devices, larger error bars for WLCM measurements suggest that their pixel/voxel dimensions are larger than that of AFM.

In Fig. 2.5 the roughness factor increases from 1, which represents an ideally smooth surface. This behavior is expected since as the topography is more finely defined for a fixed scan-size, the surface area increases. The minimum value of roughness factor ($r_{min} = 1$) is independent of the scan-size. Additionally, a rapid rise of the roughness factor is seen for resolutions larger than 256x256 pixels for any scan-size and for both instruments (AFM and WLCM). Since greater resolution means smaller sampling interval, there is a critical sampling interval for which surface features of short wavelengths start to appear in the topography (the fineness of

the topography has been captured due to the increase of the resolution). As, these features are the most fluctuating components of a surface, therefore, they contribute significantly to surface area and hence the observed rapid rise in r value. It is interesting to note that the rapid rise of the r occurs regardless of the pixel size which is different for each device. This suggests that the observed increase should be due to the nature of the surface roughness. This cannot be due to instrumentation as if this was the case one would have expected to see a dependence of the location where the rise begins on the type of instrument used (note that the wavelengths captured by each device is different at a given resolution).
Considering Fig. 2.4, one can conclude that the Fig. 2.5 suggests that the titanium surfaces studied are fractals in nature or have a strong fractal component. Moreover, the r value which should be considered as the correct one for titanium surfaces is the computed value from the topography data captured at maximum resolution of the device, regardless of the scan-size considered.
From the above results, the roughness factor measurements are strongly affected by the spatial resolution of the surface topography. These findings should be general regardless the surface treatment and material. Accordingly, for a fixed scan-size, the maximum spatial resolution should be used for the device.

2. Scan-Size Effect

Fig. 2.6 shows the variation of roughness factor with the scan size at a constant resolu-

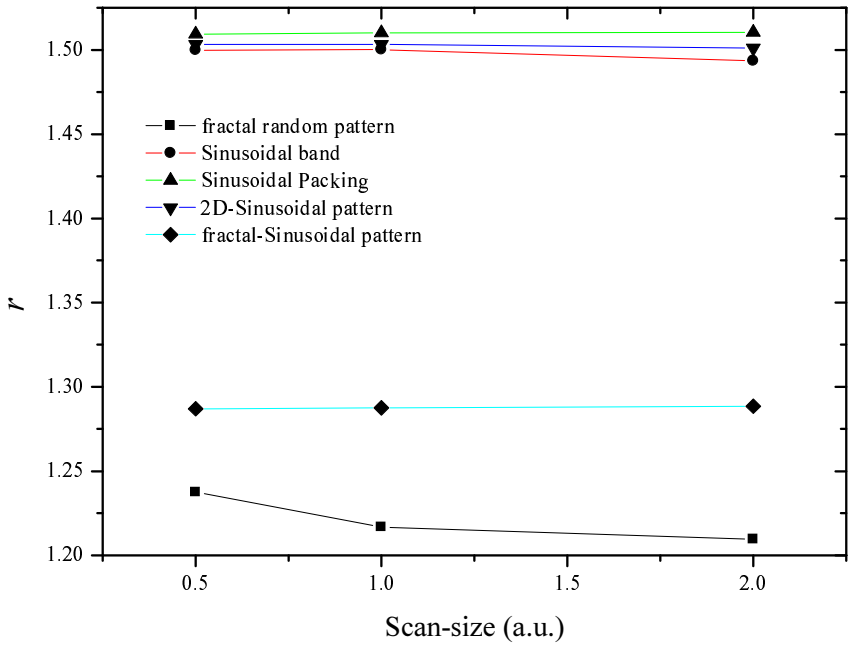

Figure 2.6: Roughness factor vs. scan-size for synthetic surfaces. The resolution was constant at 512x512 pixels, but the scan-size was changed from 0.5 to 2 a.u. The lines are to guide the eyes.

tion of 512x512 pixels. The scan-size range varied from 0.5 to 2 a.u. The ratio between resolution and the range of the scan-size explored was determined in order to satisfy the con-

dition imposed by Koinkar and Bhushan [154] (see also Section 2.1.2). Hence, for this range, no significant change in the roughness factor value was observed regardless of the roughness nature, i.e. the roughness factor remains constant. This is also confirmed experimentally by examining the data in Fig. 2.5. From Fig. 2.5, it is clear that regardless of scan-size the roughness factor remains constant for resolutions below 256x256 pixels. For resolutions higher than 256x256 pixels, e.g. the data enclosed by the ellipse in Fig. 2.5, experiments suggest that the scan-size for a given resolution does cause a slight difference (see data enclosed by the ellipse in Fig. 2.5), but this is far less than the effect of resolution. To further

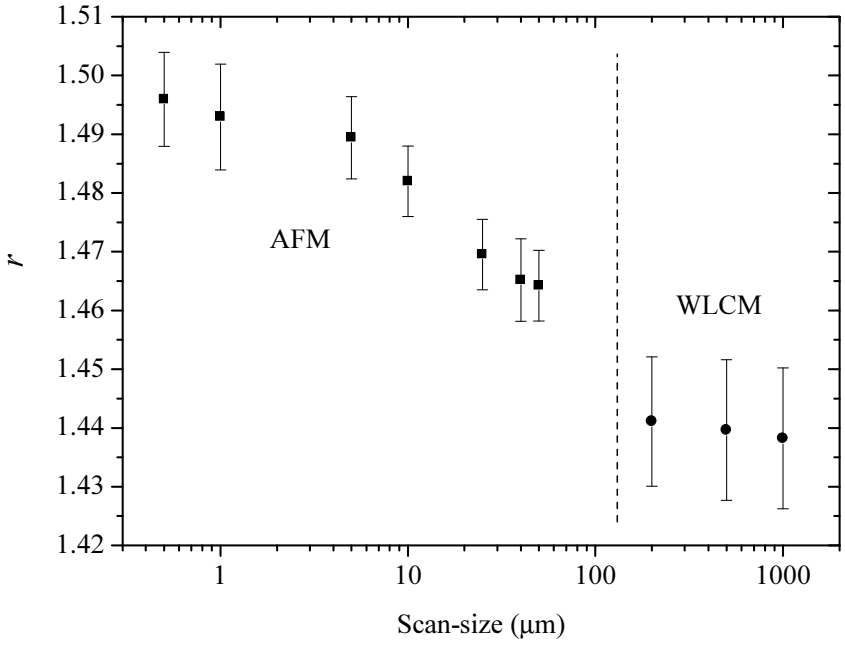

Figure 2.7: Scale dependence of roughness factor for titanium surface topographies acquired by AFM and WLCM (512x512 pixels). The dashed line is only a visual aid to distinguish the data obtained from various instruments.

highlight the findings from experiments, in Fig. 2.7, the dependence of the roughness factor with the scan-size is presented at constant resolution of 512x512 pixels. The error bars are due to the statistical sampling over ten different regions. The instrumental errors have been subtracted from the error bars of Fig. 2.5 to highlight the effect of the scan-size. In Fig. 2.7, roughness factor slightly decreases when the scan-size (i.e. the sampling interval) increases. A small drop in r value is observed as instrument to measure the r is changed. This decrease can be explained from the loss of topography fineness due to the increase of sampling interval or pixel size between WLCM and AFM. There is an additional cause to explain this drop; namely, the vertical range (voxel dimensions) of each device, because if the voxel dimensions for WLCM are larger than that for AFM, the loss of topography information is larger too. Consequently, the value of the roughness factor is lower when using WLCM. For this reason, AFM is most suitable to measure nanoscopic vertical features whereas WLCM only allows detecting microscopic ones. It should be noted that at worst the effect of scan-size on r is less of 5%, whereas the resolution effect can be as high as 50%.

As rule of thumb, scan size should be sufficiently large to contain the necessary topographical information. However, in studies of interacting interfaces, the scan-size should be closer to the characteristic length of the system.

3. The effect of the roughness values on wetting

As shown above, roughness factor does not have a unique value. As an example, the consequences of a non-unique value for roughness factor on wettability of acid etched/passivated titanium surfaces are presented. It is assumed that the apparent contact angle value does not depend on the drop volume [189]. From the measured contact angle $\theta_{app} = (54 \pm 3)^\circ$ [190] and the roughness factors from Fig. 2.7, Young's contact angle (θ_Y) was calculated using Eq. 2.2.

As it was presented previously, the effect of the tessellation algorithm used to compute the r value is between $2-3\%$. This $2-3\%$ change in r value translates into a non-significant difference in the Young's contact angle value for the system studied; especially considering the contact angle measurement techniques presents an experimental error on the order of $\pm 1^\circ$. Considering that for titanium $\theta_{app} = 54^\circ$ and $r = 1.50 \pm 0.04$ (0.04 represents a 2.5% change in r), using Eq. 2.2, the Young's contact angle obtained is $(66.9 \pm 0.5)^\circ$. Even considering the nonlinear nature of the cosine function involved in the Eq. 2.2, the error in the Young's contact angle due to the tessellation algorithm used to compute the roughness factor is always very small.

Fig. 2.8 shows the values of the Young's contact angle for water found from the Wenzel's equation (Eq. 2.2) using $\theta_{app} = 54^\circ$ and the roughness factor calculated from different spatial resolution (scan size was constant for each measurement). By definition, Young's contact angle is a material property [191] and therefore, it should not be affected by any measurement parameter for topographies. In fact, the behavior observed in Fig. 2.8 is an artifact of the resolution-sensitive character of roughness factor. The resolution dependence of the roughness factor translates into a $\approx 15^\circ$ variation of the Young's contact angle for etched/passivated titanium surfaces.

The above variation observed in contact angle due to resolution can have significant effect on interpretation of contact angle on surface energetics calculations, for example. As an example, interpreting the above data using an "equation of state" approach [192,193] to compute the solid-vapor interfacial energy (γ_{SV}) value from the θ_Y, results in the plot shown in Fig. 2.9.

The "equation of state" used is:

$$\frac{cos(\theta_{app}) + 1}{2} = \sqrt{\frac{\gamma_{SV}}{\gamma_{LV}}} e^{-\beta(\gamma_{LV} - \gamma SV^2)} \tag{2.5}$$

where γ_{LV} is liquid-vapor interfacial tension and $\beta = 0.0001247(m^2/mJ)^2$ is a constant. Eq. 2.5 may be viewed as controversial. However, the aim of this paper is only to demonstrate the influence of the resolution for acquiring topographical information that can be used to find a physical quantity as solid surface energy (γ_{LV}). The choice of Eq. 2.5 in this paper has been mainly due to its simplicity for γ_{LV} calculation. It is not the intent of this study to provide any absolute value for solid surface energy. The amount of change in γ_{SV} will likely be different using different methods, but the trend would remain the same. The liquid was assumed water at room temperature with $\gamma_{LV} = 72.5 mJ/m^2$.

Fig. 2.9 shows that the γ_{LV} decreases as resolution increases. However, because γ_{LV} is a material property, it should not depend on any measuring parameter, like resolution. Therefore, the behavior observed is an artifact of the dependence of the roughness factor with the

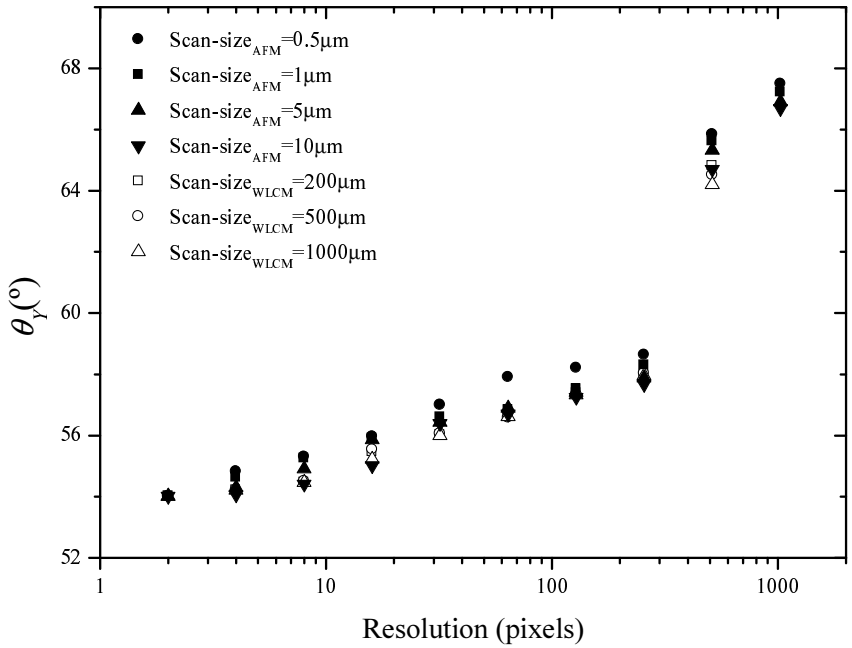

Figure 2.8: Resolution dependence of the Young's contact angle (θ_Y) found from the application of the Wenzel's equation, Eq. 2.2, for the acid etched/passivated titanium surfaces. Topographies were acquired by AFM and WLCM, changing the resolution from 2 to 1024 pixels for AFM and from 2 to 512 pixels for WLCM. The apparent contact angle (θ_{app}) for water on the titanium surface was 54°.

resolution. The resolution dependence of the roughness factor translates into $\approx 6mJ/m^2$ variation of solid-vapor interfacial tension for etched/passivated titanium surfaces.

As mentioned above, scan-size influences the r value to much lesser extent than resolution, and the results below suggest that maybe important only when considering the contact angle data interpretation for hydrophilic systems (low contact angle). To demonstrate this point we have considered two additional values of θ_{app} at hydrophilic and hydrophobic limits, i.e. 20° and 100° (note that contact angle of di-iodomethane on titanium is about 22°, and 100° is an arbitrary value to demonstrate the effect for a hydrophobic system). Analyzing the two values of 20° and 100° for θ_{app} also clarities the influence of the cosine function present in Eq. 2.2.

Fig. 2.10 shows the values of the Young's contact angle for different scan-sizes of the topography at fixed resolution (512x512 pixels) and assuming that apparent contact angles (θ_{app}) of the acid etched/passivated titanium surfaces were 20°, 54° and 100°. The Young's contact angle (given by Eq. 2.2) decreases as scan-size increases, regardless of the device used to acquire the topography, if the apparent contact angle of the surface is lower than 90°, whereas if θ_{app} is greater than 90°, the corresponding Young's contact angle increases as scan-size increases.

The effect presented in Fig. 2.10 is an artifact of the scan-size-sensitive character of roughness factor. The effect of the scan-size on the Young's contact angle is much less than the effect of the resolution, but could be important if the apparent contact angle was near 0° or

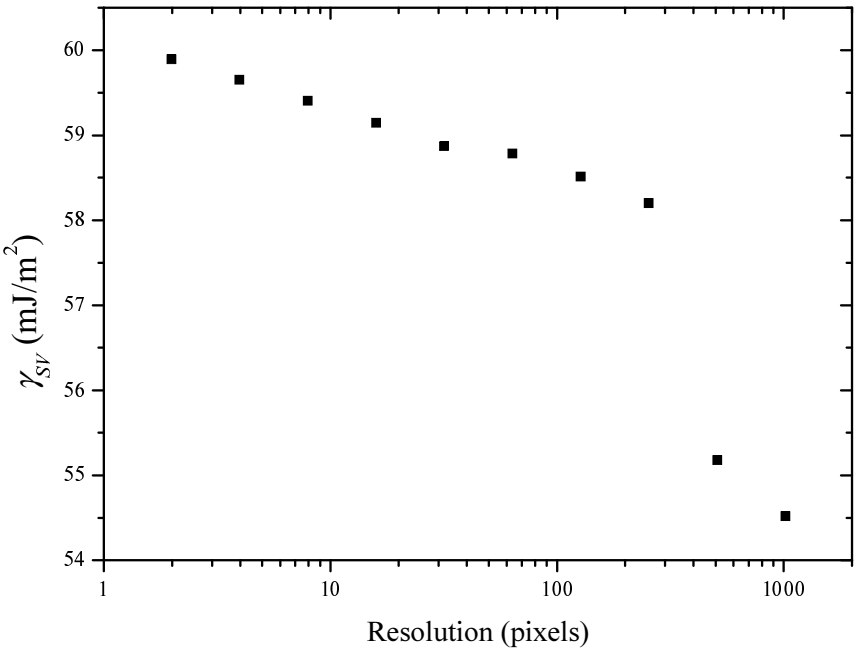

Figure 2.9: The false dependence of the surface energy for acid etched/passivated titanium surfaces seen as a result of non-unique value for r. The scan-size considered was $0.5\mu m$ and the topographies were acquired by AFM. The apparent contact angle was assumed 54°, and the γ_{SV} was calculated from Eq. 2.5.

180°.

A surface energetic analysis could be done to study the effect of scan-size of topography on the γ_{SV} values, but according to the data presented in Fig. 2.10; this effect is less significant than that of the resolution, for any apparent contact angle assumed.

2.1.5 Conclusions

Roughness factor depends on the acquisition and the treatment of the surface topography data. Therefore, the effects of the resolution, the scan-size and the instrument used to acquire the topography, as well as the tessellation algorithms used to compute the roughness factor value have been analyzed. Several important conclusions emerge from this study. Therefore, form this part of the chapter it is possible to extract some conclusions which are summarized as follows:

The value of roughness factor depends slightly, 2%, on the triangulation algorithm employed to reconstruct the topography. Therefore, the influence of the tessellation triangulation to interpret the results for finding the Young's contact angle or solid-vapor interfacial tension will be negligible. However, in order to provide a better value of the roughness factor, an average of the values computed from different triangular tessellations should be considered. Also, the meshing algorithm should be indicated in order to allow comparison of results from different studies.

The resolution of the topography affects strongly the value of the roughness factor, and

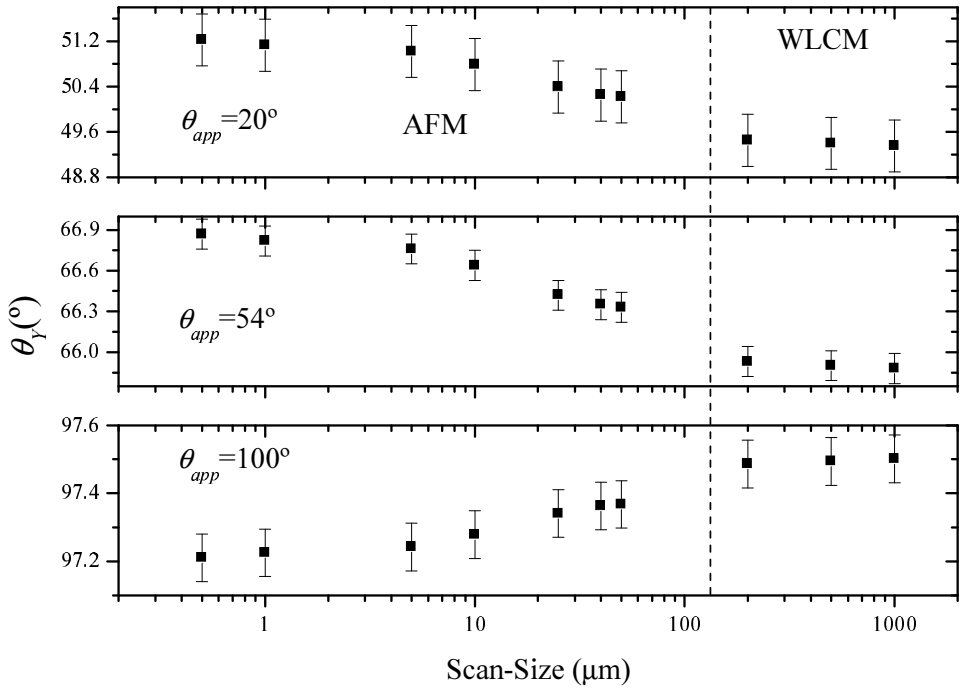

Figure 2.10: Scale dependence of the Young's contact angle (θ_Y) of acid etched/passivated titanium surfaces assuming that the apparent contact angle (θ_{app}) of those surfaces were 20°, 54°, and 100° and calculated from Eq. 2.2. The roughness factor for the different surfaces was calculated from the topographies acquired by AFM and WLCM at resolution of 512x512 pixels.

therefore any other quantity determined from it. From synthetic surfaces, the behavior of the roughness factor with the resolution has been studied. It was found that the r value will change differently with the resolution depending on the fractal or non-fractal nature of the surface roughness. For fractal patterns, the roughness factor increases rapidly from resolution greater than 256x256 pixels; for non-fractal patterns, the roughness factor increases gradually from 2x2 to 128x128 pixels and for resolutions greater than 256x256 pixels, its value remains constant. For titanium surfaces, the roughness factor increases as the resolution increases regardless of the instrument (AFM or WLCM) used to acquire the topography. From the observations done for synthetic surfaces, it has been possible to conclude that titanium surface has a fractal nature.

The effect of the scan-size on r value was evaluated using synthetic and etched/passivated titanium surfaces and two different devices (WLCM and AFM) in order to study a large scan-size range (from 0.5 to 1000μm). The behavior of the r value with the scan-size observed for synthetic surfaces predicts that the effect of the scan-size is practically negligible when the scans-size changes from 0.5 to 2 a.u. Experimentally, for the etched/passivated titanium surface, the effect of the scan-size on r value was also found to be negligible for resolution below 256x256 pixels, but for resolution greater than 256x256 pixels, the r value showed some dependence on scan-size (decreased for the same resolution) regardless of the instrument used.

The effect of the resolution on the roughness factor value can translate into significant differences when r value was used to find/interpret other quantities, such as the Young's contact angle or solid surface energy. For etched/passivated titanium surfaces with $\theta_{app} = 54°$, the Young's contact angle values ranged spanned $\approx 15°$ for resolution range from 2x2 to 1024x1024 pixels. Equally, the solid-vapor interfacial tension (computed from Eq. 2.5) changed $\approx 6mJ/m^2$ for the same resolution range. The scan-size of the topography affected calculation of the Young's contact angle and solid-liquid interfacial tension to a lesser degree.

The acquisition of meaningful topographies require, for fixed scan-size, the maximum spatial resolution allowed by the device. As rule of thumb, scan size should be sufficiently large to contain the necessary topographical information. In studies of interacting interfaces, the scan-size should be closer to the characteristic length of the system.

In increasing order of loss of information, the parameters that affect the roughness factor are: the tessellation algorithms used to mesh the topography, the scan-size employed to acquire the topography, and the resolution of the topography (number of points collected by the topography). This order of importance of the parameters studied seems to be regardless of the instrument used to acquire the topography.

Finally the following recommendations based on this study are provided to guide acquisition of surface topographies.

- Regardless of the roughness nature (fractal or sinusoidal), the surfaces images have to be acquired at maximum resolution possible for the equipment used. However, if time or computational reasons are of concern, the minimum resolution which must be used to acquire any image should be 256x256 pixels to capture necessary and meaningful information about the topography of the surface.
- Given that the scan-size plays a less important role in obtaining topographical information, there is more freedom to choose this parameter, however, it is prudent to select the scan-size that is relevant to the scale-size of the phenomenon of interest.
- These recommendations are independent of the device used to acquire the surface topography and of the tessellation algorithm used to compute the surface area.

2.2 Effect of Waviness Filtering on Surface Area Ratio Measurements by 3D Microscopy: A Numerical Study

The second part of this chapter is focused on the analysis of the effects produced on the surface morphology aspect due to the presence on it of surface features with different wavelengths, and how such presence affects to the value of surface area ratio parameter. Surface area ratio is a surface roughness parameter which directly relates the role of the surface roughness on physical phenomena as wetting and tribology. Therefore, as in general the topography of a wavy rough surface is composed of features of different spatial wavelengths, in order to exclusively consider the role of the surface roughness is necessary to filter the features which correspond to surface motifs different of roughness ones. This section presents a numerical study which takes into account the role of the direcctionality of the addition between surface waviness and roughness, which is controlled by the nature of the process (ballistic-wise or growth/erosion processes) that originates the surface. To analyze the influence of directional character of the addition between waviness and roughness on surface area ratio of a wavy rough surface, different synthetic (mathematically defined) surfaces were designed as composition of an analytically defined wavy surface and a rough surface, designed using a fractional Brownian motion algorithm.

2.2.1 Introduction

The behavior of engineered and natural surfaces can be understood from their three–dimensional topography [194–196]. In the emerging field of micro-/nanostructured surfaces, e.g. superhydrophobic surfaces, where the systems contain dual scale structure roughness, a meaningful topographic characterization is very important. Development of advanced measurement techniques in surface microscopy relies on the proper definition of surface topography and their reconstruction methods [171]. Real surfaces contain multicomponent topographic data, which should be properly processed to isolate the information of interest.

Surface features at different scales may affect differently to the surface functional behavior [197]. Surface area is especially relevant in interfacial phenomena such as wetting, tribology or cell adhesion, where the interactions depends on the contact area between bodies/phases [166, 194, 198]. The surface area ratio, r, also referred to as relative surface area[2], enables a evaluation of the surface roughness. The surface area ratio is a hybrid roughness descriptor [67] that quantifies the difference between the actual surface area, A, and the apparent or nominal surface area, A_{app}, as follows:

$$r = \frac{A}{A_{app}} \tag{2.6}$$

where A_{app} is the area of the *smooth* reference surface.

This reference surface, known as *waviness*, is the surface with the same figure and dimensions than the actual surface. If the surface were rough without waviness, A_{app} would be the area of the horizontal plane resulting from the vertical projection of the rough surface. In microscopy, the area A_{app} is known as geometrical area, A_g, and it is numerically equal to the scan–area (i.e. the product of the transversal and longitudinal scan–lengths). Some authors prefer to define the surface area ratio as A/A_g when the surface deviations are referred to the smoothness (no roughness) and the plainness (no waviness) indistinctly.

Unfortunately, surface area evaluated by microscopy is very sensitive to the measuring conditions [170, 194, 199]. Actually, the true value of surface area is experimentally inaccessible because

[2] $S_{dr} = (r - 1)100$

it would require the acquisition of infinite points (i.e. a continuous topography) and this is technically impossible. Instead, the calculation of surface area ratio from contact angle measurements is widely reported [199–202].

The current microscopes provide surface textures grouping waviness and roughness indistinctly, i.e. a compounded account of intermediate and short length scales. To assess the frictional or wetting behavior of a surface, since both properties depend on roughness, one needs to *filter* the acquired morphology of the surface. But any filtering process of raw topography results in certain loss of information. A wrong choice of filtering tool can lead to misleading values of the statistical parameters [167]. Due to this, some authors recommend that filtration should be avoided in the analysis of surface topography.

Surface roughness is governed by man–made or natural processes, which modified the initial surface at arbitrary directions. These processes can be roughly classified into ballistic [155], if the rough profile is created on the previous non-planar (horizontal) surface following the vertical direction, and growth/erosion [156], where the perturbation of the wavy surface is performed following its normal direction. Many surfaces evolve by curvature flow [199, 203]. For instance, in reactive systems, the asperities and grooves may act as preferable sites for reaction, diffusion, adsorption, nucleation, etc... This affects the evolution of the interface leading to its roughening.

By inspection of an experimental topography, generally it is not possible to know a posteriori the precursor roughening process that ruled the evolution of the surface. This uncertainty in the directionality of the superposition of roughness to waviness can lead to meaningless values of roughness parameters after the waviness filtering. The directional character of waviness filtering and its influence on the roughness descriptors are not clearly discussed in the literature [204].

To characterize conveniently surface roughness, special care should be taken for the filtering of raw topography data. The aim of this study is to analyze numerically the effect of waviness filtering on the values of surface area ratio of rough and wavy surfaces evolved by ballistic–like or growth/erosion processes, accordingly.

2.2.2 Methods

Morphology/texture of a rough surface is determined by the type of roughening process [107]. In general, a surface morphology can be considered as the mathematical superposition of the spatial elevations associated with waviness and roughness. From this hypothesis, regardless of its physical nature, the generating process of a rough surface can be grouped, at least, into *vertical* (ballistic deposition) and *normal* (growth/erosion), according to the direction upon which was performed the mentioned superposition of heights. This simplistic classification intends to understand the generic properties of very different roughening processes. Since an arbitrary space direction can be discomposed into the vertical and normal directions, a generic process, which evolves the unprocessed surface in an arbitrary direction, might be understood as a combination of ballistic–like and growth/erosion processes.

An arbitrary surface can be mathematically interpreted as the result of the addition of roughness to the waviness following two directions: the vertical one or the normal one associated to the wavy surface. Graphically, the vertical and normal additions of roughness to waviness provide different surface profiles as shown in Figure 2.11. However, instead of topography profiles like Figure 2.11(d), the standard devices (e.g. stylus profiler, confocal optical microscope, atomic force microscope) acquire single–valued topographic elevations (without overhangs, voids..) like Figure 2.11(e), arranged in regular grids.

In this study, the following terminology was used to distinguish the surfaces studied. A *pure rough* surface is defined as a surface with roughness but without waviness, a *pure wavy* surface is a surface with waviness but without roughness, and a *rough wavy* surface is a surface with both

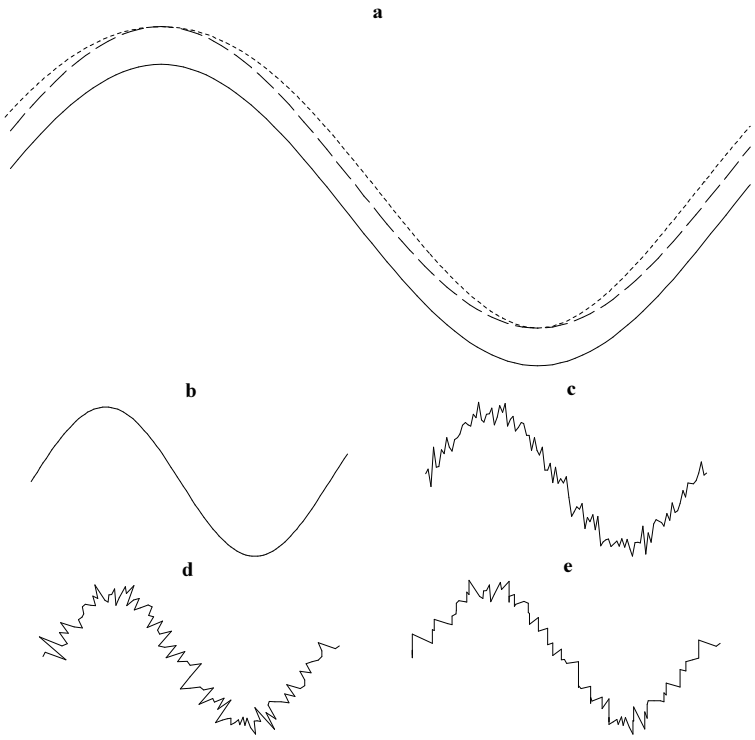

Figure 2.11: (a) Addition of a constant to a sinusoidal profile (solid line) in the vertical (dashed line) and normal (short dashed line) directions. Addition of a random function to the sinusoidal profile (b) in the vertical (c) and normal (d) directions. Instead of (d), a stylus profiler will register the profile (e) without overhangs.

roughness and waviness (see Figure 2.12). The surface area ratio of pure rough surfaces, r_{rough}, is also referred to as *roughness factor*. It is obvious from the definition (2.6) than the surface area ratio of a pure wavy surface is the unit. For rough wavy surfaces, depending on the direction (vertical or normal) of the addition of roughness to the waviness, the surface area ratio will be denoted as r_v for the vertical addition, and as r_n for the normal addition.

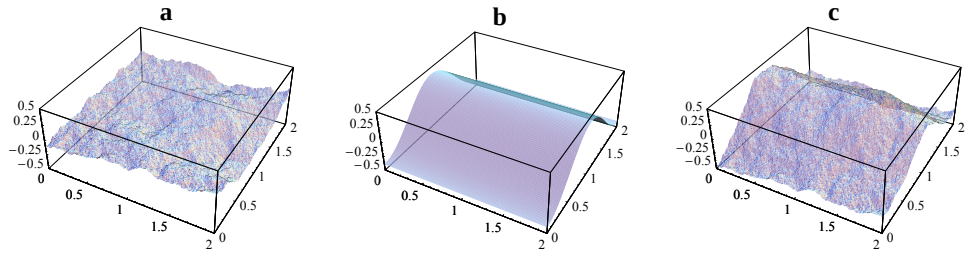

Figure 2.12: (a) Pure rough surface (roughness), (b) pure wavy surface (waviness), and the resulting rough wavy surface (c) obtained by the addition of surfaces (a) and (b). The addition can be either in the vertical or the normal directions with respect to the wavy surface.

Directional character of the addition of waviness and roughness

To measure the roughness factor, and other quantities, of a rough wavy surface, the waviness component should be first removed from the topography information. Processing of surface data requires to establish a reference or nominal surface to identify the waviness from the experimental data. Ideally, this reference surface should coincide with the surface figure (pure wavy surface), without roughness (see Figure 2.12(b)). Typically, once the reference surface has been selected a priori, the waviness is removed. This process is called *flattening* or *levelling*. Commonly, the removal of waviness is performed by subtracting, from the surface morphology, the reference surface with different methods such as: least-squares fittings [205], bicubic-Bezier surface patches or Gaussian filters [170, 171]. The least–squares fitting is typically based on the minimization of *vertical* offsets between the surface morphology data and a proposed mathematical model [205].

The waviness removal in normal direction is not commonly achieved because it would produce stretching/shrinking of the topography data, providing an irregular grid and a non-rectangular surface projection on the horizontal plane (see Figure 2.11(d)). Therefore, after filtering, the distance between two adjacent points would be different to the original sampling range and thus, the planar surface would be distorted. Due to these artifacts, which complicate the numerical treatment, the conventional software of different topometric devices only apply filtering in the vertical direction.

In general, waviness filtering is usually performed in the vertical direction by least–squares fitting or gaussian filtering [171,174]. All these operations assume the vertical expansion of surface data. For any rough wavy surface $z(x, y)$, which is a single–valued function, the roughness can be modeled as a noise function $n(x, y)$ added linearly in the vertical direction to each point of the wavy surface $f(x, y)$:

$$z(x, y) = f(x, y) + n(x, y) \tag{2.7}$$

The vertical superposition is mainly valid for roughening governed by ballistic–like processes [206]. Figure 2.12(c) shows a rough wavy surface, designed by vertical addition of waviness and roughness, whereas the isolated representations of the waviness and the roughness are shown in Figure 2.12(a) and (b), respectively.

Most processes of surface erosion or growth [156] produce perturbations in the local normal direction (e.g. acid etching, sand-blasting, curved-surface machining..). For these cases, the roughness should be considered as a noise function $n(x, y)$ added following the local normal direction to the waviness and in consequence, the rough wavy surface $z(x, y)$ would be parameterized in Cartesian coordinates as:

$$\begin{cases} x = x' + n\left(x', y'\right) \hat{x} \cdot \widehat{N}_0\left(x', y'\right) \\ y = y' + n\left(x', y'\right) \hat{y} \cdot \widehat{N}_0\left(x', y'\right) \\ z\left(x, y\right) = f\left(x', y'\right) + n\left(x', y'\right) \widehat{z} \cdot \widehat{N}_0\left(x', y'\right) \end{cases} \tag{2.8}$$

where $\{x, y\}$ are the coordinates of the final rough wavy surface, $\{x', y'\}$ the coordinates associated to both pure wavy and rough surfaces, $\widehat{N}_0$ is the unit vector normal to the waviness (Eq. (2.16)) and $\{\widehat{x}, \widehat{y}, \widehat{z}\}$ is the Cartesian vectorial basis. For relatively smooth topographies where the wavy surface slope is very small, Eq. (2.8) will be reduced to Eq. (2.7) as expected. Most height equations in this context rely on a small-slope approximation that allows one to strongly simplify the analytical formulation. However, this simplification may be at the cost of inaccuracies in the physical description. For instance, surface diffusion is severely overestimated in regions of high slopes.

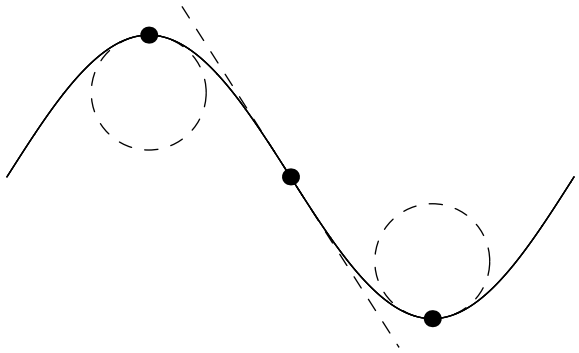

Figure 2.13: Limit regions for surface overlapping in the normal addition of roughness to waviness. Note that the radius of both circles is $1/\kappa_0$.

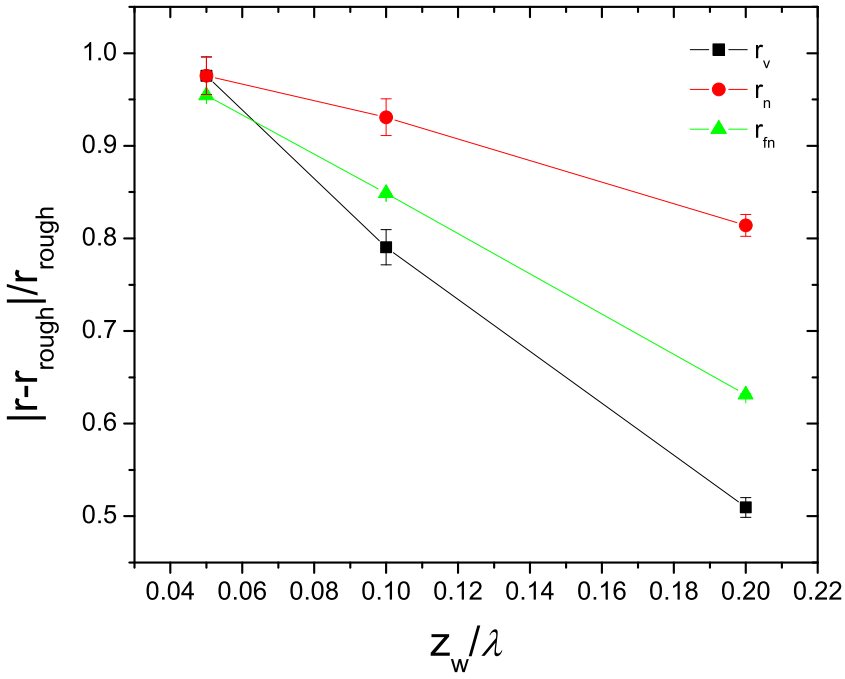

Figure 2.14: Relative variation of the surface area ratios of rough wavy surfaces generated numerically by vertical and normal additions in terms of z_w/λ for $z_r/z_w = 0.005$. The experimentally accessible values of the surface area ratio of filtered rough wavy surfaces, r_{fn}, are also plotted.

Synthetic surfaces

We used synthetic (mathematically constructed) rough wavy surfaces with stochastic roughness [170]. These surfaces were generated with a fix geometrical area ($A_g = 4$ a.u.) and a grid of 1024x1024 points. We selected this value of resolution because it is generally the maximum resolution available in the conventional instruments. The surface area ratio was computed using the same tessellation algorithm [194, 207], to exclude the influence of the tessellation method on the calculation of r-values [188, 194].

Roughness of the synthetic surfaces was produced with a fractional Brownian noise [208] with amplitude z_r (peak-to-valley distance) and zero mean, $\langle n \rangle = 0$. A zero-mean noise assures that the waviness should be parallel to the average real surface. Different realizations of the pure rough surface were produced by changing the fractal dimension from 2.1 to 2.9 in steps of 0.1. This variation in the surface texture was not significant on the values of surface area ratio [170]. We used a 2D sinusoidal surface as a simplified model of the waviness profile:

$$f(x,y) = z_w \cos\left(\frac{2\pi}{\lambda} y\right) \tag{2.9}$$

where λ is the spatial period and z_w the waviness semi-amplitude. The spatial period was fixed to 2 a.u. for all wavy surfaces used in this study. We selected a symmetric waviness because in the limit case $n(x,y) = 0$, $r_n = 1$ as happens with r_v (see Eqs. (2.20) and (2.28)). Finally, using the waviness described by Eq. (2.9) together to Eqs. (2.7) or (2.8), the rough wavy surfaces were constructed with stochastic roughness for different values of z_w/λ and z_r/z_w. To emulate the 3D microscopy, we also reproduced experimentally-accessible topographies, i.e. without overhangs, from the original surfaces created by normal addition of roughness. The surface area ratio of these rough wavy surfaces with waviness filtered in the vertical direction is symbolized as r_{fn}.

Not all values of z_w/λ and z_r/z_w are allowed for the normal addition. Surface points are

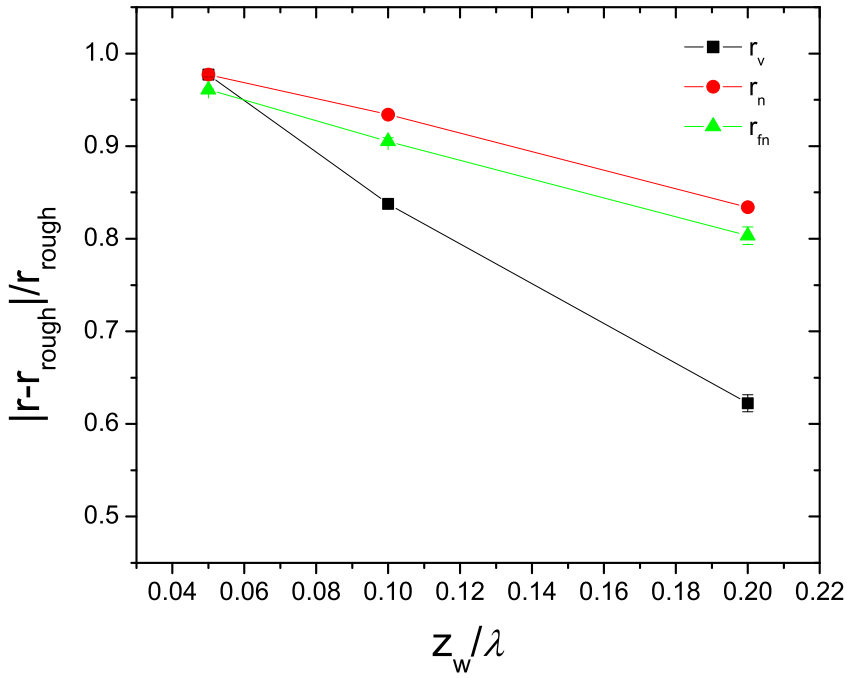

Figure 2.15: Relative variation of the surface area ratios of rough wavy surfaces generated numerically by vertical and normal additions in terms of z_w/λ for $z_r/z_w = 0.05$. The experimentally accessible values of the surface area ratio of filtered rough wavy surfaces, r_{fn}, are also plotted.

overlapped when the roughness is added to the waviness if the following condition is held:

$$\min\left(\left|\kappa_{01}^{-1}(x,y)\right|, \left|\kappa_{02}^{-1}(x,y)\right|\right) \leq \left|n(x,y)\right|, \forall (x,y) \tag{2.10}$$

where κ_{01} and κ_{02} are the principal curvatures of the waviness. The surface overlapping can be illustrated in Figure 2.13 when $n = 1/\kappa_{0i}$. For the sinusoidal waviness described by Eq. (2.9), the condition (2.10) is reduced to:

$$\left(\frac{\lambda}{2\pi z_w}\right)^2 \leq \frac{z_r}{z_w} \tag{2.11}$$

2.2.3 Results and Discussion

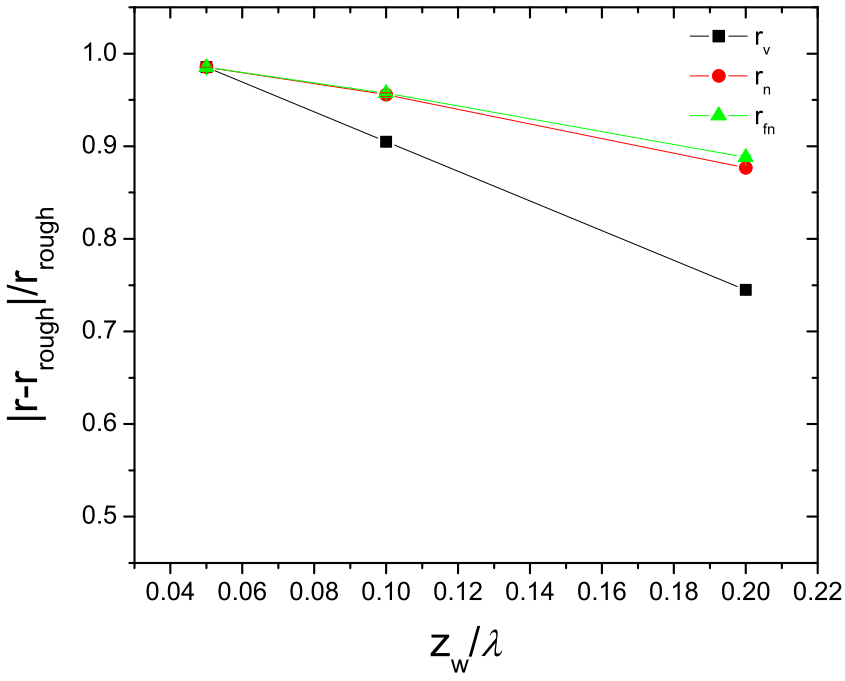

Figure 2.16: Relative variation of the surface area ratios of rough wavy surfaces generated numerically by vertical and normal additions in terms of z_w/λ for $z_r/z_w = 0.5$. The experimentally accessible values of the surface area ratio of filtered rough wavy surfaces, r_{fn}, are also plotted.

In Figs. 2.14,2.15 and 2.16, we plot the relative variation of the surface area ratios of rough wavy surfaces generated numerically by vertical and normal additions, in terms of z_w/λ for different values of z_r/z_w. Moreover, we plot the values of r_{fn}. Firstly, the surface area ratios r_v and r_n always underestimate the value of roughness factor r_{rough} although $r_n > r_v$ for all cases and mostly, $r_n > r_{fn}$. As the waviness is less fluctuating or with lower amplitude (small values of z_w/λ), both surface area ratios approach to the roughness factor because the waviness slope is small. Likewise, only when the roughness amplitude is comparable to the waviness amplitude (large values of z_r/z_w), there is a good agreement between r_n and r_{fn} regardless of the z_w/λ value. Even although the increase of surface area is inherent to the own addition of roughness as it is illustrated in Figures 2.11(c)-(d), the surface area ratio is indeed a waviness-weighted roughness factor (Eqs. (2.20)-(2.28)). However, the rough wavy surfaces generated in the normal direction will always have greater surface area ratio than those ones generated following the vertical direction with identical roughness due to the lateral growth. Therefore, r_n is closer to r_{rough} rather than

r_v. In other respects, the vertical filtering of surfaces generated in the normal direction produces greater underestimation of the r_{rough}-values than without filtering.

2.2.4 Conclusions

Algorithms based on the flattening of surface topography in the vertical direction should not be applied indiscriminately to any surface. The waviness removal can be problematic because commonly we do not know the type of roughening process which created the surface (ballistic or growth/erosion). The roughness addition to waviness is unknown to be mathematically expressed and hence filtered. Besides, the waviness filtering algorithms for surfaces generated by normal growth processes will be very complex and computationally expensive. The solution or alternative to avoid the effects produced by the waviness removal, or to compare the overall behavior of general rough surfaces with different waviness, is the waviness-weighted roughness factor. We found than the surfaces generated in the normal direction will always have greater surface area ratio, without assumptions on small slopes or absence of overhangs, and closer to the corresponding values of roughness factor.

2.3 Exact Derivation of Roughness Factor for General Wavy Rough Surface

Due to the different types of processes which can govern the evolution of a surface (i.e. the addition of roughness to the unprocessed surface), the waviness filtering has a strong directional character. This will affect any hybrid estimator of roughness [67]. Thus, an exact derivation of the surface area ratio for any general rough wavy surface, considering the directional character of the mentioned addition, is required. Accordingly, in this appendix, roughness, waviness and rough wavy surfaces will be modeled by univalued continuous functions.

In general, any curved surface S can be described by two generic curvilinear coordinates (q_1, q_2). This way, from the local position vector $\vec{r}\,(q_1, q_2)$, the unit normal vector to S is defined as:

$$\hat{N}(q_1, q_2) = \frac{1}{\left|\frac{\partial \vec{r}}{\partial q_1} \times \frac{\partial \vec{r}}{\partial q_2}\right|} \frac{\partial \vec{r}}{\partial q_1} \times \frac{\partial \vec{r}}{\partial q_2} \tag{2.12}$$

whereas the area of the surface S will be:

$$A = \int \int_S \left| \frac{\partial \vec{r}}{\partial q_1} \times \frac{\partial \vec{r}}{\partial q_2} \right| dq_1 dq_2 \tag{2.13}$$

Since the local position vector can be expressed in terms of the Cartesian unit vectors $\{\widehat{x}, \widehat{y}, \widehat{z}\}$ as:

$$\vec{r}(q_1, q_2) = x(q_1, q_2)\widehat{x} + y(q_1, q_2)\widehat{y} + z(q_1, q_2)\widehat{z} \tag{2.14}$$

the cross product in (2.12) can be generally expressed as:

$$\begin{aligned} \frac{\partial \vec{r}}{\partial q_1} \times \frac{\partial \vec{r}}{\partial q_2} &= \frac{\partial(y,z)}{\partial(q_1,q_2)}\widehat{x} + \frac{\partial(x,z)}{\partial(q_1,q_2)}\widehat{y} + \frac{\partial(x,y)}{\partial(q_1,q_2)}\widehat{z} \\ &= \frac{\partial(x,y)}{\partial(q_1,q_2)}\left(\frac{\partial(y,z)}{\partial(q_1,q_2)}\widehat{x} + \frac{\partial(x,z)}{\partial(q_1,q_2)}\widehat{y} + \widehat{z}\right) \\ &= \frac{\partial(x,y)}{\partial(q_1,q_2)}\left(\widehat{z} - \frac{\partial z}{\partial x}\widehat{x} - \frac{\partial z}{\partial y}\widehat{y}\right) \end{aligned} \tag{2.15}$$

where a coordinate transformation is achieved using Jacobians and their properties. Substituting the vector (2.15) into (2.12), the unit normal vector can be rewritten in terms of the cartesian map $z\,(x,y)$ as:

$$\widehat{N}(x,y) = \frac{1}{\sqrt{1+|\nabla z|^2}}\,(\widehat{z} - \nabla z) \tag{2.16}$$

being ∇ the surface gradient operator expressed in cartesian coordinates. Further, if the magnitude of the vector (2.15) is introduced into (2.13), the area can be expressed as:

$$A = \int_X \int_Y \sqrt{1+|\nabla z|^2}\,dxdy \tag{2.17}$$

where again the transformation property of Jacobians has been applied.

2.3.1 Addition of roughness and waviness: vertical direction

Roughness is considered as a noise function, $n(x,y)$, added locally to a generically shaped surface S_0, i.e. the waviness, in the vertical direction $\widehat{z}$. Let $f(x,y)$ be the explicit function that defines the waviness. The overall surface S will be described by:

$$z(x,y) = f(x,y) + n(x,y) \tag{2.18}$$

Substituting (2.18) into (2.17), the surface area in terms of roughness and waviness is written as:

$$A = \int_X \int_Y \sqrt{1+|\nabla f|^2}\sqrt{1+\frac{1+\nabla n\cdot\nabla(n+2f)}{1+|\nabla_S f|^2}}\,dxdy \tag{2.19}$$

Hence, the surface area ratio (2.6) is given by:

$$r_v = \left\langle \sqrt{1+\frac{\nabla n\cdot\nabla(n+2f)}{1+|\nabla f|^2}} \right\rangle_{S_0} \tag{2.20}$$

where the angled brackets stand for the surface averaging:

$$\langle \bullet \rangle_{S_0} \equiv \frac{\int_X \int_Y \bullet \sqrt{1+|\nabla f|^2}\,dxdy}{\int_X \int_Y \sqrt{1+|\nabla f|^2}\,dxdy} \tag{2.21}$$

The expression (2.20) confirms the dependence of the surface area ratio on the first derivatives of both roughness and waviness. Note that, as expected, for the case without waviness (i.e. $f(x,y) = const.$), r_v becomes equal to:

$$r_{rough} = \left\langle \sqrt{1+|\nabla n|^2} \right\rangle_{xy} \tag{2.22}$$

where the brackets stand for the following surface average:

$$\langle \bullet \rangle_{xy} \equiv \frac{\int_X \int_Y \bullet\, dxdy}{\int_X \int_Y dxdy} \tag{2.23}$$

Further, if there is no roughness (i.e. $n(x,y) = const.$), r_v is the unit as expected.

2.3.2 Addition of roughness and waviness: normal direction

Roughness is considered as a noise function added locally in the normal direction to a generically shaped surface S_0. Let $\vec{r_0}(q_1, q_2)$ be the vector that defines this initial topography (waviness) and $n(q_1, q_2)$ the noise function (roughness) [207]. If the unit normal vector to each point on the surface S_0 is $\widehat{N_0}(q_1, q_2)$, the position vector of the overall surface S will be given by:

$$\vec{r} = \vec{r_0}(q_1, q_2) + n(q_1, q_2)\widehat{N_0}(q_1, q_2) \tag{2.24}$$

If (q_1, q_2) are the curvilinear coordinates referred to the principal directions on each point over the surface S_0, the formulae of Rodrigues [207] reads:

$$\frac{\partial \widehat{N_0}}{\partial q_i} = -\kappa_{0i}\frac{\partial \vec{r_0}}{\partial q_i} \tag{2.25}$$

with $i = 1, 2$ and where κ_{0i} represents the principal curvature on the i-principal direction [207]. Applying partial derivatives to Eq. (2.24) and taking into account the result (2.25), each partial derivative of the position vector of the overall surface can be expressed as:

$$\frac{\partial \vec{r}}{\partial q_i} = (1 - \kappa_{0i}n)\frac{\partial \vec{r_0}}{\partial q_i} + \frac{\partial n}{\partial q_i}\widehat{N_0} \tag{2.26}$$

Further, if the curvilinear coordinates (q_1, q_2) are orthogonal, the cross product of the derivative vectors $\partial\vec{r}/\partial q_i$ is reduced to:

$$\begin{aligned}\frac{\partial \vec{r}}{\partial q_1} \times \frac{\partial \vec{r}}{\partial q_2} = \left(1 - (\kappa_{01} + \kappa_{02})n + \kappa_{01}\kappa_{02}n^2\right)\frac{\partial \vec{r_0}}{\partial q_1} \times \frac{\partial \vec{r_0}}{\partial q_2} - \\ - \frac{\left|\frac{\partial \vec{r_0}}{\partial q_2}\right|(1 - \kappa_{02}n)\frac{\partial n}{\partial q_1}}{\left|\frac{\partial \vec{r_0}}{\partial q_1}\right|}\frac{\partial \vec{r_0}}{\partial q_1} - \frac{\left|\frac{\partial \vec{r_0}}{\partial q_1}\right|(1 - \kappa_{01}n)\frac{\partial n}{\partial q_2}}{\left|\frac{\partial \vec{r_0}}{\partial q_2}\right|}\frac{\partial \vec{r_0}}{\partial q_2}\end{aligned} \tag{2.27}$$

From the magnitude of the vector (2.27) and the average surface (2.21), the surface area ratio (2.6) is straightforwardly derived as:

$$r_n = \left\langle \left|1 - 2H_0n + K_0n^2\right| \sqrt{1 + \left(\frac{\widehat{q_1} \cdot \nabla n}{1 - \kappa_{01}n}\right)^2 + \left(\frac{\widehat{q_2} \cdot \nabla n}{1 - \kappa_{02}n}\right)^2} \right\rangle_{S_0} \tag{2.28}$$

where H_0 and K_0 stand for, respectively, the (local) mean and Gaussian curvatures of S_0:

$$\begin{aligned} H_0 &= \frac{1}{2}(\kappa_{01} + \kappa_{02}) \\ K_0 &= \kappa_{01}\kappa_{02} \end{aligned}$$

and $\widehat{q_i}$, the $i-$coordinate unit vector.

It is worth to note that the surface area ratio (2.28) depends on the local waviness curvatures (first and second derivatives of the surface). For non-zero constant noise, i.e. when the noisy wavy surface is mathematically *parallel* to the wavy surface, the peaks are sharpened/flattened and the valleys are flattened/sharpened (see Figure 2.11(a)) according to the sign of n (growth or erosion). Locally, the surface area increases/decreases for the peaks and decreases/increases for the valleys. This leads to that, unlike r_v (Eq. (2.20)), $r_n \neq 1$ when $n = const.$. As expected, r_n becomes r_{rough} if there is no waviness ($H_0 = K_0 = 0$ or $\kappa_{01} = \kappa_{02} = 0$). Otherwise, it becomes zero if $n = 1/\kappa_{0i}$, i.e. when the non-overlapping condition (see Figure 2.13) is not fulfilled and the surface area is ill-defined.

Chapter 3

Morphological Analysis of Acid-Etched Titanium Surfaces

The work presented in this chapter has been divided into three different sections as the mathematical tools used to describe the chemical etching of titanium surfaces.

The first section, *Estimation of percolation threshold of acid-etched titanium surfaces using Minkowski functionals* published in 2010[1], is focused on the use of Minkowski functionals as they had been used to provide morphological and topological information of a rough surface such as connectivity which it may be of interest in the prediction of biointegration.

The second section is focused on the study of the chemical etching of commercially pure titanium surfaces by using the scaling behavior of these surcaces. Scaling analysis of the surface morphologies of titanium surfaces etched for different times, under identical experimental conditions, revealed self-affinity. This is important for implantalogy field due to the intensive use of titanium surfaces and alloys and because chemical etching of titanium surfaces is a common treatment used to optimize the cell response of osteoblast-like cells on the implant.

The third section of the chapter shows the behavior of the surface area ratio or roughness factor and advancing/receding contact angles with etching time. Also it is presented a model which allows for justifing the behavior observed for roughness factor. This model is based on the change of surface chemistry produced by chemicla etching and on purely geometrical aspects.

Appendix A collects a complete description of all the experimental techniques used to characterize surface roughness and chemistry of acid-etched titanium surfaces and to measure the advancing/receding contact angles of pure water on them.

[1]This work was published as a chapter entitled *Estimation of percolation threshold of acid-etched titanium surfaces using Minkowski functionals* of the book *Microscopy: Science, Technology, Applications and Education* (2010 edition) edited by A. Méndez-Vilas and J. Díaz. ISBN: 978-84-614-6191-2.

3.1 Percolation Threshold of Acid-Etched Titanium Surfaces

In order to provide to the reader a general scopus about these statistical tools, first of all, it is necesary to answer three questions, what are and what are Minkowski functionals useful for? and, finally, how are Minkowski functionals used in this work?

Minkowski functionals provide morphological and topological information of a rough surface such as connectivity. In the context of biomaterials, since the Euler characteristic relates to the possibility of fluid flow on a surface, it may be of interest in the prediction of biointegration. The Euler characteristic (third Minkowski functional) can be used to define a percolation threshold from the height level where the Euler characteristic function has its zero crossing. A high percolation threshold suggests better fluid retention properties. In this work, we studied the evolution of commercially pure titanium (grade II) subjected to an acid etching process. Each set of samples was attacked for different times, from 0 to 750 s with hydrofluoridric acid. Topographies of each sample were achieved by AFM (Nanoscope IV) in Tapping Mode. We present the evolution of the maximum-density height for the peaks and valleys with etching time and the concerning percolation thresholds.

3.1.1 Introduction

As in implantology field, cells interact at nanoscale (or submicronscale) with surface features [209,210] and surface chemistry [211,212], biomaterial surfaces are usually textured and chemically modified to enhance the cell adhesion and to assure a suitable bio-integration [213]. However, cell proliferation on rough surfaces can be driven by topography features rather than by available surface area (i.e. roughness degree) [213]. Percolation in disordered surfaces (2-D connected media) of implants affects the circulation of extracellular material, nutrient diffusion, cell adhesion and the ingrowth of bone tissue [214]. Thus, a high percolation threshold suggests better fluid retention properties, as the fluid will not be able to move freely below this threshold due to the formation of air channels.

Commercially pure titanium (c.p. Ti) fulfils important chemical and mechanical requirements for use in medical implants as it exhibits a higher specific strength, lower stiffness, and improved corrosion resistance in biological media as compared with stainless steel. The incorporation of porosity into titanium implants provides additional advantages over fully dense titanium: mechanical anchoring to bone is facilitated through tissue growth into the pores and stiffness is reduced, thus mitigating stress shielding.

Interconnectivity plays a determining role in percolation studies (long-range connectivity), where the path length between pores connected to the surrounding is investigated. However, interconnectivity has mainly been determined qualitatively. Atomic force microscopy makes possible to acquire a complete three-dimensional height map of surfaces [194]. 2-D percolation can be detected in topographies at a given level set. In this chapter, alike the valley fluid retention index [215], we report a method to estimate the percolation threshold of acid-etched titanium surfaces using Minkowski functionals [98].

3.1.2 Minkowski Functionals

Characterization of textured surfaces by means of Minkowski Functionals (MFs) allows us to analyze the spatial distribution of the sites of holes (or valleys), in detail [216]. MFs are an alternative to structure functions. Further, they are connected to physically useful parameters like

the threshold of percolation [216].

In order to compute the MFs of an arbitrary topography, a height thresholding should be applied as in Fig. 1.6. By intersecting the topography data with multiple horizontal planes, this procedure allows us to transform a height map to a stack of level sets (Fig. 3.1). Choosing a height above the highest surface peak yields an empty set; choosing a height below the deepest pit yields the full domain. Thus, MFs yield 3D characterizing functions from 2D sets.

At each level h of the level sets of a topography, N_B and N_W are referred to black and white

Figure 3.1: Transformation of the topography displayed in Fig. 1.6 a) to a stack of level sets. The height h decreases from left (h_{min}) to right (h_{max}). White areas represent material, blue represents void areas.

pixels, $N_{Bounded}$ to the bounded pixels, n_B and n_W, to isolated regions or islets. A black pixel represents a material point (bulk or surface) whereas a white pixel represents a void point (air).

The first MF, F, is the covered surface area at the level h and it is defined as:

$$F(h) \equiv \frac{N_B}{N_B + N_W} \tag{3.1}$$

The normalization by the total analyzed area is necessary to provide easy comparison of the functionals determined for images with different scan ranges. The first functional measures the relative matter amount existing underneath the level h. Indeed, the plot of the first functional in terms of level h is the bearing area curve or Abbott-Firestone curve, which is used for calculating the functional roughness parameters.

The second MF, U, is the length of contours:

$$U(h) \equiv \frac{N_{Bounded}}{N_B + N_W} \tag{3.2}$$

This functional describes the shape of the surface features, i.e. the microstructure. The second functional of a level set with multiple or spiky isolated regions is greater than a set with few or smooth regions.

Finally, the third MF, χ, is the so-called Euler characteristic:

$$\chi(h) \equiv \frac{n_B - n_W}{N_B + N_W} \tag{3.3}$$

The Euler characteristic describes the connectivity of spatial patterns. A negative Euler characteristic indicates that the surface is predominantly characterized by isolated holes (i.e. porous structure). Instead, a positive Euler characteristic points out that the surface mainly consists of isolated regions (i.e. punctiform structure). Further, the maximum value of χ is equal to the maximum density of peaks and the minimum χ, the maximum density of valleys.

The Euler characteristic has an important interpretation in the context of percolation. For a level set with a very low Euler characteristic, a fluid can be expected to be trapped in the holes. Instead, the fluid could flow freely in the case of a high Euler characteristic (see Fig. 3.2). By increasing the "sea" level from a side of the relief (rough surface), we can firstly cause flooding

of the valleys close to this side. Next, two or more near lakes will be connected. Percolation will occur when there is a net transport of liquid from the side up to the opposite side of the surface.

The Euler characteristic Eq. 3.3 can be used to define a percolation threshold as the height

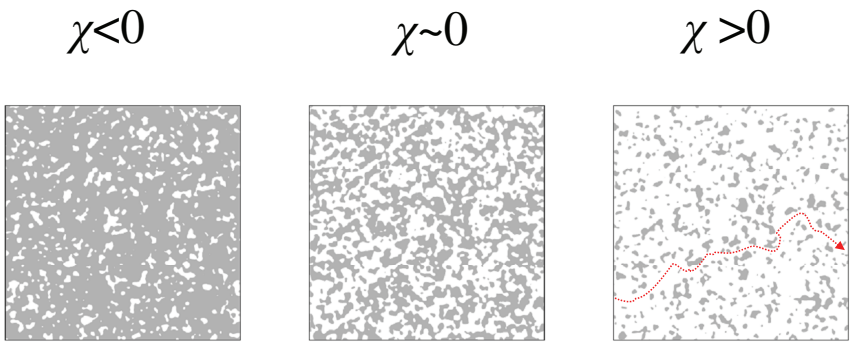

Figure 3.2: Three 2-D level sets where the Euler characteristic varies from a negative value up to a positive value. A fluid begins to percolate through a rough surface when the Euler characteristic is slightly positive (see the red path).

level where the Euler characteristic function has its zero crossing (Fig. 3.3 a)). The value of the first MF Eq. 3.1 at that height level will be equal to $1 - p_c$ where p_c is the percolation threshold (Fig. 3.3 b).

The ramified nature of percolation islets suggests to fractal behavior. For fractal-like surfaces,

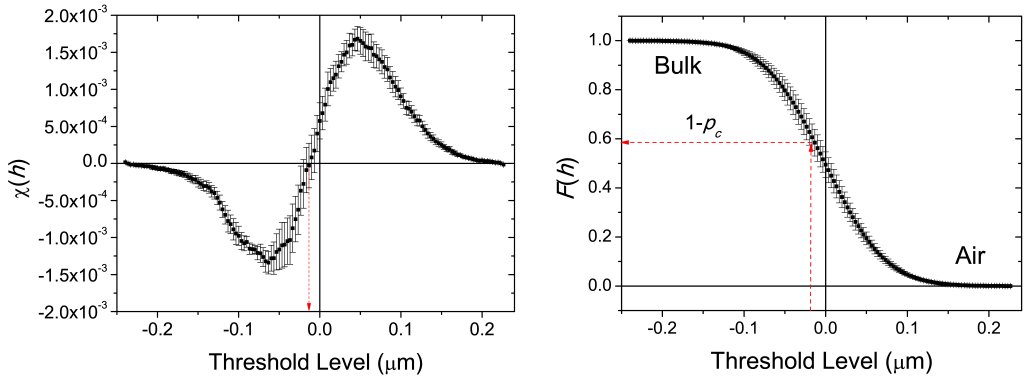

Figure 3.3: a) Zero crossing of the Euler characteristic and b) estimation of the percolation threshold from the first MF (matter amount).

due to the well-known perimeter-area relation [98], the second functional or perimeter Eq. 3.2 scales linearly with the first functional or area Eq. 3.1 as follows:

$$logU(h) \sim \frac{D_f - 1}{2} logF(h) \tag{3.4}$$

3.1.3 Materials and Methods

Since acid etching of titanium surfaces provides better results of cell culture [213], unalloyed $c.p.Ti$ surfaces (grade II, Manfredi) were attacked with hydrofluoric acid (HF). All samples were prepared with similar weight and size: disks of approximately $12mm$ in diameter and $2mm$ in thickness. The disks were polished with wetted metallographic 2400 grit SiC sandpaper and $0.05\mu m$ alumina powder in order to ensure identical initial surface conditions. Surfaces were etched by complete immersion in a similar volume of a HF solution at 10% (v/v) for different etching times. Etching was performed under gently stirring (magnetic stirrer at 100 rpm) to control the bulk mass transport.

Topographies of the textured titanium surfaces were imaged with an Atomic Force Microscope Nanoscope IV MultiMode in air (Digital Instruments, Santa Barbara, Ca, USA). The microscope was operated in tapping mode with a Si_3N_4 V-shape cantilever (stiffness, $k = 63 \pm 8N/m$) and a scan-size of $5x5\mu m^2$. The topography data were acquired in a grid of $512x512pixel^2$. All images were fitted to a plane and filtered by a Gaussian mask with a cutoff of $2.5\mu m$ in order to capture surface features below the average cell size ($\sim 10\mu m$). Three disks were used per group and three topographies were acquired per each disk.

Morphology of each sample was evaluated with a Scanning Electron Microscope Leo Gemini 1530 (Carl Zeiss, Oberkochen, Germany). Images were acquired at $x20000$ magnification with a resolution of 3072x2304 $pixel^2$.

The MFs were computed following the algorithms described elsewhere [216, 217].

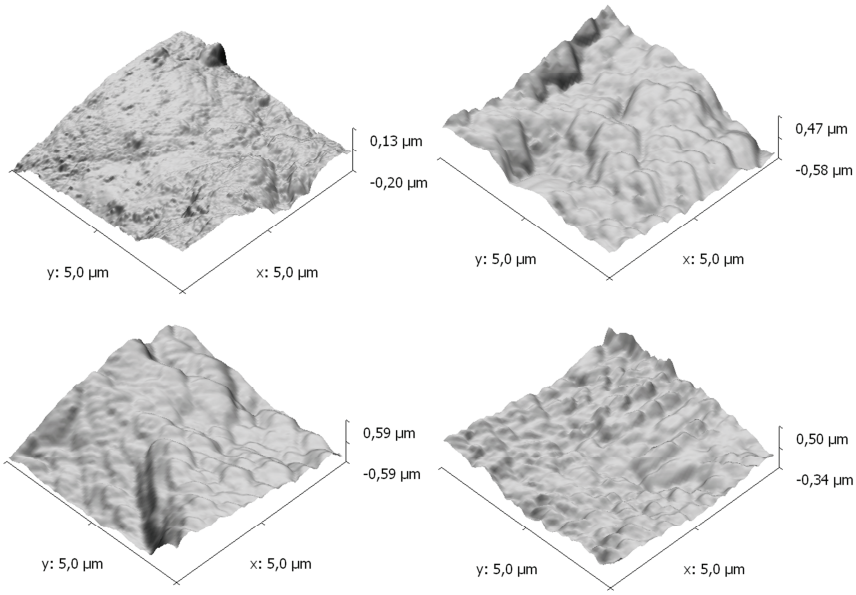

Figure 3.4: AFM topographies of titanium surfaces: (a) polished and etched for (b) 120s, (c) 180 s and (d) 300 s.

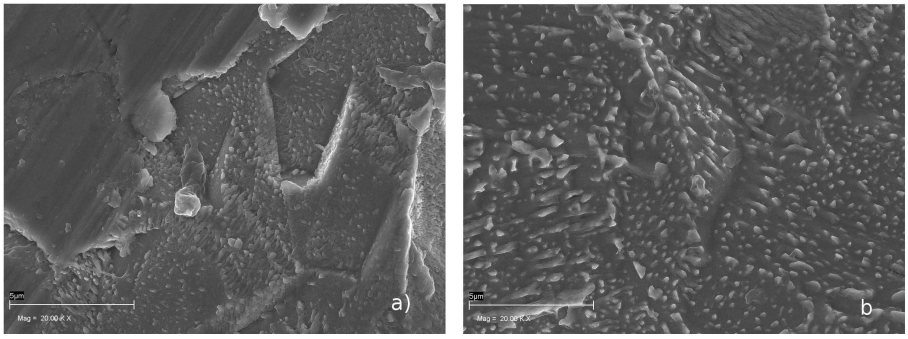

Figure 3.5: SEM pictures of titanium surfaces etched for (a) 120s and (b) 180 s. Acid etching initially produced stepped morphologies due to the crystalline grain detachment, but after 180 s, a spiky aspect was found.

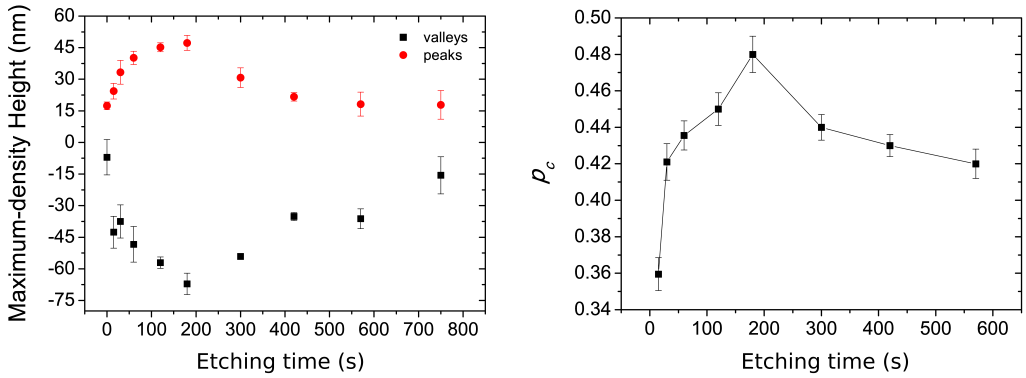

Figure 3.6: a) Evolution of the maximum-density height for the peaks and valleys, and b) percolation threshold in function of etching time.

3.1.4 Results

From Fig. 3.4, the morphology of the etched samples was angular and stepped due to the crystalline grain detachment from the amorphous structure of titanium. Moreover, at dimensions smaller than the grain structure of titanium, a secondary texture was visualized. This double-scale roughness is visualized in Fig. 3.5.

During the etching process, preferential surface sites (grain boundaries) are attacked. The local etching rate depends on grain orientation. This anisotropy affects the properties of the surface. In oxygen-rich ambients, $c.p.Ti$ surfaces are covered by a thin film of TiO_2 ($2-10nm$ of thickness), which improves the corrosion resistance of titanium. Thus, the etching kinetics is ruled by the interplay between the acid etching produced by the HF on Ti and TiO_2 and the own oxidation of Ti in aqueous solution.

The maximum densities of peaks and valleys are found at $50nm$ and $-70nm$, respectively (Fig. 3.6 a) for an etching time of 180 s. Further, the percolation threshold is maximum at 180s (Fig. 3.6 b). This optimal time should be taken into account in clinical applications. The controlling parameters on the evolution of acid-etched titanium surfaces will become the initial state of surface (oxidation, roughness), the acid concentration and the type of acid. These parameters might shift

the critical etching time.

Chemically etched surfaces have long been recognized as fractal at least over a range of dimensions smaller than the grain structure of the material [213]. However, the log-log plot in Fig. 3.7 presents two slopes, one for large areas and the other for small areas [110]. The structure at ever smaller length scales and the structure at ever larger length scales, are controlled by two separate dimensions: D_R (local) and D_f (global) The fractal reaction dimension D_R is basically the effective fractal dimension of the surface towards the etching. When $D_R > D_f$, the etched surface undergoes roughening and if $D_R < D_f$, smoothing.

Anomalous surface roughness is indentified by distinct scaling relations for the local and the global surface fluctuations. This behavior can explain why osteoblast-like cells are more sensitive to the submicron-scale features of acid-etched titanium surfaces [213].

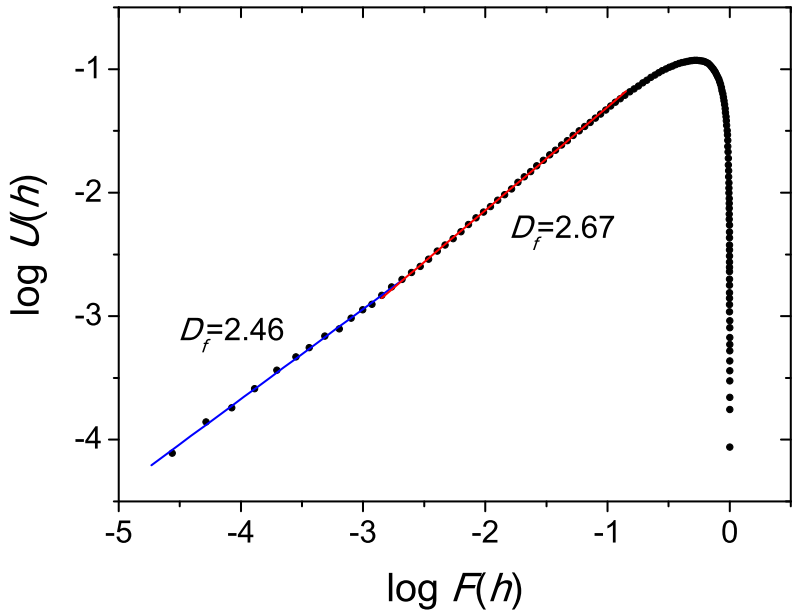

Figure 3.7: Log-log plot of the second MF in function of the first MF for etching time 570 s.

3.1.5 Conclusions

The approach of integral geometry characterization improves the quantitative analysis of topography data. Since surface characterization of biomaterials is crucial to understand the concerning biological events, the use of complementary topography analysis, like Minkowski Functionals analysis, are highly recommended. As reported Dotto and Kleinke [110], chemical etching processes produce percolation networks. This study reveals the etching time as an optimizing parameter on the evolution of acid-etched titanium surface. A roughening transition in the fractal behavior of the acid-etched surfaces verifies the double-scale roughness found with AFM and SEM. Further, cell proliferation was mediated by this specific morphology.

3.2 Kinetic Roughening of Acid-Etched Titanium Surfaces

This section studies and evaluates the kinetic roughening of hydrofluoric acid etched surfaces of commercially pure titanium for dental implants. This work was based on the scaling analysis of the titanium surface morphologies achieved at different etching times under identical experimental conditions. The surfaces were imaged with AFM (see Appendix A). All etched titanium surfaces exhibited intrinsic anomalous scaling and multiscaling. During the etching process, the oxide film found on the titanium surfaces evolved from the native thin film (in-air oxidation) towards a varying-thickness heterogeneous film created by wet oxidation. Due to the doping of the acid-etched surfaces with titanium hydrides, the roughening dynamics changed over time being observed a crossover for etching times close to 3 min due to the poisoning of the acid-etched surface. Scaling analysis of biomaterial surfaces could provide a powerful tool to examine the effect of nanoscale features of implant topography on cell growth and proliferation.

3.2.1 Introduction

Kinetic roughening phenomena correspond to processes which occur when material is added to or removed from a surface far from the equilibrium conditions. Surface roughening problem has been theoretically and experimentally studied for many different systems [107, 119], however less work has been devoted to the study of roughness dynamics when material is removed from the surface.

Anomalous kinetic roughening, which is related to a nontrivial dynamics of the local surface slope, has been reported in many numerical [108, 130] and experimental studies, such as reactive sputtering deposition [111], fracture of surfaces [131], rough fluorocarbon materials[218] and chemical etching [110, 219]. Chemical etching generally depends on etchant type, concentration, temperature, pretreatment of the surface... Dotto and Kleinke [110] reported that, for identical experimental conditions (acid concentration, solvent...), the experimental design (geometrical characteristics, stirring rate...) plays a fundamental role in the surface growth dynamics, determining the scaling framework of the etched surfaces.

Acid etching is a common surface roughening treatment of titanium for implant applications [220]. Osteoblast-like cell proliferation on acid-etched titanium surfaces is driven by topography features rather than by available surface area [213]. Understanding why cells are more sensitive to the submicron-scale features of acid-etched titanium surfaces requires to examine with detail the surfaces at the smallest scale possible [198, 215].

This work was focused on the study of the roughening dynamics of commercially pure (c.p.) titanium (Ti) surfaces subjected to hydrofluoric acid (HF) etching, commonly used in surface engineering of biomaterials [213]. We demonstrated that the HF etching of c.p. Ti surfaces obeyed anomalous scaling laws. Concretely, the global and local exponents found suggested that the experiments should be described in the framework of intrinsic anomalous scaling.

3.2.2 Theory

A generic dynamic scaling theory in kinetic roughening was analytically developed by Ramasco *et al.* [105], based on the scaling behavior of the interface width, $w(l,t) = \left\langle \left\{ [h(\vec{r},t) - \langle h \rangle_l]^2 \right\}_l \right\rangle^{1/2}$, and the structure factor or power spectral density, $PSD(k,t) = \left\langle \hat{h}(k,t)\hat{h}(-k,t) \right\rangle$, where $\{\bullet\}_l$ denotes the average over $\vec{r}(x,y)$ using a l-sized window, with $l \leq L$ being L the system size. If $l = L$, we refer to the global interface width and when $l \ll L$, to the *local interface width*. In these expressions, $\langle h \rangle_l$ denotes the average height of the surface in the l-sized window ($\langle h \rangle_L = \bar{h}$), $\hat{h}(k,t)$

symbolizes the Fourier transform of $h(\vec{r},t)$, k is the spatial frequency in the reciprocal space, t is the growth time and the angular brackets denote the average over different realizations of the system.

For a (2+1)-dimensional system $w(l,t)$ and $PSD(k,t)$ behave as:

$$w(l,t) = t^{\beta} f_{\Delta}\left(l/t^{1/z}\right) \tag{3.5}$$

$$PSD(k,t) = k^{-2(\alpha_{gl}+1)} f\left(kt^{1/z}\right) \tag{3.6}$$

$$f_{\Delta}(u) \sim \begin{cases} u^{\alpha_j} & ;u \ll 1 \\ const. & ;u \gg 1 \end{cases}$$

$$f(x) \sim \begin{cases} x^{2(\alpha_{gl}+1)} ; x \ll 1 \\ x^{2(\alpha_{gl}-\alpha_S)} ; x \gg 1 \end{cases}$$

where β is the so-called global growth exponent, the subindex $j = gl, loc$ refers to α_{gl} (also symbolized as α) and α_{loc}, which are the so-called global (computed for window size $l = L$) and local roughness exponents respectively, $z = \frac{\alpha}{\beta}$ is the dynamic exponent, and α_S is known as the spectral roughness exponent [105,129]. The lateral correlation length, ξ, is defined at the transition between the linear and the *plateau* regions of the log-log plot $w(l,t)$ vs l (see Eq. (3.5)). From the values of α, α_{loc} and α_S, four different scaling behaviors were described [105]. These scalings have been observed experimentally in different systems [106, 112].

When the local and global functions scale differently ($\alpha \neq \alpha_{loc}$), roughening is known as anomalous, making explicit the complex interplay between the global dynamics and the anisotropy effects. To describe the degree of anomaly of the system, the local growth exponent β^* is calculated as $\frac{\alpha-\alpha_{loc}}{\alpha}\beta$ [221].

Nonlocal and/or disorder effects are responsible for the anomalous roughening, and concretely for the intrinsic anomalous roughening ($\alpha_S = \alpha_{loc} \leq 1$ and $\alpha_{loc} \neq \alpha$) in different systems [130]. In acid etching problems, such effects have been usually related to the presence of surface species and the orientation of crystal planes with different affinity to the etchant agent, i.e. with different etch rate. This surface anisotropy dictates different corrosion rules limiting the kinetics of surface evolution [108, 222, 223].

As a consequence of anomalous roughening, the $PSD(k,t)$ curves obtained at different times do not overlap for large k values, but rather the curves are vertically shifted as the growth/erosion time changes. Anomalous scaling properties are also connected to multiscaling, which can be identified analyzing the scaling behavior of the structure functions, $G_q(l,t) = \left(\left\langle |h(\vec{r}+\vec{l},t) - h(\vec{r},t)|^q \right\rangle_L\right)^{1/q} \sim l^{\alpha_q}$ ($q \in \mathbb{N} - \{0\}$), where α_q is the generalized local roughness exponent [111].

3.2.3 Materials and Methods

This study was performed for the same surfaces used to evaluate the evolution of percolation threshold with etching time (see Section 3.1). Therefore, the complete description of the method used to etch titanium surfaces with HF solutions and to acquire their surface topographies with AFM and SEM can be found in Section 3.1.3.

Also, semi-quantitative chemical analysis was assessed by energy dispersive X-ray (EDX) microanalysis on the titanium samples etched at different times. The experiments were performed with a microanalysis system (Oxford Instruments INCA-200) coupled to a SEM (Zeiss LEO GEMINI 1530).

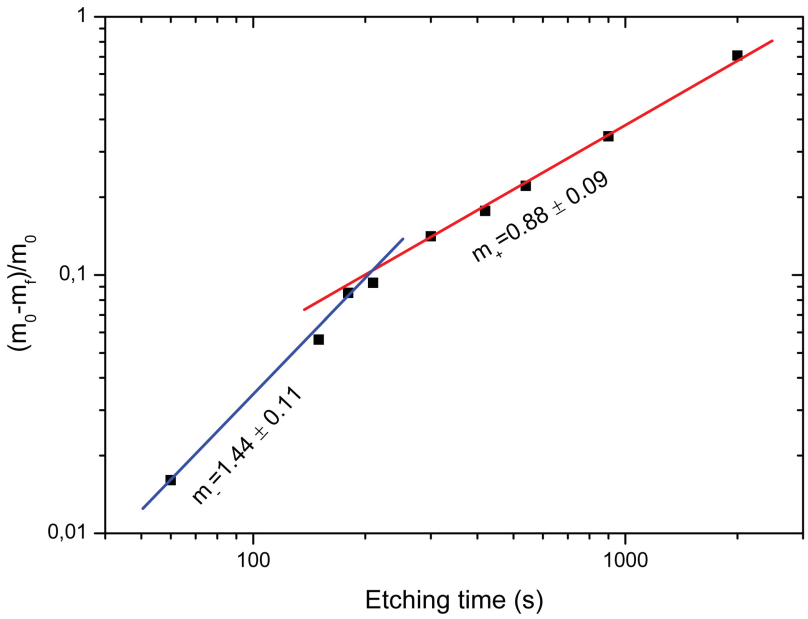

Figure 3.8: Log-log plot of the relative mass loss against the etching time. The relative mass loss rate for etching times under 3 min was $m_- = 1.44 \pm 0.11$ and for times above 3 min, $m_+ = 0.88 \pm 0.09$.

3.2.4 Results and Discussion

The HF etching rate of c.p. Ti surfaces, estimated from the mass loss of the etched surfaces at different times, decreased after 3 min (see Fig. 3.8). This behavior suggests that the etching dynamics changed significantly after this time. The mass loss of the acid-etched surfaces is just an extensive property such as area surface, it does not provide information about surface topology.

Roughness of the acid-etched c.p. Ti surfaces was characterized from the interface width $w(l,t)$, the lateral correlation length $\xi(t)$ (In Fig. 3.9 shows the interface width functions vs length scale for different etching times) and the structure factor $PSD(k,t)$. The values of global interface width ($\propto t^{\beta}$) and lateral correlation length ($\propto t^{1/z}$) in terms of the etching time, under and over 3 min, are shown in Fig. 3.10 (a) and (b), respectively. From these graphs, the values of the growth exponent $\beta^{\pm}$ and the coarsening exponent $1/z^{\pm}$ were found, where the superscript refers to etching times under $(-)$ and over $(+)$ 3 min.

Fig. 3.11 (a) and (b) show the $PSD(k,t)$ data for etching times under and over 3 min, respectively. These curves suggest the existence of spatial correlations of the surface roughness for small and large length scales (large and small k-values, respectively). The vertical shift of $PSD(k,t)$ curves shown in Fig. 3.11 (a) and (b) are clear indications that the system presented anomalous scaling. Furthermore, the slope values ($m = -2(\alpha_S + 1)$) obtained from Fig. 3.11 (a) and (b) suggest that the scaling behaviors have different α_S-values under and over 3 min.

The β^* values, obtained straightforwardly from the expression which relates β^* with α_{loc}, β and z, were corroborated from the scaling of the average surface gradient, which scales as $\overline{\langle(\nabla h)^2\rangle} \sim t^{2\beta^*}$. The values obtained for α, α_{loc}, β, β^* and $1/z$ are summarized in Table 3.1, where the anomalous scaling commented above is proved from the direct comparison of the exponent

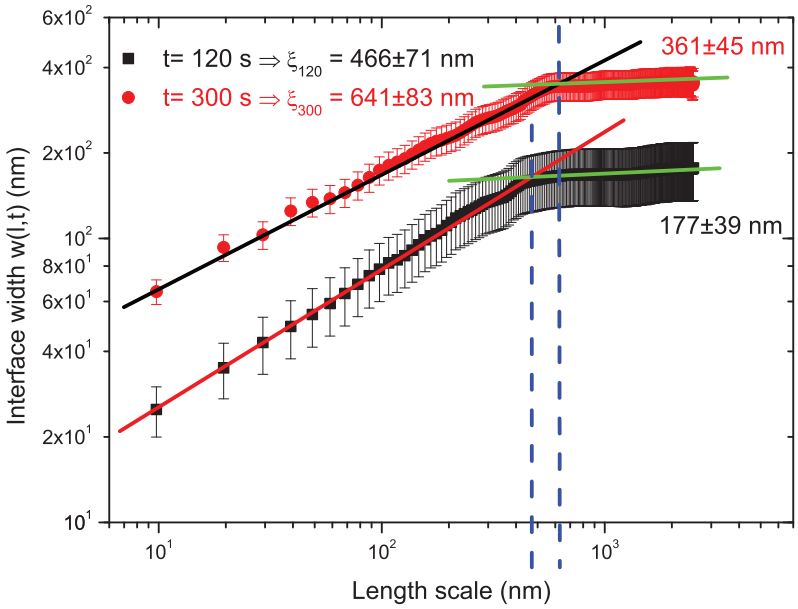

Figure 3.9: Log-log plots of the interface width against the length scale after 120 and 300 s. The values of lateral correlation length ξ for each etching time are indicated in the graph. The error bars correspond to the statistical error and the straight lines are a guide.

values.

In order to further verify that the scaling behaviors of the system correspond to intrinsic anomalous scaling, the $PSD(k,t)$ functions obtained at different etching times were rescaled (see Fig. 3.12). From Eq. (3.6), it follows that the curves $PSD(k,t)k^{2\alpha+2}$ vs $kt^{1/z}$ collapse into two different ones, one for etching times under 3 min and another for times above 3 min. The existence of these master curves [129] suggests the possibility that the etching process produced intrinsic anomalous roughening on Ti surfaces. However, the existence of two master curves, for etching times under

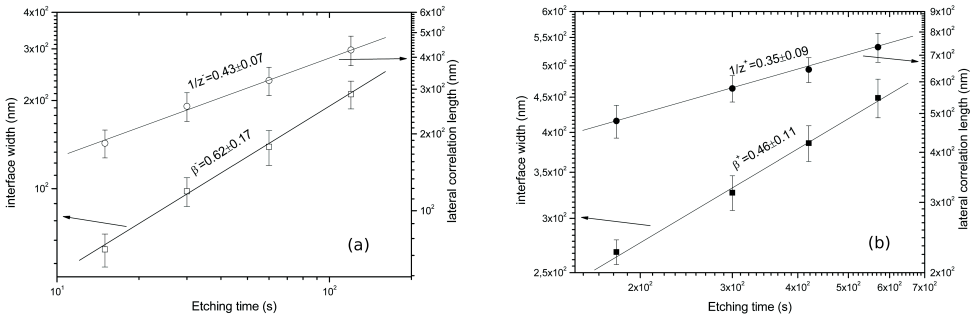

Figure 3.10: Log-log plots of the interface width and the lateral correlation length vs etching times under (a) and over (b) 3 min. The values of $\beta^{\pm}$ and $1/z^{\pm}$ are indicated in each graph, where the superscript is associated to etching times under $(-)$ and over $(+)$ 3 min.

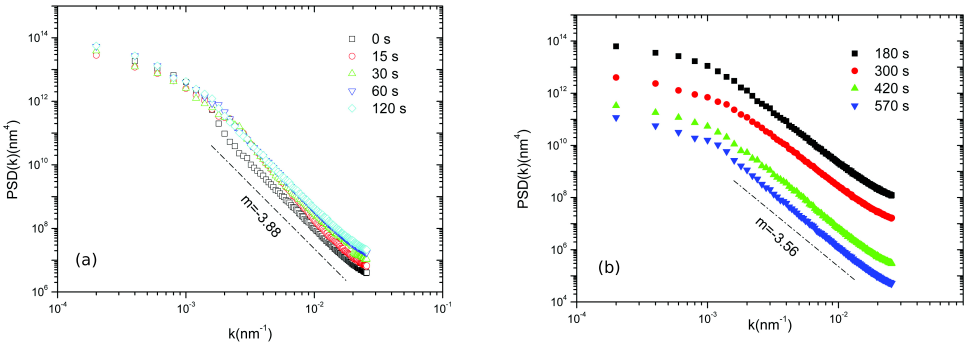

Figure 3.11: Log-log plots of the structure factor measured over regions of size $l = 1/k$ vs etching times under (a) and over (b) 3 min. The dashed straight lines are a guide to the eye, being m the slope of the linear section of $PSD(k,t)$.

and over 3 min, points out that the kinetic roughening changed at etching times close to 3 min. It is worth mentioning that since $m_1 > m_2$, then $\alpha_S < 1$, and since $m_2 \neq 0$, then $\alpha_S \neq \alpha$.

A quantitative analysis of Fig. 3.12 permits to state that acid etching really produced intrinsic anomalous roughening from the confirmation that $\alpha_S \simeq \alpha_{loc}$ [105]. Fig. 3.12 shows the collapse of the $PSD(k,t)k^{2\alpha+2}$ curves for etching times under 3 min (open symbols). The slope for small $kt^{1/z}$-values is $m_1 = 4.96 \pm 0.19$ and for large $kt^{1/z}$-values, $m_2 = 1.58 \pm 0.14$. From these slopes, it is possible to obtain the spectral and global roughness exponents, respectively. This results in $\alpha_S^- = 0.69 \pm 0.13$ and $\alpha^- = 1.48 \pm 0.10$ for etching times under 3 min. Also, Fig. 3.12 shows the collapse of the curves for etching times over 3 min (close symbols), where the slopes for small and large $kt^{1/z}$-values are $m_1 = 4.37 \pm 0.23$ and $m_2 = 1.44 \pm 0.21$, respectively. These values result in $\alpha_S^+ = 0.47 \pm 0.13$ and $\alpha^+ = 1.19 \pm 0.12$. The $\alpha^{\pm}$-values are in good agreement, within the error bars, with the values presented in Table 3.1, and the α_S-values are approximately equal to α_{loc} ones. Consequently, the etched surfaces presented intrinsic anomalous roughening. An unresolved issue is whether the system also presents multiscaling. As an illustrative example, Fig. 3.13 shows $G_q(l,t)$ vs l, corresponding to the surface etched during 5 min, for different q-values ($q = 2, 3, \ldots, 8$). It is clear that α_q depends on the q-value because the value of α_q decreases as q increases. This behavior observed in the surfaces etched before and after 3 min confirms the existence of *multiscaling*.

In reducing environments, c.p. Ti surfaces are covered by a thin film of TiO_2 (3-6 nm of thickness), which improves the corrosion resistance of titanium [220]. Despite the excellent corrosion resistance of TiO_2 in many diluted acid media, it spontaneously dissolves in HF according to the

Table 3.1: Numerical values of α, β, α_{loc}, β^* and $1/z$ for acid-etched c.p. titanium surfaces during an etching time (t). The values of α_{loc}, β and $1/z$ were experimentally obtained. Otherwise, α and β^* values were determined from the scaling relations between all these exponents.

t(min)	α	β	α_{loc}	β^*	$1/z$
$t < 3$	1.44 ± 0.18	0.62 ± 0.17	0.73 ± 0.15	0.32 ± 0.19	0.43 ± 0.07
$t \geq 3$	1.31 ± 0.11	0.46 ± 0.11	0.50 ± 0.11	0.25 ± 0.15	0.35 ± 0.09

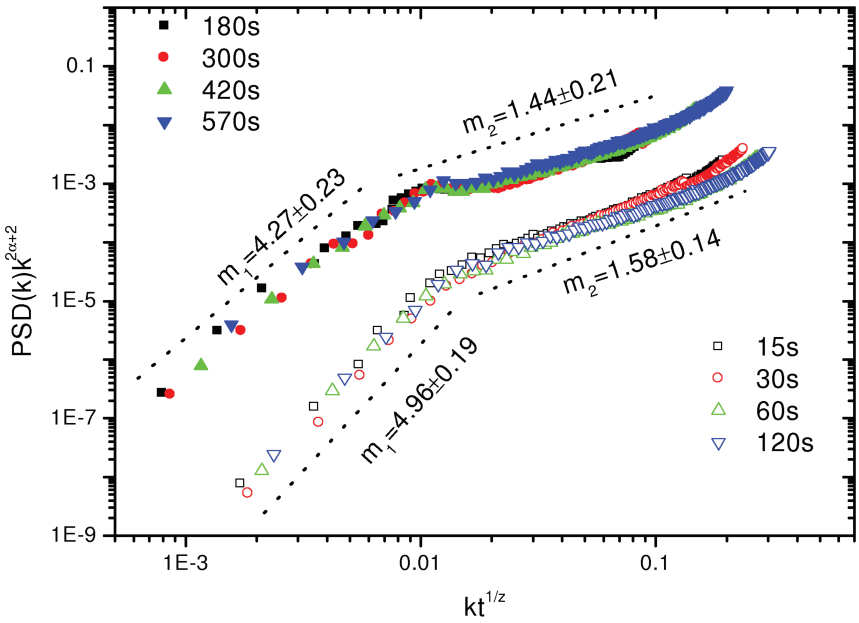

Figure 3.12: $PSD(k,t)k^{2\alpha+2}$ vs $kt^{1/z}$ in log-log scale for etching times under 3 min (open symbols) and over 3 min (close symbols). Both sets of data collapse in master curves. The dashed lines indicate the slopes of the master curves for small and large $kt^{1/z}$-values: $m_1 = 2(\alpha + 1)$ and $m_2 = 2(\alpha - \alpha_S)$, respectively.

following chemical reaction:

$$TiO_2(s) + 4HF(aq) \rightarrow TiF_4(aq) + 2H_2O \tag{3.7}$$

As TiO_2 is attacked by HF, metallic Ti appears just below the etched site and it instantaneously undergoes wet oxidation or complexation to form soluble titanium fluorides, accordingly:

$$\begin{aligned} Ti(s) + 2H_2O &\rightarrow TiO_2(s) + 2H_2(g) \\ 2Ti(s) + 6HF(aq) &\rightarrow 2TiF_3(aq) + 3H_2(g) \end{aligned} \tag{3.8}$$

Etching can also lead to the hydrogen incorporation in the surface region below the oxide and in consequence, the formation of titanium hydrides [224]:

$$Ti(s) + H_2(g) \rightarrow TiH_2(s) \tag{3.9}$$

Hence, HF acid etching also modified the surface chemistry of titanium [225, 226].

Once etching began, a heterogeneous film with varying thickness was developed on the titanium surfaces where TiO_2 and metallic Ti coexisted. Since the corrosion resistance of Ti and TiO_2 to HF action was different, the etching rate of sites occupied by Ti and TiO_2 was different as well. Measurements of EDX analysis (Fig. 3.14) confirmed the variation of the film thickness as etching time. Several authors have reported, numerically [108] and experimentally [227–229], that the etch rate anisotropy affects the properties of the surface, which turns out to be rough with an apparently non-universal roughness exponent. Under different etch rates on the surface, kinetic roughening can draw to different scaling laws for short and large scale lengths, i.e. to anomalous

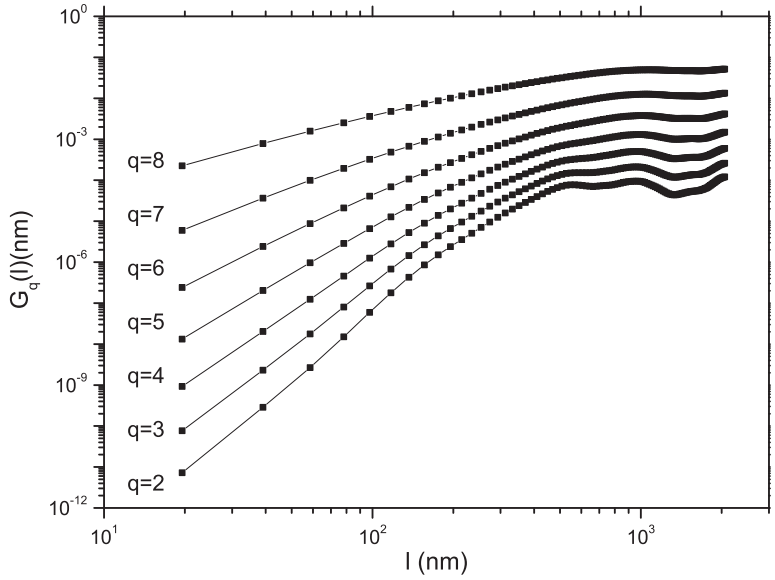

Figure 3.13: Multiscaling analysis through the computation of q-order structure functions of a titanium surface etched for 5 min.

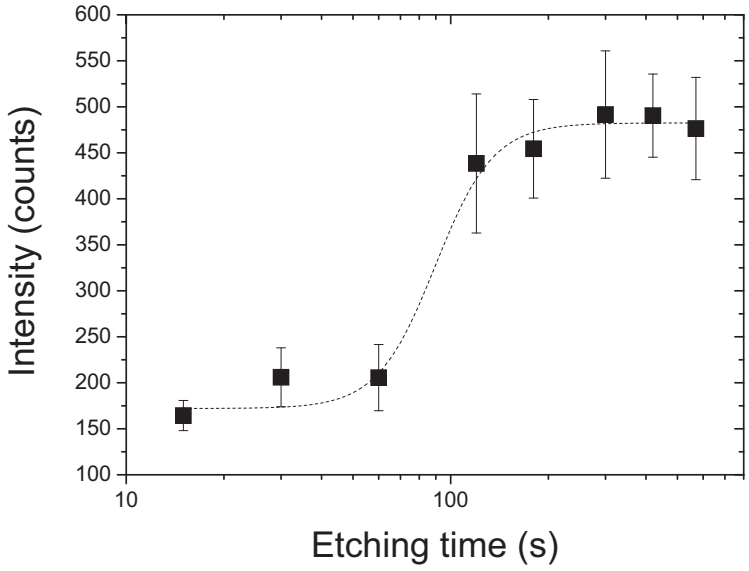

Figure 3.14: Atomic signal of titanium measured in the EDX spectra of acid-etched titanium surfaces as etching time. This signal is closely related to the thickness of oxide layer.

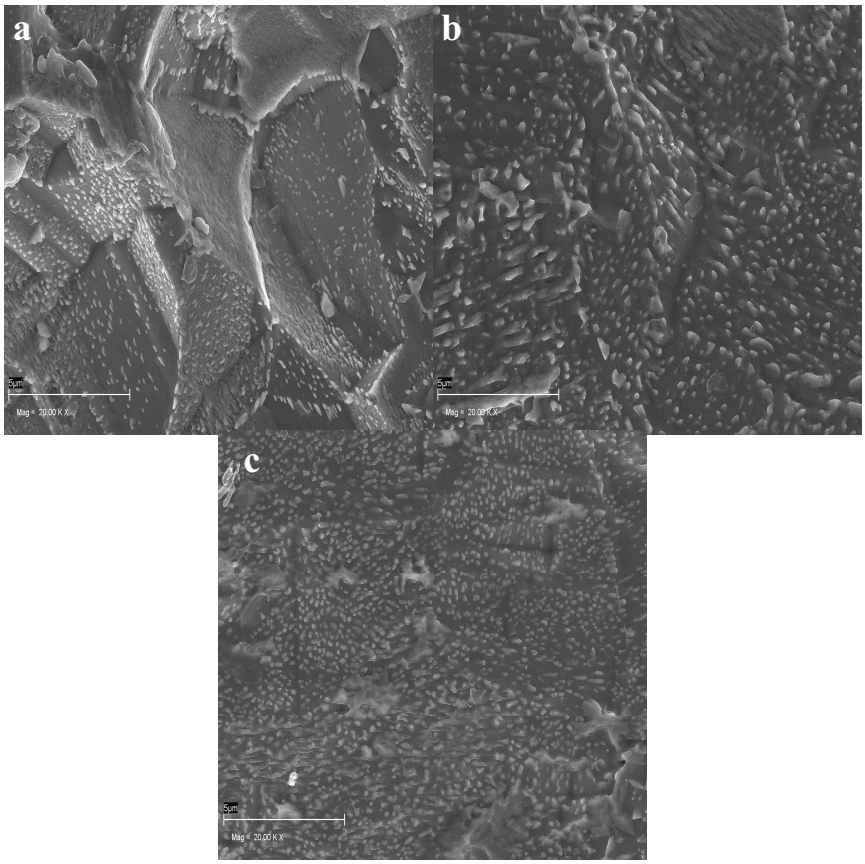

Figure 3.15: SEM pictures of titanium surfaces etched for (a) 2 min, (b) 3 min and (c) 5 min. The angular stepped morphology of shortly-etched surfaces (a) reveals the grain-structured titanium whereas the spiky aspect of long time-etched surfaces (b-c) reveals the needle-like structures of titanium hydride.

scaling and further to intrinsic anomalous scaling. Shadowing effects of the etchant flux can also enhance the anomalous behavior [127].

The difference between the two anomalous scaling behaviors described in Fig. 3.11 (a) and (b), and therefore the existence of two master curves (Fig. 3.12) seems to be produced by the TiH_2 formed in the sub-surface of titanium [224]. Aarão Reis [109, 128] described a continuous dynamic transition for etching processes due to the deposition on the surface of *poisoning* species. These species prevented the acid etching on determined regions of the surface, such as "etch-stop" material. We suspect that the titanium surfaces were significantly doped after a long HF etching ($\geq$ 3 min).

The initial period of HF etching ($<$ 3 min), in which the mass loss of titanium was small ($\leq$ 10%), represents the time required to dissolve the native oxide film and to expose the microstructure of the bulk material, with clearly visible grains and grain boundaries (Fig. 3.15(a)). This process was ruled by the interplay between the HF etching produced on TiO_2 and Ti and the wet oxidation of Ti. Once the surface doping was significant ($\geq$ 3 min), the surface morphology looked spiky (Fig. 3.15(b)) with needle-like structures, typical ones of titanium hydride [224], the grain boundaries

acted as preferential sites for etching and the roughness began to decrease (Fig. 3.15(c)). In this regime, the titanium surface mostly lost the mass (up to 70%) although at lower rate and the oxide film stabilized with a constant thickness (Fig. 3.14). The transition time between scaling behaviors could depend on the ratio between the etching rates of the Ti and TiO_2 species and the thickness of the native oxide film [127].

3.2.5 Conclusions

Kinetic roughening of HF acid-etched c.p. titanium surfaces, as growth process driven by anisotropic rules, obeyed the anomalous scaling ansatz Eqs. (3.5-3.6). Moreover, the titanium surfaces presented multiscaling and intrinsic anomalous scaling for all etching times. The evolving surface chemistry and the corrosion resistance of titanium were modulated by the competition between wet oxidation and complexation of the metallic Ti present on the surface. A dynamic transition between anomalous scalings was produced by doping of the etched titanium surfaces, due to the TiH_2 formed in the sub-surface of titanium.

Scaling analysis is helpful to understand the impact of nanoscale features of the implant topography on the cell growth and, to elucidate the complex mechanisms occurring at the implant surface in contact with the surrounding biological tissues. Further work should be addressed to apply scaling analysis and other tools of statistical physics in biomaterials surface engineering.

3.3 Roughness Factor of Acid-Etched Titanium Surfaces

As it will be shown in Chapter 4, surface roughness affects the response of osteoblast-like cells (protein adsorption, cellular differentiation, proliferation, shape, orientation and local growth of osteoblasts) [230]. Several studies have demonstrated that roughness of titanium surfaces increases the amount of adsorbed fibronectin, which acts as a promoter of cell adhesion, but decreases the amount of adsorbed albumin compared to less rough surfaces [231]. These results suggest the existence of an optimal roughness level where protein adsorption and cell adhesion could be maximized. The achievement of this optimal roughness level is an aim for implantologists and, this way, different methods have been developed [232–234]. It has been reported that acid etching of titanium surfaces estimulate earlier osseous contact than plasma-treated titanium surfaces [234, 235]. Perrin et al. showed that the above mentioned methods generate two different roughness scales on the treated surface: macro-roughness produced by sandblasting is associated to large wavelength defects and micro-roughness due to acid-etching is associated to short wavelength defects. This double scale for roughness on titanium implant surfaces may be responsible for the good osteoconductive response [236].

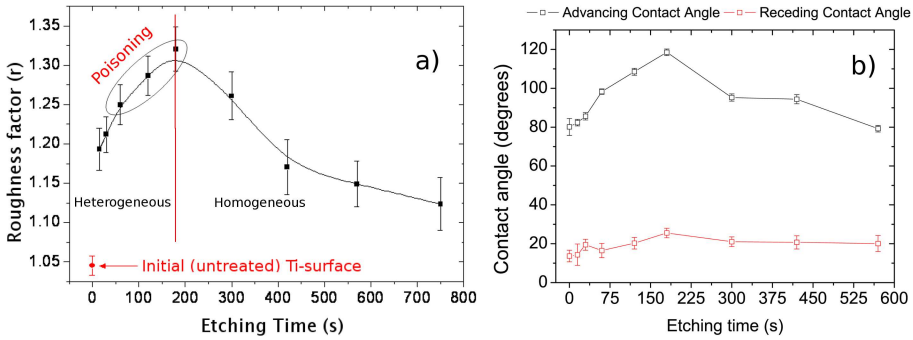

Figure 3.16: Behaviour of roughness factor (a) and advancing/receding contact angles (b) of acid-etched titanium surfaces for different etching times. Roughness factor values were obtained from the analysis of topographical data acquired by AFM. Rouhgness factor increases for etching times below 3 min and, for etching times above 3 min, roughness factor decreases. Otherwise, low-rate dynamic contact angle experiment was designed to determine advancing/reciding contact angles. Advancing/reciding contact angles were obtained from sessile drops and captive bubbles respectively.

From Sections 3.1 and 3.2, acid etching enables to produce different rough surfaces identified with different values of parameters of integral geometry and stochastic analysis. In this section, we will use the roughness factor to describe the acid-etched titanium surfaces.

The roughness factor of the acid-etched titanium surfaces was computed by using Eq. 1.5 with the topography data acquired by AFM[2]. The results are plotted in Fig. 3.16 a). This figure shows how the roughness factor changes with etching time. Firstly, for etching times below 3 min, the roughness factor increases but from this point it decreases. This suggests that the etching process on titanium undergoes a "crossover" at etching times close to 3 min validated by the stochastic analysis of the acid-etched titanium surfaces (see Section 3.2).

[2]For details about topographical acquisition and the acid etching of titanium surfaces see Sections 3.1.3 and 3.2.3.

Fig. 3.16 b) shows how the advancing and receding contact angles ($V = 50\mu l$ maximum volume of drop/bubble) change with etching time.For etching times below 3 min, advancing contact angle increases but from this point it decreases. However, the receding contact angle oscillates within the range $10 - 20°$. Fig. 3.16 b) reproduces the behavior observed for roughness factor. However, the high contact angle hysteresis of the acid-etched surfaces present cannot be just explained by roughness changes. This fact points out to a further change of surface chemistry [237]. Similar behavior with etching time was observed in the adhesion of osteoblast-like cells on acid-etched titanium surfaces conducted by O. García-Martínez and C. Ruíz[3] (unpublished results).

Similar behavior of the roughness factor and contact angle with etching time was also observed on acid-etched glass surfaces as shown in Fig. 3.17. The acid etching of glass surfaces was also performed with HF solutions under similar conditions than the used for etching of titanium surfaces. Topographies of glass surfaces were also acquired by AFM under similar conditions but the contact angles were obtained with static contact angle experiments. The existence of a critical time for the roughening kinetics of acid-etched surfaces seems to be universal.

Since this thesis is focused on acid-etched titanium surfaces, a study of the etching process of

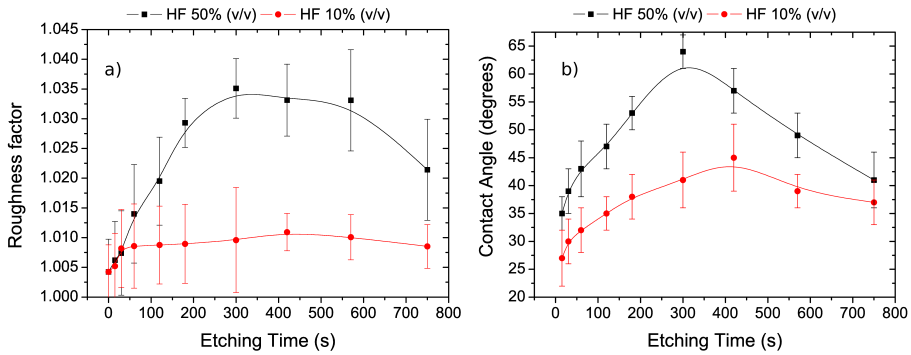

Figure 3.17: Behaviour of roughness factor r (a) and static contact angle (c) of acid-etched glass surfaces for different etching times and different acid solution concentrations. These quantities shows an increase of their values for etching times lower than a critical one and a decrease for etching time greater than it. The general trends with etching time observed for these quantities on acid-etched glass surfaces are similar to the observed on acid-etched titanium surfaces.

titanium surfaces has been performed. As it was pointed out in Section 3.2, the local etching rate depends on how topographical motifs of the surface are orientated to the etchant agent (HF) and how TiO_2 and Ti exhibit a different etching kinetics for HF [238, 239] (see chemical reactions 3.7 and 3.8). As it was explained in Section 3.2.4, kinetic roughening of acid-etched titanium surfaces is mediated by the surface poisoning produced by the formation of chemical species which prevent the acid etching and produce a continuous dynamic transition in the roughnening of the surfaces, as Aarão Reis described [109, 128]. Thus, this poisoning process joined with the morphological evolution of the surface due to etching process [240], can explain the depedence of the roughness factor with etching time. Hence, dynamics of etching may be ruled by the different corrosion resistance to HF of surface Ti and TiO_2 and by the competitive process between oxidation and complexation of Ti.

For real surfaces, it is necessary to differ between homogeneous and heterogeneous etching. In a homogeneous roughening all surface point exhibits identical behavior towards the etchant agent.

[3]Department of Nursing, School of Health Sciences, Biomedical Research Group (BIO277), University of Granada, Granada, Spain.

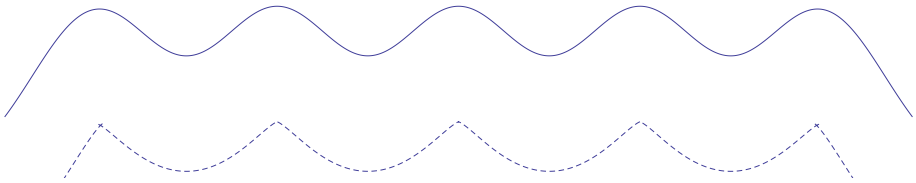

Figure 3.18: Initial profile (continuous line) and final profile (dashed line) produced by homogeneous (uniform) normal-directed erosion. The roughening process depends on the local curvatures. The peaks are sharpened and the valleys are flattened. Locally, the surface area increases for the peaks and decreases for the valleys.

Otherwise, in a heterogeneous roughening the surface points behave different. Consequently, as Fig. 3.18 illustrates, the sucessive surfaces generated by a homogeneous normal-directed roughening are allways "parallel"[4], from a geometrical point of view, to the primitive surface. However, the surfaces originated with a heterogeneous roughening[5] are not 'parallel" because their evolution is different point-to-point.

It is possible to describe the successive parallel surfaces generated by a homogeneous normal-directed etching in purely geometrical terms. Thus, if S_i is the "parallel"surface obtained when an amount of material m (m is much lower than the surface material) is removed from its primitive surface S_{i-1}, then

$$\frac{H_i(t)}{K_i(t)} = \frac{H_{i-1}(t)}{K_{i-1}(t)} - m \Rightarrow \frac{1}{2}\left(R_{i,1} + R_{i,2}\right) = \frac{1}{2}\left(R_{i-1,1} + R_{i-1,2}\right) - m \tag{3.10}$$

where H_i and K_i are the mean and Gaussian curvature of the "parallel" surface S_i and $R_{i,1}$ and $R_{i,2}$ are its principal radii of curvature.

From Eq. 3.10, we can conclude that the behavior of the surface which is suffering the erosion process depends on the geometrical properties of the primitive surface. Thus, etching ($m < 0$) of a valley-dominated primitive surface[6] ($R_{i-1,1}, R_{i-1,2} > 0$) involves that ($R_{i,1} + R_{i,2}$) increases and, therefore, the surface should be flattened as etching time increases. Otherwise, for a peak-dominated primitive surface ($R_{i-1,1}, R_{i-1,2} < 0$), ($R_{n,1} + R_{n,2}$) decreases with etching time and, consequently, the surface will be more spiky than its primitive one.

Steiner formulae [180,181] permit the traslation of the variation of mean and gaussian curvature values to surface area variation. These formulas, under the supposition that m is much lower than the total amount of material, the surface area variation (ΔA) can be written as follows:

$$Ai - A_{i-1} = \Delta A_i = \left[2H_{i-1}m - K_{i-1}m^2\right] A_{i-1} \tag{3.11}$$

By iteration, Eq. 3.11 relates the surface area A_0 of the original surface S_0 with the surface area A of the resulting surface after the etching process through

$$A - A_0 = \Delta A = \left[2H_0m - K_0m^2\right] A_0 \tag{3.12}$$

Note that Eq. 3.12 is an extension of Steiner's theorem from integral geometry to nonconvex bodies, which is valid as long as the distance m between the two surfaces is smaller than the smallest

[4]Similar conclusion is also valid for a homogeneous vertical-directed roughening applied to any wavy rough surface.

[5]It is not relevant the attack direction in a heterogeneous etching.

[6]A valley/peak-dominated surface is that one where surface area associated to valleys/peaks is greater than the area due to peaks/valleys.

radius of curvature of the surface (otherwise the surface will self-intersect)[241]. Moreover, for surfaces produced by homogeneous normal-directed roughening, surface area ratio (waviness-weighted roughness factor) strongly depends on the principal curvatures of the underlying waviness.

Therefore, from Eq. 3.12 and under the supposition that m is much lower than the total amount of material, for any erosion process ($m < 0$) is possible to conclude that if the primitive surface is a valley-dominated one then the erosion leads to surfaces where roughness factor, defined by Eq. 2.28 and which it can be simplify to $r_i = 1 + 2|m|H_{i-1} \geq 1$, decreases ($r_i < r_{i-1} \geq 1$) regardless of the etching time considered. Otherwise, if the primitive surface is peak-dominated one, then roughness factor always increases ($r_i > r_{i-1}$).

Erosion of chemically heterogeneous surfaces produces structures with different height, i.e. privileged area (peal and valleys). These privileged areas are also susceptible to be attacked through its normal direction. In purely geometrical terms, a heterogeneous erosion implies that the surface evolves with morphology due to the surface heterogeneities and the local "homogeneous" normal erosion. As consequence, if the peaks dominate the surface curvature increases and also the surface area (roughness factor). Fig. 3.19 illustrates the transition between heterogeneous erosion,

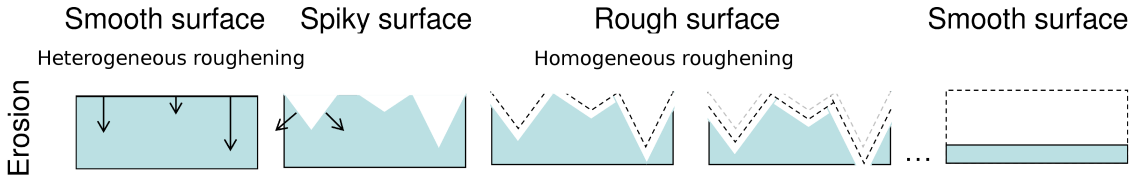

Figure 3.19: Surface etching of a smooth and chemically heterogeneous surface (the different arrows make reference to the behavior of each surface point). Our model assumes that a heterogeneous roughening changes to a homogeneous normal-directed roughening. Consequently, the roughness factor increases for times lower than a critical one and, for times greater, the roughness factor decreases. As figure shows, any homogeneous normal-directed roughening can lead to a perfectly smooth surface.

where the different affinity to the roughening agent has been represented through arrows of different length, to homogeneous normal-directed erosion.

According to the ideas presented in this section about the resulting geometries of the surfaces under etching processes and the dynamic transition presented in Section 3.2, acid etching of commercially pure titanium surfaces must be considered as a stochastic[7] erosion process of a heterogeneous surface which evolves towards a spiky surface for times lower than a critical one[8], and a valley-dominated surface for times greater than the critical time. The proposed model allow us to explain the behavior of the roughness factor with etching time (Fig. 3.16).

Fig. 3.16 a) shows a crossover between both roughening regimes. The results of Sections 3.1 and 3.2 shown that this transition between roughening regimes must be lead by surface chemistry change, i.e. by surface poisoning. Therefore, the dynamic transition between these two types of etching regimes might be modulated by both the oxidation state of the surface and the formation of etch-stop species just below it. The poisoning of the surface due to the presence of TiH is one of the responsible of the transition between roughening regimes and, consequently, of the roughness factor maximum shown in Fig. 3.16 a). Besides the presence of poisoning species on the surface, the acid concentration, the etching rate (produced by laminar or turbulent flow) the initial roughness of the surface, and the grain orientation on the untreated titanium surface, will also regulate

[7]The amplitude of the stochastic function represents to the amount m of surface material removed from the primitive surface.

[8]This critical time should be determined for each type of surface and etching process.

at some extent the time for which the roughness factor of acid-etched surfaces is maximized.

The results exposed above permit us to conclude that chemical etching can be simply represented by a constant erosion rate along the local normal direction to the surface and, which etching rate is affected by local curvature and by fluctuations in the chemical composition of the surface.

Chapter 4

Cell Adhesion

This chapter collects the results of MG-63 osteoblast-cell culture (adhesion, proliferation and morphology) on silicon[1] and titanium[2] surfaces. Silicon surfaces, with different physical and chemical properties, were obtained by changing the surface roughness and hydrophobicity through the chemical etching $NaOH$ solution and the deposition of a thin film of dimethyldichlorosilane and trichloroethylene, respectively. Each group of these surfaces was characterized in terms of surface roughness and wettability.

Since titanium is commonly used in implantology field, commercially pure titanium surfaces ($cpTi$) were modified to reproduce different surface properties. We followed different treatments: chemical etching using HF solution (eTi), blastering with different SiC metallographic papers (bTi) and the combination of both treatments ($ebTi$). Previously to the cell culture, these surfaces were characterized in terms of surface roughness, wettability and surface chemistry.

Appendix A collects a complete description of all the experimental techniques and devices used to characterize the surface roughness/chemistry and advancing/receding contact angles of water.

[1] Miguel Padial-Molina, Pablo Galindo-Moreno, Juan Emilio Fernández-Barbero, Francisco O'Valle, Ana Belén Jódar-Reyes, Juan Luis Ortega-Vinuesa, Pedro J Ramón-Torregrosa, *Role of wettability and nanoroughness on interactions between osteoblast and modified silicon surfaces* in Acta Biomaterialia, 7, 771-778, 2011.

[2] J. I. Rosales-Leal, M. A. Rodríguez-Valverde, G. Mazzaglia, P. J. Ramón-Torregrosa, L. Díaz-Rodríguez, O. García-Martínez, M. Vallecillo-Capilla, C. Ruiz, M. A. Cabrerizo-Vílchez,*Effect of roughness, wettability and morphology of engineered titanium surfaces on osteoblast-like cell adhesion* in Colloids and Surfaces A: Physicochemical and Engineering Aspects, 365, 222-229, 2009.

4.1 Introduction

The success of a dental implant is based on its osseointegration which is defined as the direct contact between the bone tissue and the implant surface, without fibrous tissue growing on the interface [242, 243]. The major challenge in Implantology is to combine current knowledge in material science, tissue engineering and biology to design and develope ideal implant surfaces, i.e. optimal biomaterial surfaces which enhance bone-cell response to the presence of these systems improving bone healing and osseointegration of the implants. In this sense, it is well-known that surface properties of a material, such as wettability, roughness, surface charge and energy or chemical functionalities, determine the amount and quality of cell adherence, proliferation and differentation [237, 244–247].

The development of biomaterials and biomedical devices for dental and orthopedics applications have to take into account the role played by physical and chemical properties of the surfaces on cell adhesion and spreading of osteoblast-like cells, as well as on subsequent processes as cell morphology, proliferation and diferentation. In this sense, it is known that surface chemistry, wettability and surface energy, govern the adhesion and spreading of osteoblast-like cells [237, 248] and, therefore, for a determined material, the *quality* of the implant can be improved through the modification of surface roughness and/or surface chemistry [249, 250]. In addition, the initial cell atachment to a biomaterial surface determines subsequent processes such as cell spreading, morphology, migration, proliferation and differentation [251]. Even, surface roughness also plays a key role on osteoblast response in terms of adhesion, spreading, differentation and differentation [252, 253], as well as on the local porduction of growth factors and cytokines [248, 254–256]. However, there is an incomplete knowledge about the potential influence of surface nanoroughness on cell behavior [257]. Furthermore, changes in surface roughness also affect to surface wettability and, consequently, to osteoblast-like cell response [258].

For implantalogy field, it would be important to determine how each one of surface properties affects on cell response. But, however, this is a nontrivial task because biomaterial surfaces, as real surfaces, usually present a high degree of heterogeneity, including type and density of functional groups, hydrophilic or hydrophobic areas irregularly distributed on them, surface texture and roughness. Consequently, these non-idealities complicate the study of the effect caused by a given parameter or property.

The topography of a surface affects the macroscopic behavior of a material [253] and, for this reason, it is matter of investigation in every material science field even implantology and tissue engenieering [249, 250, 259–261]. At cellular level, biological responses, such as cell migration, cellular production of cytoskeletal arrangements or osteoblast-like cell attachements, are directly influenced by surface topography [254, 262]. Even more, there are evidences that a suitable surface roughness, at nano and microscale, can lead to a successful osseointegration of dental implants [164, 249, 263]. Moreover, as it was mentioned above, different studies have concluded that osteoblast differentation, proliferation an matrix production [255], as well as the production of local growth factors [256] or cell adhesion and integration in biomaterial system, are also affected by surface roughness [263]. As consecuence of all this, different studies have concluded that cell adhesion can be enhanced by texturing of the surface at appropiate degree [249, 250, 263].

In addition to surface roughness and, as it was previously mentioned, surface chemistry plays a critical role on aspects related to cell adhesion and proliferation [251, 252, 264, 265] and on the interaction between implant surface and the surronding medium [266]. Surface chemistry can also be modified by the atachment of determined chemical groups to the surface to reach an optimal cell response. However, the variety of chemical groups ($-COOH$, $-NH_2$, $-PEG$,...) bound to the modified surface makes it difficult to establish a clear correlation between wettability, which it

has been demonstrated as a useful quantity to correlate surface chemistry with biological response [267] and, cell adhesion [268–270]. For instance, hydrophobic surface (i.e. surface with low water wettability) presumably decelerate primary interactions with aqueous biosystems, but biomaterial surfaces with moderate hydrophilicity improve cell growth and biocompatibility [271]. However, cell adhesion can decrease as the implant wettability is further decreases, pointing out the existence of a range of optimal surface wettability [272, 273].

It is possible conclude that the modifications of physico and physico-chemical properties of a surface can improve its interaction with cells. For example, several texturing surface treatments have been applied on titanium surfaces to optimize bone-implant contact through of developing of a roughness degree which enhaces protein adsorption on surfaces and therefore cell adhesion [274, 275]. Even more, as silicon derivatives have been introduced as bone substitutes [276] and as biomimetic agents to coats implant surfaces [277], with reported good clinical success rates and promotion of new bone tissue around these materials [278], a new application field has been opened because of silicon surfaces are alterated in terms of their physico-chemical properties by simple chemical treatments [279, 280].

Since there is a plethora of variables that can affect cell behavior, this chapter is just focused on the analysis of the role played by surface wettability and surface topography on cell responses. Silicon and titanium surfaces were used as model and biomaterial surfaces respectively and osteoblast-like cells were used as adherent cells due to their relevance for implants in bone tissues. The aims of this chapter are; to analyze the correlation between the independently controlled roughness and wettability and the proliferation and morphology of osteoblast-like cells for silicon surfaces and, to evaluate the effect of surface roughness on the adhesion and growth of osteoblast-like cells on different rough titanium surfaces obtained by distinct texturing techniques.

4.2 Materials and Methods

This section presents surface treatments used to change physical and chemical properties of silica and titanium surfaces, as surface used in dental implantology [274–278] and, also, experimental techniques employed to study how cell response was affected by these physico-chemical changes for each kind of surface.

Moreover, cell culture techniques, used for each kind of surfaces, have also been detailed in this section.

4.2.1 Surface Modification

Silicon and commercially-pure titanium surfaces were modified as follows:

- **Silicon Surfaces:** Single-side polished silicon wafers (100mm diameter, P-type, Bor $\langle 100 \rangle$ orientation, 1-30Ωcm resistivity, 525μm thickness; Si-Mat®, Landsberg, Germany) were cut into 1x1cm squares using a special wafer saw. These pieces were cleaned by immersion for 5 min in a boiling basic peroxide solution [H_2O:H_2O_2 (30% v/v):NH_4OH (25% v/v), ratio 5:1:1], rinsed in MilliQ water, immersed for 5min in a boiling acidic peroxide solution [H_2O:H_2O_2 (30% v/v):HCl (37% v/v), ratio 6:1:1] and, rinsed in deionized water. This process creates a thin, hydrated silicon dioxide layer that is highly hydrophilic [281].

  Surface Chemistry Alteration: Some pieces were rinsed twice in ethanol and once in trichloroethylene (*TCE*) (Fluka, Schnelldorf, Germany). Then, they were incubated at room temperature for 10min in TCE organic solutions of dimethyldichlorosilane (*DDS*) (Fluka, Schnelldorf,

Germany) added at 0.003%, 0.006%, 0.012% and 0.062% concentrations in order to produce degrees of different methylation. Finally, these methylated silicon wafers were rinsed in ethanol, TCE, ethanol again and, finally deionized water. This group of samples was named *H* (due to changes in *Hydrophobicity*). In fact, they were named *H1*, *H2*, *H3* and, *H4* for the corresponding increase in DDS concentrations mentioned above.

Surface Roughness Alteration: Another group of clean oxidized silicon pieces was subjected to caustic etching in aqueous sodium hydroxide solutions ([NaOH]=0.1M) at room temperature for 0, 22, 60 or 165 min. The specimens were then rinsed with water to remove the excess alkali and, rinsed in deionized water. This group of samples was named *R* (due to changes in *Roughness*). Likewise, they were named *R1*, *R2*, *R3* and *R4* for increasing etching time (0, 22, 60 and 165min, respectively).

In order to avoid any possible bacterial contamination, all surfaces were stored in a sodium azide solution ($1mg/ml$), that was enough to inhibit bacterial growing [282] and did not alter the surface properties, as we had checked in another group of samples by characterizing the surface before and after immersion in sodium azide.

- **Titanium Surfaces:** Commercially-pure ASTM grade II titanium ($cpTi$) surfaces were modified by three different methods used in the implantology in order to evaluate the effect of texture on the adhesion and growth of osteoblast-like cells. So, $cpTi$ cylinders (Manfredi, S. Secondo di Pinerolo, Italy) were suitably cut into small disks of approximately 12 mm in diameter and 2 mm in thickness. The $cpTi$ disks, previously cleaned with distilled water, were engineered as follows:

  Group 1 (control): Polished titanium (pTi). $cpTi$ surfaces were metallographically polished using silicon carbide (SiC) papers successively from grade 240, 320, 500, 800, 1200, 2000 to 4000 grits. Next, an ultra-polishing was achieved using the sequence 1-0.3-0.05μm alumina slurries and gauze. The polished disks were cleaned in distilled water by immersion in ultrasonic bath (Selecta, Barcelona, Spain).

  Group 2: Etched titanium (eTi). pTi surfaces were etched with a solution of 10% (v/v) hydrofluoric (HF) acid (Panreac, Barcelona, Spain) by complete immersion upon gently agitation for 5 min.

  Group 3: Blasted titanium bTi. pTi surfaces were blasted by alumina (99,78% Al_2O_3) particles of 110μm diameter projected at an incidence angle of 60° and 0.25MPa pressure for 3 min.

  Group 4: Blasted + etched titanium ($beTi$). pTi surfaces were blasted as in the group 3 but using alumina particles of 250-500μm. Next, these blasted surfaces were etched as described for group 2.

  After treatments, pTi, eTi, bTi and $beTi$ samples were degreased with a solution of 70% (v/v) acetone (Panreac, Barcelona, Spain) by immersion in ultrasonic bath for 20 min and afterwards, the samples were ultrasonicated in distilled water for 30min. eTi and $beTi$ samples were passivated with 30% (v/v) nitric (HNO_3) acid (Panreac, Barcelona, Spain) for 3 min and then again ultrasonicated in diluted acetone for 20 min and distilled water for 30 min. All disks were autoclaved at 121°C and 1 atm for 30 min after preparation.

4.2.2 Experimental Techniques

Experimental techniques used in this section can be grouped into three different categories according to the type of information which they extract from surfaces, i.e. surface roughness, wettability and cell culture.

- **Surface Roughness Characterization:** A detailed description of each experimental device used to roughness characterization and imaging of the surfaces can be found in Appendix A. In this section only appears the technical details employed to take the topographies and images of silica and titanium surfaces described above and, roughness parameters used to quantify roughness information provided by adquired topographies.

  AFM: Surface roughness for silica and textured titanim surfaces was characterized by a quantitative analysis using an Atomic Force Microscope (AFM) (Nanoscope IV MultiMode®, Digital Instruments, Santa Barbara, CA, USA), operating in air and working in tapping mode with a Si_3N_4 V-shape cantilever (stiffness, $k = 63 \pm 8N/m$). The topography data were sampled in a grid of $256x256pixels^2$ and all images were fitted to a plane and filtered by a Gaussian mask with a cutoff of $2.5\mu m$ in order to capture surface features below the average cell size ($\sim 10\mu m$). Three samples per group, each one of the groups of silicon and titanium surfaces, were used and three different and independent analyses were performed per each sample, analyzing areas of $2.5x2.5\mu m$.

  FESEM: For titanium surfaces FESEM images were also acquired. So, three titanium disks per each one of the groups previosuly presented were observed under a Scanning Electron Microscope Leo Gemini 1530 (Carl Zeiss, Oberkochen, Germany). In order to improve the electrical conductivity of titanium, carbon thin films were produced by sputtering on each sample.
  Morphology of each sample was evaluated from $3072x2304pixel^2$ images acquired at $x2000$ magnification. Further porosity analysis was accomplished on the eTi and $beTi$ samples. Moreover, as roughness is often associated with changes in surface chemistry (e.g. plasma deposition or acid etching), the unexpected modifications in surface chemical composition of textured titanium surfaces were analyzed using Energy Dispersive X-ray (EDX) spectra of several places of each titanium sample up to a depth of $1\mu m$. This analytical technique serves to detect the chemical elements located at the surface and thus, potential surface contamination [283].
  All the processes described in previous paragraphs were performed in Scientific Instrumentation Center of the University of Granada.

  Roughness Paramenters: Surface roughness of silicon and texturized titanium surfaces were characterizated using different parameters[3]. Obviously and, due to their massive use on implantology field, amplitude statistical parameters, i.e. arithmetic average roughness (R_a) and root mean square roughness (R_q), were employed to describe surface roughness. Moreover, surface area ratio (r), which quantifies topography variations with respect to the planar coordinates, and fractal dimension (D_f[4]), which reveals information about structural complexity and is related to the compactness degree of the space-filling structure, were also computed for every texturized surface.

[3]The mathematical definition of each one of these parameters and, also their physical interpretation, can be found in Chapter 1

[4]D_f was calculated by the box-counting method [86]

Moreover, the characterization of surface roughness of texturized titanium surfaces was also completed using the following amplitude statistical parameters: peak and valley roughness parameters (R_p and R_v, respectively), skewness (R_{sk}) and kurtosis (R_{ku}) in order to describe the height distribution of the titanium surface obtained by different texturizing techniques described above.
Statistical parameters were computed from the AFM topography data using the software of the own instrument. Surface area ratio of the surfaces was computed by a ad-hoc designed software.

- **Wettability Characterization:** Since physiological fluids are indeed aqueous saline solutions, pure water is the reference probe liquid used for measuring surface wettability of biomaterials, as titanium. For this reason, water was also used to determine the surface wettability of silicon surfaces. Surface wettability of silicon and titanium surface were measured using MilliQ sessile water drops dispensed on the surfacse with a micropipette (Eppendorf, Hamburg, Germany). Each surface was rinsed with deionized water and dried in N_2 gas before measuring the static contact angle. Surface-wettability of silicon surfaces were measured using sessile water drops ($5\mu l$ volume) on three samples per surface alteration (see subsection 4.2.1). Six different and independent experiments were performed per sample. For titanium surfaces, surface wettability was measured through the contact angle of spreading sessile drops ($2.5\mu l$ of volume). Three titanium surfaces were analyzed per group (see subsection 4.2.1) and three drops were deposited on each one.
The contact-angle values were determined by an axisymmetric drop-shape analysis (ADSA) [284, 285]. Images for the analyses were took by means of a CCD monochrome camera (Sony SSC-M370CE) coupled to a microscope (Apozoom, Leica Microsystems, Wetzlar, Germany), horizontally oriented in a thermostatically controlled room ($20°C$). Droplet images were processed in a PC by a frame grabber (DT 3155, Data Translation GmbH, Bietigheim-Bissingen, Germany). Contact angles were directly computed by ad-hoc designed software.

- **Cell Culture:** The cell culture studies on silicon and titanium surfaces were performed with human osteoblast-like cells MG-63, but the protocol used to add them to each material was different. The reason for this difference is that standard protocols for each kind of surfaces has been stablished a long time ago and these protocols are the ones that were used for each different kind of surface.

  Silicon Surfaces: Human MG-63 osteoblast-like cells (supplied by the Scientific Instrumentation Center of the University of Granada, Spain) were added at the same density to three silicon wafers per group distributed face-up in 24 well-culture plates. $0.1ml$ of a $5000 - cells/ml$ suspension was used in order to cover the entire wafer surface with a thin layer of cells guaranteeing that the cell culture would not be saturated in advance. Dulbecco's modified Eagle medium (DMEM, Sigma, St Louis, MO, USA), supplemented with 10% fetal bovine serum (FBS, Sigma) and 1% penicillin/streptomycin, was then added up to $2ml$. Culture plates were maintained at $37°C$ in a humidified $5\%CO_2/95\%$ air atmosphere. Culture medium was exchanged every 48 hours until 21 days after plating. The experiment was repeated three times both for proliferation study, ultrastructural analysis as immunophenotype characterization.
  The proliferation studies were performed as follows; Twenty-one days after plating, adherent cells were released from the surface by two sequential incubations in a non-enzymatic cell dissociation solution 0.05% trypsin and 0.02% ethylene diamine tetra-acetic acid (EDTA), Sigma, St. Louis, MO, USA] for 5 min at $37°C$. The number of adhering cells was deter-

mined by counting in a Neubauer chamber. Four counts were made for each cell suspension released from each sample. The mean number of cells was quantified per ml.
Field Emission Scanning Electron microscopy (FESEM) (LEO 1530 Gemini, Zeiss/LEO, Oberkochen, Germany) with a $5Kv$ intensity was used for ultrastructural analyses in order to evaluate the cell morphology. For these studies, after cells were cultured on the silicon wafers, another group of cell cultures were fixed in a 4% sodium cacodylate-buffered formaldehyde-glutaraldehyde fixative for 24 hours at room temperature after removing the culture media, post-fixed in 20% osmium tetroxide for 2 hours and dehydrated by serial transfers in ascending concentrations of acetone $(50 - 100\%)$. Then, they were infiltrated with liquid carbon dioxide below the critical drying point and made electrically conductive by mounting them on aluminum slabs with a silver point. Finally, samples were coated by sputter with gold/palladium to a thickness of approximately 250 Å.
Moreover, cell immunophenotype was characterized. For these studies, basal cultures of MG-63 were characterized by flow cytometric analysis [286]. Briefly, cells were transferred to universal screw-cap tubes containing sterile PBS and, cell suspensions were washed and centrifuged at $225g$ for 5 minutes, discarding the supernatant. The washing and centrifugation steps were then repeated twice. Cells were incubated for 20 minutes at room temperature with $5\mu l$ of antibody per $20\mu l$ of cell suspension. Tubes were then filled with PBS and 0.5 ml of lysine. FACScan®(Becton Dickinson, Mountain View, CA, USA) analysis was then performed using the CellQuest®Software (Becton Dickinson). HLA-ABC (Major Histocompatibility Complex class I expressed by most normal nucleated cells [287]) and vimentin (intermediate filaments present in all mesenquimal cells [288]) were used as positive controls; CD14 (transmembrane protein in macrophages for the detection of bacterial lipopolysaccharide [289]) and CD45 (leukocyte common antigen; signaling molecule on all nucleated hematopoietic cells [290]) as negative controls; CD10, CD56, actin, caldesmon, osteocalcin and Ki67 were detected for basal immunophenotype characterization. CD10 (Common Acute Lymphocytic Leukemia Antigen, CALLA) is a cell-surface enzyme expressed in cells sensitive to various hormones, exercising its function by degrading these hormones [291]. CD56 (NCAM) is a cell-surface glycoprotein implicated in cell-cell adhesion [292]. Actin is a globular protein that participates in cell motility, division and cytokinesis, accompanied by caldesmon and the establishment and maintenance of cell junctions and cell shape [293]. Osteocalcin is secreted by osteoblast playing a role in late bone mineralization and calcium ion homeostasis [294]. Finally, the Ki-67 protein is a cellular marker strictly associated with cell proliferation [295]. All antibodies were purchased from Master Diagnostica, Granada, Spain.
After cell cultures on modified silicon wafers, cells were characterized and the proliferation index calculated by immunocytochemically analyzing the expression of the markers mentioned above. For this, cells were released from silicon pieces by two sequential incubations in a non-enzymatic cell-dissociation solution (0.05% trypsin and 0.02% EDTA, Sigma) for 5 minutes at $37°C$. After cytocentrifugation, the cell button was embedded in paraffin and sectioned at $3\mu m$, dewaxed, hydrated and heat-treated in 1 mM EDTA buffer for antigenic unmasking. Sections were incubated for 60 minutes at room temperature with prediluted antibodies. The immunocytochemical study was performed on an automatic immunostainer (Autostainer 480, Lab Vision, Fremont, CA, USA) using the polymer-peroxidase-based method, followed by development with diaminobenzidine (Master Diagnostica). A millimeter grid in the eyepiece of a BH2 microscope (Olympus) with a $40x$ objective was used to count the positive number of cells per mm^2.

Titanium Surfaces: The cell attachment and spreading studies were performed with human

osteoblast-like cell MG-63 [255,274] which was purchased from American Type Cultures Collection (ATCC, Manassas, VA) and maintained as in Dulbecco's modified Eagle medium (Invitrogen, Gibco Cell Culture Products, Carlsbad, CA, USA) with $100IU/ml$ penicillin (Roger, Barcelona, Spain), $50\mu g/ml$ gentamicin (Braum Medical, Jaén, Spain), $2.5\mu g/ml$ anfotericin B (Sigma, St Louis, MO, USA), 1% Glutamine (Sigma, St Louis, MO, USA), 2% HEPES (Sigma, St Louis, MO, USA) and supplemented with 10% fetal bovine serum (FCS) (Gibco, Paisley, UK). MG-63 osteoblast-like cells were seeded on the textured titanium groups. Cultures were kept at $37°C$ in a humidified atmosphere of 95% air and 5% CO_2. The cells were detached from the culture flask with a solution of 0.05% trypsin (Sigma, St Louis, MO, USA) and 0.02% ethylene diamine tetra-acetic acid (EDTA) (Sigma, St Louis, MO, USA), and were washed and suspended in complete culture medium with 10% FCS. The cells obtained were inoculated for tests onto samples at $2x105cell/ml$ in a $24 - well$ plate (Falcon, Becton Dickinson Labware, NJ, USA) in the ratio of $2ml/well$, in which were deposited previously titanium disks. The plates were incubated to $37 \circ C$ in CO_2 (5%) atmosphere. Assay tests were performed at 180 minutes, 24, 48 and 72 hours for each surface. Cell cultures were repeated four times for each surface and time period. At the end of the culture time, disks were recovered and cleaned with medium solution. Then, cells were detached from the disks with a solution of 0.05% trypsin (Sigma, St Louis, MO, USA) and 0.02% ethylene diamine tetra-acetic acid (EDTA) (Sigma, St Louis, MO, USA) and were washed and suspended in complete culture medium with 10% FCS. The number of adhered cells was determined with a counter cytometer (Ortho Diagnostic System, Raritan, Il, USA). Number of cells was quantified per ml. One additional sample per surface treatment and time was prepared, following the protocol mentioned above for titanium surfaces, in order to evaluate the cell morphology. After the incubation period, media were removed and specimens were fixed with 4% glutaraldehyde in PBS (ph 7.2) for 20 minutes. After dehydration in graded alcohols, samples were inmersed in hexametildisilazane for 10 minutes, air dried then sputtered-coated with gold palladium. Finally, ther surface of the specimens was examinated by SEM.

Statistical Analysis of Cell Culture Studies: Statistical analysis of the data obtained from the cell culture was performed using one-way analysis of variance (ANOVA). The factor of analyisis was the surface treatment and the dependent variables were roughness parameters, wetting or cell adhesion and proliferation. Tukey's test was used to check the significance of differences between pairs of means. All statistical tests were run at 5% significance level ($p < 0.05$). The tests were applied to data of those parameters determining for the discussion.

4.3 Results and Discussion

This section of the chapter is divided in two different parts, i.e. one part describes the results obtained from the study of the silicon surfaces and the other one collects the results and discussion derived from the analysis of titanium surfaces.

4.3.1 Results for Modified Silicon Surfaces

Surface Characterization

Surface parameters are compiled in Table 4.1. It is important to note that all H-surfaces were R1 because no roughness alterations were made on them. Moreover, R1 was also considered H0

Table 4.1: Surface topographic values, water contact angles and cellular proliferation data after 21 days for each surface.

	R1-H0	R2	R3	R4	H1	H2	H3	H4
$minimum(nm)$	-2.60	-10.07	-27.96	-72.60	-2.60	-2.60	-2.6	-2.60
$maximum(nm)$	8.32	17.69	29.92	84.80	8.32	8.32	8.32	8.32
$R_a(nm)$	0.33	2.04	5.70	16.60	0.33	0.33	0.33	0.33
$R_q(nm)$	0.61	2.58	7.13	20.70	0.61	0.61	0.33	0.33
r	1.0024	1.0271	1.1340	1.3906	1.0024	1.0024	1.0024	1.0024
D_f	2.22	2.33	2.48	2.53	2.22	2.22	2.22	2.22
$\theta_{app}(^\circ)$	22°	15°	10°	7°	$16^\circ \pm 2$	$21^\circ \pm 2$	$76^\circ \pm 2$	$95^\circ \pm 2$
$Meancells/ml$	2000	6000	10000	10500	4500	10000	22000	27000

Note that all topographic values for H1-H4 are the same to that for R1 since surface modification in H1-H4 do not include topographic changes. R_a: arithmetic average roughness; R_q: root mean squared roughness; r: roughness surface ratio; θ: static water contact angle.

since R1 was not methylated.

From the observation of the AFM topographies captured for rough silica surfaces obtained by different etching time, as Fig. 4.1 shows, it is possible to conclude that $NaOH$ solutions are able to change surface topography for silica surfaces. Even more, these topographies suggests that surface roughness increases with etching time.

The values of the roughness parameters obtained from the analysis of the surface topographies

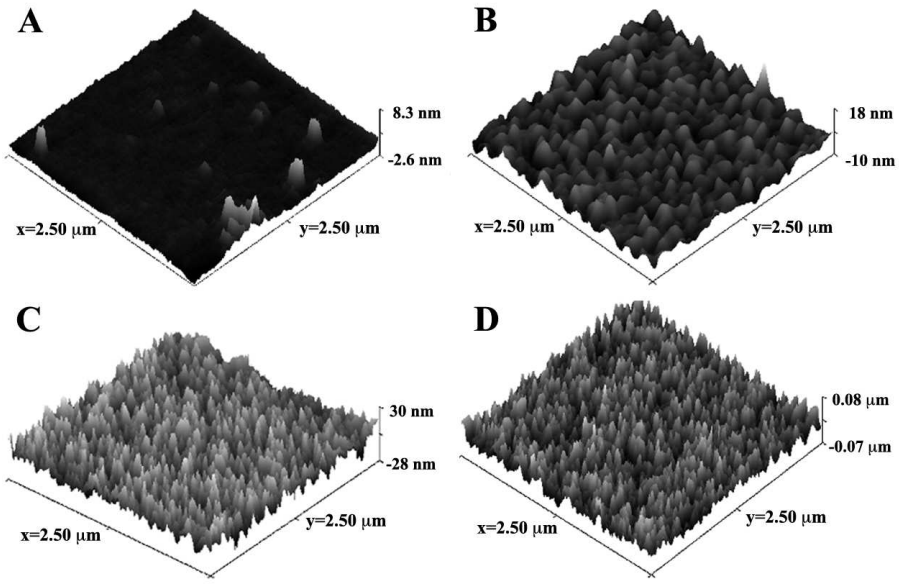

Figure 4.1: *AFM images of topography variations. A: R1, etching time=0 min. B: R2, etching time=22 min. C: R3, etching time=60 min. D: R4, etching time=165 min.*

of rough silicon surfaces support the increasing of surface roughness with etching time. So, the

values of R_a (ranging from 0.33 to 16.6 nm) and R_q (0.61 to 20.70nm) increased with etching time, confirming that the $NaOH$ solution was able to alter the silicon surface topography. The values for r (from 1.00 to 1.39) and fractal dimension (from 2.22 to 2.53) also increased with etching time. For etching times greater than 60 min, all values tended to stabilize, especially r and fractal dimension (Fig. 4.2).

With regard to contact angles, a change from 7 to 95° was observed. For R-surfaces, greater surface nanoroughness corresponded to lower water-contact angles. This behavior is in concordance with Wenzel equation (Eq. 1.27), but similar results, about the effect of nanoroughness on contact angle measurements of hydrophilic surfaces, have been recently reported by different experimental and theoretical studies [296–298]. For H surfaces, water-contact angles increased as the DDS concentration in the methylation solution increased, in an ascending sigmoidal curve (Fig. 4.3), confirming that the surface methylation took place and exerted an effect on surface wettability.

Cell Proliferation

The arithmetic mean from the proliferation study for all surfaces are shown in Table 4.1. Osteoblast-like cell proliferation on silicon surfaces with different wettability (water-contact angles ranging from $< 7°$ to 95°) showed an increasing trend both for methylated and topographically altered surfaces.

A sigmoidal relationship was observed between cells released from methylated surfaces and the methylation agent (DDS) concentration (Fig. 4.3). The same type of correlation was found for the dependency of the surface water contact angle on the DDS concentration. The high similarity between the two curves suggests a strong correlation between the number of adhering cells and the water-contact angle. In fact, a linear relation was found when plotting cells versus θ, giving a linear correlation coefficient very close to unity (R=0.98775).

An analysis of the correlation between surface roughness at a nanometer scale (R_a) and cell proliferation indicates that the number of cells rises with R_a, especially between 0 and 6 nm (Fig.

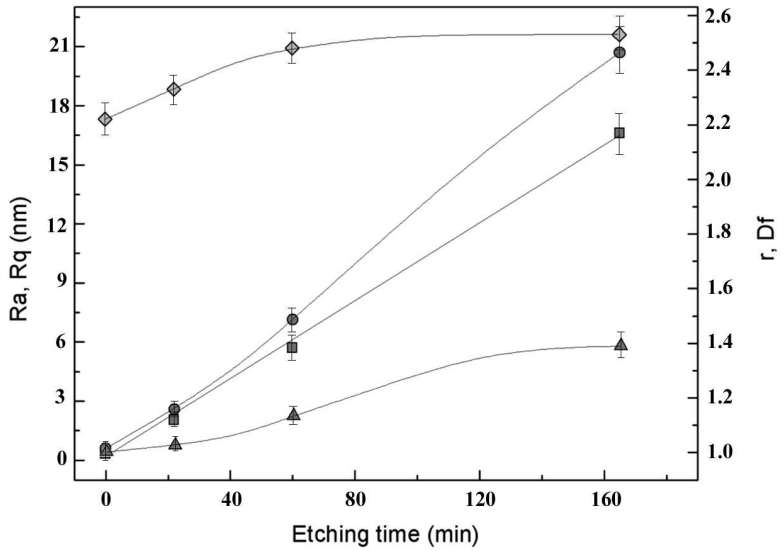

Figure 4.2: Relationship between roughness parameters vs etching time. R_a: squares; R_q: circles; r: triangles; D_f: diamonds.

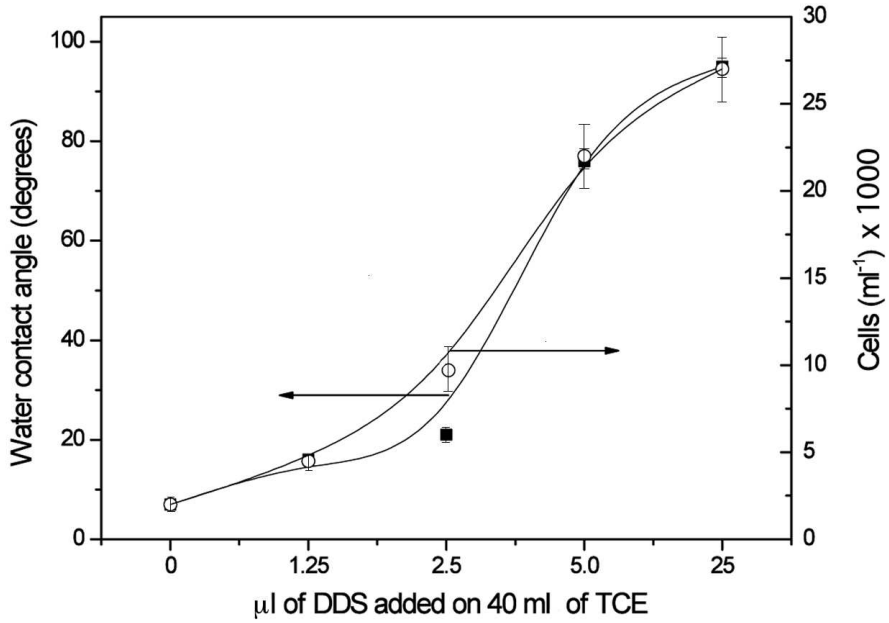

Figure 4.3: Water contact angle of methylated surfaces (squares) and number of cells released from the samples (circles) as a function of the DDS concentration in the TCE solution.

4.4). Similarly, R_q and r give a saturation value with regard to cell proliferation. However, the structural complexity, characterized by the fractal dimension, behaves in a different way (Fig. 4.5). There is no plateau in this curve, showing that cell proliferation increases with the fractal dimension. Initially, this increase was strong, but the cell proliferation appears to have restrained its growth above a certain fractal dimension value.

Cell Ultrastructural

Cultures on surfaces of low methylation presented a clear trend towards cell aggregation and coaggregation: the higher the surface hydrophilicity, the greater the surface cell concentration, including some layers of overlapped cells (Fig. 4.6 A). By contrast, the surface methylation promoted higher spreading and random distribution as well as the formation of cytoplasmatic prolongations, which increased in number and also in complexity as the water-contact angle increased. The primary prolongations usually branched into numerous secondary filaments, which often showed thicker zones resembling knots. In addition, the number of secretal-like vesicles on the cell membrane significantly augmented with the surface methylation (Fig. 4.6 B). On the other hand, cultures on rougher surfaces showed broad spreading, random distribution and dispersion, and a more cubed shape with dendritic extensions (Fig. 4.7 A). Cells seemed to grow in a confluent way, showing a flat shape with a clear trend to form groups on smoother surfaces. In addition, a great number of long and small-diameter cytoplasmatic prolongations appeared as roughness and structural complexity of the surface augment (Fig. 4.7 B).

Immunophenotype Characterization

Flow cytometric analysis confirmed immunophenotype of basal MG-63 cultures. Marker-expression analysis showed strong positivity for HLA-ABC (Fig. 4.8 A) and vimentin, as positive controls.

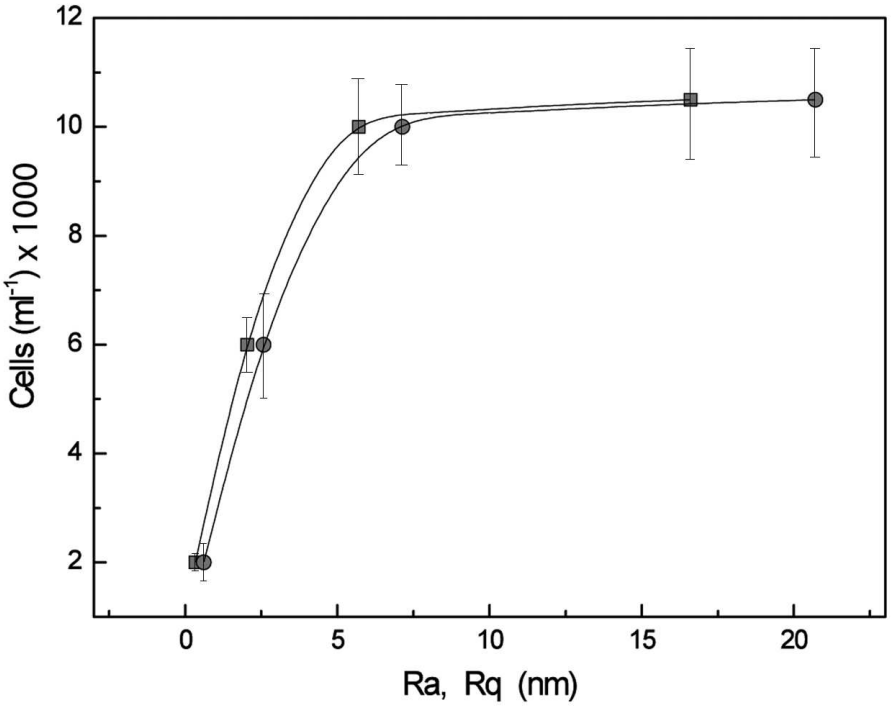

Figure 4.4: Relationship between the amount of cells released from the samples and surface roughness described by statistical roughness parameters: R_a (squares) and R_q (circles).

Expression of CD14 and CD45 were negative (Fig. 4.8 B). CD10 and CD56 were strongly expressed (Fig. 4.8 C), while actin was negatively expressed and caldesmon, osteocalcin and Ki67 were weakly expressed.

After culturing on modified surfaces, HLA-ABC and vimentin expression were strong, while CD14 and CD45 were negatively expressed in all cells cultures. CD10 and CD56 were less expressed on highly methylated or rougher surfaces than on less methylated or smoother ones. Actin was more expressed in cells cultured on methylated surfaces, while caldesmon was weakly expressed in all cell cultures. Osteocalcin expression was positive for all samples but higher on methylated ones. Expression of Ki-67 was higher on hydrophobic surfaces, registering a cell-proliferation index of 35%.

Immunophenotype characterization of MG-63 basal culture and after culturing on modified silicon surfaces is shown in Table 4.2.

4.3.2 Discussion for Modified Silicon Surfaces

Although the main purpose of this chapter is studying the relationship between cell behavior and physico-chemical surface properties, i.e. roughness and wettability, on modified silica surfaces, it is worth paying attention to the relationship between nanoroughness and wettability. The fact is that nanoroughness affects wettability of etched silica surface decreasing contact angle as etching time, i.e. nanoroughness, also increases (see Fig. 4.2 and Fig. 4.3). This behavior corresponds to the clasical one and it can be explained through the classical Young, Wenzel and Cassie-Baxter equations (see Chapter 1) which were described in previous chapters. These equations, which describe the contact angle exhibited (θ_{app}) by any solid surface when is wetted by any liquid in

Table 4.2: Immunophenotype characterization of MG-63 basal culture compared with immunocytochemical study 21 days after culturing on modified silicon dioxide surfaces (the staining intensity was estimated as follows: –: negative; +/–: weak; +: moderate; ++: strong).

Markers	Basal Level Expression	H4	R1-H0	R4
$HLA-ABC$	++	++	++	++
$Vimentin$	++	++	++	++
$CD14/CD45$	–	–	–	–
$CD10$	++	–	+	+/–
$CD56$	++	–	+	–
$Actin$	–	+	–	–
$Caldesmon$	+	+	+	+
$Osteocalcin$	+	++	+	+
$Ki67$	+	++	+/–	+

terms of the surface tensions (γ_{lv}, γ_{sv}, γ_{sl}), surface area ratio (r) and the proportion of surface area effectively wetted (f), are not depedent of the drop size and shape because surface tensions

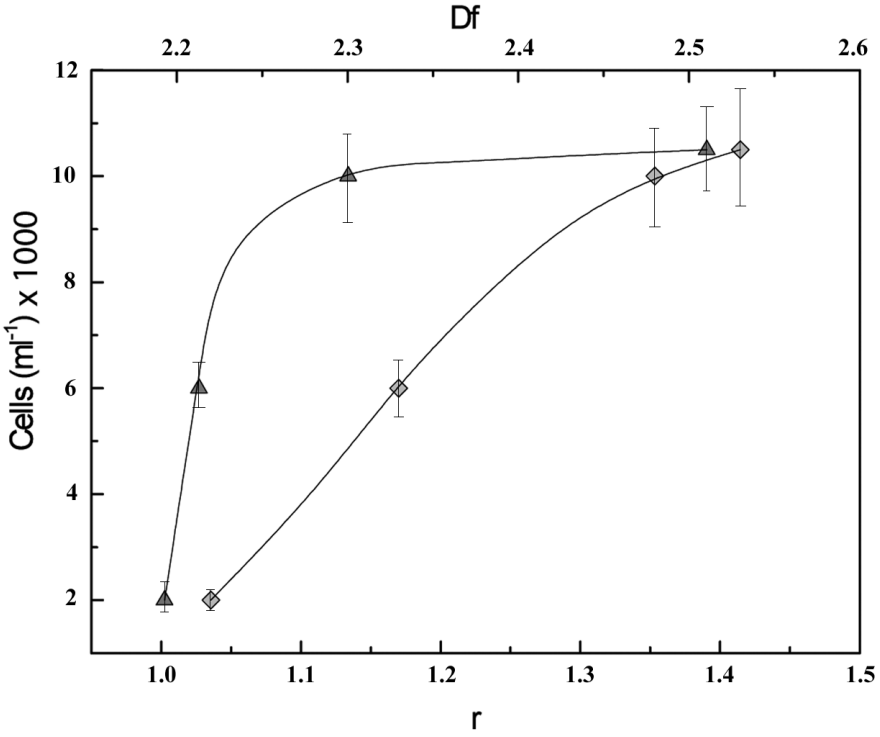

Figure 4.5: Relationship between the amount of cells released from the samples and surface roughness described by non-statistical roughness parameters: r (triangles) and D_f (diamonds).

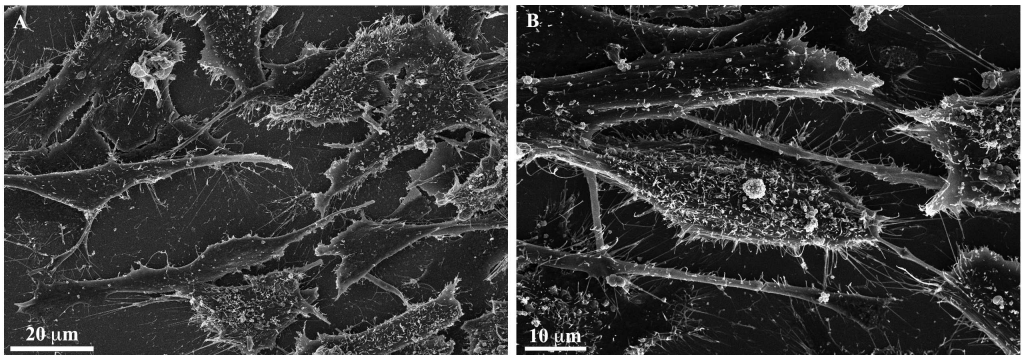

Figure 4.6: **A**: Culture on lower methylated silicon wafers (hydrophilic) showing a clear tendency to cellular aggregation and coaggregation (SEM 2,870X). **B**: Secretal-like vesicles on the cell membrane as well as numerous cytoplasmatic prolongations in highly methylated silicon surface (hydrophobic) (SEM 4,270X).

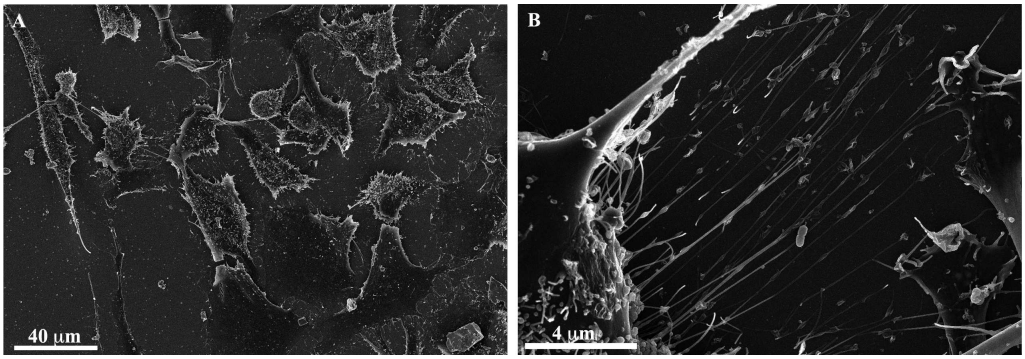

Figure 4.7: **A**: Osteoblast culture on a highly rough surface ($R_a = 16.6nm$) showing a high spreading, random distribution and dispersion (SEM 1,440X). **B**: Great number of long and low diameters cytoplasmatic prolongations observed in rougher surface with high structural complexity ($D_f = 2.53$) (SEM 9,530X).

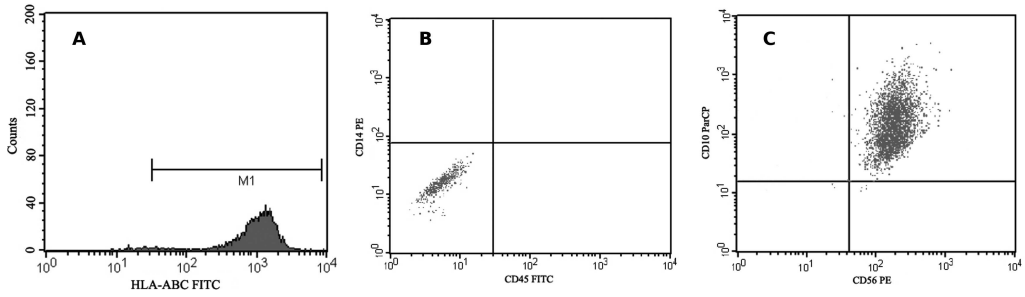

Figure 4.8: Antigenic expression of MG-63 determined by flow cytometry. **A**: Positive expression of HLA-ABC. **B**: Negative expression of CD14 and CD45. **C**: Positive expression of CD10 and CD56.

γ_{ij} as well as r and f do not depend of them. This fact involves that these equations predict that for hydrophobic homogeneous surfaces ($\theta > 90°$) θ_{app} increases as roughness increases and it decreases if the solid surface is hydrophilic ($\theta < 90°$).

However, the supposition of that θ_{app} is independent of the size and shape of the drop is not always valid. As Gao and McCarthy shown [299], the contact angle behavior is determined by interactions of the liquid and the solid at the three-phase contact line alone and that the interfacial area within the contact perimeter is irrelevant. Similar results have been observed on the contact angle of microdrops and nanodrops deposited on smooth surfaces (hydrophobic or hydrophilic) [297, 298]. As Gao and McCarthy ensured [299], Wenzel and Cassie-Baxter equations are valid only if the structure of the contact area reflects the ground state energies of contact lines and the transition states between them. So, the wetting behavior of a nanostructured surface is far from being completely understood because of the complex morphology and interactions that lead to variations of surface energy that could affect to surface wettability and, as some researchers have shown, to many biological aspects important to cell response such as fibronectin adsorption [300, 301].

Topographical features on material surfaces are important for cell and tissue response to biomaterials [252]. Micro-rough surfaces may stimulate high bone contact to material by promoting the production of local osteogenic factors as well as the expression of differentiation markers [248]. However, the role played by nanoroughness on cell response has not been unambiguously defined yet [257]. Our results in terms of R_a, R_q and r clearly demonstrate that nanoroughness played a major role in the cell proliferation on silicon surfaces for etching times lower than 60 min ($R_a : 0.33-5.70$; $R_q : 0.61-7.13$; $r : 1.0024-1.134$); however, for etching times greater than 60 min, cell proliferation appeared to be more controlled by the fractal dimension (structural complexity). The observed plateau in the proliferation study was similar to that reported by other studies [302]. Therefore, when nanoroughness reaches a high value, fractal dimension affects cell proliferation more than R_a, R_q or r values. In our study, Ki67 expression levels confirmed these observations. In contrast, Cai et al. [303] described no significant effects on cell proliferation over different nanoroughnesses.

Similarly, our study demonstrates that the fractal dimension determines cell spreading, morphology and dispersion on the surface for etching times greater than 60 min. In general, morphology on rougher silicon surfaces was similar to that observed on other rough surfaces achieved by other techniques [252]. In this sense, the expression of CD56 was higher on smoother surfaces, as in basal cultures. The higher expression on smoother surfaces may imply that cells needed to develop complex intercellular connections in order to maintain overall stability of the culture. In rougher surfaces, cells might be able to attach directly to the surface, without having to develop these intercellular networks. Additionally, the discrete increase in the expression of osteocalcin together lower expression of CD10, as discussed below, and higher Ki67 reflected a discrete immunophenotype improvement when increasing roughness. Our results in terms of immunophenotype variations confirmed previous observations by other authors both at the nano- [304] and micrometer scale [305].

Ours results also suggest that the fractal dimension of the surface plays a main role in cell morphology, both in terms of irregularity and complexity of the cell shape, as in density and length of filopodial extensions, which agrees with previous observations [306]. Fractal dimension translates directly to a larger surface area and, therefore, an increase in possible anchorage points. To clarify the importance of the fractal dimension, we should mention that conventional roughness parameters are scale dependent [307], while the fractal dimension provides a scale-independent statistical measure of the structural complexity of a surface [82]. Therefore, it is more precise when describing surface topography. As we have noted, fractal dimension might be more helpful than conventional roughness parameters for explaining the mechanisms that take place at the biomaterial surface

in contact with the surrounding biological tissues. Additionally, etched surfaces have long been recognized as fractals that enhance osseointegration [308]. Moreover, $NaOH$ treatment catalyzes the production of nanostructures outward from the surface and creates a gel-like layer over the material, allowing hydroxyapatite deposition [309]. Mendonza et al. [310] confirmed that the kinetics of HA formation is significantly accelerated by the presence of the nanostructure associated with the NaOH treatment. This behavior has also been reported with other metals such as zirconium, aluminum and titanium [311, 312].

Among the importance of nanoroughness in the cell-surface interaction, our study clearly shows a positive correlation between hydrophobicity and osteoblast-like behavior in terms of proliferation, ultrastructural morphology and immunophenotype, unlike other reports [313]. To explain this behavior it is advisable to remind the dependency existing between protein adsorption and wettability [314]. According to our results, an initial deposition of diverse proteins dissolved in the incubation medium takes place, being this deposition enhanced when the hydrophobicity of the surface increases. This is fully plausible, since protein adsorption is generally favored by hydrophobic interactions, defined as a spontaneous dehydration and subsequent approximation and contact of non-polar components in an aqueous environment, between the surface and these macromolecules. In fact, the hydrophobic interaction is one of the most important contributions that controls protein adsorption [315]. It should be noted that electrostatic interactions among the charges existing in the protein molecule and the sorbent surface also participate in the adsorption process [245]. However, if surfaces are not hydrophilic and the ionic strength is moderate or high (as that existing in our culture media), the electrostatic interactions (although they participate) are not as relevant as the attractive hydrophobic interactions. Hydrophobic interaction is characterized by a large entropy increase and a relatively small enthalpy effect. In protein adsorption, this entropic increase is also (partly) related to changes in the structure of the protein molecule. This is why the hydrophobic interaction is usually higher for soft and big proteins and it is lower for small a rigid ones [315]. For example, fibrinogen ($MW = 340kD$) interacts with a hydrophobic surface stronger that albumin ($MW = 66kD$) [280]. Moreover, albumin is, by far, the major protein component of the serum and, thus, it is more than likely that covered most of our modified surfaces at the beginning of the cell incubation. However, since it does not promote cell adhesion [264], its displacement by other adhesive proteins is needed for adhering cells to the surface material, as has been reported [280]. Therefore, in our experiments and, taking into account the results shown in Fig. 4.3, the albumin adsorbed during the early phase of osteoblast incubation has had to be significantly displaced by cell adhesive serum proteins that appear to show a higher affinity for absorbing onto hydrophobic materials due to their bigger sizes. By contrast, Arima and Iwata [264] found a decreasing number of adherent cells when the contact angle of different surfaces increased. In very short incubation times, like in the Arima and Iwata study, the displacement described above cannot effectively appear. However, in longer incubation times, the cell adhesion also augments with the hydrophobicity of the surface, as shown experimentally in this paper. Nevertheless, it should be noted that this clear correlation might disappear when working with extremely hydrophobic surfaces, where attractive hydrophobic interactions between the albumin and the surface may be highly intense and, consequently, the displacement may hardly occur [265]. Thus, our correlation between hydrophobicity and cell behavior could be explained based on the role played by the hydrophobic forces in the adsorption and displacement of serum proteins. Other studies on biomaterials are consistent with these arguments [316].

Moreover, modifying wettability and surface charge, closely related between them, protein adsorption and osteoblast proliferation and differentiation could be modulated [317]. Among that, changes in electrostatic surface charge do not modify the surface volume, like in the NaOH etching process, nor terminal chemical groups, like in the methylation process. Additionally, it has been

demonstrated a significant influence of surface charge on the acceleration and deceleration of bone like crystal growth [245].

In our study, enhanced cell activity was clearly manifested by the MG-63 adhering to highly methylated silicon surfaces. Therefore, our results may indicate that the methylation of oxidized silicon surfaces is a simple chemical treatment that promotes osteoblast-like behavior. Additionally, cell differentiation have been demonstrated by our observations of secretal-like vesicles, that agrees previous studies [310]. Moreover, immunophenotype analysis confirmed this hypothesis. Thus, there was increased actin expression in H4, considering either R1-H0 or basal MG-63 cultures as controls. This observation demonstrates better cytoskeletal organization despite the non-correspondence in caldesmon expression. It is important to mention the observed variations in CD10 expression. The lower expression of CD10 on highly methylated surfaces may indicate that cells cultured on these surfaces have a greater likelihood of cell modulation from the action of various protein mediators [318]. In this context, it follows that, in order to achieve and maintain a higher degree of differentiation in MG-63 cells, a greater hormonal regulation would be required. In addition, the higher osteocalcin expression in H4 supports osteoblast immunophenotype differentiation. As on rougher surfaces, CD56 expression was negative on highly methylated surfaces.

Finally, it should be mentioned that wetting of a surface by a liquid is significantly affected by its surface roughness [258]. In our study, the water contact angle was increasing when increased the surface nanoroughness. This could be due to the formation of $HSi(OH)_3$ clusters and $Si-H$ bonds on the surface and vigorous hydrogen bubbles during the etching process that act blocking the surface etching process on determined areas, producing local changes on the three-phase contact line and pinning defects (Fig. 4.1) [319, 320]. Recently, different studies have shown that the pinning of three-phase contact line can be responsible of wetting transition from hydrophilic to lower hydrophilic and even hydrophobic behavior on rough hydrophilic surfaces, since each defect pins the contact line individually [321], as we have observed. Furthermore, some air bubbles can be trapped in the surface. So, the wetting regime which governs this wetting phenomena is not Wenzel's regime, where liquid is directly in contact with the solid rough surface [191], but an air-water contact angle hybrid, where air bubbles and oxidized silicon regions are found. Despite the above, in the present study, more significant changes have been detected in osteoblast behavior, regarding proliferation, ultrastructural and immunophenotype analyses, when contact angles changed by altering external functional layer than increasing nanoroughness.

4.3.3 Results for Modified Titanium Surfaces

Topography

Roughness

In Fig. 4.9, AFM pictures of titanium disks belonging to the four groups (see Section 4.2.1) are displayed keeping the same scale and scan size. The roughness parameters of the textured titanium surfaces are compiled in Table 4.3. According to the amplitude parameters (R_p, R_v, R_a and R_{max}), the coarsest surfaces were the blasted ones with the largest particles ($beTi$), although they were etched later (see Fig. 4.9 (d)). In decreasing order of any amplitude parameter, the $beTi$ surfaces were followed by bTi, eTi and pTi (see Fig. 4.9 (a)). Otherwise, from the statistical parameters, the positive biased kurtosis ($R_{ku>}0$) and the negative skewness ($R_{sk} < 0$) found on the eTi samples predict a fluctuating morphology (see Fig. 4.9 (b)) with high density of valleys (i.e. microporosity), whereas sandblasting seems to produce spiky and coarse morphologies with negative biased kurtosis and positive skewness (see Fig. 4.9 (c) and (d)). This is also illustrated in Fig. 4.10 with the topography profiles of each sample. The surface area ratio (see Table 4.4)

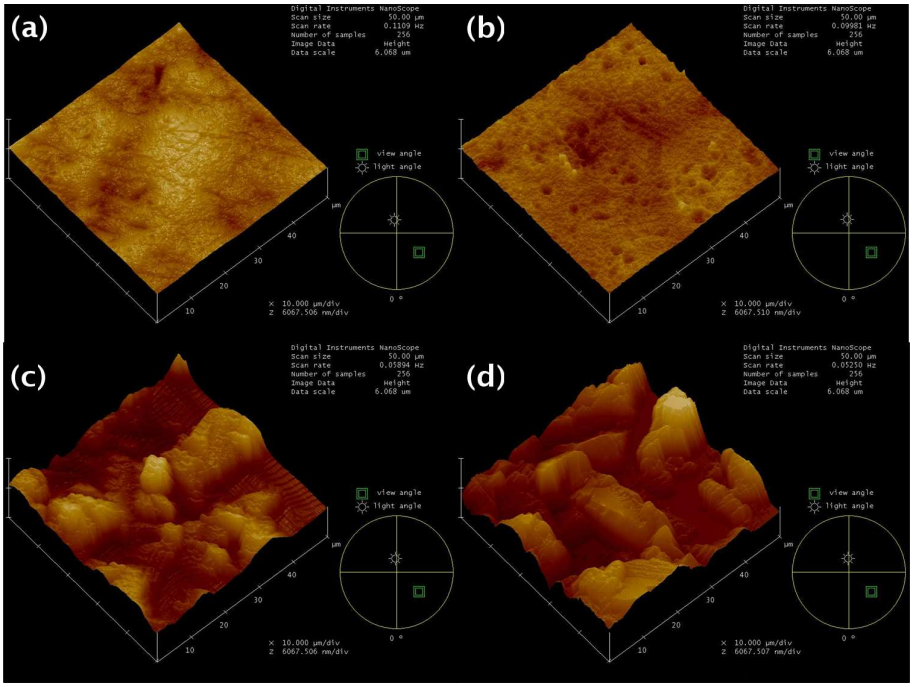

Figure 4.9: AFM pictures (256x256 points) of the textured titanium surfaces: pTi (a); eTi (b); bTi (c); $beTi$ (d). The scansize area was fixed to $50x50\mu m$.

just softened the trend of amplitude parameters since surface area is a differential parameter which takes into account variations in planar and perpendicular directions.

As expected, the greatest values of available surface area were found in the $beTi$ samples and the lowest ones in the pTi samples. However, eTi and bTi surfaces exhibited similar values of surface area. The highly fluctuating morphologies induced by etching (Fig. 4.10) compensated the coarse morphologies blasted with the smallest particles (bTi).

Fractal dimension

The values of fractal dimension computed by box-counting method are presented in Table 4.3. All samples were recognized as fractal surfaces because the expression $\mathbf{N(d)} = \boldsymbol{\alpha}\mathbf{d}^{-\mathbf{D_f}}$ was fulfilled up to a limit box size, where fractal behaviour disappeared. No significant differences between pTi, bTi and $beTi$ groups were found, although this did not mean similar morphologies. However, eTi surfaces obtained the highest fractal dimension due to their highly fluctuant morphology (space-filling ability). In spite of common belief, a fractal surface may be less rough and have more space-filling irregularities, i.e. it occupies only certain regions of the embedding space but more compactly.

Morphology

Fig. 4.11 compiles the SEM micrographs of the four groups. These images qualitatively confirmed the results obtained from AFM topographies. The reference surface (pTi) showed a smooth

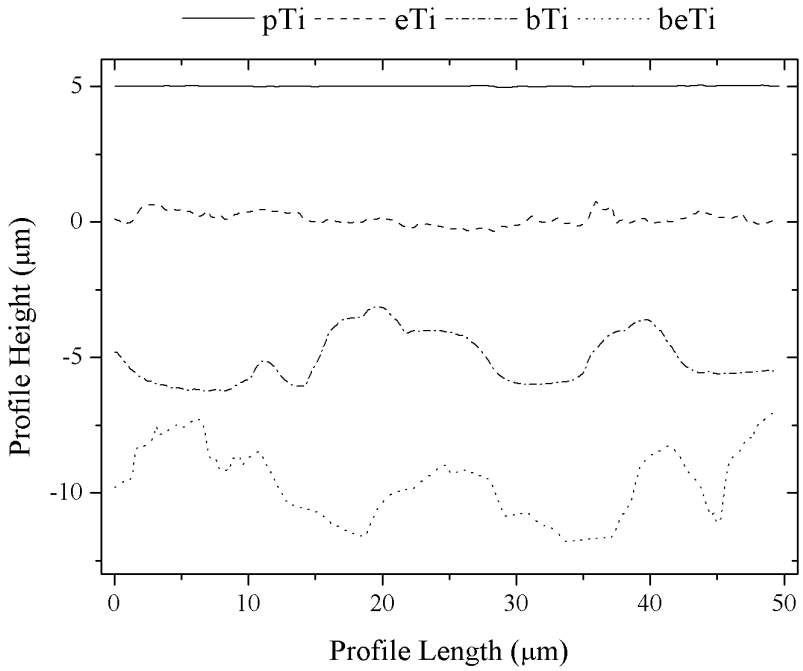

Figure 4.10: AFM profiles of the textured titanium surfaces: pTi, eTi, bTi and $beTi$. The profiles are intentionally shifted just for illustrative purposes. Sandblasting produced spiky and coarse morphologies, where the coarsest surfaces were the blasted ones with the largest particles ($beTi$) although they were etched later. However, the highly fluctuating morphologies (space-filling ability) of eTi surfaces explain that eTi and bTi surfaces exhibited similar values of surface area.

morphology without characteristic features (see Fig. 4.11 (a)). Instead, acid etching produced angular stepped morphologies with micropores from 1.5 to 2.5μm (see Fig. 4.11 (b)). This random structure manifested certain hierarchy with double scale roughness, i.e. a nano-rough texture. This indeed revealed the grain-structured titanium. Otherwise, blasting generated very irregular and coarse morphologies (see Fig. 4.11 (c)) with wide cavities ($10 - 50\mu m$ in diameter), as the size of shot alumina particles. Even it was observed the presence of alumina particles incrusted in the titanium surface, as reported [322]. These surface alterations might significantly hinder the cell adhesion. Finally, the $beTi$ surfaces exhibited a coarse morphology although less chaotic than the bTi samples and with micropores like the eTi samples (see Fig. 4.11 (d)).

Surface Chemical Composition

The EDX spectra of all samples (not shown) pointed out that surface chemistry of the textured surfaces was mostly based on titanium dioxide with a constant percentage of metallic titanium behind the protective oxide film (see the ratios of surface chemical species in Table 4.4). Silicon traces appeared on the pTi samples due to polishing with SiC papers; just as well the bTi samples contained aluminium traces due to the alumina particles trapped into them (as pointed out in the part of the results relative to the morphology). Indeed, the carbon from SiC was overshadowed in the spectra by the residual carbon originating from the reflecting film for SEM experiments. Unlike bTi samples, $beTi$ surfaces showed smaller aluminium amounts because the alumina particles were

Table 4.3: These two tables collect the value of the different roughness parameters, i.e. R_p, R_v and R_{max} (first table) and R_a, R_q, R_{sk}, R_{ku}, r and D_f, for the $cpTi$ surfaces obtained after they were submitted to the four different treatments, i.e. pTi, eTi, bTi and $beTi$. The different values for the parameters appear in this table as value $\pm$ standard deviation.

Surface	$R_p(\mu m)$	$R_v(\mu m)$	$R_{max}(\mu m)$
pTi	0.47 ± 0.21	-0.60 ± 0.19	2.35 ± 0.17
eTi	1.15 ± 0.23	-1.60 ± 0.25	3.12 ± 0.19
bTi	3.0 ± 0.9	-1.8 ± 0.7	5.7 ± 0.3
$beTi$	5.1 ± 1.6	-3.3 ± 0.9	8.2 ± 0.5

Surface	$R_a(nm)$	$R_q(nm)$	R_{sk}	R_{ku}	r	D_f
pTi	140 ± 17	149 ± 42	-0.07 ± 0.23	1.4 ± 0.7	1.02 ± 0.04	2.33 ± 0.09•
eTi	209 ± 19	268 ± 43	-0.36 ± 0.12	0.71 ± 0.19	1.10 ± 0.11	2.56 ± 0.11
bTi	861 ± 30	1022 ± 45	0.40 ± 0.19	-0.75 ± 0.25	1.15 ± 0.16	2.26 ± 0.13•
$beTi$	1370 ± 78	1639 ± 58	0.38 ± 0.11	-0.31 ± 0.21	1.33 ± 0.14	2.24 ± 0.12•

From the point of view of fractal surfaces, taking into account D_f mean values, pTi, bTi and $peTi$ surfaces were determined as statistically similar ($p > 0.05$) according to one-way ANOVA and Tukey's tests and, for this reason, they have been noted with (•) symbols.

mostly etched. Likewise, no SiC trace was found on eTi samples due to etching. Hence, whereas acid etching just recovered the original surface chemical composition of $cpTi$, blasting and polishing produced undesired surface doping.

Wettability

For rough surfaces, Wenzel equation predicts the wettability behavior of a surface according to it roughness evaluated through surface area ratio. This equation relates surface area ratio, i.e. roughness, with Young contact angle, i.e. wettability, by the following mathematica expression:

$$\cos\theta = r\cos\theta_Y \tag{4.1}$$

where θ is the apparent contact angle, r is the surface area ratio which quatifies the roughness of the surface, and θ_Y which is Young contact angle exhibited by a specific liquid, in the case pure water, on that surface, considered as an ideal one, in thermodinamical equilibrium situation.

The apparent contact angles of water drops on the textured titanium surfaces are compiled in Table 4.4. These values, measured once drop spreading was finished (1-2 seconds), corresponded to system metastates very close to advancing mode because the receding angles reported in literature are practically zero [164]. As expected for hydrophilic surfaces (see Eq. 4.1), greater surface area ratio corresponds to higher wettability (lower apparent contact angle). Hence, pTi surfaces showed the lowest wettability followed by eTi, bTi and $beTi$ surfaces. It is worth to highlight that this result can be misleading because the effect of roughness overshadows the influence of interfacial energetics. The influence of roughness on contact angle of homogeneous surfaces is a twofold issue. Phenomenologically, advancing contact angles often increase linearly with the concerning surface texture parameter [323], and just the opposite trend is observed for the receding angles. However, in addition to this effect, a drop (meniscus) in contact with a rough and chemically homogeneous

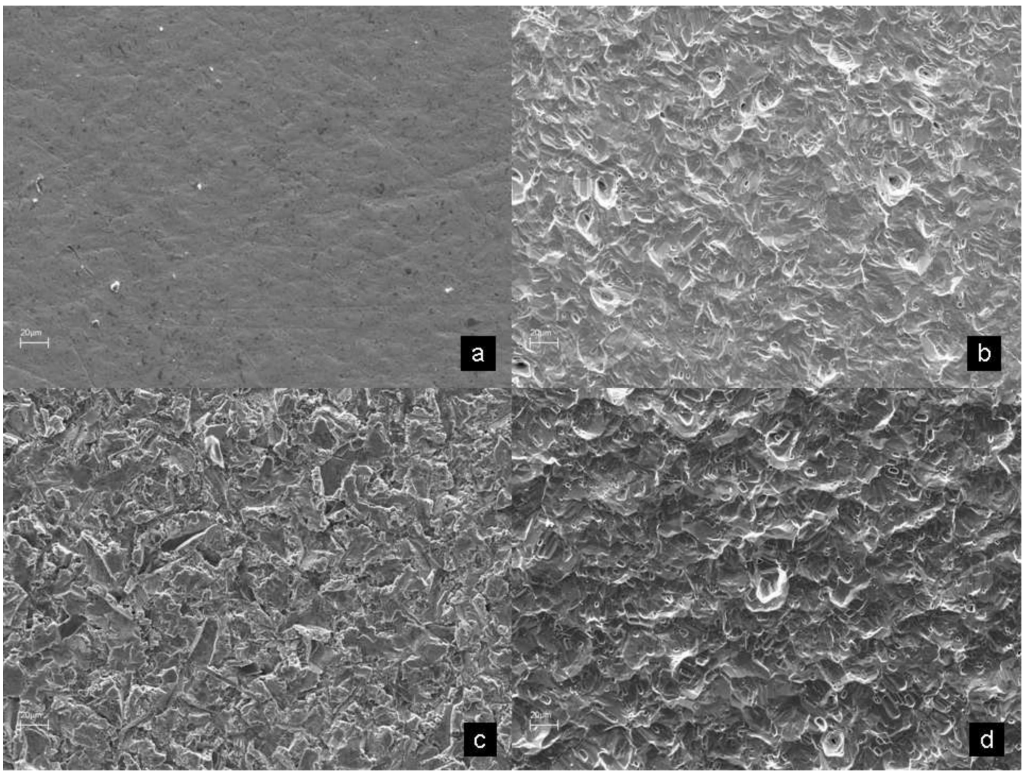

Figure 4.11: SEM images of evaluated surfaces: (a) pTi, (b) eTi, (c) bTi and (d) $beTi$ (original magnification x2000).

surface undergoes the second-order effect [166] predicted by the Wenzel law (Eq. 4.1). Although both effects can appear at once, latter effect typically dominates from intermediate values of contact angle hysteresis.

Table 4.4 collects the values of Young contact angle computed from Eq. 4.1 and the concerning values of surface area ratio (see Table 4.3) for each surface treatment. The use of Eq. 4.1 was justified by the larger drop volume ($2.5\mu l$) as regards the maximum roughness amplitude (see Table 4.3). The Young contact angles were statistically similar, except for pTi and bTi surfaces. The bTi samples exhibited the lowest value of Young contact angle due to the hydrophilic alumina content whereas the pTi samples were anomalously less hydrophilic due to the carbon excess originating from the SiC traces.

Cell Culture

Fig. 4.12 shows cell culture results. Fig. 4.13 (a) and (b) show representative cell morphologies. As expected for biocompatible surfaces, the cell adhesion rate increased on all treated titanium surfaces, although specific morphologies developed by each texturing affected differently the main events of cell adhesion. After 180 min and 24 hours, cell contact and attachment were more marked on bTi and $beTi$ surfaces than pTi and eTi surfaces. However, after 48 and 72 hours, cell spreading and proliferation were enhanced on eTi surfaces, followed by $beTi$, bTi and pTi surfaces as decreasing surface area. MG63 osteoblastic-like cells showed high adhesion on eTi surfaces, thanks to an enhanced filopodial anchorage at the nanoasperities and micropores. Otherwise, on

Table 4.4: In this table appears the Young's contact angle (θ_Y) and r and θ_{app} values which appear in Table 4.4 and the surface chemical species ratios obtained from the analysis of the EDX data for the different surface of the study, i.e. pTi, eTi, bTi and $beTi$. The values for the quantities considered appear in this table as $value \pm standarddeviation$.

Surface	$\theta(^\circ)$	Ti/TiO_2	Al/TiO_2	Si/TiO_2
pTi	$(63 \pm 6)^\circ$▼	0.14 ± 0.03	0.16 ± 0.03	0.34 ± 0.05
eTi	$(57 \pm 8)^\circ$	0.13 ± 0.03	0.00 ± 0.00	0.00 ± 0.00
bTi	$(50 \pm 10)^\circ$▼	0.14 ± 0.03	0.28 ± 0.04	0.00 ± 0.00
$beTi$	$(55 \pm 7)^\circ$	0.14 ± 0.03	0.16 ± 0.03	0.00 ± 0.00

From the point of view of wettability measured from Young contact angle, pTi and bTi surfaces were statistically dissimilar ($p < 0.05$) according to one-way ANOVA and Tukey's tests. In this sense, these kind of surface appeared marked with ▼ symbols.

the bTi samples, the cells were adherent but not confluent.

4.3.4 Discussion for Modified Titanium Surfaces

In culturing cells on biomaterial surfaces, surface free energy is an important parameter that guides the first events occurring at the biomaterial/biological interface, such as interaction of water

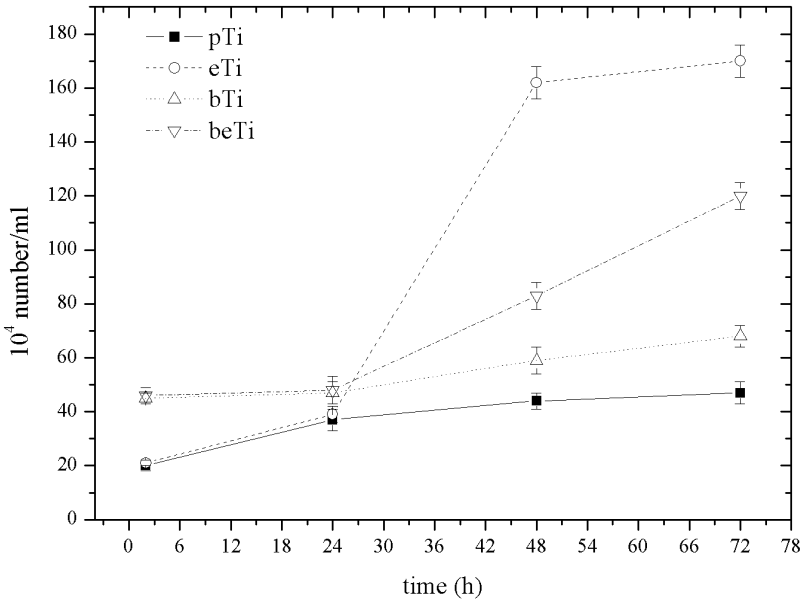

Figure 4.12: Cell adhesion and proliferation on engineered titanium surfaces as a function of time. Cell cultures were repeated four tiems for each kind of surface and time period.

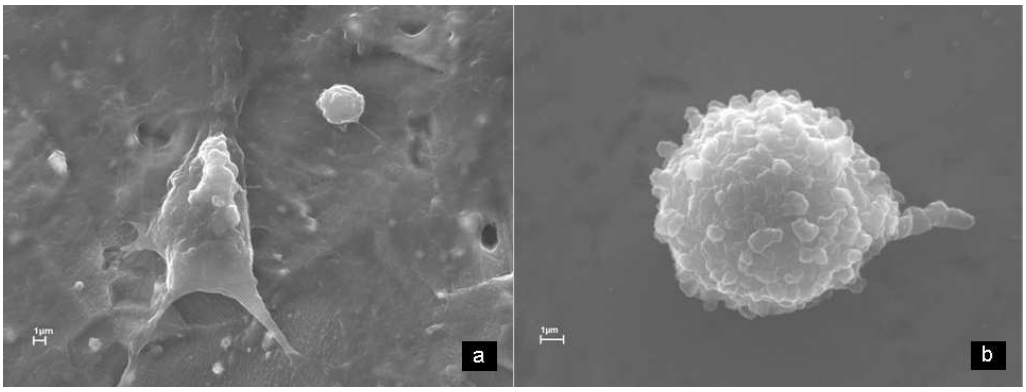

Figure 4.13: SEM micrographs of osteablast-like cells adhered to an acid-etched titanium surface (a) and to a polished titanium surface (b) after 72 h.

and proteins with biomaterial, and these events guide further response [256, 323]. Nevertheless, surface energy estimation from contact angle measurements is a hard task because biomaterial surfaces are always rough and/or heterogeneous. If surface roughness is the primary cause of hysteresis, i.e. $R_a \geq 0.1\mu m$ [324], the advancing contact angle is influenced more by the microscopic relief than by interfacial energetics. However, surface energy estimation just requires thermodynamically significant angles. Hence, for rough titanium-based surfaces, the Young contact angles computed by Eq. 4.1 from advancing contact angles can serve to detect relatively gross changes in surface energy.

The good cell response at long times on eTi samples, as regards the rest of textured groups, was explained by their particular morphology (the greatest fractal dimension and negative skewness) and surface chemical homogeneity (no traces). Chemically-etched surfaces have long been recognized as fractal, due to the stochastic character of wet etching. Particularly, the morphologies of eTi samples were angular and stepped due to the crystalline grain detachment from the amorphous structure of titanium. Moreover, at dimensions smaller than the grain structure of titanium, a secondary texture was visualized. Hence, eTi samples, even being less rough than bTi and $beTi$ groups, exhibited micro-porous and nano-rough texture. It is worth to mention that surface roughness in the range from $10nm$ to $10\mu m$ may influence the interface biology, since it is of the same order in size as cells and large biomolecules. Microporous surfaces enhance osteointegration of titanium implants, indicated by mechanical pull-out tests and histomorphometric analysis [325] or osteoblast spreading tests [308].

As far as biomaterial interactions with proteins are concerned, surface features on the nanometer scale are important. Changes in surface chemistry or roughness, of the same dimension as a protein will affect its adsorption characteristics. Instead, if the rough surface is treated as chemically homogeneous and the size of asperities is larger than the protein dimension, then roughness will simply add available surface area for adsorbing protein. This explains that beTi and bTi samples were more bioadhesive at early stages of cell attachment [164, 269, 326]. At late stages, the presence of alumina particles and the coarsely-blasted morphology, self-affine but uncomfortable for cell spreading, impaired the cell proliferation as expected [43]. Furthermore, sandblasting can also affect the corrosion resistance of titanium due to the residual surface stresses induced [322].

Fractal dimension arises as a more appropriate index of surface disorder [43, 327] rather than the amplitude roughness parameters. However, a single exponent is not enough for the complete description of fractal surfaces. Moreover, the partial information provided by fractal dimension

was refined by the values of kurtosis and skewness and confirmed by SEM pictures. Alternatively, lacunarity becomes a counterpart to the fractal dimension because it just describes the texture of a fractal surface [71]. Fractal surfaces having same fractal dimensions can look widely different because of having different lacunarity. This parameter is related to the prefactor $\boldsymbol{\alpha}$ of the expression $N(d) = \boldsymbol{\alpha} d^{-D_f}$.

HF acid etching is recommended for titanium-based dental implants rather than sandblasting based in the results of this study. As suggested in the literature, the HF treatment creates a micro- and nano-level topography that enhances adherent cells [328, 329]. Moreover, since surface characterization of biomaterials is crucial to understand the concerning biological events, the use of complementary topography analysis, like fractal analysis, in addition to statistical roughness description are highly recommended. Also, theories and experimental approaches related to wetting phenomena should be carefully employed.

4.4 Conclusions

4.4.1 Modified Silicon Surfaces

From the analysis of the results and dicussion obtained for modified silicon surfaces is possible to extract the following conclusions:

- Model silicon surfaces modified by simple chemical treatments enabled separate evaluations of the influence of surface physical parameters as roughness and wettability on cell-substrate interactions.
- Cell morphology, proliferation and differentiation clearly depend on these physical factors. All these properties are more affected by changes in surface chemistry than surfaces roughness, although surface nanoroughness also improves the MG-63 behavior.
- The surface nanoroughness also improves the MG-63 behavior, the fractal dimension being more precise for predicting it. This highlights the importance of using complementary surface-topography analyses in addition to a classical roughness description.

4.4.2 Modified Titanium Surfaces

In the same way, from the analysis of the results and discussion exposed for titanium surfaces, it is possible to conclude that:

- The presence of traces of silicon carbide and alumina found in the polished and blasted surfaces modified their surface energy, respectively. This effect seems to be determining on the failure of cell proliferation, rather than the morphology and roughness of each surface.
- Cell adhesion and proliferation on the textured titanium surfaces with similar surface chemistry (acid-etched and blasted-etched surfaces) were driven by topography features.
- Cell adhesion ($\leq 24h$) depended on the available surface area (more roughness, more cell adhesion).
- Cell proliferation ($\geq 48h$) was mediated by specific morphologies: highly fluctuating surfaces (greater fractal dimension) and punching surfaces (negative skewness). Unlike, for surfaces with similar fractal dimension and positive skewness, the cell growth basically depended on their surface area.

- Acid etching yielded angular stepped morphologies due to the crystalline grain detachment, with horizontal length scale close to the cell size ($\sim 10\mu m$).
- Blasting treatment generated pit-like surface features with high aspect ratios and chaotic morphologies. These physical surface modifications, aside from the small alumina doping, hindered the cell growth.

4.4.3 General Conclusions

Moreover, we conclude from the results of both types of modified surfaces, i.e. silicon and titanium surfaces, that:

- Both physical and chemical properties of a surface play a critical role on the cell response.
- The nanoroughness produced by surface etching has been revealed as a critical factor for the MG-63 behavior.
- The roughness characterization of surfaces employed in implantology field should be more precise and to considerer these surfaces as fractal ones. So, in this sense, the use of fractal parameters, such as fractal dimension, is recommended.

All these general findings may be useful for optimizing biomaterials

Summary and Conclusions

This thesis was mainly focused on the analysis of the role played by the surface roughness of structured biomaterial surfaces, from micro- to nano-scale topography, through a complete set of mathematical tools, from classic statistical to advanced ones. Acid etching of titanium surfaces was studied in detail because of its wide use in the field of implantology. Finally, osteoblast-like cells response was studied on modified silicon and engineered titanium surfaces in collaboration with odontological and medical research groups.

The main questions that this work addressed are: how should surface roughness be characterized and what mathematical tools should be used for it in the case of surfaces with biomedical applications? how is acid etching of titanium surfaces described through Minkowski functionals and scaling analysis? and, finally, how does surface roughness affect the osteoblast-like cell adhesion on modified silicon and engineered titanium surfaces?

This dissertation involves different aspects of surface physics related to the surface characterization, particularly the roughness characterization for the optimization of textured surfaces in biomaterial engineering. Thus, beyond the known statistical roughness, we have conducted a more complete characterization of the roughness of real surfaces.

First of all, we studied how the roughness factor (surface area ratio) measurement is altered by the topography acquisition and, particularly the role played by scan-size, topography resolution or triangular tessellation algorithms. Furthermore, from the analysis of a wide set of numerical surfaces simulated with a fractional Brownian noise, we studied how the roughness factor values are affected by waviness filtering due to the directionality effect on the addition of waviness and roughness in real surfaces. Thus, the main conclusions of this part of the thesis can be summarized as follows:

- In increasing order of loss of information, the parameters that affect the roughness factor are: the tessellation algorithms used to mesh the topography, the scan-size employed to acquire the topography, and the resolution of the topography (number of points collected by the topography). This order of importance of the parameters studied seems to be regardless of the instrument used to acquire the topography.

- Filtering processes used to isolate different surface features of a topography according to their wavelengths, specifically roughness and waviness, involve the loss of part of the surface topography information. This loss could lead to under/overestimate roughness parameters according to the direction followed to add the roughness to the waviness in the (pre-filtered) morphology. For any wavy rough surface, it is not possible to know in detail what roughening process governed its origin and evolution. Therefore, the superposition (addition) of waviness and roughness in the real surface could have happened in any direction. So, the experimental roughness factor disagrees to the actual, but experimentally inaccessible, value of roughness factor. Nevertheless, it is possible to find an estimate. This thesis proposes an alternative

based on the weighting of the surface area ratio for the raw topography data (considering waviness and roughness) by the surface associated to the waviness. Thereby, if we do not know the process that determined the surface morphology, our method reduces the error associated to the estimation of surface roughness by using the surface area ratio.

Secondly, we analyzed the morphology produced by HF acid etching on commercially pure titanium surfaces using integral geometry and stochastic analysis. Minkowski functionals (integral geometry tools) revealed information about the percolation threshold on acid-etched titanium surfaces and its change with etching time. On the other hand, stochastic analysis suggested that acid-etched surfaces of commercially pure titanium exhibit both intrinsic anomalous scaling and multiscaling regardless of etching time. Moreover, a crossover was also observed for etching times close to 3 min due to the "poisoning" of the acid-etched surface by titanium hydrides (TiH). This crossover was also found in the roughness factor for acid-etched titanium surfaces. These results points out to that a deeper characterization of surface roughness is suitable for those applications where nanoscale features play a crucial role in growth and proliferation of cells on implant surfaces. The main conclusions of this part of the thesis can be summarized as follows:

- From the integral geometry analysis we conclude that the use of Minkowski functionals is highly recommended. This set of mathematical tools allowed to classify the acid-etched of commercially pure titanium surfaces in terms of percolation networks. The etching time could be an optimizing parameter on the evolution of acid-etched titanium surfaces and, therefore, for the quality of these implant surfaces. The percolation threshold for acid-etched surfaces shown a maximum for etching times close to 3 min. Therefore, as a high percolation threshold points out to better fluid retention properties, biological fluids should penetrate better the rough exposed surface and consequently, the osteoblast-like cells response should be enhanced for acid-etched titanium when etching time is close to 3 min.

- Kinetic roughening of HF acid-etched commercially pure titanium surfaces, as growth process driven by anisotropic rules, obeyed rules of anomalous scaling. Surface evolution is mediated by surface chemistry and corrosion resistance of the surface due to the existence of a varying-thickness thin film of TiO_2. Also, regardless of etching time, acid-etched titanium surfaces exhibited both multiscaling and intrinsic anomalous scaling. Moreover, for etching times close to 3 min, the behavior of the surface changes drastically due to its poisoning. Scaling analysis might be helpful to explain the effect of surface features of implant topography on the cell growth and, to elucidate the complex mechanisms occurring at the implant surface in contact with the surrounding biological tissues. Thus, scaling analysis could serve as a link between biomaterial engineering and statistical physics. As a general recommendation, for acid etching of real surfaces, it is necessary to consider the time elapsed from the beginning of etching for identifying the roughening regime and if there is any transition between regimes.

- The maximum value of roughness factor of acid-etched titanium in terms of etching time may reveal a dynamic transition due to the competition between heterogeneous erosion and homogeneous normal-directed erosion. The transition between these two types of roughening processes might be modulated by both the oxidation state of the surface and the formation of etch-stop species just below it; poisoning due to the presence of TiO_2 and TiH on the surface. The acid concentration, the etching rate (produced by laminar or turbulent flow), the initial roughness and the grain orientation of the untreated titanium surface will also regulate at some extent the time for which the surface area of acid-etched surfaces is maximized. In terms of erosion and surface curvature, the roughness factor maximum is also interpreted as the crossover between two regimes: an initial regime where the surface is mainly composed

of peaks and the (normal-directed) etching promotes the sharpening of peaks (increasing surface area), although with decreasing heights each time, until a second regimen where the valleys dominate (further by grain detachment) whereas they are flattened by normal etching (decreasing surface area).

- This transition between roughening regimes is also observed with advancing/receding contact angle measurements and preliminary experiments of osteoblast-like cell adhesion on acid-etched titanium surfaces. Moreover, a similar behavior was also observed on acid-etched glass surfaces.

Finally, we conducted MG-63 osteoblast-cell cultures (adhesion, proliferation and morphology) on silicon (with different physical and chemical properties) and titanium surfaces (modified with different surface treatments). For silicon surfaces, the correlation between the wettability produced by methylation (on smooth surfaces) and nanoroughness (on unmethylated surfaces) produced by NaOH basic etching and the response of osteoblast-like cells was analyzed. It was possible to conclude that an increase of nanoroughness or water contact angle enhanced osteoblast behavior in terms of cell morphology, proliferation and immunophenotype. The effect caused by the methylation is more significant than the effect caused by the nanoroughness. For titanium surfaces, the effect of different texturization methods (blastering, acid etching and the combination of both) on cell adhesion and proliferation was studied. The different physicochemical treatments used to modify the surface properties of commercially pure titanium surfaces point out to that both surface chemistry and roughness affect the osteoblast-like cell response but, for surfaces with similar surface chemistry, cell adhesion and proliferation are mainly driven by roughness. From the characterization of the surface topographies in terms of fractal dimension, it was possible to assure that the surface structure generated by acid etching enhances cell adhesion and proliferation.

As nanoroughness induced by acid etching on titanium surfaces improves the cell adhesion and proliferation, surface roughness should be precisely characterized by using parameters such as fractal dimension and other tools described in this thesis.
approaches.

Resumen y Conclusiones

Esta tesis se ha centrado, principalmente, en el análisis del papel jugado por la rugosidad superficial de superficies texturizas de biomateriales, desde escala micro- a nanoscópica, mediante el uso de una extensa batería de herramientas matemáticas, desde las herramientas estadísiticas clásicas hasta las más avanzadas. Además, dado su amplio uso en el campo de la implantología, el grabado ácido de las superficies de titanio fue estudiado en detalle. Finalmente, en colaboración con grupos de investigación en medicina y odontología, se realizaron estudios sobre la respuesta celular de células osteoblásticas sobre superficies modificadas de silicio y titanio.

Las principales cuestiones que este trabajo respondió fueron: ¿cómo debe ser caracterizada la rugosidad superficial y qué herramientas matemáticas debemos emplear para ello en el caso de superficies con aplicaciones biomédicas? ¿cómo describen los funcionales de Minkowski y el análisis de escalado el grabado ácido de las superficies de titanio? y, por último, ¿cómo afecta la rugosidad superficial a la adhesión celular de osteoblastos sobre superficies modificadas de silicio y titanio.

Esta tesis aborda diferentes aspectos de la física de superficies relacionados con la caracterización superficial, particularmente, la caracterización de la rugosidad para la optimización de superficies texturizadas en ingeniería de materiales. Así, hemos realizado una caracterización completa de la rugosidad de superficies reales, más allá de la mera caracterización estadística.

En primer lugar, se estudió en qué modo se ven afectadas las medidas del factor de rugosidad (fracción de área superficial) por el método de adquisición de la topografía superficial y, en particular, el papel que juega el tamaño de la región escaneada, la resolución y el algoritmo de teselación triangular en la medida del factor de rugosidad. Además, a partir del análisis de un vasto conjunto de superficies simuladas numéricamente, mediante un algoritmo de movimiento Browniano fraccional, se estudió en qué modo se ven afectados los valores del factor de rugosidad por los procesos de filtrado de la ondulación superficial debido al efecto direccional de la adición de la ondulación y la rugosidad en superficies reales. Así, las principales conclusiones de esta parte de la tesis pueden resumirse del siguiente modo:

- En orden creciente de pérdida de información, los parámetros que afectan a la medida del factor de rugosidad son: el algoritmo de teselación utilizado par mallar la topografía, el tamaño de la región escaneada y la resolución de la topografía (el número de puntos recogidos en la topografía). El orden de importancia de los parámetros estudiados parece ser independiente del instrumento utilizado para adquirir la topografía.

- Los procesos de filtrado utilizados para aislar los rasgos característicos de la topografía de acuerdo con sus logitudes de onda, especialmente la rugosidad y la ondulación, implican la pérdida de parte de la información topográfica. Esta pérdida podría conducir la subestimación/sobrestimación de los parámetros de rugosidad dependiendo de cual haya sido la dirección seguida al añadir la rugosidad a la ondulación en la morfología prefiltrada. Dado que para cualquier superficie rugosa y ondulada, es imposible conocer en detalle qué proceso

de arrugado gobernó su origen y evolución, la superposición (adición) de la ondulación y la rugosidad en una superficie real podría suceder en cualquier dirección. Por tanto, el factor de rugosidad experimental difiere del valor real, pero experimentalmente innaccesible, del factor de rugosidad. Sin embargo, es posible encontrar un valor estimado. Esta tesis propone una alternativa basada en el promediado de los datos topográficos en bruto (incluyendo ondulación y rugosidad) por la fracción de área superficial asociada a la ondulación. De este modo, si desconocemos el proceso que determinó la morfología superficial, nuestro método reduce el error asociado a la estimación de la rugosidad superficial mediante el uso de la fracción de área superficial.

En segundo lugar, analizamos la morfología producida por el grabado con ácido fluorhídrico de superficies comercialmente puras de titanio usando geometría integral y análisis estocástico. Los funcionales de Minkowski (herramientas de geometría integral) revelaron información acerca del umbral de percolación para superficies de titanio grabadas con ácido y su dependencia con el tiempo de grabado. Por otro lado, el análisis estocástico sugirió que las superficies de titanio comercialmente puro grabadas con ácido presentan tanto escalado anómalo intrínseco como multiescalado independientemente del tiempo de grabado. Además, se observó un "crossover" para tiempos de grabado cercanos a los tres minutos debido al "envenenamiento" por hidruro de titanio de estas superficies. Este "crossover" también fue encontrado en el comportamiento del factor de rugosidad medido sobre superficies de titanio grabadas con ácido. Estos resultados apuntan a que es necesario un caracterización más profunda de la rugosidad superficial en aquellas aplicaciones para las que los rasgos superficiales de escala nanométrica jueguen un papel crucial, como es el caso del crecimiento y proliferación celular en las superficies de implantes. Las principales conclusiones de esta parte de la tesis pueden resumirse en:

- A partir del análisis mediante geometría integral concluimos que el uso de los funcionales de Minkowski es altamente recomendable. Este conjunto de herramientas matemáticas permitió clasificar el grabado ácido de superficies comercialmente puras de titanio en término de redes de percolación. El tiempo de grabado podría ser un parámetro válido para optimizar la evolución de las superficies de titanio grabadas con ácido y, por tanto, la calidad de implantes de este tipo de superficies. El umbral de percolación de las superficies grabadas con ácido muestra un máximo para un tiempo de grabado próximo a tres minutos. Por tanto, dado que valores altos del umbral de percolación suponen unas mejores propiedades en cuanto a la retención de fluidos, los fluidos biológicos podrán penetrar mejor en este tipo de superficies rugosas y, por consiguiente, la respuesta celular de osteoblastos debería mejorar para titanio grabado con ácido cuando el tiempo de grabado sea próximo a esos tres minutos.

- El arrugado cinético de superficies de titanio comercialmente puras mediante ácido fluorhídrico, como proceso de crecimiento dirigido por reglas anisótropas, sigue las leyes del escalado anómalo. La evolución superficial está regulada por la química superficial y la resistencia a la corrosión de la superficie debido a la existencia de una capa de espesor variable de dióxido de titanio. También, independientemente del tiempo de grabado, las superficies de titanio grabadas con ácido mostraron arrugado anómalo intrínseco y multiescalado. Además, para tiempos de grabado cercanos a los tres minutos, el comportamiento de la superficie cambió drásticamente debido a su envenenamiento. El análisis de escalado podría ser de ayuda cara a explicar el efecto que tienen los rasgos superficiales de un implante en el crecimiento celular y para esclarecer el complejo mecanismo que sucede en la superficie de un implante en contacto con tejidos biológicos circundantes. Así, el análisis de escalado podría servir como nexo entre la ingeniería de materiales y la física estadística. Como recomendación general, en caso de grabado ácido de superficies reales, es necesario considerar

el tiempo transcurrido desde el inicio del grabado para identificar el regimen de arrugado y si existe cualquier tipo de transición entre regímenes.

- El máximo del factor de rugosidad para superficies de titanio grabadas con ácido en función del tiempo de grabado puede revelar una transición dinámica y competitiva entre un proceso erosivo heterogéneo y uno homogéneo según la dirección normal a la superficie. La transición entre estos dos tipos de arrugado puede ser modulada tanto por el estado de oxidación de la superficie como por la formación de especies pasivantes en ella; "envenenamiento" de la superficie debido a la presencia de hidruros de titanio y dióxido de titanio sobre la superficie. La concentración de ácido, la velocidad de grabado (producido por flujo laminar o turbulento), la rugosidad inicial y la orientación de los granos para la superficie de titanio sin grabar también regularán el tiempo de grabado necesario para que el área supercial de la superficies grabadas con ácido alcance un máximo. En términos de erosión y curvatura superficial, el máximo del factor de rugosidad también se interpreta como una transición entre dos regímenes de grabado: un regimen inicial donde la superficie está formada principalmente por picos y en el que el grabado (según la dirección normal) promueve el afilado y la pérdida de altura de esos picos (aumento del área superficial), y un segundo régimen en el que dominan los valles (puede que por el despendimiento de algún grano) a la vez que son aplanados por el grabado ácido en la direción normal (disminuye el área superficial).

- Esta transición entre regímenes de grabado también fue observada en las medidas de los ángulos de contacto de avance y retroceso y en estudios preliminares de adhesión de osteoblastos en superficies de titanio grabadas con ácido. Además, un comportamiento similar al aquí descrito también fue observado en superficies de vidrio grabadas con ácido.

Por último, se llevaron a cabo cultivos celulares de osteoblastos del tipo MG63 (adhesión, proliferación y morfología) sobre superficies de silicio (con diferentes propiedades físicas y químicas) y titanio (modificadas mediante diferentes tratamientos superficiales). Para la superficies de silicio, se analizó la respuesta celular de los osteoblastos a los cambios de mojabilidad de la superficie (producidos por metilación), y a la nanorugosidad producida por el grabado básico de las superficies mediante hidróxido sódico. Se llegó a la conclusión de que un aumento tanto en la nanorugosidad superficial como en el ángulo de contacto que dicha superficie exhibe ante el agua mejora el comportamiento celular en términos de morfología, proliferación e inmunofenotipo. Los efectos causados por la metilación son más significativos que los producidos por la nanorugosidad. Para la superficies de titanio, se estudio el efecto de diferentes métodos de texturización ("blastering", grabado ácido y la combinación de ambos) sobre la adhesión y la proliferación celular. Los diferentes tratamientos fisicoquímicos usados para modificar las propiedades superficiales de las superficies de titanio comercialmente puro sugieren que tanto la química como la rugosidad superficial afectan a la respuesta celular aunque, para superficies con similar química superficial, la adhesión y proliferación celular dependen, pricipalmente, de la rugosidad de la superficie. La caracterización, mediante el cálculo de la dimensión fractal, de las superficies generadas por cada método permitió asegurar que las estructuras superficiales generadas por grabado ácido mejoran tanto la adhesión como la proliferación celular.

Dado que la nanorugosidad generada por el grabado ácido de las superficies de titanio mejora la adhesión y proliferación celular, es necesario que su caracterización se haga de un modo más preciso mediante parámetros tales como la dimensión fractal u otros descritos en esta tesis.

Todas estos hallazgos generales relacionados con el cultivo celular pueden ser de gran utilidad para optimizar tanto el diseño de biomateriales como el de las superficies de implantes. Nuestros resultados enfatizan la importancia de los estudios encaminados a esclarecer las relaciones entre el

comportamiento celular y las propieddades fisicoquímicas interfaciales y, también, con la necesidad de mejorar la caracterización de la rugosidad superficial más allá del uso de las magnitudes estadísiticas clásicas generalmente empleadas en implantología.

Appendix A

Experimental Techniques

In colloid and interface science, many reactions and events occur onto or close to the surface of materials. Hence, surface properties such as texture or surface chemistry become controlling rather than bulk properties. This way, for scientists, it is very necessary to characterize surfaces finely and also the way in which fabrication and use modify them. Imaging and chemical analysis techniques play important roles in capturing surface information. The aim of this appendix is to introduce to the experimental techniques used in this thesis.

A.1 Surface Origins

Surfaces are produced in a wide variety of processes, some tightly controlled and other uncontrolled. Maybe, the oldest technique with which mankind has produced intentional surfaces is the removal of material in the same way as a sculpture is extracted from a crude stone. However, modern fabrication of parts involves different stages: machining, grinding, polishing. These stages are applied to achieve a surface with specific macroscopic dimensions and also micro-nanoscopic features. Therefore, the mechanisms used to obtain the surface determines its texture.

Common methods to design a surface are not valid in nanotechnology because the scale of the features is too big. Hence, new methods were developed in last years in order to fabricate surfaces on a finer scale. There are a wide variety of methods, ranging from chemical etching, deposition and aggregation of particles, to plasma etching.

An important point to consider when we handle surfaces is the chemical heterogeneity. Indeed, chemical modification of surfaces is referred to as contamination, oxidation or corrosion. Surface properties such as wettability, electrical and optical properties, adhesion ... can be greatly modified by undesired thin layers or local regions with different chemical composition.

Moreover, surface texture is very critical in properties such as wettability, tribology or wear. Usually, texture is characterized from the surface information obtained directly by imaging methods. Even when the surface data are acquired by other ways, visualizing the surfaces allows to capture important qualitative information.

The typical measurement methods used to characterize surfaces are based on either some kind of microscope that provides magnified images of the surface, or scattering of radiation or particles from the surface. These methods inform about the morphology and/or chemical composition of the surface. In this work, the techniques used to acquire the texture of the surfaces were: atomic force microscopy, white light confocal microscopy and scanning electron microscopy[1] in order to

[1] In the text, these techniques have been abbreviated as AFM, WLCM and SEM respectively

cover a wide range of scan-sizes or scan-areas [2]. These tools are briefly described in the following sections.

A.2 Imaging Surfaces

A.2.1 Atomic Force Microscope (AFM)

The AFM belongs to the family of surface force apparatus (SFA). SFA family devices were developed at the beginning of the 20^{th} century to study tribology of modern machinery. They gained more and more precision as the industry and the computer sciences evolved, and, currently, they are used to "observe" the surface morphology even at atomic resolution and to measure forces down to the nanoNewton. In fact, the AFM is strongly related to the invention in 1981 of the first scanning tunneling microscope (STM), by Binnig, Quate and Gerber, capable of imaging a solid surface with real atomic resolution in three dimensions [330–332]. Few years later, in 1985, Binnig, Quate and Gerber developed and atomic force microscope [331] based on the same design as their STM [332]. This new device was able to measure on any kind of surface and could be used in different environments from the ultra high vacuum to liquids [333].

The working principle of an AFM is simple. It essentially consists of three systems working together: a force-sensing system, a detection system and a positioning system, the whole managed by control electronics and feedback systems, which are controlled by a computer [331, 333]. A scheme-up of the AFM setup is shown in fig. A.1.

The force-sensing system

The force-sensing system is the part of AFM in direct contact with the sample surface. Usually, a flexible leaf spring, called cantilever[3], and ended by a small sharp tip located and its free end, which it can have different geometry attending to the application to do, and which it is used as sensor. The coating, geometry and material of the cantilever are also important factors in AFM studies and they are conditionated by the measurements which are performed and by the measuring system. The AFM tip is the component in contact or in near contact with the surface. Forces acting between the AFM tip and the sample surface are transformed in deflections, torsions and/or bendings, of the cantilever.

The detection system

The tip-sample interaction is detected by monitoring the deflection of a laser-beam incident on the cantilever, just on the back of the tip. This laser-beam is reflected by the back side of the cantilever, which is coated with high reflectance coatings in order to facilitate this point, and it comes at a four-quadrant position-sensitive photodiode (PSPD). Bendings and torsions of the cantilever are translated into different position of the reflected laser-beam on the PSPD and thus, in changes in the output voltage of the photodiode. Small variations in the positions of the cantilever results in large displacements of the laser spot. By this way, tip displacements smaller than 1 nm are easily detectable [333, 334]. The detection system is able to record the deflection of the cantilever in three dimensions separately and simultaneously, giving the topography of the

[2] Scan-size is defined as the side length of the image, therefore, the scan-area is the product of both scan-sizes, on the X-axis and on the Y-axis.

[3] Cantiler is characterized by their dimensions, tipical dimensions are: hundreds of micrometers of length, 0.5 to 5 micrometers of thickness and around tenth micrometers of width, and their torsional and/or lateral spring constant. Also its geometry is different for different working modes and experimental situations.

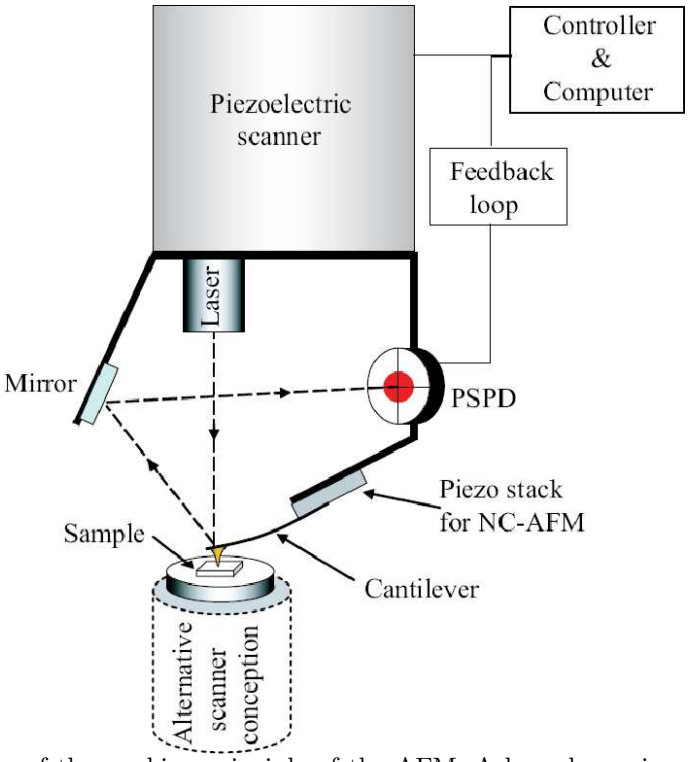

Figure A.1: Scheme of the working principle of the AFM. A laser beam is reflected on the back side of the cantilever, just on back of the tip, and then on a mirror, to finally incides on a position-sensitive photodiode (PSPD). The movement of the tip on the surface is translated on laser spot displacements on PSPD and on variations in the output voltage of the PSPD. These results, via feedback loop, in an extension or contraction of piezoelectric scanner which moves the sample.

surface. As the cantilever is a flexible leaf spring and supposing that the Hooke's law for small displacements (the interaction force between the tip and the surface is directly proportional to the cantilever deflection) is verified, it is possible to determine the interaction force between the surface and the tip, instead, from the surface topography.

Positioning system

The positioning and the fine displacement of the AFM tip relatively to the surface are done via piezoelectric scanners, whereas coarse displacement use stepper motors when available. Piezoelectric materials are ceramics that change dimensions in response to an applied electric field (voltage). Conversely, a mechanical strain of the piezoelectric material causes an electric potential, the relative position of the tip over the sample is thus controlled by the application of voltage to the piezo, resulting in extension, squeezing or bending of the piezoelectric material in order to keep the tip on the surface or to keep the distance between the tip and the surface constant[4]. Piezoelectric scanners can be designed to move in the three dimensions by expanding in some directions and contracting in others.

[4]Depending of the working mode of the AFM

How works a AFM?

The AFM may work in different modes depending on what kinds of measurements are expected or simply depending on the surface you are analyzing. Now we are going to present the main AFM modes that are commonly used and which have been used in this work.

1. Contact Mode
   As indicated by its name, the contact mode corresponds to the case where the AFM tips is always held in real contact with the surface. A feedback loop allows two basic contact modes: constant force mode and constant height mode. In the constant force mode, the piezoelectric scanner operates in order to keep the force between the tip and the surface constant controlling the vertical position of the sample relatively to the tip. Thus, the scanner responds instantaneously to the topography changes by keeping the cantilever deflection constant. For the constant height mode, the measured data are the cantilever deflection, whereas the relative distance between the tip and the surface is kept constant via the feedback loop. This mode is restricted to flat surfaces to avoid tip crashes on the surface.

2. Non-Contact Mode and Tapping Mode
   In these modes the cantilever is oscillated sufficiently close to the surface to interact with it via long-range forces (attractive or repulsive). Generally, a stiff cantilever is attached to the small piezoceramic system vibrating perpendicularly to the surface at a frequency close to the cantilever free-space resonance frequency. The tip is then scanned over the surface and each surface pixel corresponds to an average of hundreds of oscillations. The distance between the sample and the AFM tip is controlled by tracking the changes in the oscillating frequency, amplitude or phase. The resonance frequency or the oscillating amplitude is kept constant by a feedback loop, which controls the cantilever displacement normal to the surface. The difference between the Non-Contact Mode (NC-AFM) and Tapping Mode (TM-AFM) is that for NC-AFM the oscillation frequency is chosen close to, but greater than the free-space resonance frequency (the vibrating amplitude decreases significantly), whereas for TM-AFM the frequency is also close to, but smaller than the cantilever resonance frequency (the vibrating amplitude increases allowing intermittent contact).

A.2.2 White Light Confocal Microscopy (WLCM)

In 1957 Marvin Minsky "discovered" the confocal principle [335, 336]. The invention of Minsky remained largely unnoticed, probably due to the absence of strong light sources and computers to handle the large amounts of data. After the patent had expired the confocal microscope was reinvented and, finally, Brakenhoff applied the confocal principle in 1979 in a light microscope building the first practical confocal microscope [337, 338].

Brakenhoff just wanted to develop a better version of the light microscope which would also be able to do three-dimensional imaging. And, obviously, he did it. So, confocal scanning optical microscopy has emerged as a significant new technique which exhibits several advantages in comparison with conventional systems based on classical microscopy. The most important of these advantages stem from the fact that out-of-focus blur is essentially absent from confocal images, giving the capability for direct non-invasive serial optical sectioning of intact and even living specimens [339–341]. This leads to the possibility of generating three-dimensional (3D) images of thick transparent objects such as biological cells and tissues. Also, it allows profiling of the surfaces of 3D objects again by a non-contact and non-destructive method.

How works a WLCM?

In reflection mode, for a confocal microscopy, the light emitted from a point light source is imaged into the object focal plane of a microscope objective, but a confocal microscope differs from a "classical" optical microscope [339] in the fact that every moment there is formed an image of one object point while a whole image is assembled by scanning (moving a specimen or readjusting an optical system). In order to register light from only one point, a pinhole aperture is situated behind the objective lenses so that the light emitted by the studied point passes through the aperture and is detected while light from the other points is at most excluded. The second feature is that the illuminator produces not the uniform lighting of the field of view but focuses light into the studied point. This can be done by placing a second focusing system behind a sample; in this case, however, the sample should be transparent. Moreover, the objective lenses are usually expensive enough, so utilization of a second focusing system for illumination is of little preference. An alternative is the use of a beam splitter for the purpose of incident and reflected light could be focused by the same objective. Besides, such arrangement facilitates system adjustment.

It is clear that the application of the confocal scheme, which appears in fig. A.2, should

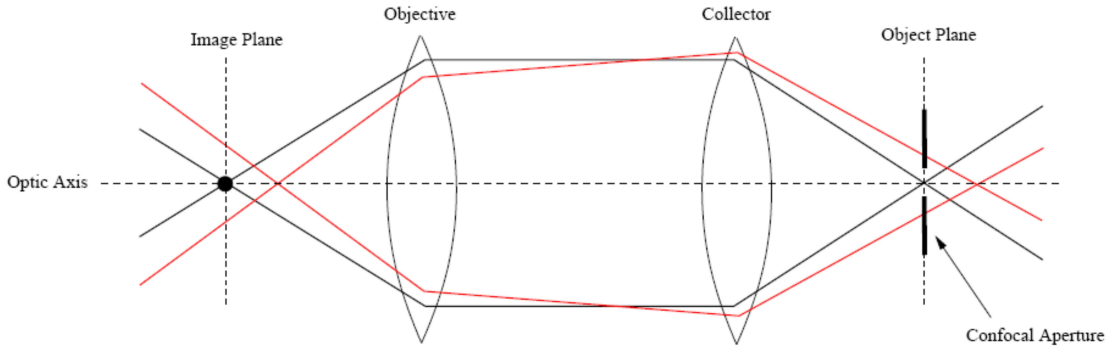

Figure A.2: Scheme of the working principle of the Confocal microscope. Light originating from within the focal plane (black) is imaged at the image plane, as in conventional microscope. Light originating outwith the focal plane (red) is not brought to a focus at the image plane, and appears as blur in a conventional microscope. A confocal aperture in the image plane ensures only a thin optical section is imaged, so that this detrimental effect is eliminated by the confocal microscope.

increase the image contrast because "stray" light from points adjacent to the studied one does not enter the detector. Note that the contrast increase is achieved at the expense of complicated scan by specimen or by light beam systems utilization [341, 342]. It is possible to find a lot of kinds of confocal microscopes in market, but all of them work with the same working optical principle, which has been described above. Thus, the principal difference between the most popular confocal microscopes (laser confocal microscope and white light microscope) is basically the illumination source used to illuminate the sample surface.[5]

A.2.3 Scanning Electron Microscopy (SEM)

Unlike scanning probe microscopy (SPM) where physical probes interact with the surface, other techniques use beam methods based on the interactions of photons, electrons, neutrons, or positrons

[5]The essential details of the confocal microscope are clearly explained for the general scientist in the http://www.physics.emory.edu/faculty/weeks/confocal/. For more detail, see [343, 344].

with the surface. Scanning electron microscopy (SEM) is briefly explained because it was used to image surfaces. Its basic principle is the same than optical microscopes although instead of using light to image the surface, it uses electrons.

Electron-surface interactions

The response of the surface to an incident electron beam is composed of different particles and interactions as schematically represented in fig. A.3.

When an incident electron passes near an atom, it can impart some of its energy to a lower

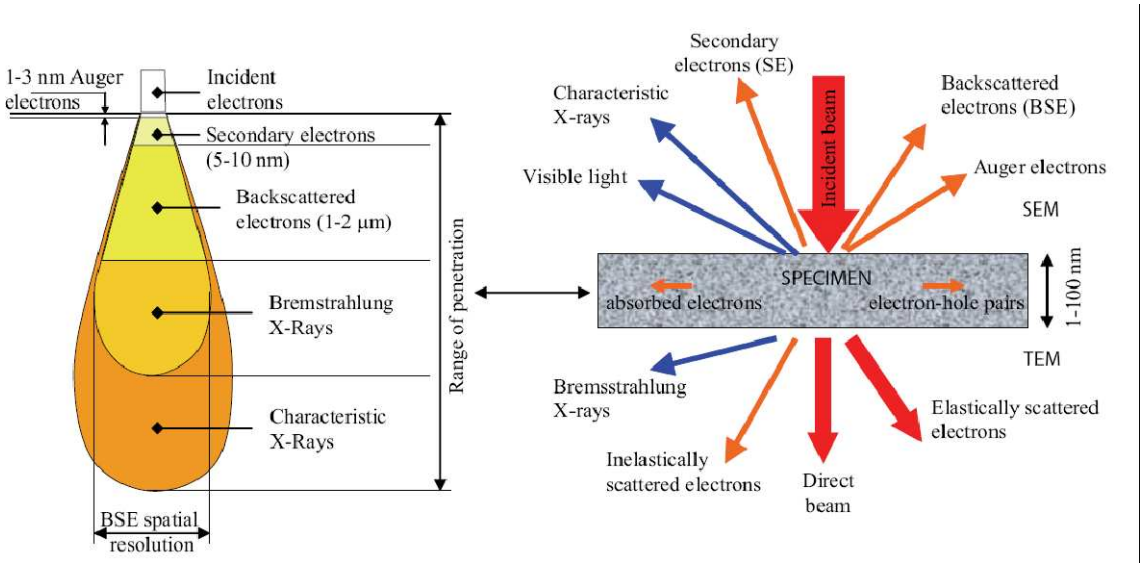

Figure A.3: Interaction of an incident electron beam with a surface resulting in diverse particles depending on the intensity of the incident beam and its range of penetration.

energy electron belonging to an atom of the studied specimen. It results in an ionization of the low energy electron. Then, this electron, called secondary electron (SE), leaves the atom with a small kinetic energy (0-30 eV) and is picked up by a detector. Due to their low energy, just SE near the surface are measured, and thus, they are principally related to the surface topography.

The holes due to SE exits let some vacancies in the shell of the atoms which will be occupied by electrons of higher energies, belonging to the atom, in order to decrease the total atom energy. This process goes with the emission of X-rays to balance the total energy of the atom which can be used to determine the surface chemistry of the surface because the X-rays are strongly related to the element from which they originated. Another possibility instead of the X-ray emission is that an electron of the outer shell leaves the atom. This electron is called an Auger electron. They are used for surface analysis and are generally not detected in SEM. Other electrons are scattered backward after colliding with an atom of the specimen. They are called backscattered electrons (BSE). The production of BSE is related to the material of the specimen and more precisely to the atomic number of its elements. Finally, some electrons of the incident beam are also absorbed in the material.

How works a SEM?

A SEM works similarly to a classical television (not a LCD, TFT or Plasma television) where what you see is what the detector sees. It consists on an electron gun which produces a coherent monochromatic electron beam that is accelerated by a cathode with help of field emission or thermionic sources. This electron beam is focused on the surface by magnetic or electrostatic lenses. After the impact between the beam and surface, the signals have to pass through a detector, which is placed in a vacuum chamber, since the thickness of the sample avoids any transmission of the information and only particles emitted close to the surface are caught.

The SEM is basically dedicated to topography studies, but may also be related to surface chemistry analysis. However, the disadvantage of this technique respect to the AFM and WLCM ones is the time allotted to the preparation of the samples to be imaged, due, for example, to the vacuum chamber which obeys to cover the surface by a conductive coating in order to avoid charge effects. Therefore, SEM cannot realize in vivo measurements.

A.3 Surface Chemistry Microanalysis (EDX)

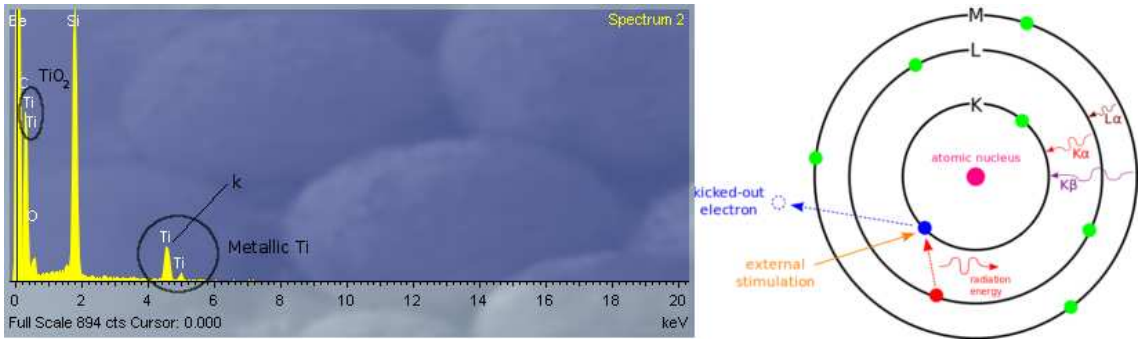

Figure A.4: In this figure it is possible to observe an EDX spectrum for commercially pure titanium (grade II). K and L peaks show the X-ray emission from the concerning atom shell (left part of the figure). Right part of the figure represents a scheme of the EDX working principle.

Energy-dispersive X-ray (EDX) spectrometry is one of the most common procedure for performing elemental analysis in electron microscopy [345]. This technique was used in conjunction with SEM. When an electron beam strikes the surface of a conducting sample, this interaction can be either elastic or inelastic. The inelastic strikes of a fast electron with the surface can lead to excitation of an atom within the sample (promoting an inner shell electron). Such an excited atom eventually returns back to the energy ground state. This return can be due to different processes as radiative transition or Auger process. For the radiative transition, the atom returns to the ground state emitting a photon (X-ray) which energy is intrinsically associated to the atom and to the energy level of the electron promoted in this process. Therefore, the analysis of the photons coming out of the sample can yield information about chemical composition of the sample. Information obtainable from such characteristic X-rays provides basis for energy dispersive X-ray microanalysis (EDX) and wavelength-dispersive X-ray microanalysis (WDX). A scheme of the EDX working principle can be observed in fig. A.4 which appears below.

This technique it is not purely a surface science technique because the X-rays are generated in a region about $2\mu m$ in depth. By moving the electron beam across the material an image of

each element in the sample can be acquired. Due to the low X-ray intensity, images usually take a number of hours to acquire. Elements of low atomic number are difficult to detect by EDX. For this reason, the detector used for EDX microanalysis is based on electron-hole pair generation in a semiconductor diode by the photon emitted from the sample. The number of electron-hole pairs created by a photon in such detector is proportional to the energy of the photon, resulting in current pulses in a suitable circuit.

Position of a peak in such spectra provides information on the type of atoms in the sample. The peak intensity (number of counts of given "size") provides information on number of photons of given energy. The number of counts of given energy is proportional to areal density of given type of atoms.

A.4 Low-rate dynamic contact angle revisited

Each solid–liquid–vapor system is characterized by a range of observable contact angles referred to as the contact angle hysteresis range. This range is defined by the advancing contact angle and the receding contact angle, which are further the most meaningful angles because they are related to the shear and tensile adhesion forces. In this thesis, the measurement of advancing and receding contact angle was performed by low-rate dynamic contact angle procedure which it is based on

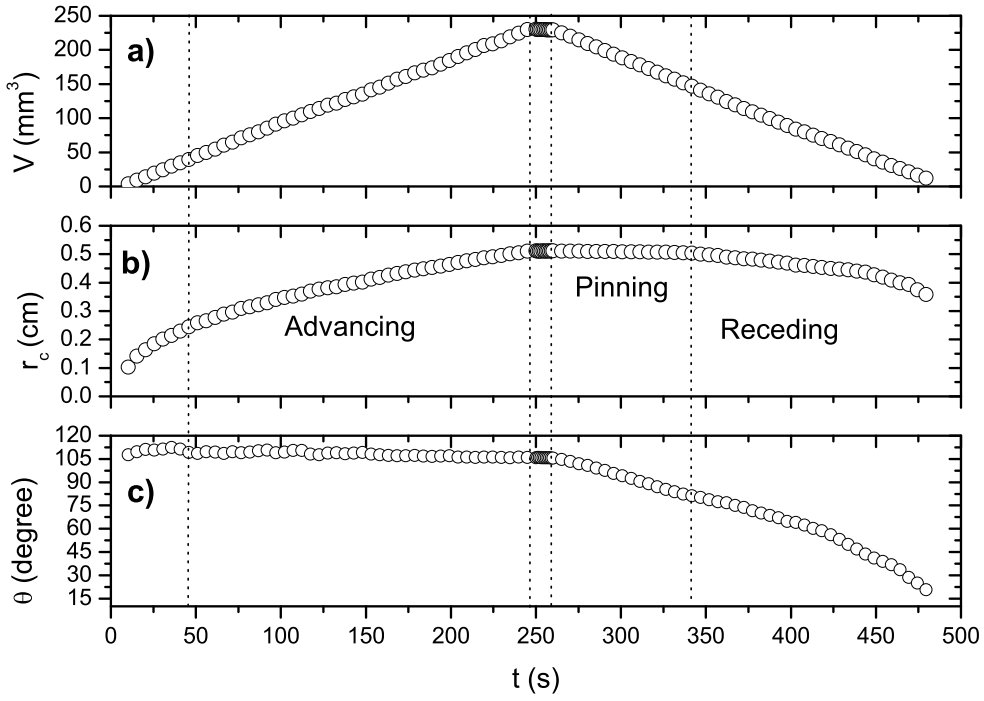

Figure A.5: A typical low-rate dynamic contact angle experiment of distilled water on a rough polytetrafluoroethylene surface: (a) volume, (b) three-phase contact radius, and (c) contact angle

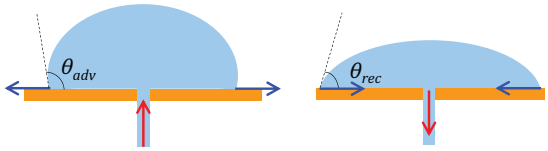

Figure A.6: Low-rate dynamic contact angle technique.

forced wetting [346]. The advancing and receding contact angle measurements are performed, respectively, by an increase or decrease in the drop volume (inversely for captive bubbles). The role of the volume variation is just to force the system to pass from one local energy minimum to the next, until it reaches the advancing/receding configuration. Thus, for a sessile drop deposited on a surface with the contact line initially pinned, if the volume is increased then the contact angle also increases. When the advancing contact angle is reached the contact line starts to move. The inverse procedure is employed to determine the receding contact angle, i.e. the contact line is initially pinned and as the volume is decreased the contact angle decreases. When the receding contact angle is reached then the contact line moves. Fig. A.5 shows the results of a typical low-rate dynamic contact angle experiment. This technique allows to measure observable contact angles of growing/shrinking sessile drops or captive bubbles [347].

In order to avoid drop vibrations and for measuring true advancing contact angles without disturbing the drop profile, Oliver et al. [348] proposed that the volume variation was performed through a small hole (0.5-1 mm diameter) drilled in the substrate and a tube is connected to this hole beneath the substrate (see Fig. A.6). Oliver et al. procedure begins with a small drop ($\sim 5\mu l$) placed on this hole and then the volume of the drop is varied by means of the tube connected to a motorized micrometer syringe. Commonly, low-rate dynamic contact angle measurements are achieved with a continuous linear variation of drop volume. The experimental set-up used for the contact angle measurements is showed in Fig. A.7. To minimize the possible vibrations,

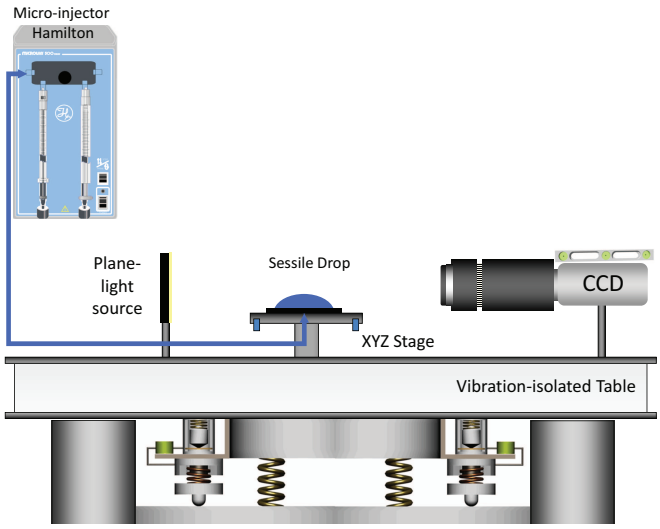

Figure A.7: Experimental device used for the low-rate dynamic contact angle measurements.

the device is mounted on a vibration-isolated optical table. Because of the drop dimensions, a microscope (Leica© Apo-Zoom) is coupled to a SONY© CCD (Charge Couple Device) camera. The interface is light-contrast illuminated by using a plane and homogeneous light source (Dolan Jenner QVABL). The video image signal is digitalized with a frame grabber connected (Data Translation DT3155) to a PC. Once the image is digitalized, the detection process provides a set of points that represents the drop profile. Next, to convert from digital to physical dimensions, a calibration process is necessary. A square grid of known side allows the conversion of pixel units to physical length units. To correct the deviations of the camera with respect to the vertical direction, a plumb line is used. In order to correct the effect of refraction index in the captive bubble experiments, the grid is immersed in the liquid. We used a software suite (Dinaten© and Contacto©) to acquire, process and calculate images. Both applications were ad-hoc developed by Dr. Juan Antonio Holgado Terriza [284]. Drop profiles were analyzed with the Axisymmetric Drop Shape Analysis-Profile (ADSA-P) technique [349, 350]. With this approach, all the drop parameters such as contact angle, contact radius, area, volume and surface tension are extracted. The liquid/air is injected/suctioned with a microinjector Hamilton© ML500 at $1\mu l/s$. A 250μl-Hamilton© syringe was used. The experiments were performed at (21-24±1)°C and 40-55% RH.

Appendix B

Scaling Laws and Dimensional Analysis

[1]In physics, it is common to find scaling laws that lead to universal behavior described by master curves. In most cases, these laws include units with non-integer exponents. A physical quantity can scale with one another by monomials with non-integer exponents, but this dependence should always be dimensionally homogeneous [125]. This detail is often implicitly ignore in scaling analysis through the inclusion of different proporcionality constants which homogenize the physical dimensions of the scaling law. However, in some cases it can confuse the non-specialist reader.

This is what happens, for example, with the statistical width w of a rough surface (i.e. the root-mean-square deviation of heights, h, on all the achievements of the system) which evolves with time. This quantity depends on the window size L where the height of the surface is averaged and time t. If the surface is self-affine and stochastic [107], the instantaneous and local height will verified the following property in a statistical sense:

$$h(\mathbf{r}, t) \approx \lambda^{-\alpha} h(\lambda \mathbf{r}, \lambda^z t) \tag{B.1}$$

where $\lambda \in \mathbb{R}^+$, and α and z are exponents which inform about the roughness and growth dynamics, respectively.
Obviously, by its own definition, statistical width w verifies the property expressed by Eq.B.1:

$$w(L, t) \approx \lambda^{-\alpha} w(\lambda L, \lambda^z t) \tag{B.2}$$

therefore, if $\lambda = L_0/L$ (where $L_0 = \text{const.}$), the statistical width of a rough surface must verify the following dependence:

$$w(L, t) = \frac{w_0}{L_0^\alpha} L^\alpha f\left(\frac{t}{t_C(L)}\right); \quad t_C(L) = \frac{t_0}{L_0^\alpha} L^z \tag{B.3}$$

where w_0 is a constant value of length, t_0 is also a constant value of time, and the f is a dimensionless function. t_C is known as a transtion time and it represents the time from which the surface width saturates due to size effects so the function f scales as [107]:

$$f(y) \sim \begin{cases} y^{\frac{\alpha}{z}} & \text{if } y << 1 \\ 1 & \text{if } y >> 1 \end{cases} \tag{B.4}$$

[1]This work has been written by M. A. Rodríguez-Valverde and P. J. Ramón-Torregrosa and appears published in Revista española de física, Volumen 24, Número 1, 2010, Página 75

However, it is common to find in the literature devoted to surface growth phenomena [107], that the dependence expressed by Eq.B.3 is simplified to:

$$w(L,t) \propto L^{\alpha} f\left(\frac{t}{L^{z}}\right) \tag{B.5}$$

This Eq. B.5 can mistakenly induce to identify the linear region of w for $t << L^{z}$!!! as it was noted by Paul Meakin [113].

Appendix C

Derivation of the Young's Equation

This derivation assumes no gravitational effects and, consequently, the drop can be modeled by surfaces with constant mean curvature, particularly as a spherical cap [132, 351]. So, let be a spherical-cap[1] drop (the spherical cap is the region of the sphere that lies above or below a given plane) with radius R, height h, and the base radius r (See Figure C.1).

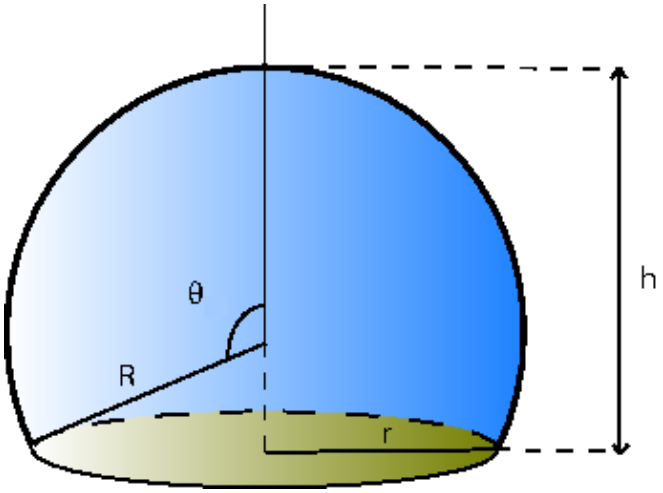

Figure C.1: Spherical-cap drop

Applying Pytagorean theorem to Figure C.1:

$$r^2 = R^2 - (h - R)^2 = 2Rh - h^2 \tag{C.1}$$

The contact angle θ is defined as the angle between a normal to the base and the unit normal to the sphere through the base perimeter. The relation between R, h and θ is given by:

$$h = R\,(1 - cos\theta) \tag{C.2}$$

[1] A complete recopliation of mathematical expressions about the geometrical relationships of a spherical cap can be found http://mathworld.wolfram.com/SphericalCap.html.

The volume of the spherical cap is determined by the following integral:

$$V = \pi R^3 \int_0^\theta sin^3\theta d\theta = \frac{\pi R^3}{12}\left(8 - 9cos\theta + cos\left(3\theta\right)\right) \tag{C.3}$$

using basic trigonometric concepts, previous expression can be rewritten as:

$$V = \frac{\pi}{3}\left(2R^3 - \left(2R^2 + r^2\right)Rcos\theta\right) \tag{C.4}$$

and, finally, the following expression can be obtained

$$V = \frac{\pi h^2}{3}\left(3R - h\right) \Rightarrow R = \frac{V}{\pi h^2} + \frac{h}{3} \tag{C.5}$$

The lateral area A_{lat} of the spherical cap, i.e. A_{lg} for wetting phenomena, is given by the integral:

$$A_{lat} = 2\pi R^2 \int_0^\theta sin(\theta)d\theta \Rightarrow A_{lat} = \frac{2V}{h} + \frac{2\pi h^2}{3} \tag{C.6}$$

The area of the base of the spherical cap, A_{base}, i.e. A_{sl} for wetting phenomena, is given by the area the circle of radius r. So, A_{base} can be expressed as:

$$A_{base} = \frac{2V}{h} - \frac{\pi h^2}{3} \tag{C.7}$$

As equilibrium condition for an ideal solid surface wetting phenomena is $dW_{tot} = 0$, consequently $\theta = \theta_{Eq}$, and therefore

$$\gamma_{sg} = \gamma_{sl} + \gamma_{lg} \cdot \left.\frac{dA_{lg}}{dA_{sl}}\right|_{V=const} \tag{C.8}$$

we can derived that:

$$\left.\frac{dA_{lg}}{dA_{sl}}\right|_{V=const} = \frac{R-h}{R} = cos\theta_{Eq} \Rightarrow \left.\frac{dA_{lg}}{dA_{sl}}\right|_{V=const} = cos\theta_{Eq} \tag{C.9}$$

Then , considering this last two expressions, Eq. (C.8) and Eq. (C.9), Young's equation is obtained

$$\gamma_{sg} = \gamma_{sl} + \gamma_{lg}cos\theta_{Eq} \tag{C.10}$$

Finally, i would like to comment that, in this appendix, Young's equation has been derived taking into account geometrical and thermodynamical arguments exclusively.

List of Figures

List of Tables

Bibliography

[1] T. Albrektsson, *The response of bone to titanium implants*, *CRC Crit. Rev. Biocomp.* **1** (1985) 53–84.

[2] P. Ducheyne, *Titanium and calcium phosphate ceramic dental implants, surfaces, coatings and interfaces*, *J. Oral Implantol.* **14** (1988) 325–340.

[3] T.G. Donley, W.B. Gillette, *Titanium endosseous implant-soft tissue interface: a literature review*, *J. Periodontol* **62** (1991) 319–338.

[4] K.E. Healy, P. Ducheyne, *The mechanisms of passive dissolution of titanium in a model biological enviroment*, *J. Biomed. Mater. Res.* **26** (1992) 319–338.

[5] R.M. Pilla, G.C. Weatherlz, *Developments in implant alloys*, *CRC. Crit. Rev. Biocomp.* **1** (1986) 371–403.

[6] E.P. Lautenschlager, P. Monaghan, *Titanium and titanium alloys as dental materials*, *Int. Dent. J.* **43** (1993) 245–253.

[7] P.I. Branemark, ch. Introction to osseointegration, pp. 11–76. Quintessence Publishing Co, Inc., 1985.

[8] D. Buser, *Effects of various titanium surface configurations on osseointegration and clinical implant stability*, in *Proceedings of the 3rd European Workshop on Periodontology Implant*, pp. 88–101, 1999.

[9] L. Postiglione, G.D. Domenico, L. Ramaglia, S. Montagnani, S. Salzano, F.D. Meglio, L. Sbordone, M. Vitale, G. Rossi, *Behavior of SaOS-2 cells cultured on different titanium surfaces*, *J. Dent. Res.* **82** (2003) 692–696.

[10] K. Mustafa, A. Wennerberg, J. Wroblewski, K. Hultenby, B.S. López, K. Arvidson, *Determining optimal surface roughness of TiO2 blasted titanium implant material for attachment, proliferation and differentiation of cells derived from human mandibular alveolar bone*, *Clin. Oral Impl. Res.* **12** (2001) 515–525.

[11] K.T. Bowers, J.C. Keller, B.A. Randolph, D.G. Wick, C.M. Michaels, *Optimization of surface micromorphology for enhanced osteoblast responses in vitro*, *Int. J. Oral Maxillofac. Implants* **7** (1992) 302–310.

[12] N. Lumbikanonda, R. Sammons, *Bone cell attachment to dental implants of different surface characteristics*, *Int. J. Oral Maxillofac. Implants* **16** (2001) 627–636.

[13] B. Feng, J. Weng, B.C. Yang, S.X. Qu, X. D. Zhang, *Characterization of titanium surfaces with calcium and phospahte and osteoblast adhesion*, *Biomaterials* **25** (2004) 3241–3248.

[14] B. Feng, J. Weng, B.C. Yang, S.X. Qu, X.D. Zhang, *Characterization of surface oxide films on titanium and adhesion of osteoblast*, *Biomaterials* **24** (2003) 4663–4670.

[15] Y. Shibata, M. Hosaka, H. Kawai, T. Miyazaki, *Glow discharge plasma treatment of titanium plates enhances adhesion of osteoblast-like cells to the plates through the integrin-mediated mechanism*, *Int. J. Oral Maxillofac. Implants* **17** (2002) 771–777.

[16] M.A. De Maeztu, J.I. Álava, C. Gay-Escoda, *Ion implantation: surface treatment for improving the bone integration of titanium and Ti6Al4V dental implants*, *Clin Oral Implants Res.* **14** (2003) 52–62.

[17] A.P. Ameen, R.D. Short, R. Johns, G. Schwach, *The surface analysis of implant materials 1. The surface composition of a titanium dental implant material*, *Clin Oral Implants Res.* **3** (1993) 144–150.

[18] M. Takeuchi, Y. Abe, Y. Yoshida, Y. Nakayama, M. Okazaki, Y. Akagawa, *Acid pretreatment of titanium implants*, *Biomaterials* **24** (2003) 1821–1827.

[19] C. Viornery, H.L. Guenther, B.O. Aronsson, P. Pechy, P. Descouts, M. Gratzel, *Osteoblast culture on polished titanium disks modified with phosphonic acids*, *J. Biomed. Mater. Res.* **62** (2002) 149–155.

[20] P.A. Ramires, A. Romito, F. Cosentino, E. Milella, *The influece of titania/hydroxyapatite composite coatings on in vitro osteoblasts behaviour*, *Biomaterials* **22** (2001) 1467–1474.

[21] C. Massaro, M.A. Baker, F. Cosentino, P.A. Ramires, S. Klose, E. Milella, *Surface and biological evaluation of hydroxyapatite-based coatings on titanium deposited by different techniques*, *J. Biomed. Mater. Res.* **58** (2001) 651–657.

[22] M.M. Bornstein, A. Lussi, B. Schmid, U.C. Belser, D. Buser, *Early loading of nonsubmerged titanium implants with a sandblasted and acid-etched (SLA) surface: 3-year results of a prospective study in partially edentulous patients*, *Int. J. Oral Maxillofac. Implants* **18** (2003) 659–666.

[23] S. Szmukler-Moncler, D. Perrin, V. Ahossi, G. Magnin, J.P. Bernard, *Biological properties of acid etched titanium implants: effect of sandblasting on bone anchorage*, *J. Biomed. Mater. Res.* **68B** (2004) 149–159.

[24] C. Larsson, P. Thomsen, J. Lausmaa, M. Rodahl, B. Kasemo, L.E. Ericson, *Bone response to surface modified implants: studies on electropolished implants with different oxide thickness and morphology*, *Biomaterials* **15** (1994) 1062–1074.

[25] J. Tomes, C. de Morgan, *Observations on the structure and development of bone*, *Phil. Trans. Roy. Soc.* **143** (1853) 109–139.

[26] C. Gegnbaur, *Ueber die Bildung des knochengewebes*, *Jena Zeitschrift Naturwissenschaften* (1864) 343–360.

[27] M. Noda, J.J. Camilliere, *In vivo stimulation of bone formation by transforming factorbeta*, *Endocrinology* **124** (1989) 2991–2994.

[28] J.W. Chow, A.J. Wilson, T.J. Chambers, S.W. Fox, *Mechanical loading stimulates bone formation by reactivation of bone lining cells in 13-week-old rats*, *J. Bone Miner. Res.* **13** (1998) 1760–1767.

[29] I. Degasne, M.F. Basle, V. Demais, G. Hure, M. Lesourd, B. Grolleau, L. Mercier, D. Chappard, *Effects of roughness, fibronectin and vitronectin on attachment, spreading, and proliferation of human osteoblast-like cells (SaOS-2) on titanium surfaces*, *Calcif. Tissue Int.* **64** (1999) 499–507.

[30] K. Kieswetter, Z. Schwartz, T.W. Hummert, D.L. Cochran, J. Simpson, D.D. Dean, *Surface roughness modulates the local production of growth factors and cytokines by osteoblast-like MG-63 cells*, *J. Biomed. Mater. Res.* **32** (1996) 55–63.

[31] J.Y. Suh, B.C. Jang, X.L. Zhu, J.L. Ong, K. Kim, *Effect of hydrothermally treated anodic oxide films on osteoblast attachment and proliferation*, *Biomaterials* **24** (2003) 347–355.

[32] D.M. Brunette, *The effects of implant surface topography on the behavior of cells*, *Int. J. Oral Maxillofac. Implants* **3** (1988) 231–246.

[33] H.G. Craighead, C.D. James, A.M.P. Turner, *Chemical and topographical patterning for directed cell attachment*, *Curr. Opin. Sol State Mater. Sci.* **5** (2001) 177–184.

[34] A.B. Ferguson, P.G. Laing, E.S. Hodge, *The ionization of metal implants in living tissue*, *J. Bone Joint Surg.* **42A** (1960) 77–90.

[35] N. Kanematu, K.I. Shibata, S. Kurenuma, K. Watanabe, A. Yamagami, Y. Nishio, T. Fujii, *Cytotoxicity of oxide anodized titanium alloy evaluated by cell and organic culture study*, *J. Gifu. Dent. Soc.* **17** (1990) 583–591.

[36] C.E. Turner, K. Burridge, *Transmembrane molecular assemblies in cell-extracellular matrix interactions*, *Curr. Opin. Cell Biol.* **5** (1991) 849–853.

[37] S.K. Sastry, A.F. Horwitz, *Integrin cytoplasmic domains: mediators of cytoskeletal linkages and extra- and intercellular initiated transmembrane signaling*, *Curr. Opin. Cell Biol.* **5** (1993) 819–831.

[38] F. Grinell, *Cellular adhesiveness and extracellular substrata*, *Int. Rev. Cytol.* **53** (1978) 65–129.

[39] D. Buser, R.K. Schenk, S. Steinemann, J.P. Fiorellini, C.H. Fox, H. Stich, *Influence of surface characteristics on bone integration of titanium implants. A histomorphometric study in mininature pigs*, *J. Biomed. Mater. Res.* **25** (1991) 889–902.

[40] K. Gotfredsen, A. Wennerberg, C. Johansson, L.T. Skovgaard, E. Hjorting-Hansen, *Anchorage of TiO2 blasted, HA-coated, and machined implants: and experimental study with rabbits*, *J. Biomed. Mater. Res.* **29** (1995) 1231–1233.

[41] A. Wennerberg, T. Albrektsson, B. Andersson, J.J. Krol, *A histomorphometric and removal torque study of screw-shaped titanium implants with three different surface topographies*, *Clin. Oral Implants Res.* **6** (1995) 24–30.

[42] A. Wennerberg, T. Albrektsson, B. Andersson, *Bone tissue response to commercially pure titanium implants blasted with fine and coarse particles of aluminum oxide*, *Int. J. Oral MAxillofac. Implants* **11** (1996) 38–45.

[43] K. Anselme, M. Bigerelle, B. Noel, E. Dufresne, D. Judas, A. Iost, P. Hardouin, *Qualitative and quantitative study of human osteoblast adhesion on materials with various surface roughness*, *J. Biomed. Mater. Res* **49** (2000) 155–166.

[44] M. Bigerelle, K. Anselme, B. Noel, I. Ruderman, P. Hardouin, A. Iost, *Improvement in the morphology of Ti-based surfaces: a new process to increase in vitro human osteoblast response*, *Biomaterials* **23** (2002) 1563–1577.

[45] B.D. Boyan, V.L. Sylvia, Y.H. Liu, R. Sagun, D.L. Cochran, C.H. Lohmann, D.D. Dean, J. Schwartz, *Surface roughness mediates its effects on osteoblasts via protein kinase A and phospholipase A2*, *Biomaterials* **20** (1999) 2305–2310.

[46] R. Stangl, B. Rinne, S. Kastl, C. Hendrich, *The influence of pore geometry in CPTi-Implants. - A cell culture investigation*, *Eur. Cell Mater.* **2** (2001) 1–9.

[47] F.A. Akin, H. Zreiqat, S. Jordan, M.B.J. Wijesundara, L. Hanley, *Preparation and analysis of macroporous TiO2 films on Ti surfaces for bone-tissue implants*, *J. Biomed. Mater. Res.* **57** (2001) 588–596.

[48] B. Kasemo, J. lausmaa, *Biomaterial and implant surface: A surface science approach*, *Int. J. Oral Maxillofac. Implants* **3** (1988) 247–259.

[49] J.C. Keller, R.A. Draughn, J.P. Wightman, W.J. Dougherty, S.D. Meletiou, *Characterization of sterilized cp titanium surfaces*, *Int. J. Oral Maxillofac. Implants* **5** (1990) 360–367.

[50] K. Mustafa, J. Pan, J. Wroblewski, C. Leygraf, K. Arvidson, *Electrochemical impedance spectroscopy and X-ray photoelectron spectroscopy analysis of titanium surfaces cultured with osteoblast-like cells derived from human mandibular bone*, *J. Biomed. Mater. Res.* **59** (2002) 655–664.

[51] M. Ahmad, D. Gawronski, J. Blum, J. Goldberg, G. Gronowicz, *Differential response of human osteoblast-like cells to commercially pure (cp) titanium grades 1 and 4*, *J. Biomed. Mater. Res.* **46** (1999) 121–131.

[52] A. Okumura, M. Goto, T. Goto, M. Yoshinari, S. Masuko, T. Katsuki, T. Tanaka, *Substrate affects the initial attachment and subsequent behavior of human osteoblastic cells (Saos-2)*, *Biomaterials* **22** (2001) 2263–2271.

[53] M. Morra, C. Cassinelli, G. Cascardo, P. Cahalan, L. Cahalan, M. Fini, R. Giardino, *Surface engineering of titanium by collagen immobilization. Surface characterization and in vitro and in vivo studies*, *Biomaterials* **24** (2003) 4639–4654.

[54] J.Y. Martin, Z. Schwartz, T.W. Hummert, D.M. Schraub, J. Simpson, J. Lankford, D.D. Dean, D.L. Cochran, B.D. Boyan, *Effect of titanium surface roughness on proliferation, differentiation, and protein synthesis of human osteoblast-like cells (MG63)*, *J. Biomed. Mater. Res.* **29** (1995) 389–401.

[55] J.Y. Martin, D.D. Dean, D.L. Cochran, J. Simpson, B.D. Boyan, Z. Schwartz, *Proliferation, differentiation, and protein synthesis of human osteoblast-like cells (MG63) cultured on previously used titanium surfaces*, *Clin. Oral Impl. Res.* **7** (1996) 27–37.

[56] D. Dowson, *History of tribology.* Professional engineering publishing limited London and Bury St Edmunds, London, 1998.

[57] J.F. Archard, *Elastic deformation and the laws of friction*, *Proc. R. Soc. Lond. A* **243** (1957) 190–205.

[58] A.E. Norton, *Lubrication.* McGraw Hill, New York, 1985.

[59] J.T. Burwell, *Survey of possible wear mechanism*, *Wear* **1** (1957) 119–141.

[60] B.N.J. Persson, *Theory of rubber friction and contact mechanics*, *J. Chem. Phys.* **115** (2001) 3840–3861.

[61] B.N.J. Persson, E. Tosatti, *The effect of surface roughness on the adhesion of elastic solids*, *J. Chem. Phys.* **115** (2001) 5597–5610.

[62] D.J. Whitehouse, ch. Surface characterization and roughness measurement in engineering, pp. 413–461. Springer Berlin Heidelberg, 2000.

[63] D.J. Whitehouse, *The effect of surface roughness on the adhesion of elastic solids*, *Proc. Inst. Mech. Eng.* **182** (1968) 436.

[64] B.N.J. Persson, O. Albohr, U. Tartaglino, A.I. Volokitin, E. Tosatti, *On the nature of surface roughness with application to contact mechanics, sealing, rubber friction and adhesion*, *J. Phys. Condens. Matter.* **17** (2005) R1.

[65] D.J. Whitehouse, R.E. Reason, *The Equation of the mean line of surface texture found by an electric wave filter.* Rank Taylor Hobson, Leicester, 1965.

[66] C. Brown, S. Siegmann, *Fundamental scales of adhesion and area-scale fractal analysis*, *Int. J. Mach. Tool. Manufact.* **41** (2001) 1927–1933.

[67] E.S. Gadelmawla, M.M. Koura, T.M.A. Maksoud, I.M. Elewa, H.H. Soliman, *Roughness parameters*, *J. Mat. Proc. Technol.* **123** (2002) 13–1945.

[68] *ISO TC 213 workgroup 16, geometrical product specifications (GPS)-surface texture: areal-part 2: terms, definitions and surface texture parameters. standar proposal N756*, 2005. Geneva 437.

[69] L. Blunt, X. Jiang, *Advanced techniques for assessment surface topography - Development of a basis for the 3D surface texture standards SURFSTAND.* Kogan Page Science, London, 2003.

[70] K.J. Stout, L. Blunt, *Methods for the development of surface parameters in three dimensions.* Kogan Page Science, London, 2000.

[71] B. Mandelbrot, *The fractal geometry of nature.* Freeman and Company, New York, 1977.

[72] M. Barnsley, *Fractals everywhere.* Academic Press Inc., San Diego, 1988.

[73] J. Feder, *Fractals.* Plenum Press, New York, 1988.

[74] P. Pfeifer, *Fractal dimension as working tool for surface-roughness problems*, *Appl. Surf. Sci.* **18** (1984) 146–164.

[75] T.R. Thomas, B.G. Rosen, N. Amini, *Fractal characterisation of the anisotropy of rough surfaces*, *Wear* **232** (1999) 41–50.

[76] M.A. Issa, M.A. Issa, Md.S. Islam, A. Chudnovsky, *Fractal dimension—-a measure of fracture roughness and toughness of concrete*, *Eng. Fract. Mech.* **70** (2003) 125–137.

[77] M. Pearson, G. Landini, R.M. Shelton, *Image and fractal analysis of osteoblastic cells in viscous media*, *J. Mater. Sci. Mater. Med.* **10** (1999) 761–765.

[78] A.N. dos Reis, J.C.M. Mombach, M. Walter, L.F. de Avila, *The interplay between cell adhesion and environment rigidity in the morphology of tumors*, *Physica A* **322** (2003) 546–554.

[79] R.D. Hazlett, *Fractal applications: wettability and contact angles*, *J. Colloid Interface Sci.* **137** (1990) 527–533.

[80] Y.S. Kim, K.H. Moon, J.H. Lim, *Surface fractals and wetting properties of porous anodes strengthened by Ni_3Al for molten carbonate fuel cell*, *Adv. Mater. Res.* **27** (2007) 861–864.

[81] A.K. Bisoi, J. Mishra, *On calculation of fractal dimension of images*, *Patt. Recogn. Lett.* **22** (2001) 631–637.

[82] D. Chappard, I. Degasne, G. Hure, E. Legrand, M. Audran,M. Basle, *Image analysis measurements of roughness by texture and fractal analysis correlate with contact profilometry*, *Biomaterials* **24** (2003) 1399–1407.

[83] T. Klov, E. Skjetne, J. Gudmundsson, *Fracture roughness characterization by shadow image analysis. International*, *Int. J. Fracture* **117** (2002) 85–100.

[84] S. Mahovic-Poljacek, D. Risovic, K. Furic, M. Gojo, *Comparison of fractal and profilometric methods for surface topography characterization*, *Appl. Surf. Sci.* **254** (2008) 3449–3458.

[85] A. Giorgilli, D. Casati, L. Sironi, L. Galgani, *An efficient procedureto compute fractal dimensions by box counting*, *Phys. Lett. A* **115** (1986) 202–206.

[86] W. Zahn, A. Zösch, *The dependance of fractal dimension on measuring conditions of scanning probe microscopy*, *Fresenius J. Analen. Chem.* **365** (1999) 168–172.

[87] W. Zahn, A. Zösch, *Characterization of thin film surfaces by fractal geometry*, *Fresenius J. Analen. Chem.* **358** (1997) 119–121.

[88] D. Nečas, P. Klapetek, *Gwyddion-Free SPM (AFM, SNOM/NSOM, STM, MFM,...) data analysis software*, 2015. Visited 15-10-2015.

[89] K. Jacobs, S. Herminghaus, K.R. Mecke, *Thin liquid polymer films rupture via defects*, *Langmuir* **14** (1998) 965–969.

[90] S. Herminghaus, K. Jacobs, K.R. Mecke, J. Bischof, A. Fery, M. Ibn-Elhaj, S. Schlagowski, *Spinodal dewetting in liquid crystal and liquid metal films*, *Science* **282** (1998) 916–919.

[91] F.D.E. Latief, B. Biswal, U. Fauzi, R. Hilfer, *Continuum reconstruction of the pore scale microstructure for Fontainebleau sandstone*, *Physica A* **389** (2010) 1607–1618.

[92] *ISO 4287:1997. Geometrical product specifications (GPS)-surface texture: profile method*, 1997. Geneva 437.

[93] M. Pfestorf, U. Engel, M. Geiger, *3D-surface parameters and their application on deterministic textured metal sheets*, *Int. J. Mach. Tool. Manufact.* **38** (1998) 607–614.

[94] F. Sacerdotti, F. Benati, C. Butler, B. Griffiths, *Closed regions: a proposal for spacing parameters for areal surface measurements*, *Meas. Sci. Technol.* **13** (2002) 556–546.

[95] K.R. Mecke, H. Wagner, *Euler characteristic and related measures for random geometric sets*, *J. Stat. Phys.* **64** (1991) 843–850.

[96] M. Kerscher, ch. Statistical analysis of large-scale structure in the universe, pp. 36–71. Springer, Berlin, 2000.

[97] G. Matheron, *Random sets and integral geometry*. J. Wiley & Sons, New York, 1975.

[98] K.R. Mecke, ch. Additivity, convexity, and beyond: applications of Minkowski functionals in statistical physics, pp. 111–184. Springer, Berlin, 2000.

[99] R. Hilfer, ch. Local porosity theory and stochastic reconstruction for porous media, pp. 203–241. Springer, Berlin, 2000.

[100] K.R. Mecke, Th. Butcher, H. Wagner, *Robust morphological measures for large scale structure in the universe*, *Astron. Astrophys.* **288** (1994) 697–714.

[101] D. Klain, G.C. Rota, *Introduction to geometric probability*. Cambridge University Press, London, 1997.

[102] J. Ohser, F. Mucklich, *Statistical analysis of microstructures in materials science*. John Wiley & Sons, New York, 2000.

[103] J. Becker, G. Grun, R. Seemann, H. Mantz, K. Jacobs, K.R. Mecke, R. Blossey, *Complex dewetting scenarios captured by thin-film models*, *Nature Materials* **2** (2003) 59–63.

[104] E.J. Abbott, F.A. Firestone, *Specifying surface quality: a method based on accurate measurement and comparison*, *Mechanical Engineering* **55** (1933) 569–572.

[105] J.J. Ramasco, J.M. López, M.A. Rodríguez, *Generic dynamic scaling in kinetic roughening*, *Phys. Rev. Lett.* **84** (2000) 2199–2202.

[106] R. Cuerno, L. Váquez, ch. Universality issues in surface kinetic roughening of thin solid films, pp. 111–184. Nova Science Publishers, New York, 2004.

[107] A.-L. Barabási, H.E. Stanley, *Fractal concepts in surface growth*. Cambridge University Press, Cambridge, 1995.

[108] R. Cafiero, *Kinetic roughening with anisotropic growth rules*, *Phys. Rev. E* **63** (2001) 046108.

[109] F.D.A. Aarão Reis, *Dynamic transition in etching with poisoning*, *Phys. Rev. E* **68** (2003) 041602.

[110] M.E.R. Dotto, M.U. Kleinke, *Scaling laws in etched Si surfaces*, *Phys. Rev. B* **65** (2002) 245323.

[111] M.A. Auger, L. Vázquez, R. Cuerno, M. Castro, M. Jergel, O. Sánchez, *Intrinsic anomalous surface roughening of TiN films deposited by reactive sputtering*, *Phys. Rev. B* **73** (2006) 045436.

[112] A.S. Balankin, D. Morales, O. Susarrey, D. Samayoa, J. Martínez-Trinidad, J. Márquez, R. García, *Self-similar roughening of drying wet paper*, *Phys. Rev. E* **73** (2006) 065105(R).

[113] P. Meakin, *Fractals, scaling and growth far from equilibrium.* Cambridge University Press, New York, 1998.

[114] T. Vicksek, *Fractal growth phenomena.* World Scientific, Singapore, 1992.

[115] R.S. Sayles, T.R. Thomas, *Surface topography as a nonstationary random process*, *Nature* **271** (1978) 431–434.

[116] G.R. Jafari, S.M. Fazeli, F. Ghasemi, F.S.M. Vaez Allaei, M. Reza Rahimi Tabar, A. Iraji Zad, G. Kavei, *Stochastic analysis and regeneration of rough surfaces*, *Phys. Rev. Lett.* **91** (2003) 22601.

[117] E. Quartarone, P. Mustarelli, C. Poggio, M. Lombardini, *Surface kinetic roughening caused by dental erosion: an atomic force microscopy study*, *J. Appl. Phys.* **103** (2008) 104702.

[118] F. Family, T. Vicksek, *Dynamics of fractal surfaces.* World Scientific, Singapore, 1991.

[119] P. Meakin, *The growth of rough surfaces and interfaces*, *Phys. Rep.* **235** (1993) 189–289.

[120] H.G.E. Hentschel, F. Family, *Scaling in open dissipative systems*, *Phys. Rev. Lett.* **66** (1991) 1982–1985.

[121] V.K. Horvath, F. Family, T. Vicsek, *Dynamic scaling of the interface in two-phase viscous flows in porous media*, *J. Phys. A* **24** (1991) L25.

[122] A. Be'er, Y. Lereah, H. Taitelbaum, *The dynamics and geometry of solid-liquid reaction interface*, *Physica A* **285** (2000) 156–165.

[123] A. Be'er, Y. Lereah, I. Hecht, H. Taitelbaum, *The roughness and growth of a silver-mercury reaction interface*, *Physica A* **302** (2001) 297–301.

[124] S.V. Buldyrev, A.-L. Barabasi, F. Caserta, S. Havlin, H.E. Stanley, T. Vicsek, *Anomalous interface roughening in porous media: experiment and model*, *Phys. Rev A* **45** (1992) R8313–R8316.

[125] J. Palacios, *Análisis dimensional.* Espasa-Calpe S.A., Madrid, 1964.

[126] J. Krug, *Origins of scale invariance in growth processes*, *Adv. Phys.* **46** (1997) 139–149.

[127] E. Zakka, V. Constantoudis, E. Gogolides, *Roughness formation during plasma etching of composite materials: a kinetic Monte Carlo approach*, *IEEE Trans. Plasma Sci.* **35** (2007) 1359–1369.

[128] F.D.A. Aarão Reis, *Dynamic transition in deposition with a poisoning species*, *Phys. Rev. E* **66** (2002) 027101.

[129] J.M. López, M.A. Rodríguez, R. Cuerno, *Power spectrum scaling in anomalous kinetic roughening of surfaces*, *Physica A* **246** (1997) 329–347.

[130] J.M. López, M. Castro, R. Gallego, *Scaling of local slopes, conservation laws, and anomalous roughening in surface growth*, *Phys. Rev. Lett.* **94** (2005) 166103.

[131] S. Morel, J. Schmittbuhl, J.M. López, G. Valentin, *Anomalous roughening of wood fractured surface*, *Phys. Rev. E* **58** (1998) 6999–7005.

[132] P.G. de Gennes, F. Brochard-Wyart, D. Quéré, *Capillarity and wetting phenomena. Drops, bubbles, pearls, waves.* Springer, New York, 2004.

[133] H. Emmerich, *The diffusive interface approach in materials science: thermodynamic concepts and applications of phase-field models.* Springer, New York, 2003.

[134] M.A. Rodríguez-Valverde, *Caracterización interfacial de emulsiones de interés tecnológico.* PhD thesis, University of Granada, 2002.

[135] J. Lyklema, *Fundamentals of interface and colloid science.* Elsevier, New York, 2005.

[136] T. Young, *An essay on the cohesion of fluids*, *Phil. Trans. Roy. Soc.* **95** (1805) 65–87.

[137] P.S. Laplace, ch. Supplement a la theorie de l'action capillaire, pp. 419–498. De L'Imprimerie de Crapelet: Chez J.B.M. Duprat, Paris, 1806.

[138] F.J. Ruiz-Cabello, *Efecto de la rugosidad y heterogeneidad superficial en fenómenos de mojado.* PhD thesis, University of Granada, 2009.

[139] T. Chen, M.S. Chiu, C.N. Weng, *Derivation of the generalized Young-Laplace equation of curved interfaces in nanoscaled solids*, *J. Appl. Phys.* **100** (2006) 074308.

[140] Y. Larther, *A very simple derivation of Young's law with gravity using a cylindrical meniscus*, *Langmuir* **13** (1997) 7299–7300.

[141] P.S. Swain, R. Lipowsky, *Contact angles on heterogeneous surfaces: a new look at Cassie's and Wenzel's laws*, *Langmuir* **14** (1998) 6772–6780.

[142] A. Marmur, *Soft contact: measurement and interpretation of contact angles*, *Soft Matter* **2** (2006) 12–18.

[143] P. Roura, J. Fort, *Local thermodynamic derivation of Young's equation*, *J. Colloid Interface Sci.* **272** (2004) 420–429.

[144] M.A. Rodríguez-Valverde, F.J. Montes Ruiz-Cabello, M.A. Cabrerizo-Vílchez, *Wetting on axially-patterned heterogeneous surfaces*, *Adv. Colloid Interface Sci.* **138** (2008) 84–100.

[145] R.N. Wenzel, *Resistance of solid surfaces to wetting by water*, *Ind. Eng. Chem.* **28** (1936) 988–994.

[146] R.N. Wenzel, *Surface roughness and contact angle*, *J. Phys. Chem.* **53** (1949) 1466–1467.

[147] D. Quéré, *Wetting and roughness*, *Annu. Rev. Mater. Res.* **38** (2008) 71–99.

[148] A.B.D. Cassie, *Contact angles*, *Discussion Faraday Society* **3** (1948) 11–16.

[149] S. Brandon, N. Haimovich, E. Yeger, A. Marmur, *Partial wetting of chemically patterned surfaces: the effect of drop size*, *J. Colloid Interface Sci.* **263** (2003) 237–243.

[150] N.A. Patankar, *On the modeling of hydrophobic contact angles on rough surfaces*, *Langmuir* **19** (2003) 1249–1253.

[151] T.S. Chow, *Nanoscale surface roughness and particle adhesion on structured substrates*, *Nanotechnology* **18** (2007) 115713.

[152] I.J. Ford, *Effect on friction for multi-asperity contact between surfaces*, *J. Phys. D Appl. Phys.* **26** (1993) 2219–2225.

[153] S. Semal, T.D. Blake, V. Geskin, M.J. de Ruijter, G. Castelein, J. De Coninck, *Influence of surface roughness on wetting dynamics*, *Langmuir* **15** (1999) 8765–8770.

[154] V.N. Koinkar, B. Bhushan, *Effect of scan size and surface roughness on microscale friction measurements*, *J. Appl. Phys.* **81** (1997) 2472–2479.

[155] T. Ichihara, T. Baba, T. Komoda, N. Koshida, *Correlation between nanostructure and electron emission characteristics of a ballistic electron surface-emitting device*, *J. Vac. Sci. Technol. B* **22** (2004) 1372–1376.

[156] G. Carter, *The physics and applications of ion beam erosion*, *J. Phys. D Appl. Phys.* **34** (2001) R1–R22.

[157] H.F. Li, C.F. Cheung, X.Q. Jiang, W.B. Lee, S. To, *A novel robust Gaussian filtering method for the characterization of surface generation in ultra-precision machining*, *Precis. Eng.* **30** (2006) 421–430.

[158] H. Zahouani, R. Vargiolu, P. Kapsa, J.L. Loubet, T.G. Mathia, *Effect of lateral resolution on topographical images and three-dimensional functional parameters*, *Wear* **219** (1998) 114–123.

[159] G.J. Simpson, D.L. Sedin, K.L. Rowlen, *Surface roughness by contact versus tapping mode atomic force microscopy*, *Langmuir* **15** (1999) 1429–1434.

[160] J. Krim, I. Heyvaert, C. Vanhaesendonck, Y. Bruynseraede, *Scanning tunneling microscopy observation of self-affine fractal roughness in ion-bombarded film surfaces*, *Phys. Rev. Lett.* **70** (1993) 57–60.

[161] S. Hyun, L. Pei, J.F. Molinari, M.O. Robbins, *Finite-element analysis of contact between elastic self-affine surfaces*, *Phys. Rev. E* **70** (2004) 026117.

[162] C. Portesi, S. Borini, G.B. Picotto, E. Monticone, *AFM analysis of MgB_2 films and nanostructures*, *Surf. Sci.* **601** (2007) 58–62.

[163] T.S. Chow, *Nanoadhesion between rough surfaces*, *Phys. Rev. Lett.* **86** (2001) 4592–4595.

[164] F. Rupp, L. Scheideler, D. Rehbein, D. Axmann, J. Gels-Gerstorfer, *Roughness induced dynamic changes of wettability of acid etched titanium implant modifications*, *Biomaterials* **25** (2004) 1429–1438.

[165] D. Quéré, *Rough ideas on wetting*, *Physica A* **313** (2002) 32–46.

[166] R.V. Bathomarco, G. Solorzano, C.N. Elias, R. Prioli, *Atomic force microscopy analysis of different surface treatments of Ti dental implant surfaces*, *Appl. Surf. Sci.* **233** (2004) 29–34.

[167] G. Udupa, M. Singaperumal, R.S. Sirohi, M.P. Kothiyal, *Characterization of surface topography by confocal microscopy I: principles and the measurement system*, *Meas. Sci. Technol.* **11** (2000) 315–329.

[168] H. Kamusewitz, W. Possart, *Wetting and scanning force microscopy on rough polymer surfaces: Wenzel's roughness factor and the thermodynamic contact angle*, *Appl. Phys. A Mater.* **76** (2003) 899–9025.

[169] C.Y. Poon, B. Bhushan, *Comparison of surface roughness measurements by stylus profiler, AFM and non-contact optical profiler*, *Wear* **190** (1995) 76–88.

[170] L. Lai, E.A. Irene, *Area evaluation of microscopically rough surfaces*, *J. Vac. Sci. Technol. B* **17** (1999) 33–39.

[171] J. Raja, B. Muralikrishnan, S. Fu, *Recent advances in separation of roughness, waviness and form*, *Precis. Eng.* **26** (2002) 222–235.

[172] U. Wendt, K. Stiebe-Lange, M. Smid, *On the influence of imaging conditions and algorithms on the quantification of surface topography*, *J. Microscopy* **207** (2002) 169–179.

[173] J. Kumar, M.S. Shunmugam, *Fitting of robust reference surface based on least absolute deviations*, *Precis. Eng* **31** (2007) 102–113.

[174] S.J. Ahn, *Least squares orthogonal distance fitting of curves and surfaces in space*. Springer, Berlin, NY, 2004.

[175] S.J. Ahn, W. Rauh, M. Recknagel, *Least squares orthogonal distance fitting of implicit curves and surfaces*, *Lecture notes in computer science* **2191** (2001) 398–405.

[176] W. Li, A. Amirfazli, *Microtextured superhydrophobic surfaces: a thermodynamic analysis*, *Adv. Colloid. Interf. Sci.* **132** (2007) 51–68.

[177] M. Miwa, A. Nakajima, A. Fujishima, K. Hashimoto, T. Watanabe, *Effects of the surface roughness on sliding angles of water droplets on superhydrophobic surfaces*, *Langmuir* **16** (2000) 5754–5760.

[178] C. Yang, U. Tartaglino, B.N.J. Persson, *Influence of surface roughness on superhydrophobicity*, *Phys. Rev. Lett.* **97** (2006) 116103.

[179] W. Li, A. Amirfazli, *A thermodynamic approach for determining the contact angle hysteresis for superhydrophobic surfaces*, *J. Colloid. Interf. Sci.* **292** (2005) 195–201.

[180] M.P. do Carmo, *Differential geometry of curves and surfaces*. Prentice-Hall, Englewood Cliffs, 1976.

[181] J. Oprea, *Differential geometry and its applications*. Prentice-Hall, Upper Saddle River, NJ, 1997.

[182] T. Jossang, J. Feder, *The fractal characterization of rough surfaces*, *Phys. Scripta* **T44** (1992) 9–14.

[183] G. Palasantzas, *Wetting on rough self-affine surfaces*, *Phys. Rev. B* **51** (1995) 14612–14615.

[184] A. Dathe, P. Baveye, *Dependence of the surface fractal dimension of soil pores on image resolution and magnification*, *Eur. J. Soil Sci.* **54** (2003) 453–466.

[185] M. Gopi, S. Krishnan, C.T. Silva, *Surface reconstruction based on lower dimensional localized Delaunay triangulation*, *Comput. Graph Forum* **19** (2000) C467.

[186] G. Franceschetti, A. Iodice, M. Migliaccion, D. Riccio, *Scattering from natural rough surfaces modeled by fractional Brownian motion two-dimensional processes*, *IEEE Trans. Antenn. Propag.* **47** (1999) 1405–1415.

[187] B.B. Mandelbrot, J.W. van Ness, *Fractional brownian motions, fractional noises and applications*, *SIAM Review* **10** (1968) 422–437.

[188] J.C. Russ, *The image processing handbook*, vol. th. CRC Press, Inc., Boca Raton, FL, USA, 2006.

[189] A. Amirfazli, A.W. Neumann, *Status of the three-phase line tension*, *Adv. Colloid Inter. Sci.* **110** (2004) 551–560.

[190] L. Ponsonnet, K. Reybier, N. Jaffrezic, V. Comte, C. Lagneau, M. Lissac, C. Martelet, *Relationship between surface properties (roughness, wettability) of titanium and titanium alloys and cell behavior*, *Mat. Sci. Eng. C Bio. S.* **23** (2003) 551–560.

[191] P.G. de Gennes, *Wetting: statics and dynamics*, *Rev. Mod. Phys.* **57** (1985) 827–863.

[192] D. Li, A.W. Neumann, *A reformulation of the equation of state for interfacial-tensions*, *J. Colloid Inter. Sci.* **137** (1990) 304–307.

[193] D. Li, A.W. Neumann, *Equation of state for interfacial-tensions of solid-liquid systems*, *Adv. Colloid Inter. Sci.* **39** (1992) 299–345.

[194] P.J. Ramón-Torregrosa, M.A. Rodríguez-Valverde, A. Amirfazli, M.A. Cabrerizo-Vílchez, *Factors affecting the measurement of roughness factor of surfaces and its implications for wetting studies*, *Coll. Surf. A* **323** (2008), no. 1-3 83–93.

[195] T.S. Chow, *Wetting of rough surfaces*, *J. Phys. Condens. Mat* **10** (1998) L445–L451.

[196] G. Palasantzas, J.Th.M. de Hosson, *Wetting on rough surfaces*, *Acta Materialia* **49** (2001) 3533–3538.

[197] K.Tønder, *Dynamics of rough slider bearings: effects of one-sided roughness/waviness*, *Tribology International* **29** (1996) 117–122.

[198] M.G. Donoso, A. Méndez-Vilas, J.M. Bruque, M.L. González-Martin, *On the relationship between common amplitude surface roughness parameters and surface area : Implications for the study of cell material interactions*, *Int. Biodeterior. Biodegrad* **59** (2007) 245–251.

[199] H. Kamusewitz, W. Possart, *Wetting and scanning force microscopy on rough polymer surfaces: Wenzel's roughness factor and the thermodynamic contact angle*, *Appl. Phys. A Mater.* **76** (2003) 899–902.

[200] R.R. Deshmukh, A.R. Shetty, *Comparison of surface energies using various approaches and their suitability*, *J. Appl. Polym. Sci.* **107** (2008) 3707–3717.

[201] H. Kamusewitz, W. Possart, ch. The static contact angle hysteresis and Young's equilibrium contact angle, pp. 101–114. VSP, Utrecht, 2006.

[202] R.J. Good, M.K. Chaudhury, C. Yeung, *A new approach for determining roughness by means of contact angles on solids*, in *First International Congress on Adhesion Science And Technology*, pp. 181–197, 1998.

[203] I.V. Katardjiev, *A kinematic model of surface evolution during growth and erosion: Numerical analysis*, *J. Vacuum. Sci. Tech. A* **7** (1989) 3222–3232.

[204] S. Mezghani, H. Zahouani, *Characterisation of the 3D waviness and roughness motifs*, *Wear* **257** (2004) 1250–1256.

[205] J. Kumar, M.S. Shunmugam, *A new approach for filtering of surface profiles using morphological operations*, *Int. J. Mach Tools Manuf.* **46** (2006) 260–270.

[206] J.G. Yu, J.G. Amar, *Scaling behavior of the surface in ballistic deposition*, *Phys. Rev. E* **65** (2002) 102–113.

[207] D.T. Lee, B.J. Schachter, *Two algorithms for constructing delaunay triangulations*, *Itnl. J. Computer. Information. Sci.* **9** (1980) 219–242.

[208] R.E. Maeder, *The Mathematica Programmer: Fractional brownian motion*, *Mathematical J.* **6** (1995) 38–48.

[209] M.J. Dalby, N. Gadegaard, A.S.G. Curtis, R.O.C. Oreffo, *Nanotopographical control of human osteoprogenitor differentiation*, *Curr. Stem Cell Res. Ther.* **2** (2007) 129–138.

[210] C.M. Bidan, K.P. Kommareddy, M. Rumpler, P. Kollmannsberger, P. Fratzl, J.W.C. Dunlop, *Geometry as a factor for tissue growth: towards shape optimization of tissue engineering scaffolds*, *Adv. Healthcare Mater.* **2** (2013) 186–194.

[211] C.N. Salinas, K.S. Anseth, *The enhancement of chondrogenic differentiation of human mesenchymal stem cells by enzymatically regulated RGD functionalities*, *Biomaterials* **29** (2008) 2370–2377.

[212] J. Park, S. Bauer, K. van der Mark, P. Schmuki, *Nanosize and vitality: TiO_2 nanotube diameter directs cell fate*, *Nano Lett.* **7** (2007) 1686–1691.

[213] J.I. Rosales-Leal, M.A. Rodríguez-Valverde, G. Mazzaglia, P.J. Ramón-Torregrosa, L. Díaz-Rodríguez, O. García-Martínez, M. Vallecillo-Capilla, C. Ruiz, M.A. Cabrerizo-Vílchez, *Effect of roughness, wettability and morphology of engineered titanium surfaces on osteoblast-like cell adhesion*, *Colloids Surf., A* **365** (2010) 222–229.

[214] J. Chen, *Nanobiomechanics of living cells: a review*, *Interface Focus* **4** (2014).

[215] A.Méndez-Vilas, M.G. Donoso, J.L. González-Carrasco, M.L. González-Martín, *Looking at the micro-topography of polished and blasted Ti-based biomaterials using atomic force microscopy and contact angle goniometry*, *Colloids Surf., B* **52** (2006) 157–166.

[216] J. Schmäehling, *Statistical characterization of technical surface microstructure*. PhD thesis, University of Heidelberg, 2006.

[217] J. Steele, *Characterizing 3D microstructure using the Minkowski functionals*, *Microsc. Microanal.* **13** (2007) 1658–1659.

[218] A. Terriza, R. Alvárez, A. Borrás, J. Cotrino, F. Yubero, A.R. González-Elipe, *Roughness assessment and wetting behavior of fluorocarbon surfaces*, *J. Colloid Interface Sci.* **376** (2012) 274–282.

[219] D. Aurongzeb, *Etch front roughening in wrinkly metal*, *Appl. Surf. Sci.* **253** (2006) 1717–1721.

[220] D.M. Brunette, P. Tengvall, M. Textor, P. Thomsen, *Titanium in Medicine: Material Science, Surface Science, Engineering, Biological Responses and Medical Applications*. Springer Verlag, Heidelberg and Berlin, 2001.

[221] J.M. López, *Scaling approach to calculate critical exponents in anomalous surface roughening*, *Phys. Rev. Lett.* **83** (1999) 4594–4597.

[222] R. Cafiero, V. Loreto, P. Prosini, *Anisotropy and non-universality in kinetic roughening*, *Europhys. Lett.* **42** (1998) 389–394.

[223] S.B. Santra, B. Sapoval, *Critical fluctuations and self-organized fractality in chemical reactions: Spontaneous gradient percolation in the etching of random solids*, *Physica A* **266** (1999) 160–172.

[224] S. Szmukler-Moncler, M. Bischof, R. Nedir, M. Ermrich, *Titanium hydride and hydrogen concentration in acid-etched commercially pure titanium and titanium alloy implants: a comparative analysis of five implant systems*, *Clin. Oral Impl. Res.* **21** (2010) 944–950.

[225] M. Morra, C. Cassinelli, G. Bruzzone, A. Carpi, G. Di Santi, R. Giardino, M. Fini, *Surface Chemistry Effects of Topographic Modification of Titanium Dental Implant Surfaces: 1. Surface Analysis*, *Int. J. Oral Maxillofac. Implants* **18** (2003) 40–45.

[226] M. Morra, C. Cassinelli, G. Bruzzone, A. Carpi, G. Di Santi, R. Giardino, M. Fini, *Surface Chemistry Effects of Topographic Modification of Titanium Dental Implant Surfaces: 2. In Vitro Experiments*, *Int. J. Oral Maxillofac. Implants* **18** (2003) 46–52.

[227] T. Yoshinobu, A. Iwamoto, H. Iwasaki, *Scaling analysis of SiO_2/Si interface roughness by atomic force microscopy*, *Jpn. J. Appl. Phys.* **33** (1994) 383–387.

[228] M. Elwenspock, *On the mechanism of anisotropic etching of silicon*, *J. Electrochem. Soc.* **140** (1993) 2075–2080.

[229] H. Seidel, L. Csepregi, A. Henberger, H. Boumgartel, *Anisotropic etching of crystalline silicon in alkaline solutions I. Orientation dependence and behavior of passivation layers*, *J. Electrochem. Soc.* **137** (1990) 3612–3626.

[230] J.Y. Martin, Z. Schwartz, T.W. Hummert, D.M. Schraub, J. Simpson, J. Lankford, D.D. Dean, D.L. Cochran, B.D. Boyan, *Effect of titanium surface-roughness on proliferation, differentiation, and protein-synthesis of human osteoblast-like cells (Mg63)*, *J. Biomed. Mater. Res.* **29** (1995) 389–401.

[231] D.D. Deligianni, N. Katsala, S. Ladas, D. Sotiropoulou, J. Amedee, Y.F. Missirlis, *Effect of surface roughness of the titanium alloy Ti-6Al-4V on human bone marrow cell response and on protein dsorption*, *Biomaterials* **22** (2001) 1241–1251.

[232] C.J. Hsieh, *Studies on surface modifications of material for tissue engineering applications*. University of Pittsburgh, 2006.

[233] S. Ban, Y. Iwaya, H. Kono, H. Sato, *Surface modification of titanium by etching in concentrated sulfuric acid*, *Dental Materials* **22** (2006) 1115–1120.

[234] D.L. Cochran, P.V. Nummikoski, F.L. Higginbottom, J.S. Hermann, S.R. Makins, D. Buser, *Evaluation of an endosseous titanium implant with a sandblasted and acid-etched surface in the canine mandible: Radiographic results*, *Clin. Oral Implan. Res.* **7** (1996) 240–252.

[235] T. Ogawa, S. Ozawa, J.H. Shih, K.H. Ryu, C. Sukotjo, J.M. Yang, I. Nishimura, *Biomechanical evaluation of osseous implants having different surface topographies in rats*, *J. Dent. Res.* **79** (2000) 1857–1863.

[236] D. Perrin, S. Szmukler-Moncler, C. Echikou, P. Pointaire, J.P. Bernard, *Bone response to alteration of surface topography and surface composition of sandblasted and acid etched (SLA) implants*, *Clin. Oral Implan. Res.* **13** (2002) 465–469.

[237] M.A. Fernández-Rodríguez, A.Y. Sánchez-Treviño, E. De Luna-Bertos, J. Ramos-Torrecillas, O. García-Martínez, C. Ruiz, M.A. Rodríguez-Valverde, M.A. Cabrerizo-Vílchez, *Wettability and osteoblastic cell adhesion on ultrapolished commercially pure titanium surfaces: the role of the oxidation and pollution states*, *J. Adhes. Sci. Technol.* **28** (2014) 1207–1218.

[238] Y.A. Buslaev, V.A. Bochkareva, N.S. Nikolaev, *The reaction of titanium dioxide with hydrofluoric acid*, *Russian Chemical Bulletin* **11** (1962) 361–364.

[239] E.M.M. Sutter, G.J. Goetz-Grandmont, *The behavior of titanium in nitric-hydrofluoric acid solutions*, *Corrosion Sci.* **30** (1990) 461–476.

[240] K.S. Kim, J.A. Hurtado, H. Tan, *Evolution of a surface-roughness spectrum caused by stress in nanometer-scale chemical etching*, *Phys. Rev. Lett.* **83** (1999) 3872–3875.

[241] U. Schwarz, G. Gompper, ch. Bicontinuous Surfaces in Self-assembling Amphiphilic Systems, pp. 107–151. Birkhäuser Basel, 2002.

[242] P.I. Branemark, B.O. Hansonn, R. Adell, U. Breine, J. Lindstrom, O. Hallen, A. Ohman, *Osseointegrated titanium implants in the treatment of the edentulous jaw*, *Scand. J. Plast. Reconstr. Surg.* **11** (1977) 171–175.

[243] T. Albrektsson, P.I. Branemark, H.A. Hanson, J. Lindstrom, *Osseointegrated titanium implants. Requirements for ensuring a long-lasting, direct bone anchorage in man*, *Acta Orthop. Scand.* **52** (1981) 155–170.

[244] S.H. Jun, E.J. Lee, S.W. Yook, H.E. Kim, H.W. Kim, Y.H. Koh, *Nanostructured poly(epsilon-caprolactone)-silica xerogel fibrous membrane for guided bone regeneration*, *Acta Biomater.* **6** (2010) 302–307.

[245] S. Bodhak, S. Bose, A. Bandyopadhyay, *Role of surface charge and wettability on early stage mineralization and bone cell-materials interactions of polarized -Hydroxyapatite*, *Acta Biomater.* **5** (2009) 2178–2188.

[246] Okada, H. Ito, A. Nagai, J. Komotori, H. Imai, *Adhesion of osteoblast-like cells on nanostructured hydroxyapatite*, *Acta Biomater.* **6** (2010) 591–597.

[247] D. Botticelli, T. Berglundh, D. Buser, J. Lindhe, *The jumping distance revisited. An experimental study in the dog*, *Clin. Oral. Implant. Res.* **14** (2003) 35–42.

[248] L. Le Guehennec, M.A. López-Heredia, B. Enkel, P. Weiss, Y. Amouriq, P. Layrolle, *Osteoblastic cell behaviour on different titanium implant surfaces*, *Acta Biomater.* **4** (2008) 535–543.

[249] J. Park, S. Bauer, K.A. Schlegel, F.W. Neukam, K. von der Mark, P. Schmuki, *TiO_2 nanotube surfaces: 15nm an optimal length scale of surface topography for cell adhesion and differentiation*, *Small* **5** (2009) 666–671.

[250] M. Vandrovcová, L. Bačáková, *Adhesion, growth and differentation of osteoblasts on surface-modified materials developed for bone implants*, *Physiol. Res.* **60** (2011) 403–417.

[251] K. Anselme, *Osteoblast adhesion on biomaterials*, *Biomaterials* **21** (2000) 667–681.

[252] M. Bachle, R. J. Kohal, *A systematic review of the influence of different titanium surfaces on proliferation, differentiation and protein synthesis of osteoblast-like MG63 cells*, *Clin. Oral Implants Res* **15** (2004) 683–692.

[253] H. Assender, V. Bliznyuk, K. Porfyrakis, *How surface topography relates to materials properties*, *Science* **9** (2002) 973–976.

[254] R.G. Flemming, C.J. Murphy, G.A. Abrams, S.L. Goodman, P.F. Nealy, *Effects of synthetic micro- and nano-structured surfaces on cell behavior*, *Biomaterials* **20** (1999) 573–588.

[255] J.Y. Martin, Z. Schwartz, T.W. Hummert, D.M. Schraub, J. Simpson, J. Lankford, D.D. Dan, D.L. Cochran, B.D. Boyan, *Effect of titanium surface roughness on proliferation, differentiation, and protein synthesis of human osteoblast-like cells (MG63)*, *J. Biomed. Mater. Res.* **29** (1995) 389–401.

[256] K. Kieswetter, Z. Schwartz, T.W. Hummert, D.L. Cochran, J. Simpson, D.D. Dean and B.D. Boyan, *Surface roughness modulates the local production of growth factors and cytokines by osteoblast-like MG-63 Cells*, *J. Biomed. Mater. Res.* **32** (1996) 55–63.

[257] A. Wennerberg, T. Albrektsson, *Effects of titanium surface topography on bone integration: a systematic review*, *Clin. Oral Implants Res* **20** (2009) 172–184.

[258] S.R. Paital, N.B. Dahotre, *Wettability and kinetics of hydroxyapatite precipitation on a laser-textured Ca-P bioceramic coating*, *Acta Biomater.* **5** (2009) 2763–2772.

[259] R.A. Gittens, T. McLachlan, R. Olivares-Navarrete, Y. Cai, S. Berner, R. Tannenbaum, Z. Schwartz, K.H. Sandhage, B.D. Boyan, *The effects of combined micron-/submicron-scale surface roughness and nanoscale features on cell droliferation and differentiation*, *Biomaterials* **32** (2011) 3395–3404.

[260] Y. Wu, J.P. Zitelli, K.S. Tenhuisen, X. Yu, M.R. Libera, *Differential response of saphylococci and osteoblasts to varying titanium sufrace roughness*, *Biomaterials* **32** (2011) 951–960.

[261] R.A. Gittens, R. Olivares-Navarrete, T. McLachlan, Y. Cai, S.L. Hyzy, J.M. Schneider, Z. Schwartz, K.H. Sandhage, B.D. Boyan, *Differential response of osteoblast lineage cells to nanotopographically-modified, microroughened titanium-aluminium-vanadium alloy surfaces*, *Biomaterials* **33** (2012) 8986–8994.

[262] H.H. Huang, C.T. Ho, T.H. Lee, T.L. Lee, K.K. Liao, F.L. Chen, *Effect of surface roughness of ground titanium on initial cell adhesion*, *Biomol. Eng.* **21** (2004) 93–97.

[263] S. Mwenifumbo, M. Li, J. Chen, A. Beye, W. Soboyejo, *Cell/surface interactions on laser micro-textured titanium-coated silicon surfaces*, *J. Mater. Sci. Mater. Med.* **28** (2007) 9–23.

[264] Y. Arima, H. Iwata, *Effect of wettability and surface functional groups on protein adsorption and cell adhesion using well-defined mixed self-assembled monolayers*, *Biomaterials* **28** (2007) 3074–3082.

[265] H. Schweikl, R. Muller, C. Englert, K.A. Hiller, R. Kujat, M. Nerlich, G. Schmalz, *Proliferation of osteoblasts and fibroblasts on model surfaces of varying roughness and surface chemistry*, *J. Mater. Sci. Mater. Med.* **18** (2007) 1895–1905.

[266] D.V. Kilpadi, J.E. Lemons, *Surface energy characterization of unalloyed titanium implants*, *J. Biomed. Mater. Res.* **28** (1994) 1419–1425.

[267] A.W. Adamson, A.P. Gast, *Physical chemistry of surfaces.* Wiley, NY, 1997.

[268] X. Zhu, J. Chen, L. Scheideler, R. Reichl, J Geis-Gerstorfer, *Effects of topography and composition of titanium surface oxides on osteoblast responses*, *Biomaterials* **25** (2004) 4087–4103.

[269] L. Hao, J. Lawrence, K.S. Chian, *Osteoblast cell adhesion on a laser modified zirconia based bioceramic*, *J. Mater. Sci. Mater. Med.* **16** (2005) 719–726.

[270] M.C. Advincula, F.G. Rahemtulla, R.C. Advincula, E.T. Ada, J.E. Lemons, S.L. Bellis, *Osteoblast adhesion and matrix mineralization on sol-gel derived titanium oxide*, *Biomaterials* **27** (2006) 2201–2212.

[271] M.I. Janssen, M.B. Van Leeuwen, T.J. van Coten, J. de Vries, L. Dijkhuizen, H.A. Wösten, *Promotion of fibroblast activity by coating with hydrophobins in the beta-sheet end state*, *Biomaterials* **25** (2004) 2731–2739.

[272] R.E. Baier, *Surface behavior of biomaterials: the theta surface for biocompatibility*, *J. Mater. Sci. Mater. Med.* **17** (2006) 1057–1062.

[273] F. Rupp, L. Scheideler, J. Geis-Gerstorfer, *Effect of heterogenic surfaces on contact angle hysteresis: dynamic contact angle analysis in material sciences*, *Chem. eng. Technol.* **25** (2002) 877–882.

[274] M. Bächle, R.J. Kohal, *A systematic review of the influence of different titanium surfaces on proliferation, differentiation and protein synthesis of osteoblast-like MG63 cells*, *Clin. Oral. Implants Res.* **15** (2004) 683–692.

[275] A. Bagno, C. Di Bello, *Surface treatments and roughness properties of Ti-based biomaterials*, *J. Mater. Sci. Mater. Med.* **15** (2004) 935–949.

[276] D. Arcos, M. Vallet-Regi, *Sol-gel silica based biomaterials and bone tissue regeneration*, *Acta Biomater.* **6** (2010) 2874–2888.

[277] M. Padial-Molina, P. Galindo-Moreno, G. Avila-Ortiz, *Biomimetic ceramics in implant dentistry*, *Minerva Biotec.* **21** (2009) 173–186.

[278] P. Galindo-Moreno, G Avila, J.E. Fernandez-Barbero, F. Mesa, F. O'Valle-Ravassa, H.L. Wang, *Clinical and histologic comparison of two different composite grafts for sinus augmentation: a pilot clinical trial*, *Clin. Oral Implants Res.* **19** (2008) 755–759.

[279] M.E.R. Dotto, M.U. Kleinke, *Kinetic roughening in etched Si*, *Physica A* **295** (2000) 149–153.

[280] J.L. Ortega-Vinuesa, P. Tengvall, I. Lundstrom, *Aggregation of HSA, IgG, and fibrinogen on methylated silicon surfaces*, *J. Colloid Interf. Sci.* **15** (1998) 228–239.

[281] B. Walivaara I. Lundstrom, P. Warkentin, P. Tengvall, *Differential surface binding of albumin, immunoglobulin G and fibrinogen*, *Biomaterials* **15** (1994) 786–795.

[282] M.L. Snyder, H.C. Lichstein, *Sodium azide as an inhibiting substance for gram-negative bacteria*, *J. Infect. Dis.* **67** (1940) 113–115.

[283] M. Morra, C. Cassinelli, *Evaluation of surface contamination of titanium dental implants by LV-SEM: comparison with XPS measurements*, *Surf. Interface. Anal.* **25** (1997) 983–988.

[284] H.A. Wege, J.A. Holgado-Terriza, J.I. Rosales-Leal, R. Osorio, M. Toledano, M.A. Cabrerizo-Vílchez, *Contact angle hysteresis on dentin surfaces measured with ADSA on drops and bubbles*, *Colloids Surf. A: Physicochem. Eng. Aspects* **206** (2002) 469–483.

[285] M.A. Rodriguez-Valverde, M.A. Cabrerizo-Vilchez, P. Rosales-Lopez, A. Paez-Duenas, R. Hidalgo-Alvarez, *Contact angle measurements on two (wood and stone) non-ideal surfaces*, *Coll. Surf. A* **206** (2002) 485–495.

[286] J.E. Fernández-Barbero, P. Galindo-Moreno, G. Ávila-Ortiz, O. Caba, E. Sánchez-Fernández, H.L. Wang, *Flow cytometric and morphological characterization of platelet-rich plasma gel*, *Clin Oral Implants Res.* **17** (2006) 687–693.

[287] A.S. Daar, S.V. Fuggle, J.W. Fabre, A. Ting, P.J. Morris, *The detailed distribution of MHC class II antigens in normal human organs*, *Transplantation* **38** (1984) 287–292.

[288] E. Fuchs, K. Weber, *Intermediate filaments: structure, dynamics, function and disease*, *Annu. Rev. Biochem.* **63** (1994) 345–382.

[289] R.L. Kitchens, *Role of CD14 in cellular recognition of bacterial lipopolysaccharides*, *Chem. Immunol.* **74** (2000) 61–82.

[290] N.D. Huntington, D.M. Tarlinton, *CD45: direct and indirect government of immune regulation*, *Immunol. Lett.* **94** (2004) 167–174.

[291] E. Oliva, *CD10 expression in the female genital tract: does it have useful diagnostic applications?*, *Adv. Anat. Pathol.* **11** (2004) 310–315.

[292] J.E. Rabinowitz, U. Rutishauser, T. Magnuson, *Targeted mutation of Ncam to produce a secreted molecule results in a dominant embryonic lethality*, *Proc. Natl. Acad. Sci. USA* **93** (1996) 6421–6424.

[293] G.J. Doherty, H.T. McMahon, *Mediation, modulation, and consequences of membrane-cytoskeleton interactions*, *Annu. Rev. Biophys.* **37** (2008) 65–95.

[294] N.K. Lee, H. Sowa, E. Hinoi, M. Ferron, J.D. Ahn, C. Confavreux, R. Dacquin, P.J. Mee, M.D. McKee, D.Y. Jung, Z. Zhang, J.K. Kim, F. Mauvais-Jarvis, P. Ducy, G. Karsenty, *Endocrine regulation of energy metabolism by the skeleton*, *Cell* **130** (2007) 456–469.

[295] T. Scholzen, J. Gerdes, *The Ki-67 protein: from the known and the unknown*, *J. Cell Physiol.* **182** (2000) 311–322.

[296] E. Daryaei, M. Reza Rahimi Tabar, A.Z. Moshfegh, *Surface roughness analysis of hydrophilic SiO_2/TiO_2/glass nanobilayers by the level crossing approach*, *Physica A* **392** (2013) 2175–2181.

[297] G.O. Berim, E. Ruckenstein, *Nanodrop on a nanorough hydrophilic solid surface: contact angle dependence on the size, arrangement, and composition of the pillars*, *J. Colloid Int. Sci.* **359** (2011) 304–310.

[298] G.O. Berim, E. Ruckenstein, *Contact angle of a nanodrop on a nanorough solid surface*, *Nanoscale* **7** (2015) 3088–3099.

[299] L. Gao, T.J. McCarthy, *How Wenzel and Cassie were wrong*, *Langmuir* **23** (2007) 3762–3765.

[300] M.B. Hovgaard, K. Rechendorff, J. Chevallier, M. Foss, F. Besenbacher, *Fibronectin adsorption on tantalum: the influence of nanoroughness*, *J. Phys. Chem. B* **112** (2008) 8241–8249.

[301] Chao Luo, Long Li, Jinrong Li, Guang Yang, Shan Ding, Wei Zhi, Jie Weng, Shaobing Zhou, *Modulating cellular behaviors through surface nanoroughness*, *J. Mater. Chem.* **22** (2012) 15654–15664.

[302] P. Linez-Bataillon, F. Monchau, M. Bigerelle, H.F. Hildebrand, *In vitro MC3T3 osteoblast adhesion with respect to surface roughness of Ti_6Al_4V substrates*, *Biomol. Eng.* **19** (2002) 133–141.

[303] K. Cai, J. Bossert, K.D. Jandt, *Does the nanometre scale topography of titanium influence protein adsorption and cell proliferation?*, *Colloid Surf. B Biointerfaces* **49** (2006) 136–144.

[304] T.J. Webster, R.W. Siegel, R. Bizios, *Osteoblast adhesion on nanophase ceramics*, *Biomaterials* **20** (1999) 1221–1227.

[305] C.H. Lohmann, E.M. Tandy, V.L. Sylvia, A.K. Hell-Vocke, D.L. Cochran, D.D. Dean, B.D. Boyan, Z. Schwartz, *Response of normal female human osteoblasts (NHOst) to 17-beta-estradiol is modulated by implant surface morphology*, *J. Biomed. Mater. Res.* **62** (2002) 204–213.

[306] P. Rico, J.C. Rodríguez Hernández, D. Moratal, G. Altankov, M. Monleon Pradas, M. Salmeron, *Substrate-induced assembly of fibronectin into networks: influence of surface chemistry and effect on osteoblast adhesion*, *Tissue Eng. Part A* **15** (2009) 3271–3281.

[307] A. Wennerberg, T. Albrektsson, *Suggested guidelines for the topographic evaluation of implant surfaces*, *Int. J. Oral Maxillofac. Implants* **15** (2000) 331–344.

[308] R. L. Sammons, N. Lumbikanonda, M. Gross, P. Cantzler, *Comparison of osteoblast spreading on microstructured dental implant Surfaces and cell behavior in an explant model of osseointegration: a scanning electron microscopic study*, *Clin. Oral. Impl. Res.* **16** (2005) 657–666.

[309] J. Zhou, C. Chang, R. Zhang, L. Zhang, *Hydrogels prepared from unsubstituted cellulose in NaOH/urea aqueous solution*, *Macromol. Biosci.* **7** (2007) 804–809.

[310] G. Mendonça, D.B. Mendonça, F.J. Aragao, L.F. Cooper, *Advancing dental implant surface technology- from micron- to nanotopography*, *Biomaterials* **29** (2008) 3822–3835.

[311] H.M. Kim, T. Kokubo, S. Fujibayashi, S. Nishiguchi, T. Nakamura, *Bioactive macroporous titanium surface layer on titanium substrate*, *J. Biomed. Mater. Res.* **52** (2000) 553–557.

[312] M. Uchida, H.M. Kim, F. Miyaji, T. Kokubo, T. Nakamura, *Apatite formation on zirconium metal treated with aqueous NaOH*, *Biomaterials* **23** (2002) 313–317.

[313] K. Das, S. Bose, A. Bandyopadhyay, *Surface modifications and cell-materials interactions with anodized Ti*, *Acta Biomater.* **3** (2007) 573–585.

[314] C.J. Wilson, R.E. Clegg, D.I. Leavesley, M.J. Pearcy, *Mediation of biomaterial-cell interactions by adsorbed proteins: a review*, *Tissue Eng.* **11** (2005) 1–18.

[315] W. Norde, *Adsorption of proteins from solution at the solid-liquid interface*, *Adv. Colloid Interface Sci.* **25** (1986) 267–340.

[316] T. Sawase, R. Jimbo, K. Baba, Y. Shibata, T. Ikeda, M. Atsuta, *Photo-induced hydrophilicity enhances initial cell behavior and early bone apposition*, *Clin. Oral Implants Res.* **19** (2008) 491–496.

[317] E.S. Thiana, Z. Ahmad, J. Huang, M.J. Edirisinghe, S.N. Jayasinghe, D.C. Ireland, R.A. Brooks, N. Rushton, W. Bonfield, S.M. Best, *The role of surface wettability and surface charge of electrosprayed nanoapatites on the behaviour of osteoblasts*, *Acta Biomater.* **6** (2010) 750–755.

[318] G. Ávila Ortiz, *El plasma rico en plaquetas como inductor de procesos de proliferación y diferenciación celular epitelio-mesenquimal*. PhD en Odontología, Universidad de Granada, 2006.

[319] P. Akhter, A. Baig, A. Mufti, *Dissolution of Si(100) layers in NaOH aqueous solutions*, *J. Phys. D Appl. Phys.* **22** (1989) 1924–1927.

[320] T. Baum, J. Satherley, D.J. Schiffrin, *Contact angle, gas bubble detachment, and surface roughness in the anisotropic dissolution of Si(100) in aqueous KOH*, *Langmuir* **14** (1998) 2925–2928.

[321] C. Ishino, K. Okumura, *Wetting transitions on textured hydrophilic surfaces*, *Eur. Phys. J. E.* **25** (2008) 415–424.

[322] C. Aparicio, F.J. Gil, C. Fonseca, M. Barbosa, J.A. Planell, *Corrosion behavior of commercially pure titanium shot blasted with different materials and sizes of shot particles for dental implant Applications*, *Biomaterials* **24** (2003) 263–273.

[323] F. Rupp, L. Scheideler, N. Olshanska, M. de Wild, M. Wieland, J. Geis-Gerstorfer, *Enhancing surface free energy and hydrophilicity through chemical modification of microstuctured titanium implant surfaces*, *J. Biomed. Mater. Res.* **76A** (2006) 323–334.

[324] M. Morra, E. Occhiello, F. Garbassi, *Knowledge about polymer surfaces from contact angle measurements*, *Adv. Colloid. Interf. Sci.* **32** (1990) 79–116.

[325] G. Giavaresi, M. Fini, A. Cigada, R. Chiesa, G. Rondelli, L. Rimondini, P. Torricelli, N.N. Aldini, R. Giardino, *Mechanical and histomorphometric evaluations of titanium implants with different surface treatments inserted in sheep cortical bone*, *Biomaterials* **24** (2003) 1538–1594.

[326] C.N. Elias, Y. Oshida, J.H. Cavalcanti Lima, C.A. Muller, *Relationship between surface properties (roughness, wettability and morphology) of titanium and dental implant renoval torque*, *J. Mech. Behav. Biomed. Mat.* **1** (2008) 234–242.

[327] D. Chappard, I. Degasne, G. Huré, E. Legrand, M. Audran, M.F. Bas, *Image analysis measurements of roughness by texture and dractal analysis correlate with contact profilometry*, *Biomaterials* **24** (2003) 1399–1407.

[328] J. Guo, R.J. Padilla, W. Ambrose, I.J. De Kok, L.F. Cooper, *The effect of hydrofluoric acid treatment of TiO_2 grit blasted titanium implants on adherent osteoblast gene expression in vitro and in vivo*, *Biomaterials* **28** (2007) 5418–5425.

[329] S.F. Lamolle, M. Monjo, M. Rubert, H.J. Haugen, S.P. Lyngstadaas, J.E. Ellingsen, *The effect of hydrofluoric acid treatment of titanium surface on nanostructural and chemical changes and the growth of MC3T3-E1 cells*, *Biomaterials* **30** (2009) 736–742.

[330] R. Young, J. Ward, F. Scire, *The topogaphiner: an instrument for measuring surface microtopography*, *Rev. Sci. Instrum.* **43** (1972) 999–1011.

[331] G. Binning, C.F. Quate, Ch. Geber,, *Atomic force microscope*, *Phys. Rev. Lett.* **56** (1986) 930–933.

[332] G. Binning, H. Horner,, *Scanning tunneling microscopy: from birth to adolescence*, *Rev. Mod. Phys.* **59** (1987) 615–625.

[333] F.J. Giessibl, *Advances in atomic force microscopy*, *Rev. Mod. Phys.* **75** (2003) 949–983.

[334] S.M. Hues, R.J. Colton, E. Meyer, H.J. Guntherodt, *Scanning probe microscopy of thin films*, *MRS Bull.* **18** (1993) 41–50.

[335] M. Minsky, *U.S. patent 3013467, Microscopy Apparatus*, Dec., 1961.

[336] M. Minsky, *Memoir on inventing the confocal scanning microscope*, *Scanning* **10** (1988) 128–138.

[337] G.J. Brakenhoff, *Imaging modes in confocal scanning light microscopy (CSLM)*, *J. Microscop.* **117** (1997) 233–242.

[338] G.J. Brakenhoff, P. Blom, P. Barends, *Confocal scanning light microscopy with high aperture immersion lenses*, *J. Microscop.* **117** (1979) 219–232.

[339] R.H. Webb, *Confocal optical microscopy*, *Rep. Prog. Phys.* **59** (1996) 427–471.

[340] N.A.M. Verhaegh, D. Asnaghi, H.N.W. Lekkerkerker, *Transient gels in colloid-polymer mixtures studied with fluorescence confocal scanning laser microscopy*, *Physica A* **264** (1999) 64–74.

[341] D.B. Murphy, *Fundamentals of Light Microscopy and Electronic Imaging.* Wiley-Liss, New York, 2001.

[342] T. Jiubin, Z. Jie, *A small probe with a gradient index lens for confocal measurement*, *Sensors and Actuators A* **104** (2003) 121–126.

[343] T. Wilson, *Confocal microscopy.* Academic Press, San Diego, 1990.

[344] J. Pawley, *Handbook of biological confocal microscopy*. Springer Press, New York, 2006.

[345] D.B. Williams, C.B. Carter, *Transmission electron microscopy: A textbook for materials science*. Plenum Press, New York, 1996.

[346] D.Y. Kwok, R. Lin, M. Mui, A.W. Neumann, *Low-rate dynamic and static contact angles and the determination of solid surface tensions*, *Colloids Surf., A* **116** (1996) 63–77.

[347] D.Y. Kwok, T. Gietzelt, K. Grundke, H.J. Jacobasch, A.W. Neumann, *Contact angle measurements and contact angle interpretation .1. Contact angle measurements by axisymmetric drop shape analysis and a goniometer sessile drop technique*, *Langmuir* **13** (1997) 2880–2894.

[348] J.F. Oliver, C. Huh, S.G. Mason, *Resistance to spreading of liquids by sharp edges*, *J. Colloid Interface Sci.* **59** (1977) 568–581.

[349] C.N.C. Lam, R. Wu, D. Li, M.L. Hair, A.W. Neumann, *Study of the advancing and receding contact angles: liquid sorption as a cause of contact angle hysteresis*, *Adv. Colloid Interface Sci.* **96** (2002) 169–191.

[350] P. Cheng, A.W. Neumann, *Computational Evaluation of Axisymmetrical Drop Shape Analysis-Profile (ADSA-P)*, *Colloids and Surfaces* **62** (1992) 297–305.

[351] P. Roura, J. Fort, *Local thermodynamic derivation of Young's equation*, *J. Colloid Interface Sci.* **272** (2004) 420–429.